Are You Bound or Just Projected? The Behavior of Substructures From Expansion to Galaxy Clusters

Lucas C. Kimmig

Munich 2022

Gebunden oder nur Projiziert? Die Eigenschaften von Substrukturen im Expandierenden Raum und in Galaxienhaufen

Lucas C. Kimmig

München 2022

Are You Bound or Just Projected? The Behavior of Substructures From Expansion to Galaxy Clusters

Lucas C. Kimmig

Master's Thesis

at the University Observatory Munich

Ludwig Maximilian University

Submitted by

Lucas C. Kimmig

born in Wiesbaden

Supervised by

Klaus Dolag

Veronica Biffi

Munich, 22.04.2022

Contents

Contents

Chapter 1

Introduction

The Universe has and still does hold many fascinating wonders that have inspired humanity for millennia. One such puzzle is that of its composition, dominated by components which have continuously evaded direct observation: the aptly named dark matter and dark energy. Currently, the consensus is that the latter is responsible for the observed accelerating expansion of the Universe. However, its nature remains elusive with a multitude of models for its properties. Under the paradigm of the concordance cosmology of ΛCDM, the behavior of the Universe implies the presence of a force acting on all scales. Although it is thus accounted for in current state-of-the-art cosmological simulations, many of the finer details still require a more thorough analysis. In particular, the question of its perturbative effects on orbits has often been restricted to the simplest variants: circles. Yet the fewest real orbits actually are circles, instead exhibiting a zoo of potential configurations. Understanding the impact that the interplay of the elusive dark matter and dark energy has on visible matter can allow deeper insight into their nature as well as the consequences of their presence for all structures in the Universe, from the highest to the lowest redshifts.

The largest of the collapsed structures are galaxy clusters. They have played a vital role in furthering humanity's understanding of the Universe. From providing the first indication of dark matter (Zwicky, 1933) to eventually demonstrating its existence (Lynds & Petrosian, 1986; Soucail et al., 1987; Fort & Mellier, 1994), from posing a challenge to cosmological frameworks with their massive sizes to playing a vital role in constraining the highest precision cosmology today (Voit, 2005), much is owed to these great giants. And yet, there is plenty which is still to be learned from them. They contain some of the highest baryon fractions of all known collapsed objects, on the order of the mean fraction. This makes them prime targets to study baryonic processes on a large range of scales (Cimatti et al., 2019). Furthermore, they can be probed at practically all wavelengths, from X-ray emission due to their hot intracluster medium (Sarazin, 1988) to optical from the galaxies and intracluster light (Contini, 2021), millimeter wavelengths from the distortions in the cosmic microwave background due to the Sunyaev-Zeldovich effect (Sunyaev & Zeldovich, 1972), and finally even radio wavelengths due to synchrotron emission from relativistic electrons (Allen et al., 2011).

Due to their large masses, they further offer a unique opportunity to use the bending of light by the presence of mass, known as gravitational lensing, to directly study the distri-

bution of the otherwise invisible dark matter. Recent findings from both weak and strong gravitational lensing observations (Jauzac et al., 2016) exhibit substructures present within the massive galaxy cluster Abell 2744, which Schwinn et al. (2017) showed cannot be reproduced in simulations when using the typical structure finders. This is because a significant portion of the mass was found by Schwinn et al. (2018) to be contributed from the main halo using the dark matter only simulation `Millenium-XXL` (Angulo et al., 2012). This raises two questions: first, whether this is also reproducible for a fully hydrodynamical simulation and at higher resolution, and second, which differences generally arise between projected and three-dimensional galaxy cluster properties. The latter in particular has far reaching implications for future comparison projects between gravitational lensing observations and cosmological simulations involving substructure.

In summary, this thesis has four central goals:
- Explore the impact of expansion on bound structures characterized by general orbits as well as extended mass profiles.
- Analyze the relationships of galaxy cluster substructure properties in two and three dimensions.
- Develop a conversion function between bound and projected substructure masses.
- Determine whether the extreme substructure masses in Abell 2744 are reproducible within the fully hydrodynamical simulation suite `Magneticum Pathfinder`.

Chapter 2 first introduces the cosmological framework for ΛCDM before deriving the behavior of orbits around a point mass when within an expanding frame, including a comparison with a reduced code developed for cosmological simulation. The scope is broadened then to study the impact of expansion on extended mass distributions in Chapter 3. Chapter 4 provides a brief overview of the history of galaxy cluster observations before presenting a deeper look into the current understanding of their properties as well as structure formation within the Universe as a whole. The methods commonly employed to observe galaxy clusters are discussed in Chapter 5. Chapter 6 develops the method to determine projected substructure masses, with Chapter 7 analyzing more closely the potential tracers for substructure. Chapter 8 presents the results for the projected properties, develops a conversion function to convert three to two dimensional substructure masses and answers whether Abell 2744 can be reproduced. Finally, Chapter 9 summarizes the findings of this work and provides an outlook into exciting future prospects.

Chapter 2

Friedmann-Lemaître versus Archimedes: Do Not Bother My Circles

Cosmological simulations have quickly become one of the most powerful tools to test physical understanding and models of a large variety of objects and systems. Many of the relevant processes for structure formation in the Universe involve a highly non-linear regime making it practically impossible to fully develop in analytical models (Springel, 2005). But for all the varied physical processes increasingly included within the simulations, the questions of the underlying foundation, of the model of the large scale behavior of the Universe itself, is still an ongoing debate (Ellis et al., 2012). The highly mathematical framework can be daunting to understand, making it difficult to intuit the impact it has on the resulting processes within the simulations themselves. Yet it is highly important to have a base comprehension of where the chosen cosmological model could be significant, and where it is not.

This chapter develops an overview of the most key way in which the current standard model of cosmology, a Universe with cold dark matter and a cosmological constant Λ commonly summarized as ΛCDM, directly influences the behavior of orbits of bound structures within it. Section 2.1 introduces the additional term which arises in the equation of motion, where in Section 2.2 a step backwards must be taken to the underlying metric itself which is the progenitor of the term. Therein, a general understanding of the equations is first discussed within a Newtonian context before considering the extension of the metric to the inclusion of a point mass. The force which is experienced by a particle for this case is then transformed in Section 2.3 into a comoving formulation, recovering the initial term from Section 2.1 under the Newtonian limit. An interpretation of the metric used within cosmological simulations is discussed. The picture is then extended to the behavior of the Hubble constant and other parameters for the ΛCDM cosmology in Section 2.4, with a special emphasis on typical measures of bound structures. Afterwards, Section 2.5 goes over one of the typical perturbation theory approaches employed to analyze circular orbits around a point mass potential from the literature, arriving at an initial understanding of how strongly which bound structures are affected. This understanding is subsequently deepened in Section 2.6 by deriving general analytical solutions for the behavior of orbits within such point mass

potentials, with a key tool employed being the effective potential. In Section 2.7 the theoretical conclusions are compared to a specially made simulation, reduced to just the typical comoving implementation to best facilitate this. The findings are then summarized and discussed in Section 2.8.

2.1 Getting Things Moving

Over time, all larger simulation codes have adopted practically the same implementation of the standard model of cosmology, namely a ΛCDM-cosmology (see for example Blumenthal et al. 1984) with a Friedmann-Lemaître-Robertson-Walker (FLRW) metric (Friedmann, 1922; Robertson, 1935; Lemaître, 1927; Walker, 1937). However, the equation of motion always features the same additional term relative to a pure Newtonian case, taking the form in comoving coordinates as:

$$\ddot{x}(t) = -2H(t)\,\dot{x}(t) + \frac{F(x,t)}{a^3(t)}, \tag{2.1}$$

with $F(x,t) = -GM/x^2(t)$ the gravitational force and $a(t)$ the scale factor. This striking term $-2H(t)\,\dot{x}(t)$ is immediately noticeable, and is present consistently. For example it can be found for `GADGET` in section 5.6 (Equations 53-55 and 59-62) from Springel et al. (2001) as well as with a slight amendment for `Gadget` 2 as per section 4.1 (Equations 27 and 28) from Springel (2005). The latter is the same implementation as for `Gadget` 3 and therefore also for `Magneticum Pathfinder` (Dolag, 2022; Hirschmann et al., 2014; Teklu et al., 2015), which is the simulation used for the later chapters of this thesis. For `Illustris` (Vogelsberger et al., 2014), there is a split-up in the implementation of gas versus dark matter, with the former done via the code `Arepo` (Springel, 2010) where the term is described in section 7.3 (Equations 115-117) and the latter via a TreePM method, where the cosmology is implemented as in section 2.3 (Equations 8 and 9) from Xu (1995). All of these codes employ the same functional equation of motion for the collisionless dark matter particles, which raises the simple question: Where does the additional term come from?

2.2 The Expanding Metric

At the core of any discussion of cosmological simulations lies the model of the Universe that is assumed, the fundamental systems within which the simulation runs. When taking inertial systems as the basis, one arrives at Newtonian mechanics, but these have since been superseded by general relativity (GR). A core new feature there lies in the interaction between spacetime and the bodies within it, allowing warping and twisting of the fabric of spacetime (the metric) itself. Furthermore, energy itself also warps spacetime, as it is seen to be equivalent to mass. To calculate how any system evolves, one would have to solve the

Einstein Field Equations (Ellis et al., 2012),

$$G^{\mu\nu} = \frac{8\pi G}{c^4} T^{\mu\nu}, \tag{2.2}$$

where $G^{\mu\nu}$ is the Einstein tensor, $T^{\mu\nu}$ is the stress-energy tensor and μ, ν are the spacetime indexes (t, x, y, z). Unfortunately, this proves to be quite troublesome for any realistically complex systems.

2.2.1 Assumptions and Newtonian "Derivation"

The most common models of the Universe then must make some initial assumptions to simplify these equations. On very large scales, for ΛCDM it is assumed to be:

- isotropic, so possessing uniformity in all orientations
- homogeneous, so $\rho' = p' = 0$

where primes denote derivatives with respect to space. From these assumptions alone, it is possible to derive a faux-Newtonian "derivation" (following roughly Hamilton 2020): homogeneity gives $\rho = const$ and isotropy implies a spherical symmetry that here is taken to be a sphere of radius a, such that the total mass of the Universe is then $M = \frac{4}{3}\pi\rho a^3$. Taking an outer shell of mass m and determining the force felt as $-GMm/a^2$, it follows under the assumption of the total energy being conserved:

$$\frac{1}{2}m\dot{a}^2 + \frac{-GMm}{a} = E = const \equiv -\frac{kmc^2}{2}$$

$$\frac{\dot{a}^2}{a^2} + \frac{-2G \cdot 4\pi\rho a^3}{3a^3} = -\frac{kc^2}{2a^2}$$

$$\frac{\dot{a}^2}{a^2} \equiv H^2 = \frac{8\pi G}{3}\rho - \frac{kc^2}{a^2} \tag{2.3}$$

This first equivalence $E = -kmc^2/2$ cannot be derived by a Newtonian treatment and instead comes from general relativity, and in a more rigid derivation k is a measure for the curvature, with $k = 0$ representing a flat metric. As curvature of the underlying space is not a part of the Newtonian treatment, this equivalence is to be treated with caution. Nonetheless, this recovers the form of the first Friedmann equation, and by assuming adiabatic expansion the second can be derived. Via the first law of thermodynamics:

$$dE + pdV = 0$$

$$\xrightarrow{E=c^2\rho V} d\left(c^2\rho\frac{4\pi a^3}{3}\right) + pd\left(\frac{4\pi a^3}{3}\right) = 0$$

$$c^2 d(\rho a^3) + pd(a^3) = 0$$

$$\frac{1}{dt}\dot{\rho} + 3\left(\rho + \frac{p}{c^2}\right)\frac{\dot{a}}{a} = 0$$

$$\dot{\rho} = -3\left(\rho + \frac{p}{c^2}\right)\frac{\dot{a}}{a} \tag{2.4}$$

If Equation 2.3 is then multiplied by a^2 and differentiated with respect to time it takes the form:

$$2\dot{a}\ddot{a} = \frac{8\pi G}{3}(\dot{\rho}a^2 + 2\rho a\dot{a})$$

$$\xrightarrow{\text{Equation 2.4}} 2\dot{a}\ddot{a} = \frac{8\pi G}{3}a\dot{a}\left(-\rho - 3\frac{p}{c^2}\right)$$

$$\frac{\ddot{a}}{a} = -\frac{4\pi G}{3}\left(\rho + 3\frac{p}{c^2}\right) \tag{2.5}$$

This represents the second Friedmann equation, and together both equations are indeed equivalent to those derived by careful treatment of the derivation (see Arnau Romeu (2014) for a nice example of this). They are discussed further in Section 2.3, but also immediately raise an interesting question. The derivation of the second law required the assumption of *adiabatic* expansion, that is to say the entropy is conserved. This is indeed the case for an FLRW universe even with a different mix of particles (Hamilton, 2020). And yet clearly entropy *does increase*, so what is happening here? It is the fluctuations away from perfect homogeneity and isotropy, the core assumptions of the FLRW metric, that allow entropy to increase. Thus, fundamentally, the FLRW is at best an approximation of the actual metric, and at worst can lead to false conclusions if employed without caution.

2.2.2 A Static Treatment

If one were to require the Universe to remain static, this is equivalent to setting the condition of $a(t) = a = const$ for the scale factor. It follows then that $H \propto \dot{a}^2 = 0$ and then from Equation 2.3:

$$\frac{8\pi G}{3}\rho = \frac{kc^2}{a^2} \longleftrightarrow \rho_{\text{static}} = \frac{3kc^2}{8\pi G a^2}.$$

Thus to remain static the Universe must have a density exactly equal to ρ_{static}. This, however, requires also $\ddot{a} = 0$, such that with Equation 2.5 this would imply that there is a dominant vacuum energy with an equation of state as $c^2\rho_{\text{static}} = -\frac{1}{3}p$. This universe is unstable, in the sense that any slight perturbation to either curvature or the cosmological constant density will either cause fully accelerated expansion or re-collapse into a singularity (Ellis et al., 2012).

2.2.3 The Expanding de Sitter Universe

If this term from a dominant vacuum energy is added, but the Universe is allowed to expand Equation 2.3 gives:

$$H^2 = \frac{8\pi G}{3}\rho_v = \frac{\Lambda c^2}{3}.$$

This results in $a(t) = a_0 \exp H(t - t_0)$ which is then an exponentially expanding Universe. For some models of inflation this is essentially what occurs, where for the example of the

single field slow-roll model in the phase where $-\dot{H}/H^2 \ll 1$ this solution is exactly recovered – see Kamionkowski & Kovetz (2016). Note that the curvature term has been ignored because it goes as $\propto a^{-2}$ and thus quickly vanishes for such an expanding Universe – which is also the reason why inflation of this kind predicts a flat Universe. Hence though not of importance for later times, the expanding de Sitter Universe is of great interest when considering the very early phases.

2.2.4 Recovering the Friedmann-Lemaître-Robertson-Walker Metric

From the assumptions of homogeneity and isotropy it is possible to derive the well-known FLRW metric when working in the general relativistic framework. This is done by assuming further the cosmic matter-energy fluid to be perfect (i.e., dissipation-less) and by modifying Equation 2.2, namely adding a cosmological constant Λ,

$$G^{\mu\nu} + \Lambda g^{\mu\nu} = \frac{8\pi G}{c^4} T^{\mu\nu}, \qquad (2.6)$$

where $g^{\mu\nu}$ is the metric tensor. The Λ term is added because observations find the Universe to be flat (Komatsu et al., 2011; Planck Collaboration, 2020), $k = 0$, such that without it the requirements of homogeneity and isotropy would give $\rho = 0$ for the fluid. The full derivation of the FLRW metric starting just from this Equation 2.6 is quite tedious – see Mitra (2012) – but recovers the well-known result as their Equation 59:

$$ds^2 = dt^2 - a^2(t)\left(\frac{d\hat{r}^2}{1 - k\hat{r}^2} + \hat{r}^2 d\Omega\right). \qquad (2.7)$$

Note that the term should indeed have a plus as written here in front of the $\hat{r}^2 d\Omega$ term, which can be seen when plugging in their results into Equation 58 from Mitra (2012). Furthermore, it should be noted that this derivation is done in the comoving frame, thus confirming the FLRW metric in this form to be the comoving version (so $\hat{r}$ is the comoving position). This is a non-trivial observation, as prior derivations would implicitly assume Weyl's postulate, stipulating that there exists a family of spatial hyperslices everywhere orthogonal to the world lines of the fluid particles. Sometimes this additionally includes the stipulation that all world lines are timelike geodesics and originate from/cross only in one point (the Big Bang).

The intuitive understanding of the consequence of this postulate is that there exists a reference frame for each time t, such that the fundamental fluid particles can define a comoving frame where their physical coordinates are constant (at least relative to the impact of expansion), as seen in Figure 2.1. The mathematical consequence is that no terms as $dt \cdot dxyz$ appear in the metric, creating a clear 3+1 split between space and time. A good description of the impact of this postulate and how in prior derivations of the FLRW metric it is implicitly and necessarily assumed is given in Rugh & Zinkernagel (2010), with Equation 1 therein the natural fundamental form of the metric when assuming Weyl's postulate. The
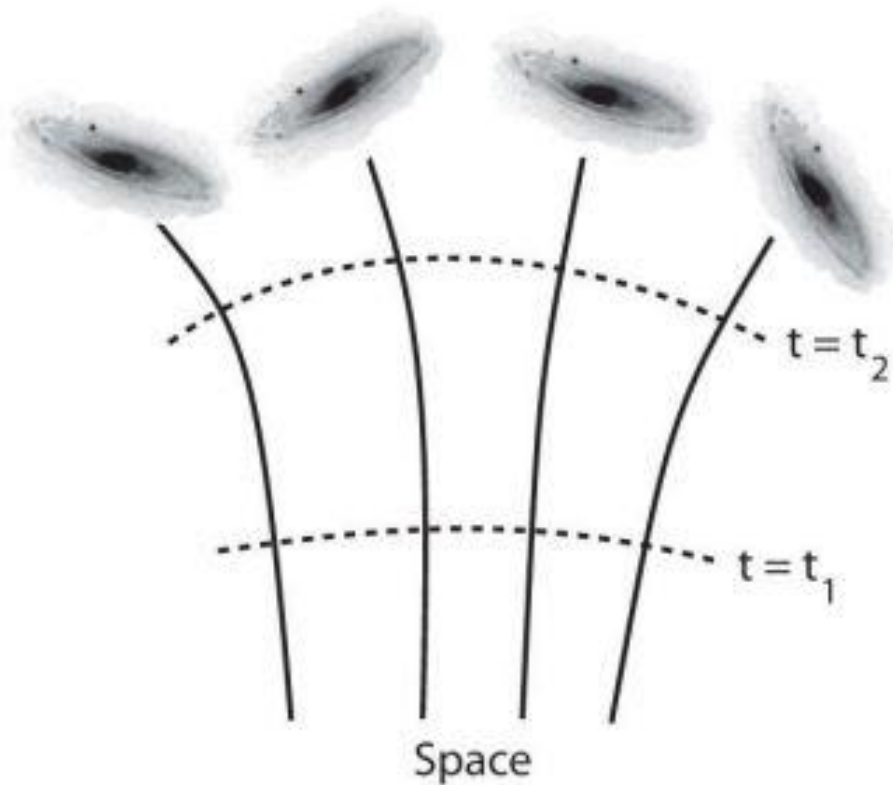
Figure 2.1: Illustration of the Weyl postulate as given by Melia (2012), showing the orthogonal hypersurfaces (dashed lines) at different times given by their position along the timelike geodesics of the fundamental fluid particles (solid lines). Each dashed line thus defines a comoving frame.

cosmological principle (homogeneity and isotropy) then provides the form of the spatial component after the split and recovers Equation 2.7.

2.2.5   From the Metric to Force Terms

The typical FLRW metric of the Universe as given in Equation 2.7 makes as assumptions for large scales: homogeneity, isotropy, no diffusion terms and entropy conservation, as discussed prior. However, the Universe fulfills none of those conditions on smaller scales, such that there must be a transition at some scale and subsequently also in the metric employed. A possible bridge between the large-scale FLRW metric and smaller scales is the one given by McVittie (1933). Here the smaller scale metric employed is the Schwarzschild metric for non-expanding isotropic coordinates, such that the asymptotic behavior of the McVittie metric at large/small scales collapses to FLRW/Schwarzschild. A full derivation and extension (accounting also for the closed/open form of the metric, not just the flat $k = 0$ variant) of this metric using geometric algebra on the basis of GR is done by Nandra et al. (2012). It is important to note here that usage of the Schwarzschild metric at small scales necessarily defines an event horizon within which no matter can take part in expansion. The final metric

for a flat Universe follows as Equation 23 therein (given in natural units $c = G = 1$):

$$\mathrm{d}s^2 = \left[1 - \frac{2M}{r} - r^2 H^2(t)\right]\mathrm{d}t^2 + 2rH(t)\left(1 - \frac{2M}{r}\right)^{-1/2}\mathrm{d}r\mathrm{d}t - \left(1 - \frac{2M}{r}\right)^{-1}\mathrm{d}r^2 - r^2\mathrm{d}\Omega^2,$$
(2.8)

where M is the mass of the particle giving rise to the Schwarzschild portion of the metric, r the physical distance of any test particle to this point-mass, and where $\mathrm{d}\Omega^2 = \mathrm{d}\omega^2 + sin^2(\omega)\mathrm{d}\phi^2$ and t is the cosmic time. For easier comparability to following derivations, Equation 2.8 is converted to SI-units by noting $2M/r \equiv r_s/r = (2GM/c^2)/r$. Furthermore, it is sensible to define $(2GM/c^2)/r \equiv \delta$, which is then a measure for the distance r of the test particle with $\lim_{r\to\infty} \delta = 0$. Additionally, another variable is defined as $\sigma \equiv r/(c/H(t))$, thus representing a measure for the distance of the test particle relative to the horizon scale $c/H(t)$. The form of Equation 2.8 in SI-units then is:

$$\mathrm{d}s^2 = c^2\left[1 - \delta - \sigma^2\right]\mathrm{d}t^2 + \frac{2c\sigma}{\sqrt{1-\delta}}\mathrm{d}r\mathrm{d}t - \frac{1}{1-\delta}\mathrm{d}r^2 - r^2\mathrm{d}\Omega^2$$
(2.9)

In this metric, the total background density is equivalent to that obtained from FLRW, which intuits one of the core principles that the McVittie metric essentially describes a point-mass within an otherwise spatially-flat FLRW background. Geodesic motion of a test particle within such a metric (for example orbiting the central mass while both lie in the expanding frame given by FLRW) gives the equation of motion through solving the Euler-Lagrange equations, as done by Nandra et al. (2012). The resulting acceleration for the particle in the case of a flat Universe ($k = 0$) is given by Equation 61 therein:

$$\ddot{r} = \frac{L^2}{r^3}\left(1 - \frac{3M}{r}\right) - \frac{M}{r^2} + rH^2(t) - \frac{2r^2 H(t)H'(t)}{1 - \frac{2M}{r} - r^2 H^2(t)}\dot{r}\dot{t}$$

$$+ \frac{rH'(t)}{\sqrt{1 - \frac{2M}{r}}\left(1 - \frac{2M}{r} - r^2 H^2(t)\right)}\dot{r}^2 + \frac{rH'(t)\sqrt{1 - \frac{2M}{r}}}{1 - \frac{2M}{r} - r^2 H^2(t)}\left(1 + \frac{L^2}{r^2}\right)$$
(2.10)

where it should be noted that this is also in natural units ($c = G = 1$). Dots denote differentiation with respect to the proper time τ, while primes are with respect to the cosmic time t. $L = r^2\dot{\phi}$ is the peculiar angular momentum per mass of the test particle, with $\dot{phi}$ the angular speed. Converting again to SI-units gives:

$$\ddot{r} = \frac{L^2}{r^3}\left(1 - \frac{3}{2}\delta\right) - \frac{c^2\delta}{2r} + c\sigma H(t) - \frac{2\sigma rH'(t)}{c(1 - \delta - \sigma^2)}\dot{r}\dot{t}$$

$$+ \frac{rH'(t)}{c^2\sqrt{1-\delta}\left(1 - \delta - \sigma^2\right)}\dot{r}^2 + \frac{rH'(t)\sqrt{1-\delta}}{1 - \delta - \sigma^2}\left(1 + \frac{L^2}{c^2 r^2}\right)$$

$$\ddot{r} = \frac{L^2}{r^3}\left(1 - \frac{3}{2}\delta\right) - \frac{c^2\delta}{2r} + c\sigma H(t) + \frac{rH'(t)\sqrt{1-\delta}}{1 - \delta - \sigma^2}\left[\frac{2\sigma\dot{r}\dot{t}}{c\sqrt{1-\sigma}} + \frac{\dot{r}^2}{c^2(1-\sigma)} + \left(1 + \frac{L^2}{c^2 r^2}\right)\right].$$
(2.11)

This is the full form of the force for a test particle traveling in an expanding background which includes a fixed point-mass.

Finally, to compare with the force the test particle would feel in a non-expanding, purely Newtonian universe, it can be noted that the Newtonian gravitational acceleration is exactly the term $a_{\text{Newton}} = GM/r^2 = c^2\delta/(2r)$, while the centrifugal acceleration is $a_{\text{cent}} = r\dot{\phi}^2 \equiv r\omega^2 = L^2/r^3$. *All other terms* arise from the general relativistic treatment of the expanding McVittie metric.

2.3   From the Force Terms to Cosmological Simulation Codes

Given the complicated form of the force-law of a test particle in an expanding universe with one other mass m at fixed position as given in Equation 2.11 (i.e, for the McVittie metric), it is reasonable to seek out approximations. To this end, the values of the parameters (δ, σ) are considered, noting that for any scales where particle to particle forces matter their separation r is significantly smaller than the Hubble length, i.e., $\sigma = r/(c/H(t)) \ll 1$. Similarly, aside from incredibly dense objects the interaction occurs also on scales significantly larger than the Schwarzschild radius, i.e., $\delta = r_s/r \ll 1$. These conditions combined are also called the "weak-field" approximation when expanding to first order (Nandra et al., 2012). Additionally assuming the test particles to be moving at non-relativistic comoving velocities $\dot{r} \approx 0$ it follows further that the proper and coordinate time are approximately the same, $\dot{t} = 1$. In this combined "Newtonian" limit it follows that $1 - \sigma, 1 - \delta, 1 - \delta - \sigma^2 \approx 0$, as well as $c \to \infty$, such that Equation 2.11 becomes:

$$\ddot{r} = \frac{L^2}{r^3} \cdot 1 - \frac{c^2\delta}{2r} + c\sigma H(t) + \frac{rH'(t) \cdot 1}{1}[0 + 0 + 1]$$

$$\ddot{r} = \frac{L^2}{r^3} - \frac{GM}{r^2} + rH^2(t) + rH'(t) = \frac{L^2}{r^3} - \frac{GM}{r^2} + \frac{\ddot{a}}{a}r = \frac{L^2}{r^3} - \frac{GM}{r^2} - q(t)H^2(t)r, \quad (2.12)$$

where in the final step the deceleration parameter $q = -(H'(t)/H^2(t) + 1)$ was introduced. Note that in the following the centrifugal term is dropped as the comoving frame chosen is not co-rotating to the test particle. For this limit it can then be seen that the apparent "force" felt by the particle through the addition of the expanding background is the term $-q(t)H^2(t)r$, matching the result found in Equation 62 of Nandra et al. (2012). Some caution must be kept when working with varying frames of definition, as for example simply equating the change in physical coordinate r with a change in proper distance is true only for the case of a flat Universe $k = 0$ (Nandra et al., 2012). Nonetheless, there is a certain beauty when considering that gravity itself is also more accurately formulated as a distortion of spacetime, and that the mass and energy as the cause for this distortion further impact the large-scale behavior, which in turn manifests as a separate force-like term from the drag in the expanding behavior of spacetime. An exceedingly simple variant on the derivation of Equation 2.12 directly from the Newtonian limit of the metric (Equation 2.10) has been shown by Nesseris & Perivolaropoulos (2004).

It is important to emphasize two key points: firstly, that the additional term is not a force in the true sense but instead a pseudo-force appearing depending on the coordinate system chosen (see also Section 2.5) and secondly, it is not the act of expanding which causes the additional term (as all terms $\dot{a}$ cancel), but rather the acceleration or deceleration of the expansion. expansion $\dot{a} > 0$ causes particles to join the Hubble flow as their peculiar momentum decays with time relative to the recession velocity (Davis et al., 2003), but whether they join it by receding from an observer or by coming towards them, passing them by and then joining it on the other side is determined by q, with the former happening for $q < 0$ and the latter for $q > 0$ (Davis et al., 2003).

There are a few things to note for the initial form of Equation 2.11. Firstly, as the point-mass forms the basis of the Schwarzschild portions of the metric this does not account for coupled interaction back from the test particle. As such this is not the metric for multiple particles lying within an expanding background, as in this case one would have to include a Schwarzschild metric portion for every point-mass to model the local distortions of spacetime individually. Furthermore, realistic systems have extended distributions of mass, i.e., are not point-like. The Newtonian limit defined here, however, is equivalent to requiring the local dynamics to be essentially Newtonian in nature, thus allowing the modeling of multiple point masses without the need for individual Schwarzschild modeling. Furthermore, this allows the shell theorem (Newton, 1687) to be applied, such that for an extended mass distribution which is spherically symmetric in nature a particle orbiting would feel a gravitational force equivalent to a point mass at the center, while all mass outside would have a net zero force. This allows the equation of motion in Equation 2.12 derived originally for a particle orbiting a point mass also to be applied to such extended mass distributions, which is done in Chapter 3.

By adopting a flat Universe, Equation 2.7 simplifies such that a comoving frame can be defined which has a direct proportionality to the physical frame dependent on only the scale factor $a(t)$,

$$r(t) = a(t) \cdot x(t). \tag{2.13}$$

Finally, Equation 2.12 and Equation 2.1 can then be related directly by noting $-q(t)H^2(t)r = \ddot{a}x$ such that:

$$-\frac{GM}{r^2} - q(t)H^2(t)r \overset{!}{=} \ddot{r}(t) = \frac{\mathrm{d}^2(ax)}{\mathrm{d}t^2} = \ddot{a}x + 2\dot{a}\dot{x} + a\ddot{x}$$

$$-\frac{GM}{(ax)^2} + \ddot{a}x = \ddot{a}x + 2\dot{a}\dot{x} + a\ddot{x}$$

$$\Leftrightarrow a\ddot{x} = -\frac{GM}{(ax)^2} - 2\dot{a}\dot{x}$$

$$\ddot{x}(t) = -2H(t)\dot{x}(t) + \frac{F(x,t)}{a^3(t)}, \tag{2.14}$$

where in the final step $F(x,t) \equiv -GM/x^2(t)$ and the form of Equation 2.12 is fully recovered. Interestingly then, in the comoving frame the dependency on $\ddot{a}$ disappears, meaning that the

impact of the acceleration of the expanding Universe on a particle inherently matches that from transforming to a comoving frame.

This, however, is not where some implementations stop. The velocity dependence that arises can be somewhat tedious to account for, especially when employing integrators such as the Leapfrog KDK where force calculations want to be purely position dependent to split up "kick" and "drift" steps – see Binney & Tremaine (2008) for more. As such it is elegant to transform to another frame, akin to the comoving one but which results in simpler force laws. It turns out to be useful to define the time-coordinate as $\tau = \ln(a)$ for this system, such that – denoting derivatives in τ with primes – for a given variable g:

$$\dot{g} = \frac{\mathrm{d}g}{\mathrm{d}t} = \frac{\mathrm{d}a}{\mathrm{d}t}\frac{\mathrm{d}\ln(a)}{\mathrm{d}a}\frac{\mathrm{d}g}{\mathrm{d}\ln(a)} = \frac{\dot{a}}{a}g' = H(a)g'. \tag{2.15}$$

Note that τ is *not* the proper time. Defining $p \equiv a^2\dot{x}$ and its derivative in τ gives:

$$p' \stackrel{(2.15)}{=} \frac{1}{H(a)}\dot{p} = \frac{1}{H(a)}\left(2a\dot{a}\dot{x} + a^2\ddot{x}\right) = \frac{a}{H(a)}\left(2\dot{a}\dot{x} + a\ddot{x}\right)$$

$$\stackrel{(2.1)}{=} \frac{a}{H(a)}\left(2\dot{a}\dot{x} - 2\dot{a}\dot{x} + \frac{F(x,a)}{a^2}\right) = \frac{F(x,a)}{\dot{a}}, \tag{2.16}$$

which is effectively the new acceleration term, while for the velocity:

$$x' \stackrel{(2.15)}{=} \frac{1}{H(a)}\dot{x} = \frac{p}{a^2H(a)}. \tag{2.17}$$

The set of variables for the new transformed system are then (x, x', p') with the time variable τ, and is equivalent to the set of parameters employed for `GADGET-2` (Springel, 2005) and thus also for `Magneticum Pathfinder` (Dolag, 2022), with the advantage that both time-dependent variables, (x', p'), are dependent only on the time τ and one other variable, allowing a split up of the time integration steps. Note that therein the integration is however done with a TreePM method as opposed to a Leapfrog KDK.

2.4 ΛCDM and Different Cosmologies

To understand what the results from Section 2.2 imply for bound structures in the Universe, it is first necessary to be able to quantify them as well as the large-scale properties of the Universe itself. To this end, this section will explore some of the critical parameters for a flat FLRW Universe $k = 0$ which will later allow for simpler forms of the equations.

From Equation 2.3 for a flat FLRW universe $k = 0$ it follows that the total energy density ρ must be equal to the critical density (Binney & Tremaine, 2008), defined as:

$$\rho_c(t) \equiv \frac{3H^2(t)}{8\pi G}. \tag{2.18}$$

Under the current understanding, if the current critical density is defined as $\rho_{c,0} \equiv \rho_c(t = 0)$ and the fraction contained in matter is $\Omega_{m,0} \equiv \rho_m(t = 0)/\rho_{c,0}$, it follows that the observed total matter density is *smaller* than the critical density with only $\Omega_{m,0} \leq 0.3$ (Binney & Tremaine, 2008). A possible solution is the presence of other forms of energy, with differing equations of state. It is in large parts this discrepancy which is a key motivator for the existence of dark energy.

The definition of the critical density allows Equation 2.3 to take a simple form even in the presence of mutliple forms of energy. Defining $\Omega_i(t) \equiv \rho_i(t)/\rho_c(t)$, with ρ_i the different components of the total energy density, Equation 2.3 takes the form:

$$1 = \Omega = \Omega_m + \Omega_r + \Omega_\Lambda.$$

Often the behavior of the energy densities is replaced with their current values (denoted by subscript "0"), considering that the energy densities ρ_i all vary differently with volume as $\Omega_i(t) = \Omega_{0,i} \cdot a^{l_i}(t)$, such that instead pulling all time dependence into the scale factor directly:

$$\frac{H^2(a)}{H_0} = \Omega_{0,r} \cdot a^{-4} + \Omega_{0,m} \cdot a^{-3} + \Omega_{0,\Lambda}$$

$$H(a) = H_0\sqrt{\Omega_{0,r} \cdot a^{-4} + \Omega_{0,m} \cdot a^{-3} + \Omega_{0,\Lambda}} \tag{2.19}$$

Note that the equation of state for dark energy considered here is that for ΛCDM, i.e., $p_\Lambda = w\rho_\Lambda = -1 \cdot \rho_\Lambda$, hence $\Omega_\Lambda(t) = \Omega_{0,\Lambda} \cdot a^0(t) = \Omega_{0,\Lambda}$.

To understand the implications of Equation 2.34, it is first necessary to examine the behavior of the term $a/\ddot{a}$. This is done for three possible cosmologies, where all are taken to be flat $\Omega_k = 0$. The phases considered are a matter or dark energy dominated phase ($\Omega_m = 1$ or $\Omega_\Lambda = 1$) as well as an intermittent phase $0 < \Omega_m < 1$. Beginning with the first Friedmann equation, given in the form Equation 2.19 and assuming $\Omega_r(t) \approx 0$ for the times considered, it can be rearranged as:

$$\frac{da}{dt}a^{-1} = \frac{\dot{a}}{a} = H(a) = H_0\sqrt{\Omega_{0,m} \cdot a^{-3} + \Omega_{0,\Lambda}}$$

$$\frac{da}{\sqrt{\Omega_{0,m} \cdot a^{-1} + \Omega_{0,\Lambda} \cdot a^2}} = dt H_0$$

$$\int \frac{da}{\sqrt{\Omega_{0,m} \cdot a^{-1} + \Omega_{0,\Lambda} \cdot a^2}} = \int dt H_0 \tag{2.20}$$

For the cases $\Omega_m = 1$ or $\Omega_\Lambda = 1$ this is analytically solvable as the typical results $a(t) \propto t^{2/3}$ or $a(t) \propto \exp t$, where it should however be cautioned that it is important to define a relative time and scale factor. Taking a_0 to be the scale factor at time t_0 it follows then for $\Omega_m = 1$ that:

$$a_m(t) = \left[H_0 \cdot \frac{3}{2}(t - t_0) + a_0^{3/2}\right]^{2/3}, \tag{2.21}$$
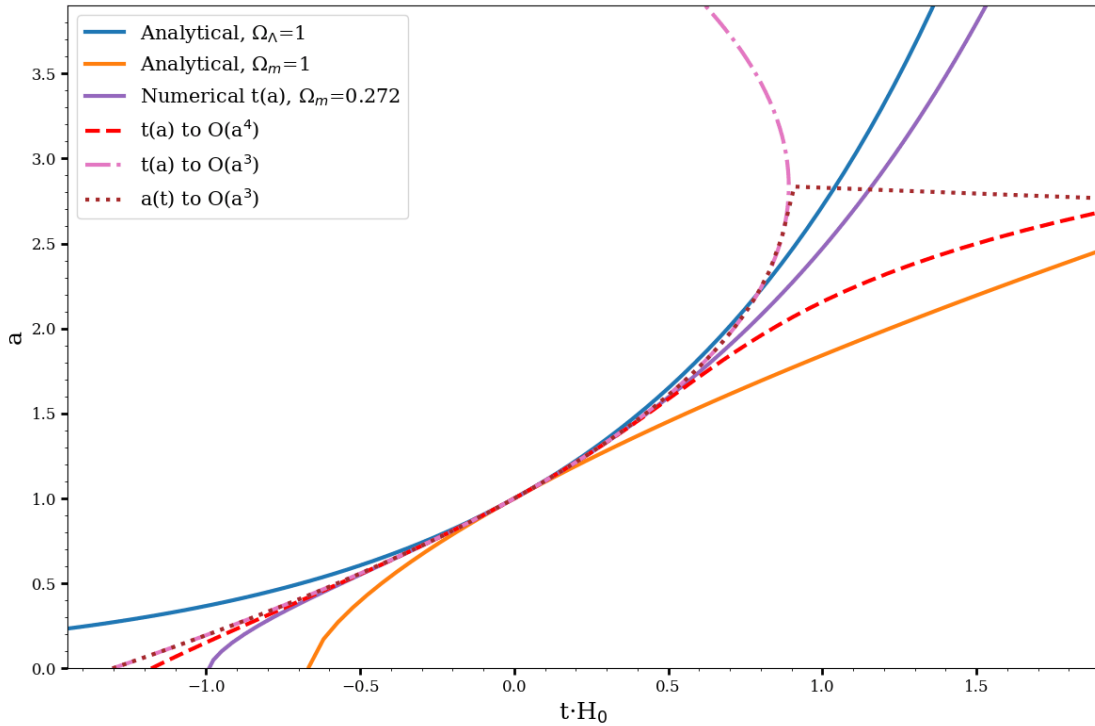
Figure 2.2: The scale factor as a function of coordinate time (defined relative to $a_0 = 1$ at $t_0 = 0$) for the case of a dark energy (blue) and mass (orange) dominated Universe, as well as the numerically integrated form for an intermittent variant with $\Omega_m = 0.272$ and $\Omega_\Lambda = 0.728$ (purple), in accordance with the WMAP-7 parameters (Komatsu et al., 2011). The analytical approximations out to third and fourth order of $t(a)$ are depicted in red and pink, with the inversion $a(t)$ of the third order line in brown.

while for $\Omega_\Lambda = 1$

$$a_\Lambda(t) = a_0 \cdot \exp\left(H_0 \cdot (t - t_0)\right), \tag{2.22}$$

with the subscripts denoting the dominant phase (matter or dark energy).

The intermittent phase $0 < \Omega_m, \Omega_\Lambda < 1$ unfortunately is not analytically solvable, though it can be numerically integrated. However, even an approximated form of $a(t)$ would allow for functional form of $a(t)/\ddot{a}(t)$, which in turn would allow exact tracing of the impact of expansion with time (see also Section 2.5). To this end, Appendix A.1 discusses more extensively a Taylor expansion of the integrand on the left in Equation 2.20.

The resulting relations between the scale factor a and the coordinate time t are plotted for the three cases, as well as for the analytical approximations of both $t(a)$ and the inversion $a(t)$ from Appendix A.1, in Figure 2.2. The purple line for the chosen WMAP-7 parameters (Komatsu et al., 2011) shows the bend downwards resulting from matter-domination for early times, resulting in an age of the Universe of $t_{age} = 1/H_0 \approx 13.9\,\text{Gyr}$, somewhat larger than the values found by Komatsu et al. (2011) due to the exclusion of the radiation term Ω_r here which would further increase the downwards trend. At later times, the scale factor begins to increase exponentially as the Universe becomes dominated by dark energy. The form of $a(t)$ is reproduced quite well by the analytical forms of $t(a)$ from the Taylor expansion as well as
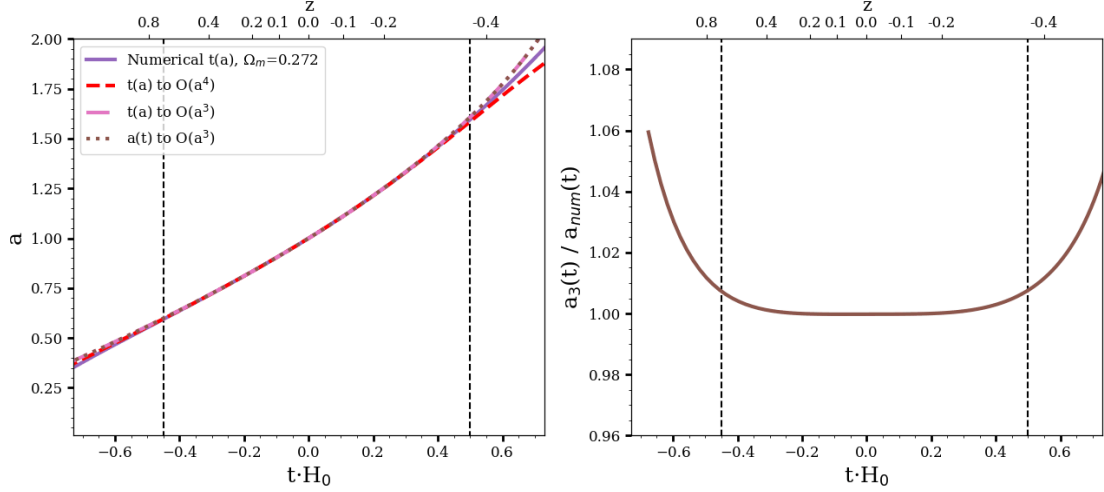
Figure 2.3: The scale factor as a function of time (defined relative to $a_0 = 1, t_0 = 0$) for the case of a dark energy (blue) and mass (orange) dominated Universe, as well as the numerically integrated form for an intermittent variant with $\Omega_m = 0.272$ and $\Omega_\Lambda = 0.728$ (green), in accordance with the WMAP-7 parameters (Komatsu et al., 2011).

the analytical inversion $a(t)$ in Appendix A.1, where the latter fails beyond $t \cdot H_0 > 0.8$ as the third order $t(a)$ bends around here and therefore would require two y-values for one x-value.

Figure 2.3 shows on the left a zoomed in region of the $a - t$ relation for a cosmology with $\Omega_m = 0.272$ and $\Omega_\Lambda = 0.728$ as per WMAP-7 (Komatsu et al., 2011). Depicted are the curve from the numerical integration in purple, as well as the Taylor series of $t(a)$ up to order 3 (pink) or 4 (red), with both fitting the immediate range around $a_0 = 1$ quite well. The inversion $a(t)$ of the third order $t(a)$ is the brown line, showing a good match to the numerical line. This can be seen more clearly on the right, where the ratio of the two is plotted as a function of coordinate time. For the range $-0.45 < H_0 t < 0.5$ the deviation is below 1%. This would therefore allow generally for an approximated analytical form of $\ddot{a}$ and subsequently of the expanding force in Equation 2.12, however the derivatives quickly grow to unwieldy sizes and are as such not pursued here further.

2.4.1 Critical Overdensities

Having defined the large scale properties of an expanding Universe, it is then necessary to do the same for some typical measures of bound structures within it. This is accomplished by defining regions of overdensities which have a mean density that is a factor Δ_c higher than the critical density $\rho_c(a)$ as given in Equation 2.18. The total mass within the region M_{Δ_c} is then governed entirely by its extend r_{Δ_c} and the critical density, as:

$$M_{\Delta_c}(a) = \frac{4\pi}{3} r_{\Delta_c}^3(a) \cdot \Delta_c \rho_c(a) = \frac{4\pi}{3} r_{\Delta_c}^3(a) \cdot \Delta_c \cdot \frac{3H^2(a)}{8\pi G} = \frac{\Delta_c}{2} \cdot \frac{r_{\Delta_c}^3(a) \cdot H^2(a)}{G},$$

$$M_{\Delta_c}(a) \overset{(2.19)}{=} \frac{\Delta_c}{2} \cdot \frac{r_{\Delta_c}^3(a) \cdot H_0^2}{G} \left(\Omega_{0,r} \cdot a^{-4} + \Omega_{0,m} \cdot a^{-3} + \Omega_{0,\Lambda} \right) \qquad (2.23)$$

or equivalently

$$r_{\Delta_c}(a) = \left(\frac{2}{\Delta_c} \cdot \frac{GM_{\Delta_c}}{H^2(a)} \right)^{1/3}, \tag{2.24}$$

where it should be emphasized that as the critical density changes with time (i.e., with scale factor) so is the definition of M_{Δ_c} and subsequently r_{Δ_c} time dependent. One commonly used measure is that for $\Delta_{200} = 200$, where then M_{200} is the mass within a sphere of mean density 200 times the critical density, given via Equation 2.23 as:

$$M_{200}(a) = 100H^2(a)\frac{r_{200}^3}{G}. \tag{2.25}$$

2.5 The Impact on Bound Systems

There has been much debate about bound systems within an expanding Universe over the years. Clearly, there appears an additional term $\ddot{a}/a \cdot r$ in the equation of motion as Equation 2.12, but what is its impact? Can bound systems even survive, or is the influence of expansion negligible? To this end, the simplest system to consider is a particle on a circular orbit around a point mass. Early analyses done by McVittie (1933) found constant orbital radii for fixed coordinates in the solar system, though this interpretation was challenged by Ferraris et al. (1996) when more closely scrutinizing the chosen coordinate system. As discussed by Cooperstock et al. (1998) this type of back and forth happened quite frequently within the community at the time, and found both decreasing and constant proper orbital radii which were difficult to compare due to varying choices of coordinate systems. Their own calculation in the "locally inertial frame" (Landau & Lifshitz, 1975) find *decreasing* orbital radii for the case of a matter-dominated flat universe. For the following analyses in Section 2.6 and Chapter 3 it is useful here to retread for a ΛCDM-Universe some of the underlying mathematics employed for the cases of the matter-dominated (Cooperstock et al., 1998) and phantom-energy as well as quintessence dark energy-dominated Universes (Nesseris & Perivolaropoulos, 2004). The derivation in the following closely adheres that presented by Cooperstock et al. (1998) but adds some of the crucial intermediate steps.

First, the base setup is for a circular orbit of a test particle around a mass m within the locally inertial frame of the particle. The equation of motion is then Equation 2.12, where here it is advantageous to instead work in cylindrical coordinates (r, θ, z) with the orbit occurring in the plane perpendicular to z. This implies that all forces work centrally and only (r, θ) must be considered, or equivalently the Cartesian coordinates x, y. Equation 2.12 has then the form (note the use of vectors, such that the centrifugal term is not present yet but arises implicitly from the cylindrical coordinate system):

$$\ddot{\boldsymbol{r}} = -\frac{GM}{r^2}\hat{\boldsymbol{e}}_r + \frac{\ddot{a}}{a}\boldsymbol{r}$$

$$\Leftrightarrow \frac{\mathrm{d}^2}{\mathrm{d}t^2} \begin{pmatrix} r\cos\theta \\ r\sin\theta \end{pmatrix} = -\frac{GM}{r^2} \begin{pmatrix} \cos\theta \\ \sin\theta \end{pmatrix} + \frac{\ddot{a}}{a} \begin{pmatrix} r\cos\theta \\ r\sin\theta \end{pmatrix} \tag{2.26}$$

where the split up into $(x, y) = (r \cos \theta, r \sin \theta)$ has made two equations arise as:

$$\frac{d^2 (r \cos \theta)}{dt^2} = \frac{d}{dt}(\dot{r} \cos \theta - r\dot{\theta} \sin \theta) = \cos \theta (\ddot{r} - r\dot{\theta}^2) - \sin \theta (2\dot{r}\dot{\theta} + \ddot{\theta})$$

$$= -\frac{GM}{r^2} \cos \theta + \frac{\ddot{a}}{a} r \cos \theta = \cos \theta \left(-\frac{GM}{r^2} + \frac{\ddot{a}}{a} r \right), \qquad (2.27)$$

$$\frac{d^2 (r \sin \theta)}{dt^2} = \frac{d}{dt}(\dot{r} \sin \theta + r\dot{\theta} \cos \theta) = \sin \theta (\ddot{r} - r\dot{\theta}^2) + \cos \theta (2\dot{r}\dot{\theta} + \ddot{\theta})$$

$$= -\frac{GM}{r^2} \sin \theta + \frac{\ddot{a}}{a} r \sin \theta = \sin \theta \left(-\frac{GM}{r^2} + \frac{\ddot{a}}{a} r \right). \qquad (2.28)$$

As both equations must hold for all θ, two conditions follow:

$$2\dot{r}\dot{\theta} + \ddot{\theta} = 0, \qquad (2.29)$$

$$\ddot{r} - r\dot{\theta}^2 = -\frac{GM}{r^2} + \frac{\ddot{a}}{a} r, \qquad (2.30)$$

where the latter exactly recovers Equation 2.12. Assuming then the impact of expansion to be perturbative in nature, i.e., $r(t) = r_0 + \delta r(t)$ and $\theta(t) = \theta_0(t) + \delta\theta(t)$, and then noting that the unperturbed angle of a circular orbit $\theta_0(t)$ changes with time according to the initial angular velocity,

$$\theta_0(t) = \omega_0 \cdot t = \sqrt{\frac{GM}{r_0^3}} t, \qquad (2.31)$$

Equation 2.29 becomes:

$$2\delta\dot{r} \cdot \left(\omega_0 + \delta\dot{\theta} \right) + (r_0 + \delta r_0) \cdot (0 + \delta\ddot{\theta}) = 2\delta\dot{r} \cdot \omega_0 + r_0 \cdot \delta\ddot{\theta} = 0,$$

$$\Leftrightarrow \delta\ddot{\theta} = -\frac{2\omega_0}{r_0} \delta\dot{r} \;\rightarrow\; \delta\dot{\theta} = -\frac{2\omega_0}{r_0} \delta r, \qquad (2.32)$$

where terms of higher order in the perturbations were dropped in the first step. The last step was an integration in t and then equals exactly Equation 4.6 from Cooperstock et al. (1998). Similarly, Equation 2.30 is then:

$$\frac{d^2 (r_0 + \delta r)}{dt^2} - (\omega_0 + \delta\dot{\theta})^2 \cdot (r_0 + \delta r) = -\frac{GM}{(r_0 + \delta r)^2} + \frac{\ddot{a}}{a} \cdot (r_0 + \delta r),$$

$$\delta\ddot{r} - \omega_0^2 \cdot (r_0 + \delta r) - 2\delta\dot{\theta} \cdot r_0 = -\frac{GM}{r_0^2} \cdot \frac{1}{1 + 2\frac{\delta r}{r_0}} + \frac{\ddot{a}}{a} \cdot (r_0 + \delta r),$$

$$\stackrel{(2.32)}{\Leftrightarrow} \delta\ddot{r} - \omega_0^2 \cdot (r_0 + \delta r) - 2 \left(-\frac{2\omega_0}{r_0} \delta r \right) \cdot r_0 = -r_0 \omega_0^2 \cdot \left(1 - \frac{2\delta r}{r_0} \right) + \frac{\ddot{a}}{a} \cdot (r_0 + \delta r),$$

$$\delta\ddot{r} + \omega_0^2 \delta r - \frac{\ddot{a}}{a} \cdot (r_0 + \delta r) = 0, \qquad (2.33)$$

which recovers Equation 4.9 from Cooperstock et al. (1998) except that the term from expansion does not assume matter-domination, and further does not drop its δr term. Arguing

that the change in perturbation varies only slowly with time and is therefore small relative to the other two terms, it follows finally:

$$\delta r(t) = -\frac{r_0}{1 - \omega_0^2 \cdot \frac{a(t)}{\ddot{a}(t)}}. \tag{2.34}$$

For the actual radius with time it follows finally that

$$r(t) = r_0 \left(1 - \left(1 - \omega_0^2 \cdot \frac{a(t)}{\ddot{a}(t)}\right)^{-1}\right). \tag{2.35}$$

The temporal dependence of the perturbation in the radius then is entirely given by the ratio of $a/\ddot{a}$, while its radial dependence is governed by the remaining term ω_0^2. This results in an interesting conclusion for the relative perturbation of the radius as typically $\omega_0^2 a/\ddot{a} \gg 1$ (see Equation 2.39) such that for a given time t:

$$\frac{\delta r}{r_0} \propto \omega_0^{-2} = \frac{r_0^3}{GM(\leq r_0)} \propto \frac{1}{\rho(\leq r_0)} \tag{2.36}$$

where $M(\leq r_0), \rho(\leq r_0)$ are the mass and density within the circular orbit at r_0 and where the density profile is assumed to be spherically symmetric, with the sign of the perturbation dictated by $\ddot{a}$. The radial behavior of the relative perturbation is then entirely dictated by the mean *density* within the circular orbit, with a higher density resulting in a smaller perturbation and vice versa. Therefore, comparing the impact of expansion between different bound structures, say between a galaxy and galaxy cluster, must be treated with caution. It is not a difference in mass of the bound structure which dictates whether expansion has a larger impact or not – if a characteristic radius is chosen based on the density within, for example, the resulting perturbation of a circular orbit at that distance *is equal* for any size of bound structure. For a main halo with a typical density profile $\rho(r) \propto r^{-2}$ it follows $\omega_0^2 \propto r_0^1/r_0^3 = r_0^{-2}$ such that $(\delta r/r_0) \propto r_0^2$. A circular orbit at twice the distance is therefore perturbed four times as strongly by expansion for such density profiles.

2.6   Probing Implications on Forces and Potentials

Considering then that expansion indeed perturbs circular orbits as per Equation 2.35, this raises the question of how this perturbation changes with time. Though the dependence on the coordinate time t cannot be given analytically – due to $a(t)$ not having an analytical form, see also Section 2.4 – it is possible to instead work with the scalefacter a and subsequently redshift z as a measure of time directly.

Futhermore, although the analysis of circular orbits around a point-mass potential from Section 2.5 on the basis of perturbation theory as per Cooperstock et al. (1998) is a good starting point, it will be extended to an entirely analytical form considering also orbits of varying forms in Section 2.6.2.

To understand the following implications of both Equation 2.12 and Equation 2.35, it is necessary to first find the form of $\ddot{a}/a$ for the chosen cosmology. Here ΛCDM is assumed such that the Universe is flat, $\Omega_k \approx 0$, and for the later times considered dominated by matter and dark energy $\Omega_m + \Omega_\Lambda = 1$. Dark energy has an equation of state as $p = w\rho$ with $w = -1$, where the impact of expansion on orbits for the cases of $w < -1$ and $-1 < w < -1/3$ are extensively covered by Nesseris & Perivolaropoulos (2004). In the following, all plots will assume ΛCDM with $\Omega_m = 0.272$ and $\Omega_\Lambda = 0.728$, in accordance with the WMAP-7 parameters (Komatsu et al., 2011), unless specifically noted otherwise. Taking Equation 2.19 for this flat cosmology with only matter and dark energy it follows:

$$\frac{\ddot{a}}{a} = \frac{1}{a}\frac{\mathrm{d}a}{\mathrm{d}t}\frac{\mathrm{d}(H(a)/a)}{\mathrm{d}a} = \frac{\dot{a}H_0}{a}\frac{\Omega_{0,\Lambda}a - \Omega_{0,m}/(2a^2)}{\sqrt{\Omega_{0,m}a^{-1} + \Omega_{0,\Lambda}a^2}} = \frac{\dot{a}H_0}{a}\frac{\Omega_{0,\Lambda}a - \Omega_{0,m}/(2a^2)}{\dot{a}/H_0},$$

$$\frac{\ddot{a}}{a} = H_0^2\left(\Omega_{0,\Lambda} - \frac{\Omega_{0,m}}{2a^3}\right), \tag{2.37}$$

This has very interesting implications, as the term from expansion *vanishes* at

$$a_{\mathrm{NT}} = \left(\frac{\Omega_{0,m}}{2 \cdot \Omega_{0,\Lambda}}\right)^{1/3} \approx 0.5717 \tag{2.38}$$

or equivalently at $z_{\mathrm{NT}} \approx 0.7493$. For comparison, $\Omega_{0,m} = 0.3147$ as per Planck Collaboration (2020) finds $z_{\mathrm{NT}} = 0.6331$ while $\Omega_{0,m} = 0.3$ results in $z = 0.67$ as also stated by Nandra et al. (2012). At this point the Universe switches from decelerated to accelerated expansion, $q = 0$, and as such orbits which previously under matter domination were slightly perturbed inwards now are instead increasingly perturbed outwards as dark energy beings to dominate. This can be seen directly by considering the resulting fluctuation in a circular orbit at a characteristic radius r_x defined by Equation 2.24, given as:

$$\omega_{\Delta_c}^2 \cdot \frac{a}{\ddot{a}} = \frac{GM_{\Delta_c}}{r_{\Delta_c}^3} \cdot \frac{a}{\ddot{a}} \stackrel{(2.23),(2.37)}{=} \frac{\Delta_c}{2} \cdot \frac{\Omega_{0,\Lambda} + \Omega_{0,m}/a^3}{\Omega_{0,\Lambda} - \Omega_{0,m}/(2a^3)}. \tag{2.39}$$

which when plugged into Equation 2.35 takes the form:

$$r_{\Delta_c}(a) = r_{0,\Delta_c}(a)\left(1 - \left(1 - \frac{\Delta_c}{2} \cdot \frac{\Omega_{0,\Lambda} + \Omega_{0,m}/a^3}{\Omega_{0,\Lambda} - \Omega_{0,m}/(2a^3)}\right)^{-1}\right). \tag{2.40}$$

This is the perturbation at different times of a circular orbit at a radius enclosing a mean density a factor Δ_x higher than the mean density for a matter and dark energy dominated flat Universe. Note that this is not an actual orbit as $r_{0,\Delta_c}(a)$ changes with time (see Equation 2.24).

The resulting perturbations are plotted in Figure 2.4. As depicted on the left, the general behavior of circular orbits goes from being perturbed inward for the matter dominated phase $a < a_{\mathrm{NT}}$ to being perturbed outwards for Λ-dominated times. For particles orbiting farther inwards at r_{500}, the overall distortion between $z = 4$ and $z = 0$ is on the order of just 0.5%.
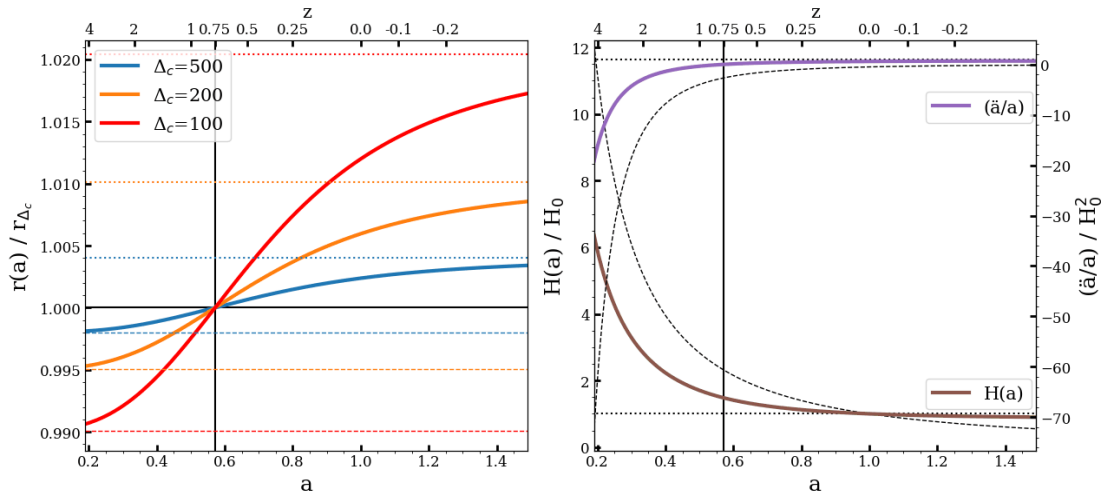
Figure 2.4: *Left:* The perturbation from a Newtonian circular orbit at r_{Δ_c} as a function of scale factor a for different overdensities, with the limiting cases of $\Omega_m = 1$ (dashed) and $\Omega_\Lambda = 1$ (dotted). The black lines denote the Newtonian case (horizontal) and the transition from matter to dark energy dominated (vertical). r_{Δ_c} here varies with time. *Right:* The Hubble parameter (purple) from Equation 2.19 and the acceleration term $\ddot{a}/a$ (brown) given by Equation 2.37 as a function of scale factor a, with the limiting cases and vertical black line as before.
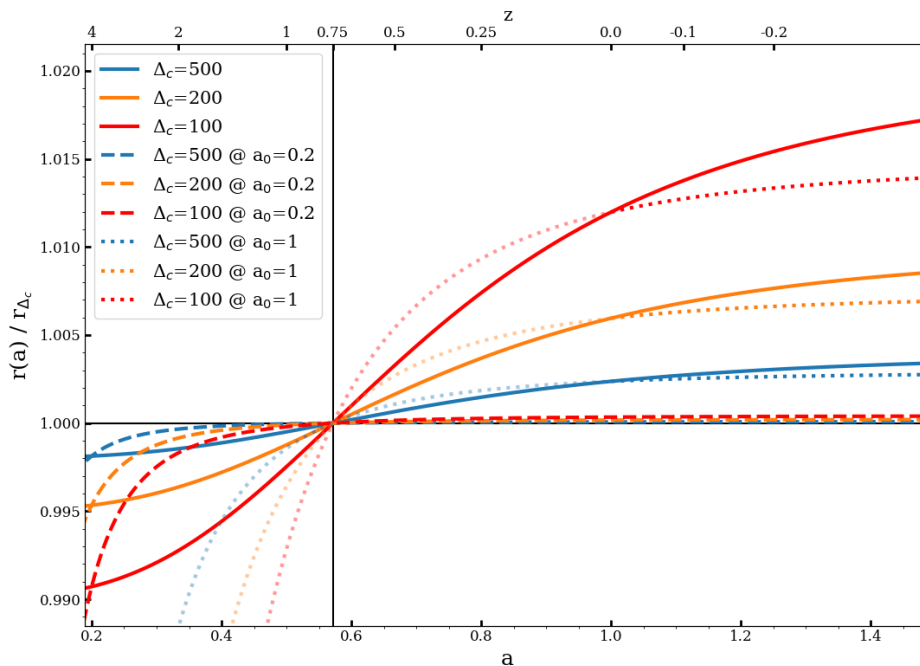
Figure 2.5: The perturbation from a Newtonian circular orbit at r_{Δ_c} as a function of scale factor a for different overdensities, with colored solid lines as in Figure 2.4 depicting the perturbation for circular orbits at each time a. Dashed lines represent the temporal behavior of an orbit initialized at $a = 0.2$ for a fixed system, while dotted are for a starting time $a = 1.0$. Radii are given as a fraction of their *initial* r_{Δ_c}, i.e., the scaling relates directly to a fixed physical size. The black lines denote the Newtonian case (horizontal) and the transition from matter to dark energy dominated (vertical).

This effect increases farther out as the density within the orbit decreases, as per Equation 2.36, up to slightly over 2% difference for r_{100} between $z = 4$ and $z = 0$.

Given instead a fixed real orbit which is circular at a_0 with $r_0 = r_{\Delta_c}(a_0)$ and w_0, i.e., around a fixed central mass, Equation 2.40 becomes:

$$r(a) = r_0 \left(1 - \left(1 - \frac{\Delta_c}{2} \cdot \frac{\Omega_{0,\Lambda} + \Omega_{0,m}/a_0^3}{\Omega_{0,\Lambda} - \Omega_{0,m}/(2a^3)} \right)^{-1} \right). \tag{2.41}$$

This is depicted in Figure 2.5 for varying overdensities and when initializing the circular orbit at different times, with the colored solid lines as in Figure 2.4. As can be seen from the dashed lines for a system initialized at $a = 0.2$, the perturbation of a circular orbit around a fixed system behaves differently from the circular orbits at different times. This is because the density enclosed by the original orbit at $a = 0.2$ stays constant, i.e., increases in density contrast against the decreasing background $\rho_c(a)$. As it is the density contrast which dictates the strength of the expanding term, this increased contrast leads to decreased perturbations. This demonstrates that orbits starting at early times also change most strongly at early times, becoming less and less perturbed with time. The same is depicted for a system initialized at $a = 1$ with the dotted lines, where the times $a < 1$ are faded as it is unclear if the orbit at earlier times would not be unbound at some point. It should be emphasized that the radii here are defined relative to their enclosed density as opposed to the mass or radius in absolute values to highlight the fact that the relative impact from expansion is only dependent on the former.

2.6.1 Acceleration and the Turnaround Radius

Turning then away from circular orbits to more general properties, this section examines the acceleration experienced by a particle around a central point mass M. The frame of reference is fixed on the central mass, such that Equation 2.12 loses the angular momentum term. Through the fixed choice of cosmology resulting in Equation 2.37 this acceleration can be put into more explicit terms as:

$$\ddot{r}(r, a) = -\frac{GM}{r^2(a)} + \frac{\ddot{a}}{a} r(a) = -\frac{GM}{r^2(a)} + H_0^2 \left(\Omega_{0,\Lambda} - \frac{\Omega_{0,m}}{2a^3} \right) \cdot r(a). \tag{2.42}$$

The distance where no acceleration is felt by a particle is then

$$r_{\text{turn}} \equiv \left(\frac{GM}{H_0^2 \cdot (\Omega_{0,\Lambda} - \Omega_{0,m}/(2a^3))} \right)^{1/3}. \tag{2.43}$$

It follows that for all times $a < a_{\text{NT}} = 0.572$ as per Equation 2.38 there exists no such radius, because there the expanding term also points inwards. Only once expansion begins to accelerate do there exist radii $r > r_{\text{turn}}$ where a particle at rest would get accelerated away from the mass M to eventually join the Hubble flow.

These parameters can be related to typical scaling parameters defined through overdensities relative to the critical density as in Section 2.4.1. Defining $A_{\Delta_c} \equiv GM_{\Delta_c}/r_{\Delta_c}^2$ as the
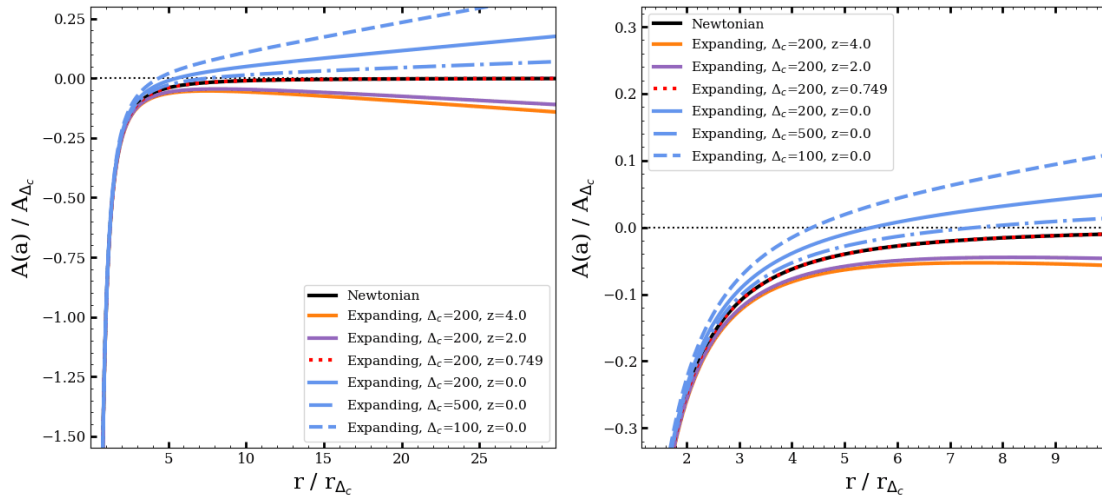
Figure 2.6: *Left:* The acceleration scaled according by A_{Δ_c} resulting from a point mass for the purely Newtonian (black) versus expanding (colored) cases as a function of distance r. Different times z are depicted in different colors for the case of $\Delta_c = 200$, where the Newtonian case is z independent. For $z = 0$ additionally $\Delta_c = 100, 500$ are shown as dash-dotted and dashed lines, respectively. *Right:* The same, zoomed in to the central region.

magnitude of purely Newtonian acceleration at a distance r_{Δ_c} and $b \equiv r/r_{\Delta_c}$, where for now the central mass is assumed to be point like, Equation 2.42 takes the form:

$$\frac{\ddot{r}(b, a)}{A_{\Delta_c}(a)} = -\frac{1}{b^2} + \frac{b}{\Delta_c/2} \cdot \frac{\Omega_{0,\Lambda} + \Omega_{0,m}/a^3}{\Omega_{0,\Lambda} - \Omega_{0,m}/(2a^3)}. \tag{2.44}$$

Figure 2.6 depicts the resulting accelerations experienced by a particle around a point mass for the Newtonian (black) and expanding (colored) cases. There is little deviation in the behavior for radii $r < r_{200}$. It can be seen that for $z = 0.749$ or equivalently $a = 0.5717 = a_{\mathrm{NT}}$ the acceleration for the expanding and Newtonian background are identical. For $z = 0$ in blue the expanding term points outwards and there exist radii for which the acceleration is away from the central mass, $A > 0$, with the crossing point given by Equation 2.43. As shown by the three blue lines, a lower density (dashed) leads to a smaller ratio r/r_{Δ_c} of the transition point, which corresponds to the statement that for a fixed central mass M the transition radius is a fixed value r, i.e., r/r_{Δ_c} varies.

2.6.2 The Effective Potential

Orbits of particles within a central potential must not be exclusively circular – rather they *cannot* be circular due to the varying acceleration from expansion as seen in Figure 2.5. To understand real orbits the simple perturbation theory approach from Section 2.5 has to be extended to account for all types of orbits, which is best accomplished by considering the effective potential. This describes the potential actually felt by the particle within its own inertial system, i.e., including frame-dependent terms such as the angular momentum and the acceleration from expansion.

Equation 2.30 already describes the effective acceleration felt by the orbiting particle within its own locally inertial frame, and as such a conversion to the effective potential per unit mass follows as:

$$\frac{V_{\text{eff}}(r, a)}{m} = -\int dr \left(\frac{L^2}{r^3} - \frac{GM}{r^2} + \frac{\ddot{a}}{a} r \right) = \frac{L^2}{2r^2} - \frac{GM}{r} - \frac{\ddot{a}}{a} \cdot \frac{r^2}{2}. \tag{2.45}$$

As the expanding term is central, $\parallel \hat{r}$, the angular momentum is still conserved, $L = const$. However the acceleration varies with time, meaning that when expansion is significant the total energy of the orbit is not conserved anymore (see for example Noether 1918 or Appendix D.1 from Binney & Tremaine 2008).

Defining then

$$b \equiv \frac{r}{r_{\Delta_c}} \tag{2.46}$$

as the ratio between the radius and extent of the mass distribution and

$$l \equiv \frac{L}{\sqrt{GM_{\Delta_c} \cdot r_{\Delta_c}}} \tag{2.47}$$

as the fractional specific angular momentum of a Newtonian spherical orbit at r_{Δ_c}, Equation 2.45 can be written as:

$$\frac{V_{\text{eff}}(r, a)}{m} = \frac{l^2 \cdot (GM_{\Delta_c} r_{\Delta_c})}{2 \cdot b^2 r_{\Delta_c}^2} - \frac{GM_{\Delta_c}}{b r_{\Delta_c}} - \frac{\ddot{a}}{a} \cdot \frac{b^2 r_{\Delta_c}^2}{2},$$

$$\frac{V_{\text{eff}}(r, a)}{m} = \frac{GM_{\Delta_c}}{r_{\Delta_c}} \cdot \left[\frac{l^2}{2 \cdot b^2} - \frac{1}{b} - \frac{r_{\Delta_c}^3}{GM_{\Delta_c}} \cdot \frac{\ddot{a}}{a} \cdot \frac{b^2}{2} \right]. \tag{2.48}$$

By noting that $v_{\Delta_c}^2(a) \equiv GM_{\Delta_c}/r_{\Delta_c}$ is the circular velocity at r_{Δ_c} for an object of mass M_{Δ_c},

$$V_{\Delta_c}(a) \equiv m \cdot v_{\Delta_c}^2(a) \tag{2.49}$$

can be identified as the Newtonian effective potential for a particle at rest at r_{Δ_c}. Note that this value can either be fixed for a given structure at a_0 or can vary with time if defined for the current overdensity. Plugging Equation 2.39 in Equation 2.48 then gives:

$$\frac{V_{\text{eff}}(r, a)}{V_{\Delta_c}(a)} = \left[\frac{l^2}{2 \cdot b^2} - \frac{1}{b} - \frac{b^2}{\Delta_c} \cdot \frac{\Omega_{0,\Lambda} + \Omega_{0,\text{m}}/a^3}{\Omega_{0,\Lambda} - \Omega_{0,\text{m}}/(2a^3)} \right]. \tag{2.50}$$

For an overdensity $\Delta_c = 100$ the resulting effective potential for particles with varying angular momenta l is depicted in Figure 2.7 at $a = 0.2$ (left) and $a = 1$ (right). First it should be noted that as the scale factor $V_{100}(a)$ varies here with time the absolute values vary between the panels. This is also the reason why both the matter- (dotted) and dark energy-dominated (dashed) cases appear identical with time, as per Equation 2.49 the expanding term's a-dependency vanishes such that different times are simply scaled in their absolute values *but not* in their shape. The actual behavior for ΛCDM lies between these two extremes,
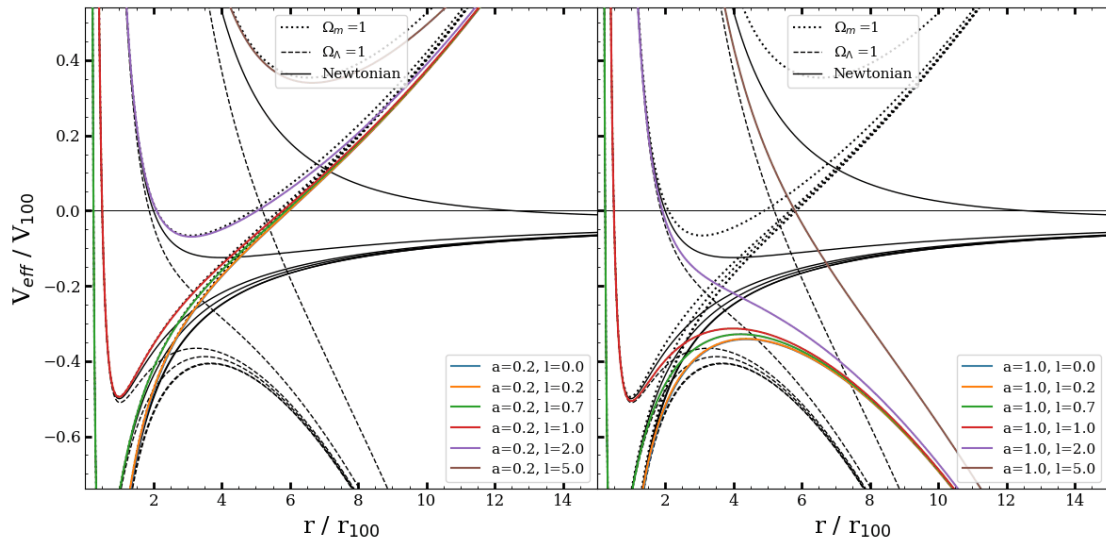
Figure 2.7: *Left:* The effective potential at $a = 0.2$ scaled with $V_{100}(a = 0.2)$ resulting from a point mass for the purely Newtonian (black) versus expanding (colored) cases as a function of distance r, with the cases of $\Omega_m = 1$ (dotted) and $\Omega_\Lambda = 1$ (dashed) depicted for comparison. *Right:* The same for $a = 1$ scaled with $V_{100}(a = 1)$.
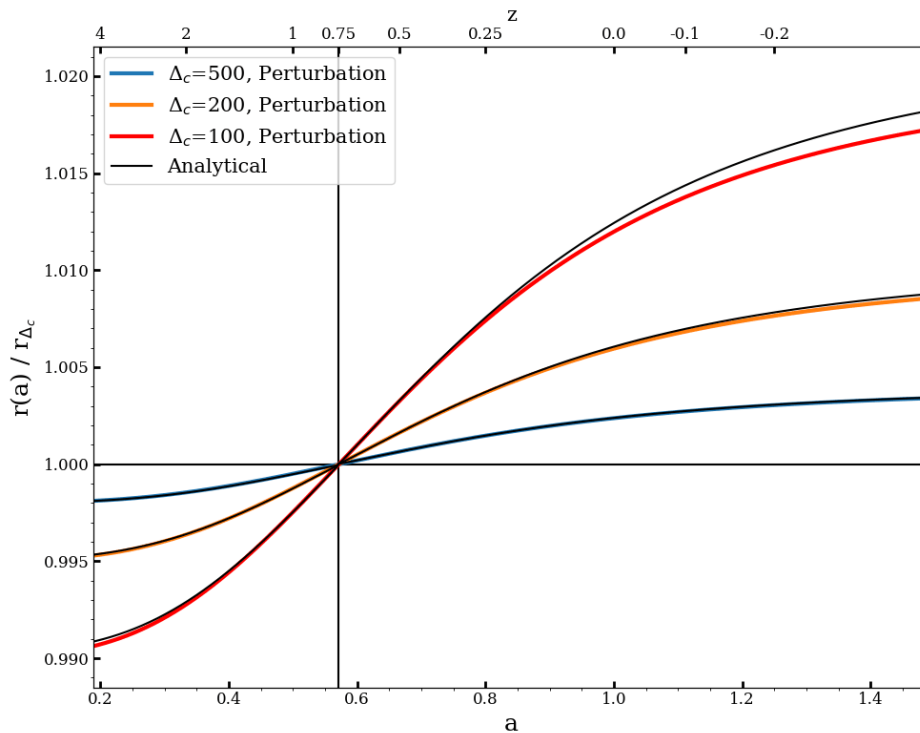
Figure 2.8: The perturbation from a Newtonian circular orbit at r_{Δ_c} as a function of scale factor a for different overdensities for the approximation Equation 2.34 (colored) as from Cooperstock et al. (1998) and analytical roots of Equation 2.51. The horizontal and vertical black lines denote the Newtonian case and the transition from matter to dark energy dominated, respectively.

transitioning towards dark energy domination at later times as expected with a brief moment at $a = a_{\text{NT}}$ where the curves equal the Newtonian ones. For small radii all cases behave practically identical.
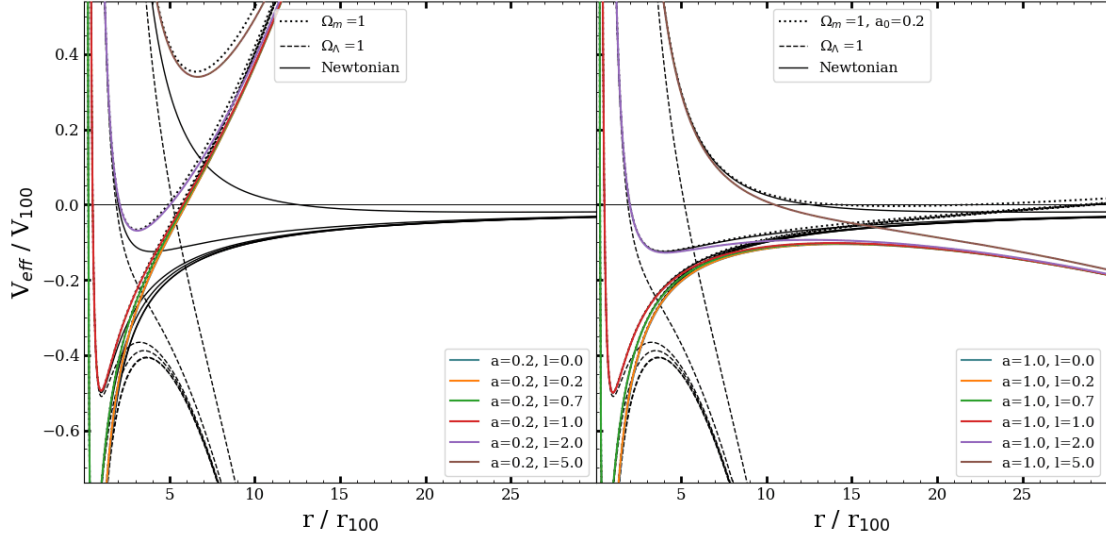
Figure 2.9: *Left:* The effective potential at $a = 0.2$ scaled with $V_{100}(a = 0.2)$ resulting from a point mass for the purely Newtonian (black) versus expanding (colored) cases as a function of distance r, with the cases of $\Omega_m = 1$ (dotted) and $\Omega_\Lambda = 1$ (dashed) depicted for comparison. *Right:* The same for $a = 1$ scaled with $V_{100}(a = 0.2)$.

Of special interest is the case of $l = 1$ (red line) as it has the angular momentum of a circular orbit at r_{Δ_c}. The behavior of just this curve is further plotted in isolation in Figure A.5, where it can also be seen explicitly that for $a = a_{NT}$ the Newtonian curve is reproduced. By definition, the curve's minimum describes a circle as considered for the perturbation approach in Section 2.5. As found there in Equation 2.34, the minimum changes with increasing time towards slightly higher values r/r_{100}. Given the analytical form in Equation 2.50 it is possible to define also an analytical form of Equation 2.34 by requiring the derivative to be zero as:

$$\frac{dV_{\text{eff}}}{db} = -\frac{l^2}{b^3} + \frac{1}{b^2} - b \cdot \frac{2}{\Delta_c} \frac{\Omega_{0,\Lambda} + \Omega_{0,m}/a^3}{\Omega_{0,\Lambda} - \Omega_{0,m}/(2a^3)} \overset{!}{=} 0$$

$$0 = -l^2 + b - b^4 \cdot \frac{2}{\Delta_c} \frac{\Omega_{0,\Lambda} + \Omega_{0,m}/a^3}{\Omega_{0,\Lambda} - \Omega_{0,m}/(2a^3)}. \tag{2.51}$$

The form recovered is that of a quartic $e \cdot b^4 + f \cdot b^3 + g \cdot b^2 + h \cdot b + j$, where the roots are analytical and given for example by Weisstein (2022c). As e in this case is a function of a, so are the roots varying with time. The resulting analytical solution is compared in Figure 2.8 against Equation 2.34. For an overdensity of $\Delta_c = 500$ and $\Delta_c = 200$ the orbits are only weakly disturbed by the expanding term such that the perturbative result is generally sufficient. There do start to appear some differences for the latter case at very low and high a, i.e., the farther away from the Newtonian transition point at a_{NT} the stronger the difference. The strongest deviation for $\Delta_c = 100$ is however only on the order of 10% different from the perturbative approximation, which means that the impact of expansion on circular orbits at all times is small and the result from Equation 2.34 can be generally applied.

A striking feature of Figure 2.7 is that for matter-domination generally expansion strongly accelerates particles towards each other, allowing in principle for bound orbits of any energy

and angular momentum as the effective potential increases for large radii as r^2. Even orbits with a very high angular momentum, for example $l = 5$, appear to be able to possess a circular orbit. This, however, does not mean that these orbits would actually be able to occur in this way as the potential changes with time. Furthermore, it appears that unlike the statements made in Section 2.5 the minima for $l = 4$ and $l = 5$ disappear with time, such that there do exist circular orbits that are entirely pulled apart by expansion.

To better understand the implications for actual systems, it is necessary to take a fixed system initialized at $a_0 = 0.2$, i.e., where the scaling variables do not vary with time, where for example $r_{100} = r_{100}(a_0)$ and $V_{100} = V_{100}(a_0)$. The resulting effective potential is shown in Figure 2.9. The left panel simply equals a zoomed-out version of the left panel from Figure 2.7, because this is the time when the system is initialized. However, as seen on the right the impact of expansion is actually not as severe as perhaps expected. This is as the initial overdensity $\Delta_c = 100$ at $a = 0.2$ grows to much larger values as the critical density decreases with time, and a larger density contrast leads to a smaller impact from expansion. Therefore, a system formed at earlier times does not actually converge to the dark energy-dominated (dashed) curves. Another thing of note is that for system within a purely matter-dominated (dotted) universe the impact from expansion decreases with time as $\propto a^3$, slowly converging to the Newtonian effective potential, while for dark energy-domination no change occurs with time and the impact of expansion is always the same.

Taking then for example a particle with $l = 5$ on a circular orbit at $a = 0.2$, such that it has a total specific energy of $e_5 \approx 0.34 \cdot V_{100}$, it follows from the right panel that at $a = 1$ no bound orbit exists anymore. Expansion has successfully removed a particle on a circular orbit – but how is this possible? Here the perturbative approach from Section 2.5 breaks down and the deviation as already noted in Figure 2.8 grows to infinity. Mathematically this corresponds to the real positive double root of Equation 2.51 for the initial circular orbit vanishing, instead resulting in one positive real root for the inner intersection at around $b \approx 4.7$, one negative real root at $b \approx -7.6$ and then a complex root pair. Physically, however, it is not as simple to state that the initial set-up ever even was a real orbit. To see this, take again the example circular orbit with $l = 5$ for an object with some fixed M_{100} at $a = a_0 = 0.2$, such that $r_5 \approx 6.5 \cdot r_{100}$. Assuming the central object to have a density profile as $\rho = f \cdot r^{-2}$, with f constant, then

$$M(< r_{100}) = \int dr\, 4\pi r^2 \cdot f r^{-2} = 4\pi \cdot f r_{100} \overset{!}{=} M_{100} \Leftrightarrow f = \frac{M_{100}}{4\pi \cdot r_{100}}$$

$$\rho(r_5) = \frac{M_{100}}{4\pi r_{100}} \frac{1}{(6.5 \cdot r_{100})^2} = \frac{M_{100}}{4\pi r_{100}^3} \cdot (6.5)^{-2} = \frac{100 \rho_c}{3} \cdot (6.5)^{-2} \approx 0.8 \cdot \rho_c \quad (2.52)$$

Clearly this is not a real orbit then unless the density profile were to fall off even flatter than r^{-2}. Furthermore, the orbital period is given as $T = 2\pi \sqrt{r_5^3/(G \cdot M_{100})}$, which for $M_{100} = 1 \times 10^{12}\, M_\odot$ would be $T \approx 6\,\text{Gyr}$. Comparing with Figure 2.2 this would correspond to one orbit being completed from $a_0 = 0.2$ to $a_{\text{end}} \approx 0.54$, at which point the Universe has

already almost entered the dark energy dominated phase. Therefore, direct conclusions can be difficult to make without a physical comparison or actual simulated systems.

Nonetheless, the initial interpretation there are orbits which are disturbed by expansion so strongly as to be end up unbound holds true – if a particle is initially infalling from far out and would originally end up bound, the flattening of the effective potential can lead to it exiting again instead. Though it has never completed a full orbit, this does have potential implications for the inflow of material into the bound structure itself. Furthermore, this analysis does not account for two body interactions which could temporarily elevate a particle to higher energies that would normally simply return to the central potential, but due to expansion manage to break the threshold and are accelerated away. Overall then, the general behavior holds true: for matter domination the effective potential is pushed upwards, accelerating the particles towards each other, while for dark energy domination the reverse is true. As such, the transition from early to late times experiences a continuous decrease in the effective potential felt by a particle in a central potential, increasingly significant with distance.

2.7   Simply Simulating

Finally, to see an actual orbit there is no way to avoid simulating the system. The code employed here utilizes a Leapfrog KDK where force calculations are split up into "kick" and "drift" steps – see Binney & Tremaine (2008) – and for the expanding case the additional terms are accounted for by transforming into coordinates (x, x', p') with the time variable τ as described in Section 2.3. This corresponds to the typical comoving implementation for GADGET (Springel et al., 2001), and is used here to simulate particle orbits within a point mass potential. The reduction to only the cosmological formulation without the inclusion of any additional physics allows for a direct comparison to the theoretical findings from Section 2.6.

General bound orbits can be either circles or ellipses, depending on whether their total specific energy has one or two crossing points with the effective potential. These crossing points can be determined to predict the possible evolution of the orbits, including elliptical ones. Defining $V \equiv V_{\text{eff}}(r, a_0)/V_{\Delta_c}(a_0)$ as the fractional fixed total energy of a particle, and multiplying Equation 2.50 by b^2 gives:

$$0 = \frac{b^4}{\Delta_c} \cdot \frac{\Omega_{0,\Lambda} + \Omega_{0,m}/a^3}{\Omega_{0,\Lambda} - \Omega_{0,m}/(2a^3)} + b^2 \cdot V + b - \frac{l^2}{2}. \tag{2.53}$$

This, akin to Equation 2.51, is a quartic and as such has analytical solutions. These have the form $b(V, l, a, \Delta_c)$ such that when assuming the effect of expansion to be merely perturbative the first two parameters are constant with time and only the direct dependency on a in the expanding term remains. This will again break down when the orbits gain sufficient energy from expansion to become unbound. Δ_c defines the scaling parameters which are used for the other variables, i.e., if $\Delta_c = 100$ then V, L, b must be stated as fractions of their $\Delta_c = 100$ equivalents. For an ellipses, $b(V, l, a, \Delta_c)$ has two real positive solutions, corresponding to
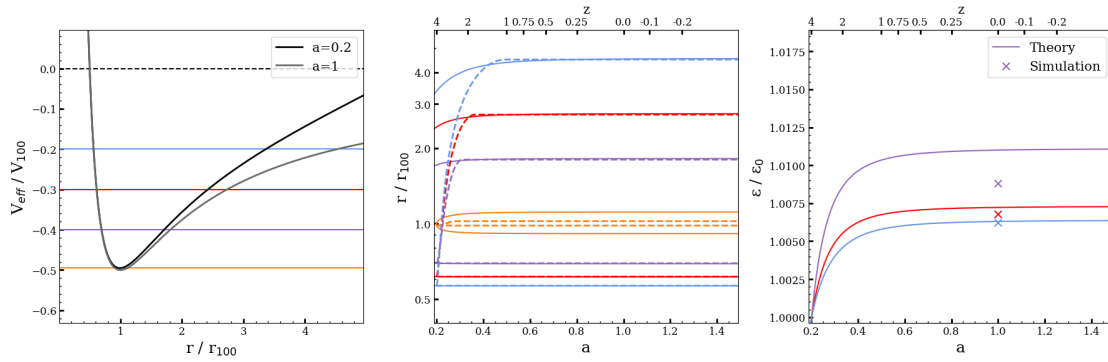
Figure 2.10: *Left:* The effective potential scaled with a fixed $V_{100}(a = 0.2)$ resulting from a point mass for the expanding case at two times, $a = 0.2$ and $a = 1$, as a function of distance r/r_{100}. Horizontal colored lines indicate each chosen particle's energy. *Center:* The theoretical evolution (solid lines) of the inner and outer radii of an orbit with total energy as given for the same color on the *left*. Dashed lines are the minimum and maximum radii of the simulated equivalent orbits around a central mass $M = 1 \times 10^{12}\,\mathrm{M_\odot}$, with the initial rise occurring as the particle makes its first orbit outwards. *Right:* The theoretical evolution (solid lines) of the eccentricity of the orbits as a function of scale factor, given as a ratio to the original eccentricity. Crosses denote the eccentricity of the last full orbit at $a = 1$ of the simulated equivalents.

the lengths of the semi-minor and major axes which are subsequently referred to as the inner r_{in} and outer radius r_{out}. The particle is then a length r_{in} away from the central mass at the periapsis, and r_{out} at the apoapsis.

The simulation is then initialized at $a = 0.2$ for a central mass of $M = 1 \times 10^{12}\,\mathrm{M_\odot}$ with particles i orbiting around it at varying distances. All orbits are chosen to have the same total angular momentum $l = 1$ scaled according to $\Delta_c = 100$, with varying total specific energies e_i as depicted by the colored horizontal lines on the left in Figure 2.10. The roots from Equation 2.53 then provide the starting positions, either initializing at the periapsis $r_i = r_{in}$ or the apoapsis $r_i = r_{out}$. Here $r = r_{in}$ is chosen. As $l = 1$, so $L = v_{100}/r_{100}$, the velocity can be derived as $v_i = v_{100} \cdot (r_i/r_{100})$. The resulting minimum and maximum radii of the simulated orbits are depicted in the center of Figure 2.10 as dashed lines, where an overall good match is found to the theoretical results from Equation 2.53. Especially interesting is the orange orbit which corresponds to a circle initially, but is slightly perturbed to instead trace an ellipse. The effect within the simulation is here somewhat smaller than the predicted one, but is present nonetheless. Given the simulated orbits, it is then possible to determine an increase in ellipticity versus the original orbits. This is shown on the right in Figure 2.10 as crosses, compared to the predicted increase. Indeed, the ellipticity of the orbits in the simulation has increased. The greatest relative increase of around 0.85% is found for the orbit farthest in also as predicted, with a minor offset present. The original circle orbit is not depicted as its initial ellipticity is $\epsilon_0 = 0$ and thus ϵ/ϵ_0 is undefined.

It is interesting to note that the exact same results are found when instead initializing a scaled up variant with a central mass of $M = 1 \times 10^{15}\,\mathrm{M_\odot}$, as can be seen in Figure A.6. This shows what was emphasized in Section 2.5, that it is the overdensity which defines the impact of expansion, not the absolute scale itself. To further see this, the same simulation is
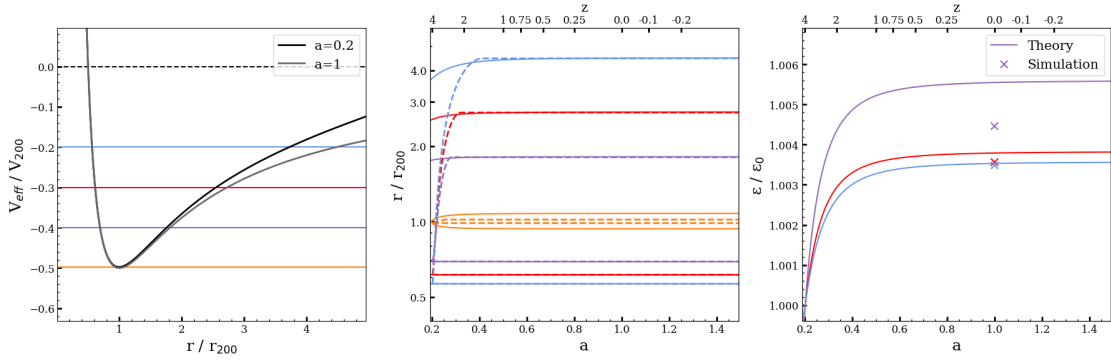
Figure 2.11: *Left:* The effective potential scaled with a fixed $V_{200}(a = 0.2)$ resulting from a point mass for the expanding case at two times, $a = 0.2$ and $a = 1$, as a function of distance r/r_{200}. Horizontal colored lines indicate each chosen particle's energy. *Center:* The theoretical evolution (solid lines) of the inner and outer radii of an orbit with total energy as given for the same color on the *left*. Dashed lines are the minimum and maximum radii of the simulated equivalent orbits around a central mass $M = 1 \times 10^{12}\, M_\odot$, with the initial rise occurring as the particle makes its first orbit outwards. *Right:* The theoretical evolution (solid lines) of the eccentricity of the orbits as a function of scale factor, given as a ratio to the original eccentricity. Crosses denote the eccentricity of the last full orbit at $a = 1$ of the simulated equivalents.

run also for parameters scaled according to an overdensity of $\Delta_c = 200$ with a central mass $M = 1 \times 10^{12}\, M_\odot$ with the result depicted in Figure 2.11. Here the change in eccentricity is lessened as the orbits lie farther in and are thus less affected by expansion, only reaching around 0.45 or 0.55% at the highest for the simulated and theoretical cases. The trend to higher eccentricity increase with lower initial orbital radii as found in Figure 2.10 persists here. Similarly, the initial circle orbit in orange expands to an ellipse, though even less so than for Figure 2.10.

As both r_{in} and r_{out} are solutions to Equation 2.53, one could conclude that it should make no difference whether the particle orbit is initialized at one or the other. However, as can be seen in Figure 2.12, there is a clear discrepancy between the two cases, with particles initialized at the periapsis reaching much farther out to the theoretical values. When instead starting at the apoapsis the orbits do not reach as far as predicted by the theory, instead only going out to their initial position r_{out}. This can also be seen in Figure A.7, where they also do not reach as far in as expected leading to *decreasing* eccentricities. One possible explanation is that the derivation of the effective potential were faulty, that the periapsis and apoapsis belong to two different orbits and so should not agree. This can be tested by initializing the orbits in a "frozen" expanding background, so simulating in a Newtonian non-comoving frame but adding the contribution from expansion at $a = 0.2$ as a fixed acceleration term. If the values belong to a single orbit at $a = 0.2$, within this frame they should trace identical ellipses. This is exactly what is found in Figure 2.13 on the left where the Newtonian orbits with the additional expansion term stay on the same orbits shifted by half a period. Furthermore, the extent matches the crossing points of the effective potential as in Figure 2.10, indicating that the interpretations of the orbits on the basis of the effective potential as done so far are correct. Another noticeable feature is the differing orbital periods between the bottom two
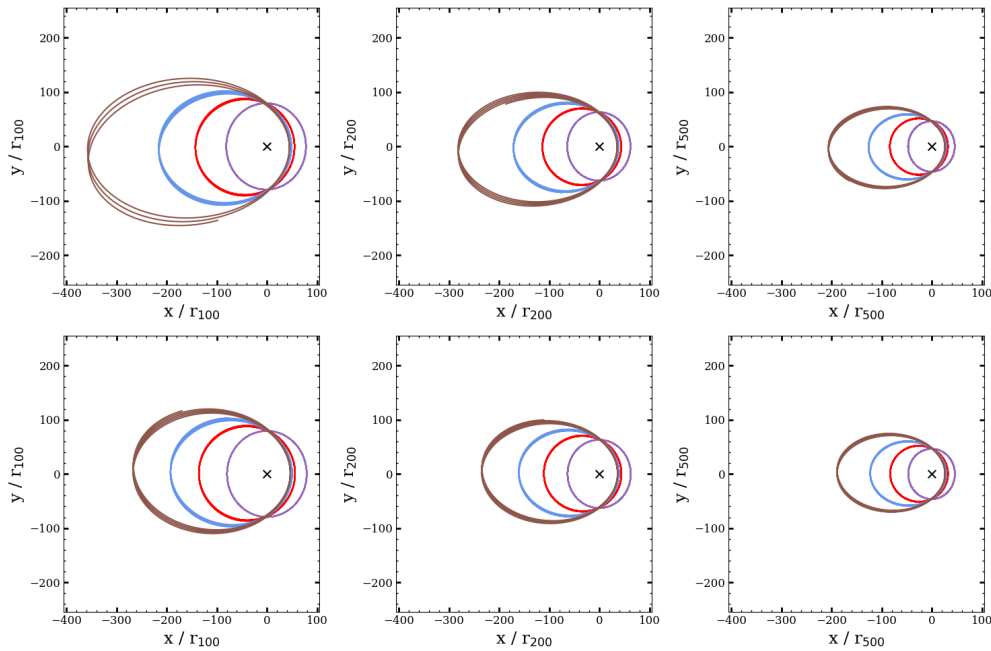
Figure 2.12: The orbits in the plane, initialized at the periapsis (*top row*) and the apoapsis (*top row*) for different overdensities from left to right as $\Delta_c = 100$ to $\Delta_c = 500$, with the black x indicating the location of the central point mass. The differences between the top and bottom row are increasingly lessened the higher the overdensity. Furthermore, the varying additional term from expansion also leads to a precession of the orbits.

orbits, which arises due to the fast that the potential on the left is as steep as the one at $a = 0.2$ for the whole time while the expanding case flattens the potential and thus the particle orbits slower there – see also Figure 2.9. Note further that only for the expanding case on the right do the times correspond to varying scale factors as can be seen on the top, as the left is frozen at $a = 0.2$.

As the only remaining explanation then, it appears that when initialized at the apoapsis the particles *lose energy* compared to those at the periapsis, or conversely that those at the periapsis *gain energy*. This is theoretically possible as the force is not time independent due to the expansion term and as such energy is not conserved. The specific total energy of the particles ´in the locally inertial system of the central mass is given by

$$ e = \frac{v^2}{2} - \frac{GM}{r} - \frac{r^2}{2} \cdot H_0^2 \cdot \left(\Omega_{0,\Lambda} - \frac{\Omega_{0,m}}{2a^3} \right). \tag{2.54} $$

The resulting energies are plotted on the left in Figure 2.14, with the colors corresponding as before to the orbits. Note the presence of three additional orbits farther out which. Dashed lines represent particles initialized at the apoapsis, with solid lines for those starting at the periapsis. Immediately, the former rapidly loses energy as the particle falls towards the central point mass and then rises again in a hump before reaching a relatively stable energy. As can be seen from the right this final stable energy approximately corresponds to the initial Newtonian energy of the orbit, given by Equation 2.54 without the expanding term $\propto r^2$. Note further that for orbits farther out the Newtonian energies begin fluctuating, indicating that here the expanding term alternatively adds or removes some energy.
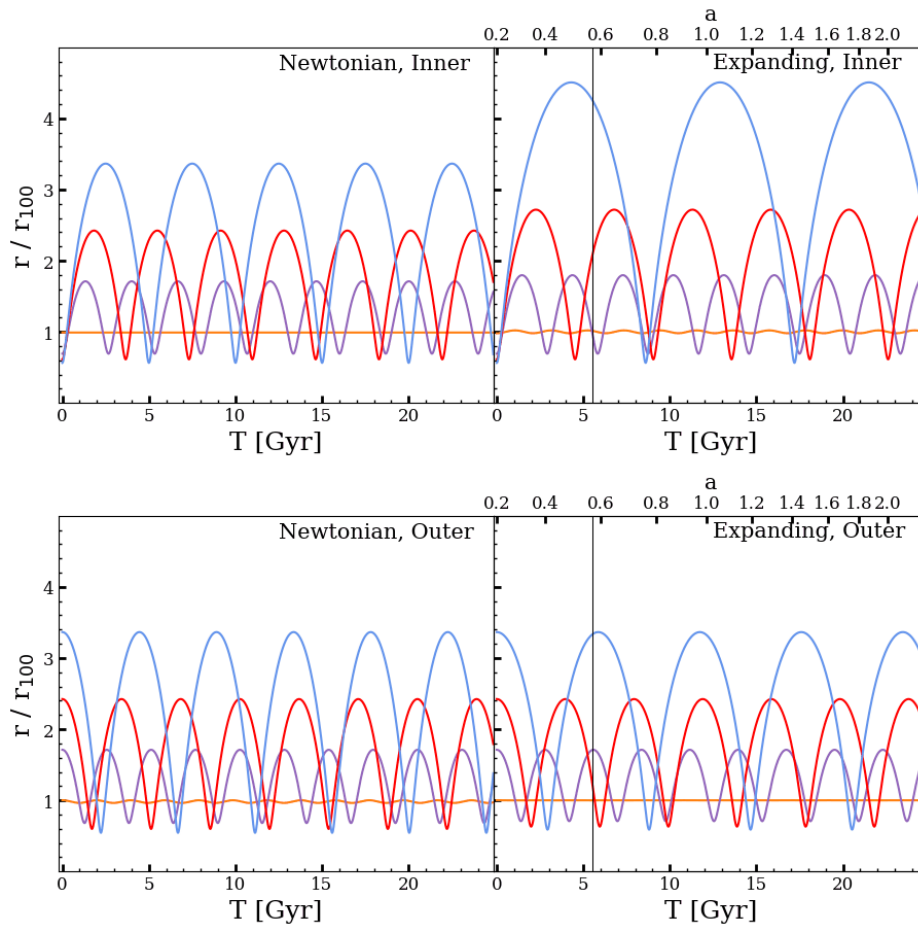
Figure 2.13: Radii as a function of time of orbits with equal angular momentum $l = 1$ (as defined in Section 2.6) for varying total peculiar energies. The *top* row is initialized at the periapsis and the *bottom* row at the apoasis. The *left* depicts the "Newtonian" potential, where simply an additional force term is added to mimic the effective potential during expansion at $a = 0.2$ but no comoving frame used, while the *right* is for the fully comoving implementation. There the corresponding scale factor is given for the latter, with a_{NT} highlighted as a thin vertical black line. The colors correspond to those in Figure 2.10 and Figure 2.12.
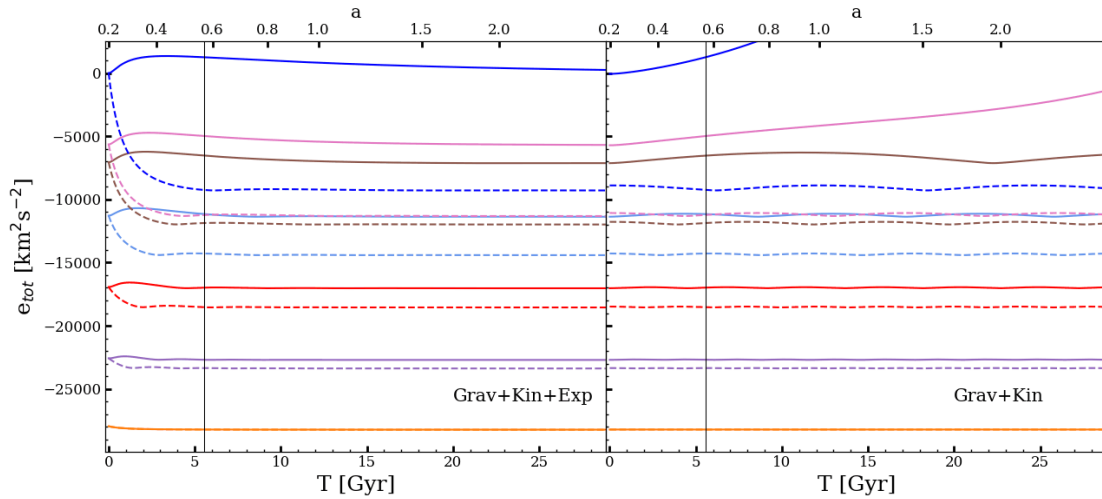
Figure 2.14: *Left:* The total energy as given by Equation 2.54 of the orbits within the locally inertial system of the central mass. Solid lines are the orbits initialized at the periapsis, with dashed those at the apoapsis. The colors correspond to those in Figure 2.10 to Figure 2.13, with three additional orbits farther out. Their radii can be seen in Figure A.8. a_{NT} is highlighted as a thin vertical black line. *Right:* The same for the Newtonian energy, given as Equation 2.54 without the expanding term $\propto r^2$.

To better understand this, one can picture the effective potential felt by the particles as a slide pointing towards the center. At high z this slide is further pushed upwards, becoming steeper due to matter domination. Were the particle starting at the apoapsis able to complete a half an orbit then under the same initial potential, it would rapidly accelerate and arrive at the center exactly where the periapsis is as was seen on the left in Figure 2.12. However, this does not happen. While the particle is falling inwards, the expanding term continuously flattens out the slide, such that the particle has to expend increasingly more kinetic energy. The result is that it does not reach as far into the center as it would have for the initial potential, instead settling on an orbit of lower energy. Conversely, the particle starting at the pericenter would for the initial potential have to expend more energy when moving away from the central mass as the slide was stepper. As expansion flattens out, however, the slide it originally had to climb becomes more shallow and thus allows it to reach farther out with its kinetic energy. This is why the solid lines experience the initial jump in energy on the left of Figure 2.14. Furthermore, after the initial rise or fall all orbits exhibit the converse behavior, corresponding to them reaching the other half of their orbit and thus going from infalling to outgoing and vice versa. This also therefore reverses the effects, but as the potential changes most rapidly at higher a the resulting amplitude is lessened. Generally, then, it makes a crucial difference *where* a particle is on its orbit in addition to its energy, unlike the Newtonian case where the definition of equal angular momentum and energy ensures the same orbits.

Finally, three additional orbits can be seen that are added to test the border of energies for which at $a = 1$ bound orbits become impossible. The orbits are then initialized with $l = 1$ at $V = -0.125, -0.1, 0 \cdot V_{100}$ colored as brown, pink and blue, and from the theory as per Figure 2.9 should correspond to an orbit barely staying bound, an orbit just slightly over the

threshold and one which rapidly becomes unbound even before $a = a_{NT}$. As can be seen from the Newtonian energy on the right, this is exactly what occurs when initialized at the periapsis (solid lines): the blue particle rapidly gains energy as it is increasingly accelerated away from the central mass, removed entirely. The pink orbit starts out with a fluctuation which initially rises with the same slope as the brown curve. Unlike that one, however, it does not stop and eventually even increases its slope outwards as expansion takes over. This can also be seen from the radii plotted in Figure A.8, where for the top right the two orbits (blue and pink) become unbound. As is visible on the top left, this is not the case for the Newtonian case with the expanding term frozen at $a = 0.2$ added. The energies then do correspond to stable elliptical orbits at the time they are initialized, however when moving outwards as expansion flattens the slide as described above they manage to make it over the hump and escape. Conversely, when initialized at the apoapsis (bottom row) the increasingly flat slide does not allow them to reach as far in and they stay bound on lower energy orbits.

Reinterpreting the results, when a particle with an initial kinetic energy K falls into a potential well frozen at $a = 0.2$ and would gain kinetic energy up to a value $(1 + n) \cdot K$ at its nearest point, with $n > 0$, it then loses an equal amount as it leaves the potential and leaves with the same kinetic energy K. The net change in kinetic energy is then 0. However, in an expanding Universe the potential well flattens out as it falls in. Therefore, as it reaches its nearest point it would instead have $(1 + f) \cdot K$ with $0 < f < n$. As it then leaves the potential well increasingly flattens such that it only requires $p \cdot K$ to leave, with $0 < p < f$, resulting in a net gain in kinetic energy $(f - p) \cdot K$. In the case of a photon, this is equivalent to a blueshift as it passes through a flattening potential well and is known as the integrated Sachs-Wolfe (Sachs & Wolfe, 1967) or also Rees-Sciama effect (Rees & Sciama, 1968). It is the same principle here which results in the asymmetry between the orbits.

2.8 So What Was the Point?

This chapter has focused on the behavior of bound structures within an expanding Universe, placing a special interest on the cosmological implementations of current state-of-the-art simulation codes. This implementation was found to be generally consistent between varying codes in Section 2.1. Section 2.2 then introduced and discussed the mathematical foundation of the typical Friedmann-Lemaître-Robertson-Walker metric as well as its extension to including a local point mass distortion for the standard ΛCDM cosmological model. The comoving formulation of this extended metric, known as the McVittie metric (McVittie, 1933), is shown for the Newtonian limit to equal the cosmological implementations within the codes in Section 2.3. The physical interpretation of this limit is discussed as local weak-field distortions within a large-scale homogeneous and isotropic, expanding background. For the case of a flat metric, the behavior of the scale factor was analyzed with differing cosmological constants in Section 2.4, introducing a semi-analytic form to approximate the non-analytical dependency of the scale factor on time. Bound structures within such an expanding flat background are then found to be perturbed away from circular orbits in Section 2.5 using a

typical perturbation theory approach from the literature (Cooperstock et al., 1998). It is found to be possible instead to derive general analytical solutions for the behavior of orbits within such point mass potentials in Section 2.6, finding that it is the density contrast of the bound structure versus the critical density which solely dictates the impact of expansion. Orbits enclosing higher densities are less influenced by the expanding background. This is adverse to some of the typical interpretations in that it is not the absolute scale which is responsible for the larger impact of expansion on systems such as galaxy clusters relative to galaxies, but rather that they are less concentrated due to their later formation redshifts (Binney & Tremaine, 2008). To check the validity of the cosmological implementations derived in Section 2.3, Section 2.7 employs a specially made simulation reduced to just those parts of the simulation code. Simulated orbits around a point mass potential were found to match the theoretical expectations from Section 2.6, with the effective potential felt by the particles flattening out towards later times. This results in more eccentric orbits at later times for equal orbital energies. By comparing scaled variants of the system and finding equal behavior it was demonstrated that it is indeed the density contrast and not the absolute scale which defines the impact of expansion. Finally, a discrepancy in the evolution of orbits initialized at different points within a single orbit at $a = 0.2$ was discovered and subsequently interpreted as an integrated Sachs-Wolfe (Sachs & Wolfe, 1967) or Rees-Sciama (Rees & Sciama, 1968) like effect which arises from varying central potentials and also applies to orbiting particles.

Chapter 3

Does Extension Change Expansion?

One of the mentioned greatest strengths of cosmological simulations lies in their ability to analyze highly non-linear processes of incredibly complex structures. This is of great use when wanting to compare with observations, as structure within the Universe is typically extended in nature, being comprised of many substructures as opposed to point like. Simulations of extended mass distributions therefore allow important consistency checks for theoretically models such as those presented in Chapter 2, as effects from N-body interactions can at times be underestimated in their impact.

This chapter has as a goal to check the analyses and conclusions for orbits within point mass potentials from Section 2.6 also for extended structures. Section 3.1 introduces some of the most common density profiles which well match extended structure present in the Universe and considers for them the evolution of orbits with time by examining the effective potential for an expanding background. This will provide an indication whether or not the findings from Section 2.6 are likely also to hold for extended structures. To also consider the impact of N-body interactions, Section 3.2 then presents the evolution of both a Plummer- and Hernquist-sphere in the same simulation framework from Section 2.7 for a Newtonian and expanding metric. The findings are summarized in Section 3.3, with an outlook provided for future research into processes where the impact of expansion could be significant.

3.1   Expansion with Extended Profiles

When considering the orbits of particles within a potential that itself lies within an expanding background, to understand the core concepts it is useful to reduce the complexity of the problem by beginning with a point mass potential as was done in Chapter 2. However, for real physical systems the central mass M need not be a point mass, but could also be modeled as an extended mass distribution $M(< r)$. Here then different common density profiles and their subsequent behavior when subjected to an expanding background are analyzed.

To start, it should be noted that of all terms appearing in Equation 2.45 – and so similarly for Equation 2.42 – it is only the gravitational term which varies for an extended mass distribution. The expanding term, $r \cdot (\ddot{a}/a)$, is dependent only on the distance to the center

and time, while the angular momentum can vary independently from the underlying mass distribution as it is also dependent on the orbits and distance to the center. Fortunately, this allows the introduction of mass profiles without significantly increasing the complexity of the mathematics. Furthermore, as most common density profiles are spherically symmetric, it follows from the shell theorem (Newton, 1687) that it is only the total mass contained within the considered radius r,

$$M(\leq r) = \int_0^r \mathrm{d}r' 4\pi r' \rho(r'), \qquad (3.1)$$

which is of relevance while that outside has no impact. Defining $M_f(\leq b) \equiv M(\leq r)/M_{\Delta_\mathrm{c}}$ as the fraction of mass present within the radius $r = b \cdot r_{\Delta_\mathrm{c}}$ relative to M_{Δ_c}, such that $M_f(\leq 1) = M(\leq r_{\Delta_\mathrm{c}})/M_{\Delta_\mathrm{c}} = 1$ by definition, it follows for an extended mass distribution that the acceleration from Equation 2.44 takes the form:

$$\frac{\ddot{r}(b,a)}{A_{\Delta_\mathrm{c}}(a)} = -\frac{M_f(b)}{b^2} - \frac{b}{\Delta_c/2} \cdot \frac{\Omega_{0,\Lambda} - \Omega_{0,\mathrm{m}}/(2a^3)}{\Omega_{0,\Lambda} + \Omega_{0,\mathrm{m}}/a^3}. \qquad (3.2)$$

Unfortunately, it is not quite as simple for the effective potential, as the integral over the force in Equation 2.45 gains a dependency on r in the mass for extended profiles. Instead, it is sensible here to use Poisson's equation $\nabla^2\Phi(r) = 4\pi G\rho(r)$, where $\Phi(r)$ is the gravitational potential. For Equation 2.50 this means that the gravitational term as scaled there for a general potential $\Phi(r)$ takes the form:

$$\left(\frac{1}{b}\right)_{\mathrm{point}} = \frac{r_{\Delta_\mathrm{c}}}{GM_{\Delta_\mathrm{c}}} \cdot \Phi(r), \qquad (3.3)$$

such that the form for an extended mass profile of the effective potential is:

$$\frac{V_{\mathrm{eff}}(r,a)}{V_{\Delta_\mathrm{c}}(a)} = \cdot \left[\frac{l^2}{2 \cdot b^2} - \frac{r_{\Delta_\mathrm{c}}}{GM_{\Delta_\mathrm{c}}} \cdot \Phi(r) - \frac{b^2}{\Delta_c} \cdot \frac{\Omega_{0,\Lambda} - \Omega_{0,\mathrm{m}}/(2a^3)}{\Omega_{0,\Lambda} + \Omega_{0,\mathrm{m}}/a^3}\right]. \qquad (3.4)$$

The scaling of the effective potential then occurs according to the Newtonian effective potential for a particle at rest $V_{\Delta_\mathrm{c}}(a)$.

3.1.1 Mass Profiles

To plug the mass profiles into the equations for the expanding background, their enclosed mass and potential must be determined as a function of radius. Here the chosen profiles are introduced and their forms for $M_f(< b)$ given. The first profile considered is the singular isothermal sphere, which is one of the simplest models and describes structures with a density slope of r^{-2}. Such profiles are commonly used in applications such as gravitational lensing, because they fit the observed projected profiles well and also have nice analytical properties – see for example Brimioulle et al. (2013) – though they typically require an additional cutoff radius to constrain their extent. This variant is not considered here. Instead, for the base

singular isothermal sphere the density is defined as:

$$\rho_{\mathrm{sis}}(r) \equiv \frac{\sigma_0^2}{2\pi G r^2} \tag{3.5}$$

where σ_0^2 is the central velocity dispersion. Equation 3.1 then gives:

$$M_{\mathrm{sis}}(\leq r) = \frac{2\sigma_0^2}{G} \cdot r. \tag{3.6}$$

Here and for many subsequent profiles the relation $M_{\Delta_c} = M(< r_{\Delta_c})$ allows the canceling of one of the parameters of the profile. For the single isothermal sphere it follows that $\sigma_0^2 \overset{!}{=} GM_{\Delta_c}/(2 \cdot r_{\Delta_c})$, such that:

$$M_{\mathrm{sis,f}}(\leq b) = \frac{M_{\mathrm{sis}}(< r)}{M_{\Delta_c}} = \frac{M_{\Delta_c} \cdot r}{M_{\Delta_c} \cdot r_{\Delta_c}} = b. \tag{3.7}$$

Defining $A_{\mathrm{sis}} \equiv GM(< r)/r^2 = (GM_{\Delta_c}/r_{\Delta_c})/r$ as the magnitude of the acceleration from a SIS-profile, the potential is then:

$$\Phi_{\mathrm{sis}}(r) = \int \mathrm{d}r\, A_{\mathrm{sis}} = \frac{GM_{\Delta_c}}{r_{\Delta_c}} \int \mathrm{d}r\, r = \frac{GM_{\Delta_c}}{r_{\Delta_c}} \cdot \ln(r) + const. \tag{3.8}$$

This shows that there are any number of potentials which reproduce the form of the density and enclosed mass for the singular isothermal sphere (Binney & Tremaine, 2008). As such a constant must be defined, which is chosen here to have $\Phi_{\mathrm{sis}} = -\Phi_{\mathrm{point}}$ at r_{Δ_c}. By then taking $a_s \equiv e \cdot r_{\Delta_c}$, where e is Euler's constant, it follows for the gravitational term in Equation 3.4:

$$\frac{r_{\Delta_c}}{GM_{\Delta_c}} \cdot \Phi_{\mathrm{sis}}(b) = \ln\left(e^{-1} \cdot b\right). \tag{3.9}$$

At $r = r_{\Delta_c}$ the term becomes equal to -1. Note that this choice is done to better compare the behavior of the isothermal slope within the plots.

The second profile considered here is the Plummer density profile (Plummer, 1911), which was originally introduced to described globular clusters. its profile is

$$\rho_{\mathrm{p}}(r) \equiv \frac{3M_0}{4\pi a_p^3}\left(1 + \frac{r^2}{a_p^2}\right)^{-5/2} \tag{3.10}$$

with M_0 the total mass and a_p the so-called Plummer radius setting the size of a central core where the potential flattens out. This dampened central region has the nice consequence of avoiding diverging forces when simulating multiple particles, hence why a similar principle is used in N-body simulations under the term "softening" – see Section 3.2 and Binney &

Tremaine (2008). Defining then $c_p \equiv r_{200}/a_p$ gives

$$M_{\mathrm{p,f}}(\leq b) = \left(\frac{1 + c_p^{-2}}{1 + c_p^{-2} \cdot b^{-2}} \right)^{3/2}. \tag{3.11}$$

$M_{\Delta_c} = M(< r_{\Delta_c})$ was used to define $M_0 = M_{\Delta_c} \cdot (1 + c_p^{-2})^{3/2}$ For large radii this approaches the finite mass M_0. The gravitational term in the effective potential from Equation 3.4 is then:

$$\frac{r_{\Delta_c}}{G M_{\Delta_c}} \cdot \Phi_{\mathrm{p}}(b) = \frac{c_p \left(1 + c_p^{-2} \right)^{3/2}}{\sqrt{1 + c_p^2 b^2}}. \tag{3.12}$$

For the centers of elliptical galaxies, the Hernquist model (Hernquist, 1990) is found to be a good match (Binney & Tremaine, 2008). The corresponding density profile is

$$\rho_{\mathrm{h}}(r) \equiv \frac{M_0}{2\pi} \frac{a_{\mathrm{h}}}{r} \frac{1}{(r + a_{\mathrm{h}})^3}, \tag{3.13}$$

with M_0 the total mass and a_{h} the Hernquist scale radius such that when defining $c_{\mathrm{h}} \equiv r_{200}/a_{\mathrm{h}}$ it follows that:

$$M_{\mathrm{h,f}}(\leq b) = \left(\frac{1 + c_{\mathrm{h}}^{-1}}{1 + c_{\mathrm{h}}^{-1} \cdot b^{-1}} \right)^2, \tag{3.14}$$

where again $M_{\Delta_c} = M(< r_{\Delta_c})$ gives $M_0 = M_{\Delta_c} \cdot (1 + c_{\mathrm{h}}^{-1})^2$. This gives the nice form:

$$\frac{r_{\Delta_c}}{G M_{\Delta_c}} \cdot \Phi_{\mathrm{h}}(b) = \frac{c \cdot \left(1 + c_{\mathrm{h}}^{-1} \right)^2}{(1 + c_{\mathrm{h}} b)}. \tag{3.15}$$

Finally, the density profiles of relaxed dark matter halos are found to match the Navarro-Frenk-White (NFW) density profile (Navarro et al., 1996), albeit with discrepancies towards the center. The profile is defined as:

$$\rho_{\mathrm{NFW}}(r) \equiv \frac{\rho_0}{\frac{c \cdot r}{r_{\Delta_c}} \left(1 + \frac{c \cdot r}{r_{\Delta_c}} \right)^2} \tag{3.16}$$

and gives:

$$M_{\mathrm{NFW,f}}(\leq b) = \frac{\ln\left(1 + c \cdot b \right) + (1 + c \cdot b)^{-1} - 1}{\ln(1 + c) - \frac{c}{1+c}} \tag{3.17}$$

where $c \equiv R_{\mathrm{s}}/r_{\Delta_c}$, with R_{s} is the concentration of the mass distribution within r_{Δ_c}. Note that the profile does not have a form with M_0, as it does not converge to a finite mass. The resulting gravitational term in Equation 3.4 is:

$$\frac{r_{\Delta_c}}{G M_{\Delta_c}} \cdot \Phi_{\mathrm{NFW}}(b) = \frac{1}{b} \cdot \frac{\ln(1 + cb)}{\ln(1 + c) - \frac{c}{1+c}}. \tag{3.18}$$
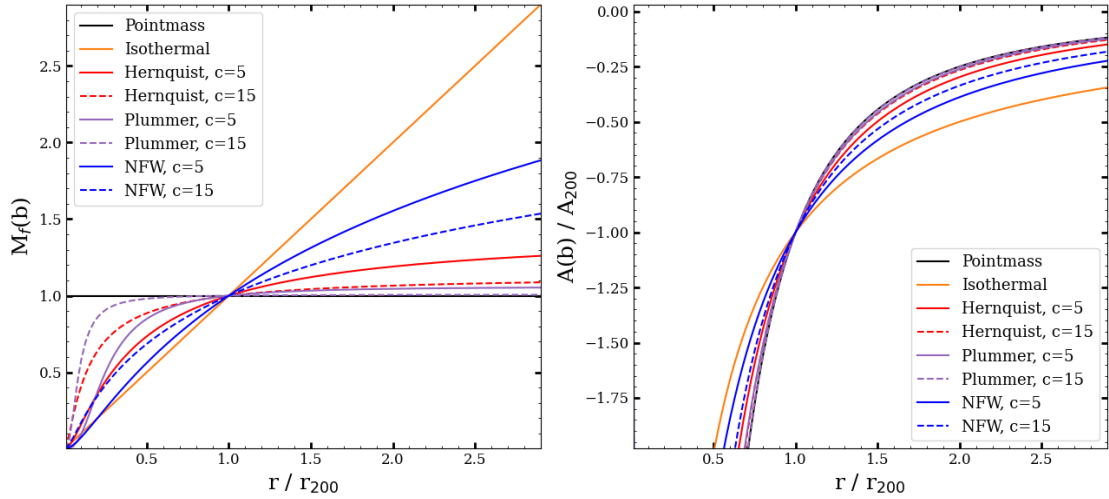
Figure 3.1: *Left:* The enclosed mass for varying extended spherically symmetric density profiles as a function of radius. *Right:* The resulting acceleration within a Newtonian frame.

3.1.2   The Resulting Forces and Potentials

These mass profiles are used to describe various different objects within the Universe. As such, it is certainly not expected for them to behave equally. Note that throughout the overdensity is set as $\Delta_c = 200$, and equal concentration parameters $c_i = 5, 15$ are used, where higher concentrations imply more point mass-like behavior. They are chosen to show the general behavior between the profiles and their dependency on the scale radii a_i. The isothermal and point mass potentials do not depend on any c_i.

To get an initial impression for their properties, the enclosed mass and acceleration are depicted in Figure 3.1. The common scaling has ensured by definition that all profiles share the same mass and acceleration at $r = r_{200}$. As can be seen on the left, for the point mass any radius encloses the same mass while for the isothermal the mass rises linearly out to infinity. Between the Plummer and Herquist profiles, the former is first flatter toward the center, then rises more steeply before also flattening off more quickly. This is because of the Plummer's flat central density and steep outer slope $\propto r^{-5}$, hence why for large radii it has a mass quite close to the point mass, quickly converging to its M_0. In comparison, the NFW profile has a generally more shallow slope in the center which persists to high radii, resulting in the diverging total mass. As $A \propto M_f$ this directly translates into the acceleration felt on the right, with the profiles that are steeper at higher radii having a stronger acceleration there. However, at higher radii all profiles are generally similar to the point mass. This means that expansion will impact them all similarly, as the differences at lower radii are where the effects of expansion are comparably negligible anyway. Consequently the results from Section 2.6 for the acceleration of a point mass within an expanding background also hold for extended profiles, which can further be seen in Figure A.9 when plotting the full form of the acceleration from Equation 3.2.

Turning then to possible resulting orbits, Figure 3.2 plots the effective potential of structures with overdensity $\Delta_c = 200$ at time times $a = 0.2$ (left) and $a = 1$ (right). The angular
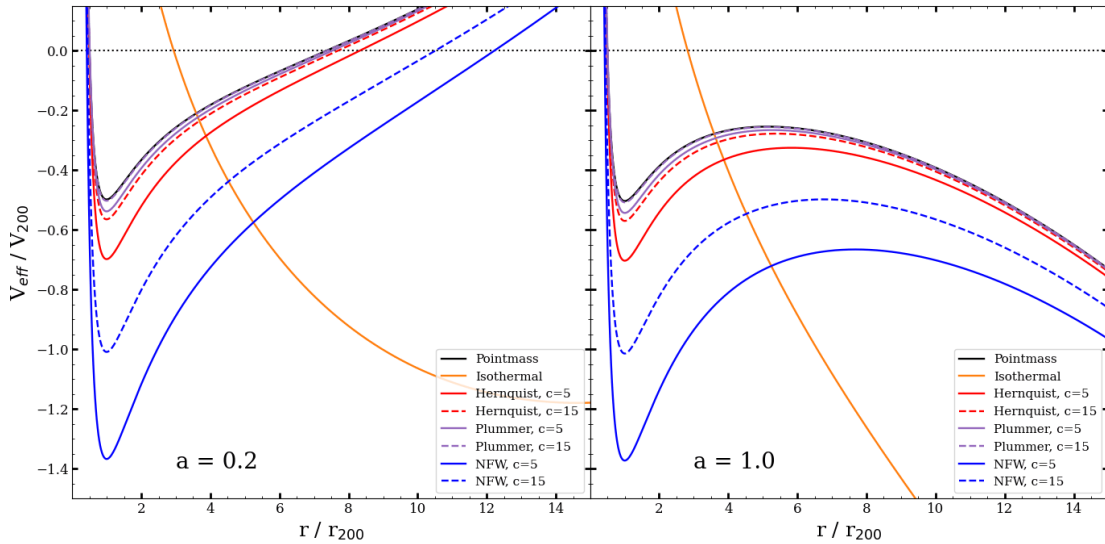
Figure 3.2: *Left:* The effective potential at $a = 0.2$ scaled with $V_{200}(a = 0.2)$ resulting from a point mass (black) and various extended profiles (colored) within an expanding frame as a function of distance r. *Right:* The same for $a = 1$ scaled with $V_{200}(a = 1)$.

momentum L is defined as the value for a point mass potential in a Newtonian frame at $b = 1$, so $l = 1$ in Equation 2.47. Aside from the isothermal density profile, the extended distributions very closely mimic the shape of the point mass at both times. Note further that the minimum of the effective potentials, i.e., the circular orbits, are all located at $b = 1$ as they should be for $l = 1$. The largest difference is the depth of the potential, where it becomes deeper the more mass is distributed farther out. This is because at the lower radii where the point mass lies significantly above the extended profiles in mass (see Figure 3.1) the angular momentum term dominates completely, masking the behavior of the gravitational potential which would find deeper potentials for the Plummer and Hernquist profiles. The total mass within r_{200} is the same by definition, but those two profiles which have it lie mostly near the center consequently have less present at $r = r_{200}$ itself and thus have a more shallow potential there, more closely matching the point mass.

It is of note that the larger radii start converging for all profiles, as expansion becomes increasingly relevant until it completely dominates. This is visible also for the isothermal profile as it begins to bend upwards on the left of Figure 3.2, which has the overall most shallow density profile and therefore highest mass (see Figure 3.1). Nonetheless, $\lim\inf \Phi_{\text{sis}}(r)/r^2 \rightarrow 0$ and the expansion term therefore is still dominant at large radii.

But what about a fixed extended object, i.e., initializing an extended profile at some earlier time and then keeping it fixed with time while the expanding background changes? With the initial profile taken as the one on the left from Figure 3.2 at $a = 0.2$ the resulting effective potentials at $a = 1$ and $a = 10$ are depicted in Figure 3.3. As can be seen, within the fixed size of the structure expansion flattens the effective potential in the outskirts, while the inner regions are largely unaffected. All profiles still trace the form of the point mass, with the minimum at $b = 1$. Furthermore, at $a = 1$ the expansion term is already nearly entirely
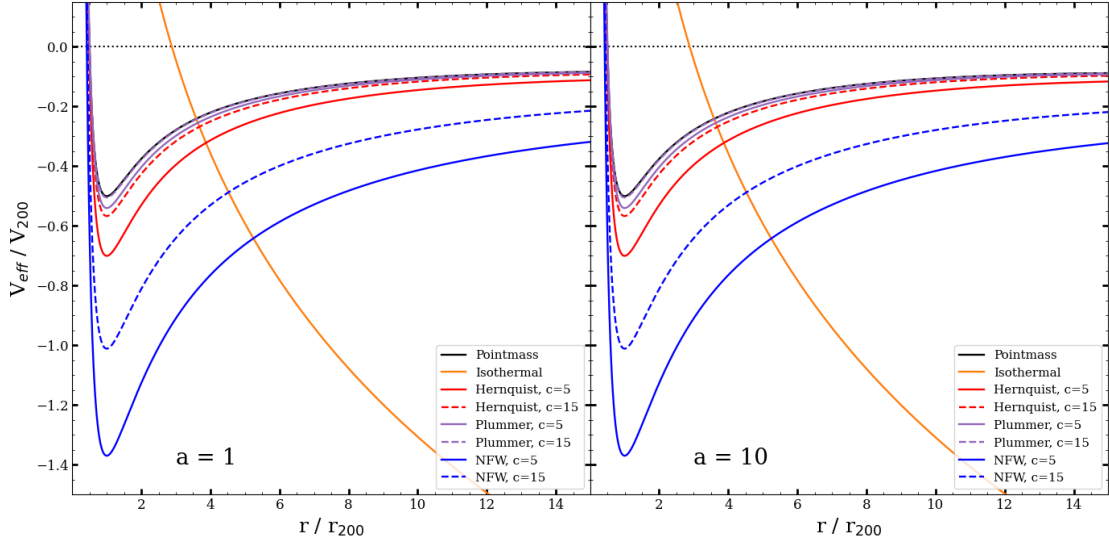
Figure 3.3: *Left:* The effective potential at $a = 1$ scaled with $V_{200}(a = 0.2)$ for a fixed structure initialized at $a = 0.2$ resulting from a point mass (black) and various extended profiles (colored) within an expanding frame as a function of distance r. *Right:* The same for $a = 10$ scaled with $V_{200}(a = 0.2)$.

dominated by dark energy, and as such does not change much to $a = 10$ as can be seen on the right. The analyses from Section 2.5 are therefore also applicable for extended profiles.

Having seen that the general behavior remains the same from the point mass to the extended profiles, what about the theoretical behavior of the extent of orbits of constant total energy? This was analytically solvable for the point mass as the solutions of Equation 2.53, where $V \equiv V_{\text{eff}}(r, a_0)/V_{\Delta_c}(a_0)$ was defined as the fractional fixed total energy of a particle relative to the total energy of a particle on a circular orbit at $b = 1$. However, for an extended profile the form becomes:

$$0 = \frac{b^4}{\Delta_c} \cdot \frac{\Omega_{0,\Lambda} + \Omega_{0,m}/a^3}{\Omega_{0,\Lambda} - \Omega_{0,m}/(2a^3)} + b^2 \cdot \left(V + \frac{r_{\Delta_c}}{GM_{\Delta_c}} \cdot \Phi(b)\right) - \frac{l^2}{2}. \tag{3.19}$$

Taking for example the Hernquist profile, the substitution to $u = 1 + c_i b$ allows the form of Equation 3.19 to become a pure polynomial. However, this gives

$$b^2 \frac{r_{\Delta_c}}{GM_{\Delta_c}} \cdot \Phi(b) \propto \left(\frac{u-1}{c_p}\right)^2 \frac{1}{u} \propto \frac{1}{u} - 2 \cdot u + u, \tag{3.20}$$

such that when multiplying the entire Equation 3.19 by u the final polynomial is now of *fifth* order, not fourth. As known from the Abel-Ruffini theorem, no general solution to these exists (see for example Tignol 2001), and as such would require numerical approximations. Similarly, the forms for the other profiles are not even transformable into polynomials. Consequently, this is not pursued here further.
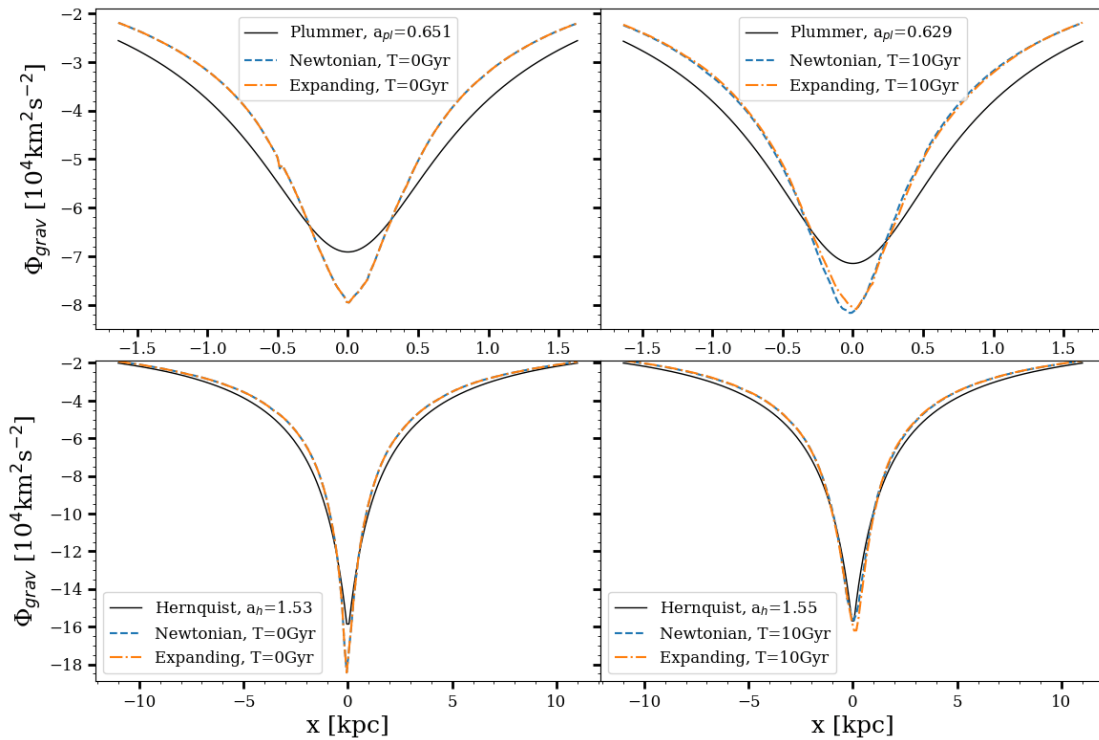
Figure 3.4: The gravitational potential along the x-direction for the Plummer (*top row*) and Hernquist (*bottom row*) spheres for the Newtonian (blue dashed) and expanding cases (orange dash-dotted). The region shows the extent of 68% of the mass. Best fits to the Newtonian case of the analytical profiles given as Equation 3.10 and Equation 3.13 are plotted as a black solid line, with scale radii as given in the legend. The left column is the start of the simulation, and the right the resulting distribution after 10 Gyr.

3.2   N-Body Orbits

N-body interactions of extended objects can have a significant impact on their evolution through processes such as close passages leading to ejections. This motivates the need to test the theoretical conclusions drawn for extended mass profiles in Section 3.1 against simulations of such profiles. For the case of a Plummer and Hernquist sphere, this section discusses the resulting evolution within a Newtonian and expanding frame by employing the simulation from Section 2.7. As mentioned in Section 3.1.1, for N-body simulations it is possible for close passages of particles to lead to diverging kicks that would completely eject the particles. To avoid this these passages can be dampened by calculating the gravitational force as that resulting from a Plummer potential $\Phi_p = -GM/\sqrt{r^2 + a_s^2}$ with a_s as a softening length. For small a_s this simply flattens the normally diverging central region, while for longer distances becoming the correct point mass potential – see Figure 3.1 where a low a_s corresponds to a large c_s.

There are 10 000 and 5000 particles with a total mass of $1 \times 10^{12}\,\mathrm{M}_\odot$ and $5.6 \times 10^{12}\,\mathrm{M}_\odot$ for the Plummer and Hernquist sphere, respectively. The spheres are first simulated for around 2 Gyr within the Newtonian frame to allow the initial distributions to relax. Afterwards, the particles are then run for 10 Gyr for the different frames, where the expanding one is initialized
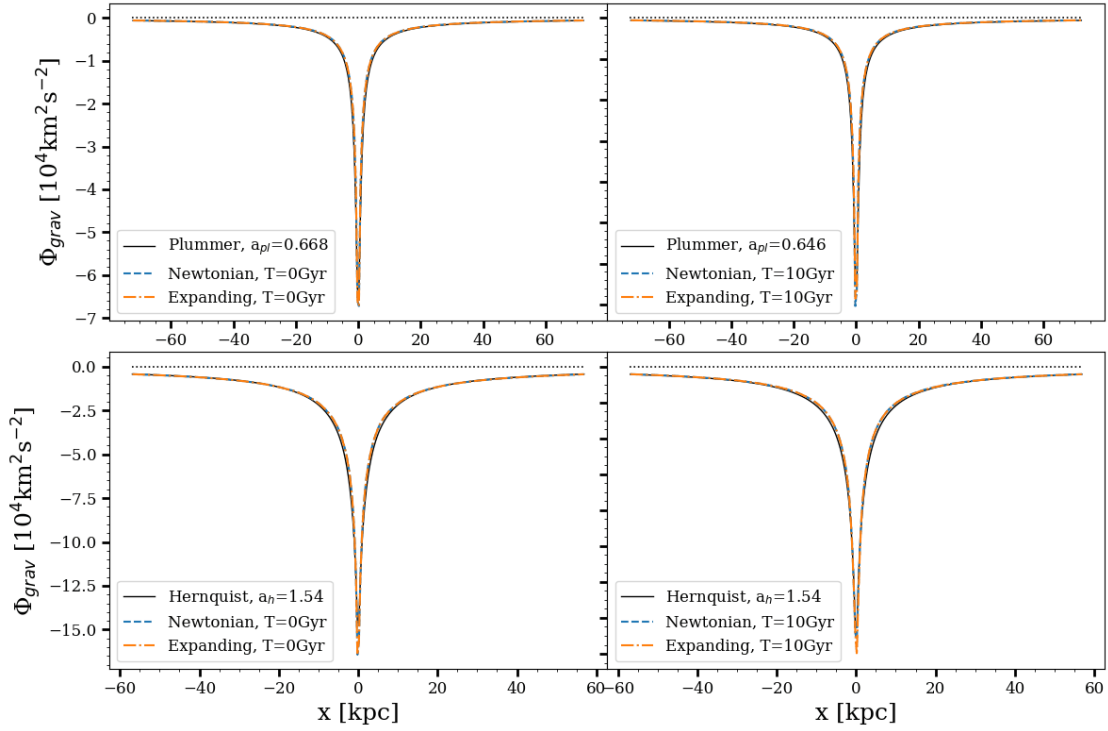
Figure 3.5: The same as Figure 3.4, but for the extent of 95% of the mass, with the dotted black line representing the zero potential line.

at $z = 2$. The softening length is chosen as $a_s = 0.022\,\text{kpc}$, where for the expanding case this is transformed into the comoving frame by multiplying with the scale factor $a(t)$.

To see which impact expansion has on these extended spheres, a good overview can be gained from considering the shape of the gravitational potential. This traces the overall distribution of mass particles and thus allows insight into the broader changes between the Newtonian and expanding cases. It is given as

$$\Phi(\boldsymbol{x}) = -G \cdot \sum_{i}^{n} \frac{m_i}{|\boldsymbol{x} - \boldsymbol{x_i}|} = -GM \cdot \sum_{i}^{n} \frac{1}{|\boldsymbol{x} - \boldsymbol{x_i}|}, \tag{3.21}$$

as all point masses have equal mass. Figure 3.6 plots the resulting potential in x-direction centered on the center-of-mass of the Plummer (top row) and Hernquist spheres (bottom row) for the central 68% of the total mass. Note that the initial potentials are initialized as identical for the Newtonian and expanding case. The Plummer sphere's center ends up being somewhat more peaked than the theoretical distribution. Nonetheless, the form after 10 Gyr on the top right is seen to be practically identical between the Newtonian and expanding cases. This shows as expected that the central regions are generally resilient against expansion. The minor differences are most likely statistical in nature. For the Hernquist sphere, the same is found with overall agreement between the expanding and Newtonian cases. Interestingly, the best fit scale radius is similarly stable in time for both spheres.

Zooming out, Figure 3.5 shows that the same can be said at larger distances. For the extent depicted, which includes 95% of the total mass, the curves are practically identical between
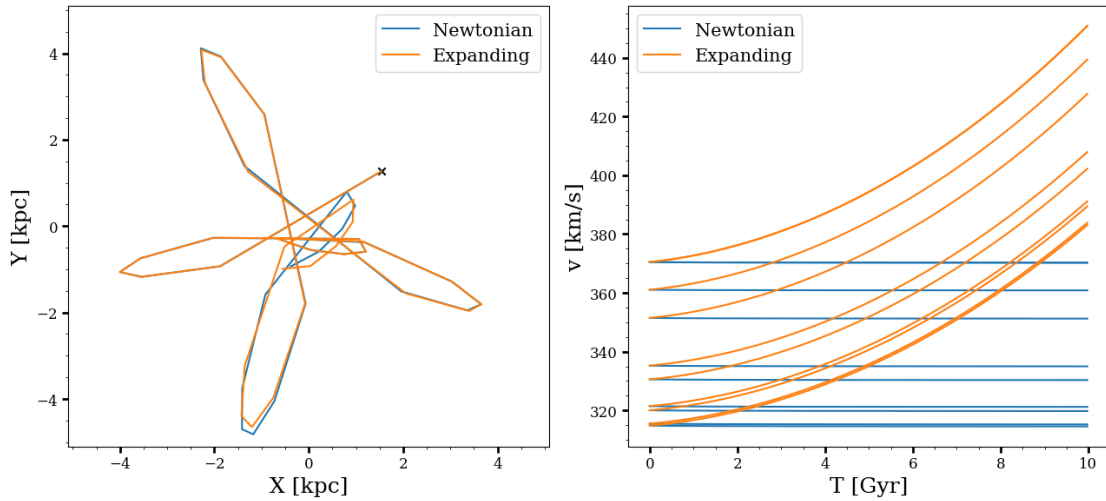
Figure 3.6: *Left:* The orbit of a chosen particle in the Newtonian and Expanding simulations for a duration of 0.8 Gyr. *Right:* The velocities as a function of time of the ten particles which escaped the farthest for the Newtonian and Expanding simulations.

the Newtonian and expanding cases for both spheres. Would expansion severely remove particles at the outskirts, where the gravitational potential is relatively shallow already at initialization (left column), then the resulting potential should drop more off more steeply. As it does not, the number of particles ejected is not strongly different between the Newtonian and expanding frames. Another thing of note is that the Hernquist sphere's scale radius is found to be more slightly more stable with time, as can be seen from the fits.

These findings do not mean that expansion has no impact whatsoever, but rather that it is relatively negligible in its overall impact on the large-scale distribution of the masses. For the example of an orbit of one chosen particle between the expanding and Newtonian cases for the Plummer sphere, as can be seen on the left in Figure 3.6 there do exist minor fluctuations between the frames which alter the trajectory. The orbit depicted is from initialization to around 0.8 Gyr, where initially the orbit stays exactly identical and then the minor deviations lead to a slight divergence. This quickly grows due to the chaotic N-body interactions within the central region such that the later times are not depicted as they do not correlate anymore. There is however one region where the difference is strongly noticeable, and that is for the particles which are ejected. The right panel in Figure 3.6 depicts the velocities of the ten particles which are ejected most strongly as a function of time. For the Newtonian case they are practically stable, decreasing very slightly with time due to the tiny gravitational attraction remaining from the Plummer sphere, while for the expanding case contrarily they begin to accelerate outwards. However, the number of particles ejected to this degree is minor, and they are at distances of over 1500 kpc for both frames. As such they have no noticeable impact on the mass distribution itself.

It must be noted here, however, that both the Plummer and Hernquist spheres, as seen in Section 3.1.2, are very peaked in their distributions. As such, much of the mass is far in the central regions which are least affected by expansion. Furthermore, the sphere is initialized at $z = 2$ in what is ostensibly a Newtonian form, because it was simulated to relaxation with a

Newtonian background. It would be interesting to instead take a sphere that is relaxed as seen at $z = 2$ itself, i.e., with adding a frozen expansion term as done in Section 2.7. This would more closely match the real impact from expansion, as there simply are no structures which evolve in a purely Newtonian frame. Instead, comparisons should always take structures at higher and lower z, though this then convolves with the changing critical density.

3.3   Looking Towards the Future

The question posed in the title of this chapter is central to interpreting the physical conse-quences of expansion on extended structures within the Universe. Summarily, it is found here that their extended nature *does not* impactfully alter the conclusions drawn for a point mass in Chapter 2. Section 3.1 introduces the considered mass profiles and derives the form in which they enter into the acceleration and the effective potential. Though there are differences for the exact values, the overall shape of the acceleration with radius matches that for the point mass, in particular for cases where the mass distribution is strongly concentrated such as for the Plummer and Hernquist profiles. The NFW profile is found to exhibit the largest difference of the two-parameter models, due to its generally more shallow distribution of mass. For the singular isothermal sphere, the static slope $\propto r^{-2}$ leads to the largest mass for high radii of all profiles, but is found not to grow rapidly enough to where it would overpower the effects of expansion at large scales. Indeed, all profiles converge to the behavior dictated by expansion at large radii, while being largely unaffected at lower radii. Furthermore, it was shown that the potentials of extended mass distributions are pulled downwards at large radii with increasing time due to expansion, again matching the behavior for the point mass. Finally, Section 3.2 analyzed the simulation of both a Plummer and Hernquist sphere, finding that the Newtonian and expanding evolution coincide. This echos the statements made in Section 2.6 in that the evolution of the central regions of the potential itself do not change strongly.

In the future, it would be interesting to consider more varied density profiles as well, for example the common Einasto profile (Einasto, 1965), originally constructed to fit stellar components of galaxies. This is found to also well describe various forms of dark matter halos (Cimatti et al., 2019) and takes the form

$$\rho(r) = \rho_{-2} \exp\left(-2n\left[\left(\frac{r}{r_{-2}}\right)^{1/n} - 1\right]\right). \tag{3.22}$$

as given in Equation 4 from Retana-Montenegro et al. (2012). As it has a variable slope n, the Einasto profile allows for a broader range of shapes that could be tested in an expanding background. Additionally of great interest is the environment. Though the bound structures themselves are found to be largely unaffected, the outskirts are not. This would potentially have an impact on for example the inflow rate and velocity of mass onto the structure, as well as for highly eccentric individual orbits. As all structure formation always occurs within

an expanding frame, it is difficult to disentangle the impact of general changes, such as later forming structures being less concentrated due to decreasing critical density, to the local impact on individual structures. One could, for example, freeze a structure within the expanding frame at an early redshift and compare its properties when evolving there versus evolving with a changing expanding background. There is still much which remains to be explored.

Chapter 4

The Elephants in the Room – Galaxy Clusters

Attention is now turned to the second to fourth questions posed in Chapter 1. As remarked there, recent studies have found discrepancies in the number, mass, concentration and distribution of substructures in very massive galaxy clusters between observations and simulations (Jauzac et al., 2016; Meneghetti et al., 2020). The particular focus will be placed on the question of the number of very massive substructures, with their distribution naturally arising in the process. Concentration in turn is discussed further in both Section 5.2.4 and Section 7.1.

Before one can understand the problem of massive substructures, however, one first must understand the structures within which they are being found, namely galaxy clusters. Section 4.1 provides an overview of the history of observations into galaxy clusters, how they have caused new issues and corresponding physical insights to arise. It is based primarily on the great summaries of galaxy clusters provided by Kravtsov & Borgani (2012) and Biviano (2000) supplemented by some portions written by Cimatti et al. (2019), with more topically focused reviews by Sarazin (1988) (X-rays) and recently by Contini (2021) (intracluster light). As galaxy clusters are the largest collapsed structures, it is of utmost importance to understand the current theory of structure formation within the concordance cosmology of ΛCDM, which is discussed in Section 4.2 at great depth. This ensures greater understanding of why substructure masses could provide challenges to ΛCDM because of their direct link through structure formation. Section 4.3 then briefly covers the current understanding of their composition, with a particular focus placed on processes affected substructures within galaxy clusters. The findings are summarized in Section 4.4.

4.1 What is a Galaxy Cluster?

Galaxy clusters are, as the name implies, clusters of galaxies, and represent the largest bound structures in the universe. They were first observed in a quantifiable manner during the year 1901 by Max Wolf as, paraphrased from the German original, a gathering of numerous small nebulaspots so tightly clustered that when observing the area one would practically

startle at the odd appearance of this "Nebelhaufen"(Wolf, 1901), translated as cluster or heap of nebulae. He found 108 of such spots clustering in what is now called the Coma Cluster, something he noticed again with 148 nebulae for the Perseus Cluster in the year 1906. Though these represent the first quantifiable measurements, as mentioned by Biviano (2000) general observations of this clustering were noted much earlier also in the Coma Cluster by William Herschel all the way back in the year 1785, when on pages 255 to 256 he mentions "the appearance of that remarkable collection of many hundreds of nebulae which are to be seen in what I have called the nebulous stratum of Coma Berenices" (Herschel, 1785), or the Coma Cluster. He likened it to a collapsed gathering of stars, speculating further that "our system, after numbers of ages, may very possibly become divided so as to give life to a stratum of two or three hundred nebulae". The Coma Cluster is continuously present in early important observations, likely due to its ideal position in the north pole relative to the galactic plane.

4.1.1   First Measurements and the Curious "Non-Luminous Matter"

Galaxy clusters can contain hundreds of galaxies on spatial scales of megaparsecs, and can reach masses exceeding $1 \times 10^{14}\,M_\odot$ (Sarazin, 1988). Our current knowledge and understanding of these extreme masses is not to be taken for granted – that they indeed are this massive was shown first through measurements of the galaxy velocities and by assuming the virial theorem for the Coma (Zwicky, 1933) and Virgo Clusters (Smith, 1936), during a time when they were still called "extragalactic nebulae". For the latter case, through simple yet robust arguments Smith (1936) concludes a total mass for Virgo of $1 \times 10^{14}\,M_\odot$. This argument for a regular structure is central, as such high velocities could theoretically also be explained by collapsing structures which would then *not* indicate such high masses (as it would not be in virial equilibrium). The lack of clustering or the expected downwards slope for a structure collapsing towards its center in Figure 4.1 indicates no such collapse is taking place, whereby it can be concluded that the structure is at least somewhat stable and subsequently that circular velocities can provide an estimate for the total mass.

Following this conclusion, however, Smith notes that with the (then common) assumption of no internebular material this mass distributed over 500 assumed nebulae in Virgo would mean an average nebula mass of $2 \times 10^{11}\,M_\odot$ – a value around 2 orders of magnitude higher than the average nebula mass estimate at the time of $6 \times 10^8\,M_\odot$ to $1 \times 10^9\,M_\odot$ from Hubble (1934). This lent credence to the similar findings for Coma as made even earlier by Zwicky (1933) – but what is then this "non-luminous" matter of which there is so much in galaxy clusters? A first clue can be gleamed from the fact that Zwicky famously termed it "dunkle materie", or "dark matter".

4.1.2   Were We Simply Using the Wrong Wavebands?

The presence of dark matter, however, was the subject of debates for many subsequent decades – spurred for example by noticing an underestimation of stellar masses in early studies (Kravtsov & Borgani, 2012). Many alternative explanations were discussed, for
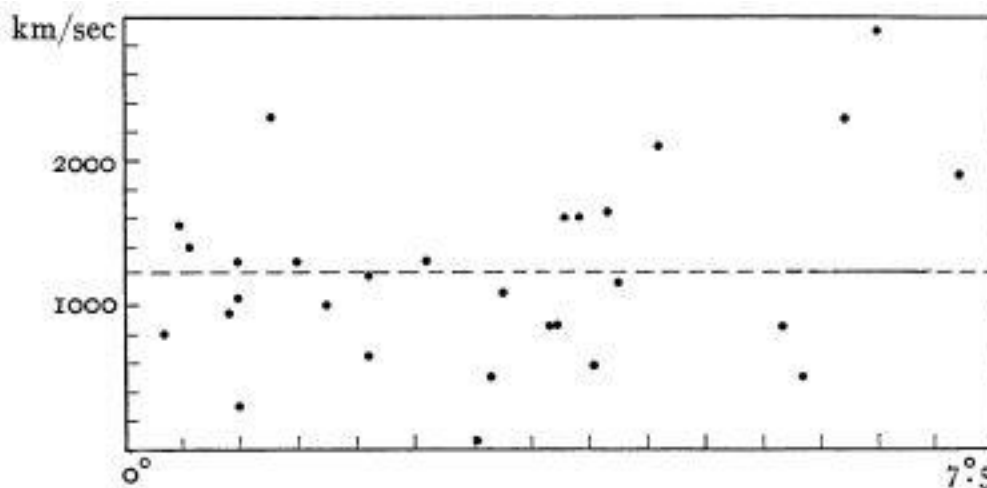
Figure 4.1: The distribution of velocities of assumed member galaxies of Virgo plotted as a function of distance to the center of the cluster. Figure 2 from Smith (1936).

example the existence of some extremely elliptical galaxies within the galaxy clusters with mass-to-light ratios ten times higher than typical values (Abell, 1965), the presence of many interlopers on hyperbolic orbits or that the galaxy clusters themselves are actually not dynamically stable, instead being in the process of disintegrating (Biviano, 2000). This was further exacerbated by theoretical considerations when moving away from the assumption of "transparent" internebular material (Smith, 1936), instead allowing for intracluster gas and dust as done by Limber (1959). Though at the time not yet conclusively observed within galaxy clusters themselves, presence of such gas in open star clusters (Drake, 1958) and the theoretical understanding of the formations of galaxies as occurring within a larger parent clustering of gas (Limber, 1959) both implied its existence – the former by assuming mergers of galaxies within the cluster would fling out their gas and dust (Spitzer & Baade, 1951), the latter by having the leftover gas from the initial formation of the galaxy persist in the cluster. It was already at this point anticipated that the intracluster medium would not necessarily follow the large-scale distribution of the galaxies, instead being prone to effects such as pressure, turbulence and magnetic field strength (Limber, 1959). Though many of the assumptions and conclusions made do not hold up to current scrutiny, say the age of the universe as 3×10^9 yr and the size of the Coma Cluster as 280 kpc leading to between 20 and 150 collisions for a typical galaxy as given by Spitzer & Baade (1951), they laid important foundations for later observations of the ICM. It is interesting here to note the consistent presence of like argumentation for clusters of stars and clusters of galaxies, present both in the very early writings (Herschel, 1785) as well as later (Spitzer & Baade, 1951).

It would then be in the year 1966 when X-ray emission was first detected as coming from a source outside of the Milky Way galaxy (Sarazin, 1988), namely in the central region of the Virgo Cluster around M87 (Byram et al., 1966). This was further strengthened by the findings of Bradt et al. (1967), excluding with high probability ($> 15/16$) cases of background fluctuations or of two distinct sources (the historic signal detected is depicted in Figure A.10),

as well as with observations of X-ray signals originating from the center of the Coma Cluster (Boldt et al., 1966). Similar observations in the following years lead Cavaliere et al. (1971) to the conclusion that there exists a "class of intense X-ray sources correlated with associations of galaxies", arguing that the signals extend beyond singular galaxies. The sources rather correlate with the densest regions of the clusters, though at the time this could not yet be conclusively linked to some underlying physical process responsible for the X-ray signal (Cavaliere et al., 1971). Many possible sources were considered such as an active nucleus, a superposition of individual galaxies, or that there was extended thermal emission from intracluster gas. The hot gas postulate, while initially tentative due to supposed time variations observed in the Virgo Cluster's emission (Cavaliere et al., 1971), would gain credence when longer observations of the Coma Cluster done with the same instrument *Ariel V* (Sanford & Ives, 1976) – as opposed to comparing multiple measurements of different experiments – found remarkably constant temporal brightness behavior with less than 20% or less variance on timescales between 6 d to 1 yr (Elvis, 1976). This would incredibly assist in the study and understanding of the evolution of galaxy clusters, as the X-ray observations allowed the detection of clusters at $z > 1$ (Rosati et al., 2002; Kravtsov & Borgani, 2012).

4.1.3   Confirming Dark Matter and Consequences for Cosmology

The famous "missing mass" problem would come to a head through two key components (Biviano, 2000). Firstly, the ever-increasing evidence, one argument of which is quite elegant in its simplicity. The large galaxy cluster masses (and so their high mass-to-light ratios) are found via the virial theorem (Zwicky, 1933; Smith, 1936), which requires the galaxy clusters to be stable. So maybe they are not (Ambartsumian, 1958), but if that is true then most galaxy clusters should, due to the large velocities and subsequent small timescales, have already disintegrated. Consequently most field galaxies would then be original galaxy cluster members, which they do not appear to be due to their clustering in space (Limber, 1962). It follows then that the large virial masses found for galaxy clusters are indeed a solid measurement – so there *is* mass missing. Similarly, the newer radio measurements allowed the observations of non-Keplerian rotation curves farther out, additionally indicating the presence of more mass (Biviano, 2000).

Secondly, the release of two impactful papers by Einasto et al. (1974) and Ostriker et al. (1974). The former employed rotation curves for 105 pairs of galaxies and found them irreproducible with just the visible mass, instead requiring what they termed a "corona" with an exponential density law. They found that the total mass contained in the coronas was an order of magnitude higher than that from the stars. This was significant because it had been suggested previously by Page (1952) that these pairs featured significantly lower mass-to-light ratios than galaxy clusters did. Meanwhile, Ostriker et al. (1974) open with the poignant sentence "There are reasons, increasing in number and quality, to believe that the masses of ordinary galaxies may have been underestimated by a factor of 10 or more". They raise the excellent point that the presence of spherical shells of mass by virtue of the shell

theorem (Newton, 1687) would not be measurable by rotation curves of the stars interior to them, hence restricting the findings of Page (1952) to small central scales for the galaxy pairs. Instead of converging, observations suggested that outside of those scales the mass of giant spiral galaxies depends on radius as $M(r) \propto r$. The measurements for the gas portion of the mass were still the result primarily of radio observations of the 21 cm-line from neutral hydrogen, emphasizing the value of the rise of X-ray observations. It would finally be the advent of gravitational lensing which set in stone the presence of dark matter (Fort & Mellier, 1994), as predicted by Zwicky (1937) many decades prior.

However, given that a majority of the now-found mass would be in the form of this dark matter, the question becomes what this mass actually is. The aforementioned observations of the hot intracluster gas however could not account for all of the missing mass that now was clearly established as real. This would go a step further to rule out baryons generally as a dark matter candidate through the theory of primordial nucleosynthesis (see Olive et al. 1981 and Cavaliere et al. 1998). Instead, the component is distributed relatively less condensed than the stellar mass is, indicating it to be collisionless (Bond et al., 1982). For lower energy candidates, termed "cold dark matter", with an initially linear power spectrum $|\delta_k|^2 \propto k^n = k^1$, the resulting density perturbations for would lead to collapse first of overdensities on the galaxy scale, with larger scales collapsing soon after. This is then a scenario of *hierarchical clustering* of galaxies (Bond et al., 1982). Interestingly, already Cavaliere et al. (1998) find good fits for a CDM cosmogony in a flat geometry with $\Omega_{0,m} = 0.3$.

4.1.4 Consequences for Cosmology

As presented for the case of dark matter, galaxy clusters offer one of the most unique observatories for insights into the Universe itself. Their identity as the largest collapsed structures offers the ability to use them as "cosmographic buoys" for the peaks in the large-scale matter density (Allen et al., 2011). They fortunately offer additionally a wide array of wavelengths with which they can be probed: X-ray from the hot intracluster medium (Sarazin, 1988; Rosati et al., 2002), optical from the galaxies and intracluster light (Contini, 2021), millimeter wavelengths from the distortions in the cosmic microwave background due to the Sunyaev-Zeldovich effect (Sunyaev & Zeldovich, 1972) and finally even radio wavelengths due to synchrotron emission from relativistic electrons (Allen et al., 2011). At their core, they have in no small part enabled the establishment of the ΛCDM reference cosmology (Voit, 2005). The discovery of dark matter by Zwicky (1933) represented just the first step to uncovering all the potential they contained in understanding the Universe.

To provide further an idea as to how such general properties can be derived through galaxies clusters, one can measure their masses and extent and therefore mass density. This density when averaged over many measurements can be concluded to provide an upper bound to the total mean matter density in the Universe. This follows from the assumption that the areas between galaxy clusters are less dense than the clusters themselves (Abell, 1965). Conversely, a lower bound can then be made by assuming *all* mass to be contained in galaxy

clusters. The upper bound can further be lowered by instead considering superclusters. This was for example the method employed by (Abell, 1965), arriving at $\rho_m \approx 1 \times 10^{-30}\,\mathrm{g\,cm^{-3}}$. Given Equation 2.18 for $H_0 = 70.4\,\mathrm{km\,s^{-1}\,Mpc^{-1}}$ this results in $\Omega_{0,m} \approx 0.11$, while for the common value of $H_0 = 50\,\mathrm{km\,s^{-1}\,Mpc^{-1}}$ at the time this gave instead $\Omega_{0,m} \approx 0.21$. This latter value was found also by Ostriker et al. (1974) and Einasto et al. (1974) during the transitionary period towards solving the missing mass problem.

Furthermore, structure formation can be constrained through comparison of the cluster mass distribution today versus at earlier times (Voit, 2005). Additionally, galaxy clusters posses the astounding property of containing a baryonic fraction nearly identical to the mean one in the Universe, indicating that unlike galaxies galaxy clusters are very efficient at keeping their baryons during infall (Cimatti et al., 2019). This results in a sort of "closed-box" nature, enabling the study of baryonic processes relevant for the formation of galaxies (Kravtsov & Borgani, 2012).

4.2   Structure Formation

For all these incredible properties and the usefulness of galaxy clusters to understanding the Universe itself, the question of how they actually formed was similarly a debate of many decades. Given that galaxies are somewhat unsurprisingly constituents of galaxy clusters this begs the question of the chicken and the egg: do galaxy clusters form from subsequent captures of galaxies, are field galaxies the result of the dissipation of galaxy clusters? Or, rather, a third option: neither. Captures were found to simply take too long to remove energy and were thus ruled out (Holmberg, 1941; Biviano, 2000), while galaxy clusters themselves were found to be stable (see Section 4.1.3). So how do they form?

4.2.1   Why Does Structure Exist At All?

To understand the formation of structure within the universe, it is necessary first to understand the cosmology. This is especially important as observation of the cosmic microwave background initially showed the Universe to be isotropic and homogeneous on large scales (Mather et al., 1990), which is also the starting point for the underlying Friedmann-Lemaître-Robertson-Walker metric – see Section 2.2. So where then do the departures from homogeneity, i.e., all structures, come from?

For the concordance cosmology of ΛCDM, the picture in brief is this: An initial phase of extremely rapid expansion freezes initial density perturbations as the Hubble length decreases, severing the regions' causal link (Liddle, 1999; Kinney, 2003). The concordance paradigm sees an inflaton scalar field responsible for this expansionary phase so rapid that the initial perturbations are originally the result of quantum fluctuations (for an excellent review see Kamionkowski & Kovetz 2016). These fluctuations produce approximately a Gaussian random field (Mukhanov, 2005). After this initial phase of extremely rapid expansion, the ensuing slower expansion and subsequent cooling allows the formation of atoms during a brief

phase termed primordial nucleosynthesis, where the plasma is dense enough to initiate nuclear fusion but not too dense to immediately destroy any formed atoms (Wagoner et al., 1967). It is further dense enough such that electromagnetism tightly binds photons to charged particles, which in turn are tightly bound to the atoms and dark matter through gravity thus resulting in a singular fluid. This persisted until the fluid had sufficiently cooled to where photons can begin streaming freely. This results in a surface of last scatter where-after it became possible for photons to travel long enough undisturbed to where they could be observed today as a homogeneous, isotropic blackbody radiation at $T = 2.725$ K, which has been redshifted to a lower temperature during time (Planck Collaboration, 2020). This is due to the curious property that a blackbody spectrum when redshifted reproduces a blackbody spectrum of lower temperature (see for example page 397 from Kutner 2003). The observation of this cosmic microwave background is one of the foundations of the concordance cosmology, and the rigidity with which is has been measured has come a long way from its historical initial observation by Penzias & Wilson (1965) where the "taping test" was still necessary. Though indeed largely homogeneous, the discovery of minuscule temperature anisotropies within the CMB subsequently allowed insight into the power of the density fluctuations seeded at all scales at the time of recombination (Smoot et al., 1992).

It is these density fluctuations which then with time collapse into the structures present within the Universe. The greatest amount of the mass which drives this collapse through gravity is contained in dissipationless dark matter and as such greatly reduces the complexity of the modeling. This allows a direct link between the observed initial conditions and resulting collapsed structures (Kravtsov & Borgani, 2012).

4.2.2   Collapse and Merging – Theory

It is the simultaneous fixation of both the cosmological background (the metric) as well as the initial conditions (which constituents are present in which amounts as well as in which distributions) that together result in the evolution of structure. Conversely through the observation and modeling of this evolution it is possible for statements to be made about the former. The mathematics as to how a spectrum of initial quantum fluctuations produces density perturbations and their evolution with time in a full general relativistic context of an expanding background Friedmann-Lemaître-Robertson-Walker metric is incredibly complex and far beyond this thesis. A good overview is given in chapters 7 and 8 from Mukhanov (2005). Instead, jumping ahead, recombination marks the transition when the photon-baryon fluid decouples and the governing equations for the evolution of over- and underdensities become dissipationless (Press & Schechter, 1974; Peebles, 1993). Note that before this the initial quantum fluctuations are also evolving, through the balance of gravity and pressure, but the end result can still largely be linearly linked to the intput spectrum (Press & Schechter, 1974). This spectrum at recombination is the farthest back where information can be directly observed, and forms the starting point of structure formation analyses. Note further that in the

Figure 4.2: Schematic of multiple over- and underdensities layed on top of each other, constructing the general density field. The dashed line indicates the characteristic overdensity δ_c beyond which at time t overdensities have collapsed to dark matter halos. Figure 1 from lecture 9 of van den Bosch (2022).

following primarily overdensities are mentioned as this is often easier to picture. However, for the linear regime both over- and underdensities grow in the same way (Mo et al., 2010).

The temperature anisotropies observed within the cosmic microwave background can be directly linked to density fluctuations because they probe the time directly after decoupling. To quantify the shape of this initial density field, one typically uses the power spectrum $P(k) \propto k^n$, corresponding to the Fourier transform of the mass density field. It describes the relative variance from the mean (and therefore presence of over- and underdensities) based on the inverse spatial scale $k = 2\pi/\lambda$. The exact formalism has k arise from a multipole expansion, such that k only implicitly represents a length and instead more correctly a surface on a sphere (Carroll, 2001). $k = 2$ corresponds to a dipole sampling of the spherical surface representing the CMB, with the variance determined by comparing the smoothed values over either pole. An initial density distribution produced by a pure Gaussian random field corresponds to an equal overlaying of powers of all scales (as a random field prefers no spatial scale over another), which then gives $P(k) \propto k^1$. This is the case of $n = 1$, which is a Harrison-Zel'Dovich spectrum (Harrison, 1970; Zeldovich, 1972; Peebles & Yu, 1970). Indeed, the most current measurements find $n = 0.9665$ (Planck Collaboration, 2020), a slight departure from the pure Gaussian random field. This departure is however consistent with current models for inflation (Mukhanov, 2005). Note that how these initial angular scales appear to observers today is dictated by the angular diameter distance, and is thus further convolved with the cosmology (Carroll, 2001).

The starting point is thus a spectrum of powers for deviations from the mean density on all spatial scales. However, unlike star formation which can be observed in various stages, it is quite difficult to view the early structure formation which results from the collapse of these overdensities. In the linear regime it is found that the density field evolves as

$\delta(x,t) = D(t)\delta_0(x)$, with $D(t)$ a growth function and $\delta_0(x)$ the extrapolated density field at a time $t = t_0$ (Mo et al., 2010). This means that for this regime all overdensities grow at the same rate independent of scale. If one pictures then the overlaying of all density perturbations into a lower-dimensional representation as in Figure 4.2, at a given time all overdensities above the critical value δ_c (dashed line) are expected to have collapsed. With time, this line moves downwards, thus finding overdensities (and underdensities) on larger scales at later times. This is the "bottom-up" hierarchical structure formation, as the overlaying leads to smaller overdensities collapsing first – see the left-most smaller scale halo which collapses, before the larger overdensity collapses at a later time when the dashed line moves down. A notable consequence is that galaxies form first, with galaxy clusters forming around them, and as such do not form within galaxy clusters themselves, answering the question posed at the beginning. The characteristic overdensity δ_c is typically derived via the spherical tophat, giving a value of around 168 when overdensity growth goes nonlinear (Mo et al., 2010).

This, however, is the linear picture. It does not describe *how long* it takes for those overdensities which break the threshold to collapse. A leap forward in the understanding of the *nonlinear* evolution came with the mechanisms described by Press & Schechter (1974), whereby the nonlinear interactions of smaller masses produce larger-mass objects – bottom-up, as described above. Though crude in its assumptions, it has proven itself with time to fit generally the results from CDM simulations (Jenkins et al., 2001), with an alternative mass functions given for example by Sheth & Tormen (1999). The core result found by Press & Schechter (1974) is, when assuming an initial gas at $t = t_0$ made of points with some characteristic seeding masses, that in a Newtonian limit the condensations of these points to larger mass structures will subsequently result in a new time t_1, where on sampling on larger scales has the gas appear again as a distribution of point particles of some characteristic mass. That is to say, structures collapse self-similarly, and bottom up, even within the non-linear regime. Note that the initial assumptions deviate from the picture in Figure 4.2, as there exists just one initial characteristic seeding mass as opposed to an overlaying of overdensities on all scales. The original derivation also requires a "fudge-factor" of 2 in addition to the deviating initial assumptions. A more correct and exhaustive approach is provided by the excursion set theory as presented by Bond et al. (1991), also known under the name "Extended Press-Schechter", which finds the same functional form from Press & Schechter (1974) for a specific choice of filtering function (a sharp k-space filter, corresponding to a spherical tophat in Fourier space van den Bosch 2022) though now with the factor 2 arising naturally.

Note that the resulting structure formation is strongly dependent not only on the choice cosmology, but also on the initial power spectrum. For example, when assuming a flat cold dark matter cosmology (which thus fixes many properties of the Universe), the change of the initial conditions of the power spectrum can still result in either smaller galaxy-scale or larger galaxy cluster-scale overdensities collapsing first as well as at the same time, with the former for a power spectrum slope (see Section 4.2.1) of $n = 1$, the second for $n = -1$ and the third for $n = 0$ (Bond et al., 1982).
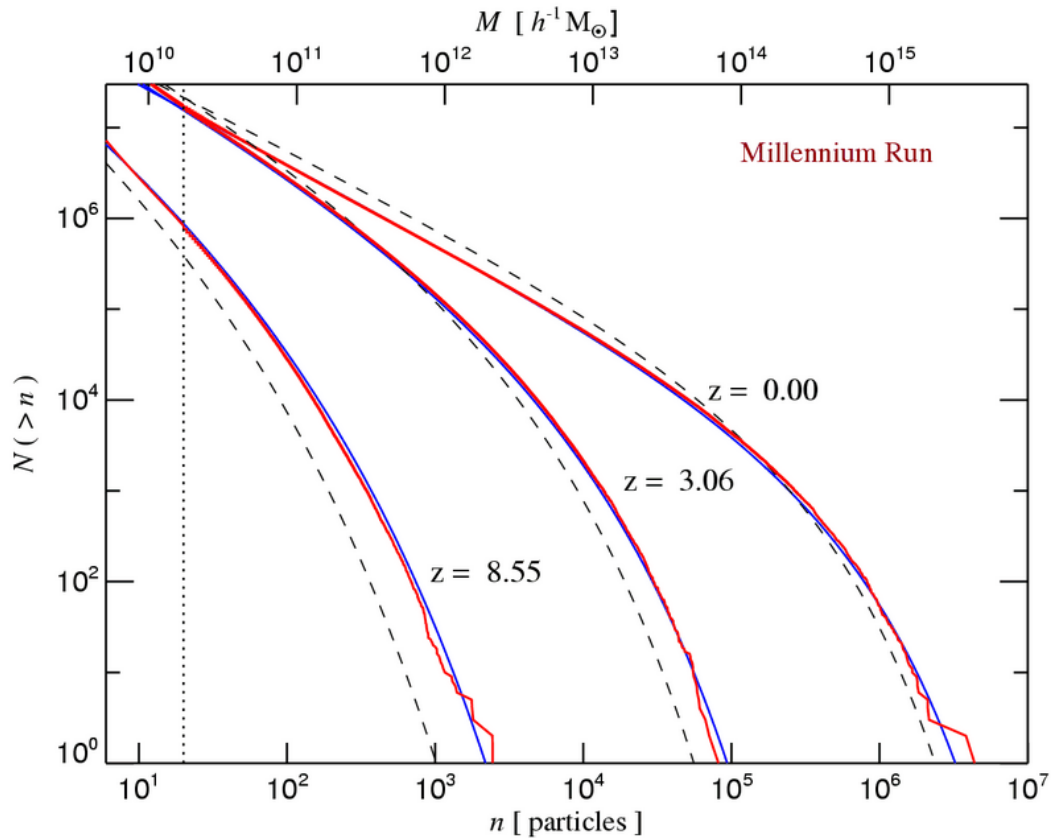
Figure 4.3: Comparison of the simulated halo mass function in red, versus in dashed gray the spherical (Press & Schechter, 1974) and in solid blue the ellipsoidal (Sheth et al., 2001) collapse Extended Press-Schechter formalisms. Figure 2 from the Max-Planck-Institute for Astrophysics research highlight of year 2004 by Springel (2004) for halos from the `Millenium Simulation` (Springel et al., 2005).

4.2.3   Collapse and Merging – The Numerical Findings

The number of crude assumptions made in the derivation of the Press-Schechter formalism result in a necessary caution towards the results. Indeed, as described by Sheth & Tormen (1999) the basic form for spherical collapse of the Press-Schechter formalism (over-) under-predicted the number of collapsed halos with masses (smaller) larger than the characteristic scale M_*, defined through the condition $\sigma(M_*) = \delta_c(t)$, see Jenkins et al. (2001) or van den Bosch (2022). Much better matching to halos from dark matter-only simulations was found for the mass function resulting from the ellipsoidal collapse model by Sheth et al. (2001), because the non-zero tidal field deviates collapse away from a spherical form (van den Bosch, 2022). This can be seen clearly in the halo mass function from the `Millenium Simulation` (Springel et al., 2005) as depicted as red lines in Figure 4.3, with the above noted behavior for the spherical collapse Press-Schechter formalism (dashed gray) while the variant with ellipsoidal collapse depicted in blue matches significantly better.

The great potential for cosmological simulations to assist in the understanding of structure formation can be found in the work by Bond et al. (1996), where filaments are shown to potentially result from the bridging of large-scale overdensities when they constructively interfere – something which is difficult to quantify analytically due to the strongly elongated

nature of the filaments (see Figures 1 and 2 therein). Another example is the direct analysis of merger events via merger trees in the `Millenium Simulation` (Springel et al., 2005) conducted by Fakhouri & Ma (2008). They find that the number of progenitors increases with the mass of the final halo, with much fewer single-progenitor galaxy clusters than galaxies (Figure 4 therein). Furthermore, Fakhouri & Ma (2008) determine that minor mergers (with large differences in mass between the merging objects, $M_2/M_1 < 0.03$) are significantly more likely than major mergers ($M_2/M_1 \geq 0.1$) for all mass ranges as can be seen in Figure 6, something which Fakhouri et al. (2010) found to hold again for the larger `Millennium-II Simulation` (Boylan-Kolchin et al., 2009). The resulting merger rates depend only weakly on the halo mass and more strongly on the mass ratios (Fakhouri & Ma, 2008) and environment (Fakhouri & Ma, 2009), with denser environments leading to a general enhancement of merger rates by factor 2 to 2.5 for all mass ratios relative to voids.

These enhanced merger rates would conversely imply halos of like total masses to have formed more recently in dense environments were their mass mostly dictated by mergers (Fakhouri & Ma, 2009). This is exactly converse to other findings (for example Wang et al. 2007), which demonstrates that it is not mergers which dictate the main source of mass for halos but rather smooth accretion from the field (Fakhouri & Ma, 2010). This smooth accretion is then decreased in denser environments relative to voids, as the deep potential wells lead to much higher relative velocities and thus suppress smooth accretion (Fakhouri & Ma, 2010), even far outside of the virial radii of the centers of the wells (Hahn et al., 2009; Behroozi et al., 2014). To give a comparison to alternative cosmologies, this behavior is further enhanced for warm dark matter models due to the lack of small scale halos, where mass growth is then dominated by diffuse accretion at all redshifts (Dhoke & Paranjape, 2021).

The overall effects of the denser environments are summarized under the term "assembly bias" (Gao & White, 2007). It is found that halos with earlier formation times z_{form} lie in denser environments (Wang et al., 2007; Hahn et al., 2007; Wetzel et al., 2007; Maulbetsch et al., 2007; Li et al., 2008; Hahn et al., 2009), with the formation redshift of a halo typically defined as the moment when it reaches half of its mass at $z = 0$. This stands against the typical Extended Press-Schechter formalism and its presumption of environmental independence, which has been attempted to be remedied by using the ellipsoidal collapse (Sheth et al., 2001) and amending the collapse condition from being purely overdensity dependent to including the shape of the initial density field (Sandvik et al., 2007). Nonetheless, this is found to be insufficient to cover the discrepancy to simulations (Hahn et al., 2009). Recent findings indicate that the assembly bias may originate overall from multiple physical processes (Han et al., 2019) and be primarily dictated by the environmental tidal field anisotropy (Ramakrishnan et al., 2019).

It can then be seen how cosmological simulations allow a more precise treatment of the non-linear regimes, accounting for more varied effects than possible analytically. The merger rate enhancement in denser environments Fakhouri & Ma (2009) as well as the major and minor merger rates generally (Fakhouri & Ma, 2008) provide a challenge to the
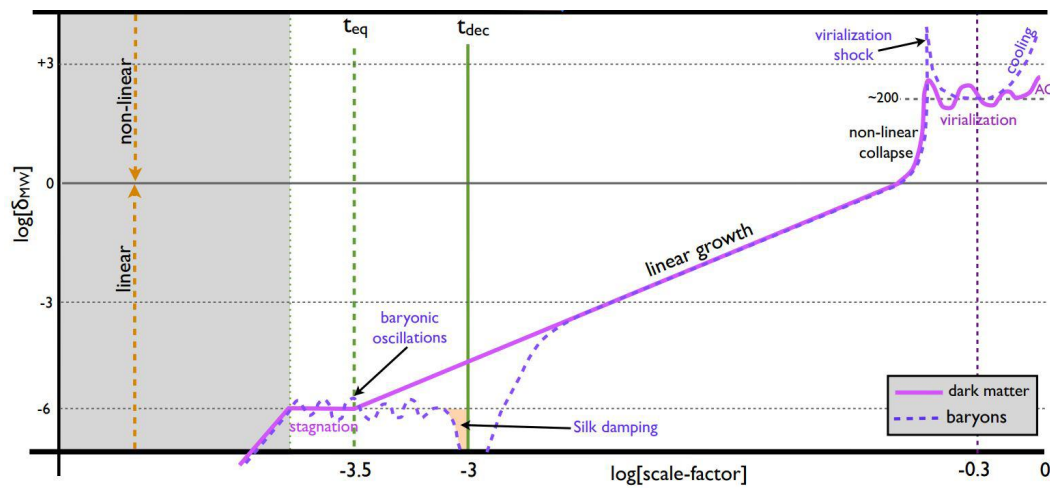
Figure 4.4: The evolution of a choice baryonic (dashed purple) and dark matter (solid pink) overdensity as a function of $\log(a)$ in a ΛCDM Universe. Overview-figure from van den Bosch (2022).

Extended Press-Schechter formalism and its statistical nature (no differentiation between spatial regions). This discrepancy to simulations exists also for higher redshifts for the halo mass function itself (Gao et al., 2004), with much subsequent work done to improve analytical modeling (Bond et al., 1991; Lacey & Cole, 1993, 1994; Giocoli et al., 2008) and calibrating it with numerical simulations (Jenkins et al., 2001; Reed et al., 2003; Yahagi et al., 2004; Gao et al., 2004). However, there exists on the side of the simulations the difficulty of how to identify halos and subhalos – see Section 5.3. As such, it is through combined analysis of a theoretical framework and then the actual simulations that this insight into hierarchical structure formation has been gained. Nonetheless, the crude assumptions must always be kept in mind, and predictions of the ellipsoidal collapse extended Press-Schechter formalism taken only in a statistical sense and always with a grain of salt.

4.2.4   Collapse and Merging – What About Baryons?

The derivations of the analytical formalisms from Section 4.2.2 and Section 4.2.3 are done for the dissipationless portion of the mass (dark matter) only, as no hydrodynamical processes were considered (Press & Schechter, 1974; Bond et al., 1991; Sheth & Tormen, 1999). Considering that most of the mass in the Universe is dark matter (Planck Collaboration, 2020) this should not deviate too strongly from the real final resulting structure. However, that is not to say that baryonic processes are of no impact. During infall, the gas is heated up and reaches extreme temperatures in the range of 1×10^7 K to 1×10^8 K (Cimatti et al., 2019), resulting in shocks before settling into a hydrostatic equilibrium (Kravtsov & Borgani, 2012). Because the baryons can more efficiently remove angular momentum through pressure, they can "cool" into more dense cores than the dissipationless dark matter can. This inclusion of baryonic physics can perhaps even alter the slope of the dark matter profile of a galaxy cluster towards the denser central regions (Rosati et al., 2014).

A summary of the overall evolution of an overdensity is given in Figure 4.4. Taking a dark matter and baryonic overdensity in the same region and considering first the former, its growth stagnates during radiation domination (known as the Meszaros 1974 effect) before beginning after t_{eq} to grow linearly during matter domination (van den Bosch, 2022; Mo et al., 2010). In contrast, the baryonic matter is tightly coupled to the photons as a plasma before recombination and thus instead begins oscillating. This persists also during the transition to matter domination, with fluctuations on small scales damped out as the radiation begins to decouple at t_{dec} via Silk (1968) dampening. The baryonic matter, now freed from the plasma, then rapidly grows in overdensity as it falls into the already-existant dark matter overdensity. Both grow linearly until they reach the critical overdensity, after which they collapse non-linearly. Here the virialization shock in the baryons is visible, leading to a much larger spike in density than present for the dissipationless dark matter which then drops before cooling again into a high density central region. Note that the presence of baryons has also been argued by Brooks et al. (2013) to lead to a flattened central dark matter density slope due to supernova feedback.

Understanding the changes to the structure formation paradigm when introducing baryonic physics is one of the core questions currently being researched today, with exciting results expected for the differences in protoclusters for dark matter only simulations (Chiang et al., 2013) to fully hydrodynamical ones (Remus et al. 2022, to be submitted) as well as for the accretion behavior through cosmic filaments onto structures from galaxies to galaxy clusters (Seidel et al. 2022, in preparation). Much is still to be learned about the interplay of the complex physics, with the closed-box nature of galaxy clusters providing a great potential for these future studies.

4.3   Substructures And Galaxy Cluster Composition

Through the combined work described in the previous section, and the concordance cosmological model of ΛCDM, an incredibly deep understanding of galaxy clusters has been achieved. They are now known to be comprised only to the *smallest* part of the matter upon which initial observations were founded, namely the stars. These make up only 1% to 5% of the total mass, while the total baryonic mass fraction is 10% to 16%, increasing with total galaxy cluster mass (Cimatti et al., 2019). Most of these baryons are then instead contained within the hot intracluster medium, while most of the total mass, around 84% to 90%, is contained in dark matter (Cimatti et al., 2019).

Given the paradigm of hierarchical structure formation as described in Section 4.2, the question of the chicken and egg is also clear. Galaxies form first, with galaxy clusters representing the latest structures to collapse. Note that the presence of such a large overdensity necessarily enhances any smaller, galaxy-scale overdensities, thus allowing many galaxies to preferentially cluster in the region. There result three main modes of mass accretion for galaxy clusters. The steady mass infall along the surrounding filaments, accretion of discrete groups or the significantly more rare event of a cluster-cluster merger (Owers et al., 2011).

It should be noted at this point that the delineation between a galaxy cluster and what is referred to as a group of galaxies is by no means rigid. Chosen borders between the two are often either a mass or number of members cutoff, typically $1 \times 10^{14} \, \mathrm{M_\odot}$ or at least 50 members (Cimatti et al., 2019). These classifications are made primarily to quantify differences between lower and higher mass environments, where for example there is an observed deviation between scaling laws for X-ray luminsities of groups and clusters (Vajgel et al., 2014; Lovisari et al., 2015; Schmidt et al., 2021). Another consequence is that the lower velocity dispersions in groups of galaxies allow for a high frequency of galaxy-galaxy interactions, enabling the formation of so-called "evolved" groups (Cimatti et al., 2019). Conversely, the rapid velocities due to the deep potential wells of galaxy clusters largely prevent such interactions, although note again that there exists no clear border but rather increasing relevance of different physical processes with central potential mass. Generally substructure within galaxy clusters undergoes a different type of evolution compared to those in the field, caused primarily by the interactions with the deep potential well itself. In which ways is it affected, and what sort of properties with time can one expect from a substructure within a galaxy cluster?

4.3.1 What Is Substructure and How Does It Evolve?

Substructure is a collapsed local overdensity within a large scale collapsed overdensity. For galaxy clusters, it can take the form of infalling galaxies or groups of galaxies. Based on hierarchical structure formation it must then either have been present during formation or have fallen in afterwards – it does not form within the galaxy cluster after formation. However, by no means does this mean that the substructures within galaxy clusters do not evolve with time – quite the opposite. After infall, they experience a variety of processes that are unique to (or enhanced within) the deep potential wells, and that thus are not (rarely) experienced by comparable objects in the field.

Even well before the substructure has fallen within the virial radius of the larger object it begins feeling the effects of the larger potential. Both mergers and smooth accretion are ceased as local dynamics become dominated by the galaxy cluster (Behroozi et al., 2014). This could potentially be explained by the increase in environmental velocities which then exceed the smaller halo's virial velocity (Wang et al., 2007; Dalal et al., 2008). Sandvik et al. (2007) however find the environmental mass insufficient for this picture, prompting alternatives such as the influence of the tidal field. There instead importance is placed on the angular momentum which arises in the hierarchical structure formation, known under the moniker of "tidal-torque theory" (Hoyle, 1949; Doroshkevich, 1970; White, 1984). The smaller halos streaming within filaments would then experience an ordered shear flow which suppresses the accretion and merger rates (Hahn et al., 2009). The impact is felt particularly early for the rate of major mergers $M_2/M_1 > 0.3$ which typically cease at more than four virial radii away from the galaxy cluster due to the tidal forces, where smooth accretion ceases comparatively closer to the galaxy cluster (Behroozi et al., 2014).

Once the substructure falls in far enough, the tidal effects become strong enough to not just prohibit further accretion but instead begin stripping material, in particular from the more diffuse dark matter halo. The extended halo feels strongly differing forces between its points most far in and out and thus has matter stripped away (Richstone, 1976; Wetzel & White, 2010). Furthermore, as the galaxies sink towards the center due to dynamical friction (Chandrasekhar, 1943) they can eventually merge with the brightest cluster galaxy (see Section 4.3.2) sitting at the center – then termed "galactic cannibalism" (Mo et al., 2010; Cimatti et al., 2019).

Another typical feature observed for galaxies within galaxy clusters is their increasing fraction of spheroidals (S0 and ellipticals) relative to spiral galaxies compared to the field (Dressler, 1980), known also as the morphology-density relation (Cimatti et al., 2019). This means that passive galaxies cluster more strongly than those which are star-forming (Wilkinson et al., 2017; Cowley et al., 2019). This is due to the additional quenching mechanisms present in the high density environments. These include starvation (Larson et al., 1980), where the lack of additional gas accretion mentioned above leads to star formation using up all the cold gas present, strangulation (Larson et al., 1980), where left-over gas from star formation would normally settle back down onto the galaxy but is instead stripped away in the dense environment, thermal evaporation (Cowie & Songaila, 1977), whereby the hot ambient gas in the ICM interacts with the colder, star-forming gas from the galaxy primarily by evaporation, galaxy harassment (Moore et al., 1996), where close galaxy-galaxy encounters (not mergers) lead to a loss of angular momentum and heating of the stellar distribution, and ram-pressure stripping (Gunn & Gott, 1972), where the galaxy feels a pressure $\propto \rho_{\text{cluster}} v^2$ against it during infall that strips less strongly bound portions of its gas. Ram-pressure stripping in particular quenches both by stripping directly the cold, star-forming gas as well as by stripping the more diffuse atomic gas, resulting in starvation occurring earlier, and is also found to be present within groups of galaxies, though with comparatively lesser strength (Roberts et al., 2021).

This can be seen also from post-starburst galaxies (PSB), which represent a transitional phase between star-formation and quiescence, one finds them to be more clustered at lower redshifts, with low-mass PSBs predominantly found in high density environments (Wilkinson et al., 2021). Thus, while for higher redshifts it tends to be feedback processes which quench star-formation in galaxies (for example via stellar feedback after major mergers – see Trayford et al. 2016), for lower redshifts ($z < 1$) it is the above quenching mechanisms which are responsible for the rapid quenching (Wilkinson et al., 2021). In particular, this has been suggested as due to ram-pressure stripping by various authors including Owers et al. (2019) and Vulcani et al. (2020), which would correlate to the findings by Lotz et al. (2021) where in the `Magneticum Pathfinder` simulation (Dolag, 2022) the fraction of PSBs peaks jumps towards the center. Furthermore, Lotz et al. (2019) argue that already single passage through the galaxy cluster is sufficient to quench star formation.

Some additional nuance arises when considering infalling groups of galaxies. The group environment is already enhanced in density relative to the field, and as such the galaxies

already begin experiencing the higher-density quenching processes. This has been seen both in simulations (Vijayaraghavan & Ricker, 2013; Han et al., 2018b) as well as observations (Bianconi et al., 2018) and thus adds another layer of complexity when considering galaxy evolution within galaxy clusters. This "preprocessing" has also been linked to cluster members which appear particularly visually disturbed, and allows the high fraction of red galaxies to be present far outside of a galaxy clusters center (Han et al., 2018b). There are many additional properties that can be considered, some which can be linked to a decreasing distance of substructures to the center such as the Butcher & Oemler (1978) effect (increasingly bluer galaxies) or the increasing stellar ages seen in Figure 10 by Saro et al. 2006, which are however to numerous to cover here. For general introductions to galaxy clusters, see the reviews by Sarazin (1988), Biviano (2000), Kravtsov & Borgani (2012) and Contini (2021) mentioned above.

One final characteristic which is of great importance is the total mass contained in substructures as a fraction of the total galaxy cluster mass f_{sub}. The quenching and stripping processes described above serve to continually remove mass from substructures which have fallen into the galaxy cluster, lowering f_{sub} with time. On the other hand, the infall of new material serves to counter the downwards trend (McBride et al., 2009). At z 0, however, the mass-loss outpaces the mass accretion rates and so f_{sub} generally decreases with time. Conversely, higher f_{sub} are indicative of either an earlier formation time or recent merger events (Jiang & van den Bosch, 2016), and has thus can be used as a tracer for relaxedness (Shaw et al., 2006; Ludlow et al., 2013; Biffi et al., 2016; Jiang & van den Bosch, 2017). Studying substructure thus can provide insight into the dynamical state of a galaxy cluster, into structure formation generally and thus also in tests between different potential dark matter variants (Bhattacharyya et al., 2021).

4.3.2 The Brightest Cluster Galaxy and Intracluster Light

Aside from the member galaxies, the over optically visible portions consist of the intracluster light (ICL) and the brightest cluster galaxy (BCG). The latter typically sit at the center of the galaxy cluster and are, as their name implies, the most luminous galaxies. They can reach luminosities up to $1 \times 10^{12}\,L_\odot$ and masses up to $1 \times 10^{13}\,M_\odot$, though distinguishing to the galaxy cluster mass is not easily accomplished due to their location (Cimatti et al., 2019). Unlike normal growth modes, BCGs grow primarily through mergers (Mo et al., 2010; Remus et al., 2017a) with their stellar masses typically growing by a factor 2 after $z = 2$ (Laporte et al., 2013). Consequently, BCGs are invariably giant ellipticals and often exhibit multiple nuclei (Cimatti et al., 2019), and are furthermore found to be inconsistent with the global luminosity function of galaxies (Tremaine & Richstone, 1977; Ragone-Figueroa et al., 2018). These mergers typically imply that the stellar mass is formed early in other galaxies and then merged into the BCG at later times, though there exists a subset of particularly overdense protoclusters which assemble the stellar mass onto the BCG much earlier (Rennehan et al., 2020).

The ICL, meanwhile, is primarily comprised of the stars which are stripped out from member galaxies as well as released during mergers with the BCG, and it contains a significant fraction of the total stellar mass within the cluster (Remus et al., 2017a). It can be difficult to spatially distinguish the delineation between BCG and ICL (as well as the extended halos of other bright ellipticals), yet in terms of kinematics Dolag et al. (2010) show through use of a hydrodynamical simulation that they can be fit by two superimposed Maxwellian distributions. Furthermore, Marini et al. (2021) find an offset in the velocity dispersions of stellar particles associated with the ICL versus BCG via the Maxwellian split from Dolag et al. (2010).

4.4 Summary

Section 4.1 has provided an overview of the history of galaxy cluster study, showing how the field blossomed into an extensive marvelous consortium involving such plentiful physical processes rarely matched in their diversity. Galaxy clusters are found to provide unique laboratories, both for cosmological models due to their status as the largest collapsed structures and baryonic physics due to their much higher retention of baryons during formation compared to galaxies. The current hierarchical structure formation paradigm resulting from the concordance cosmology of ΛCDM was discussed in Section 4.2, illuminating how analytical models such as the Extended Press-Schechter formalism must make strongly simplifying assumptions. This necessitates the need for comparisons to cosmological simulations, with many features found from these simulations, such as the environmental assembly bias, being difficult to reconcile with the theories. Section 4.3 has discussed the composition of galaxy clusters, with a particular focus on substructures within and the impact of processes such as tidal stripping and quenching. From Section 4.3.1 in particular follows that the mass contained in substructures within galaxy clusters is tightly linked to structure formation as a whole. Larger masses could imply weaker tidal fields and less stripping, or earlier formation times which allow for more accretion by the substructures before infall. Understanding substructure masses thus enables a more nuanced analysis of structure formation.

Chapter 5

Measuring with Two Measures

Before seeking new theories to replace ΛCDM, it is necessary to ensure the comparability between the methods employed.

In the following, an overview of the general methods employed for observations are described in Section 5.1. A particular focus is placed on gravitational lensing in Section 5.2, describing the typical lensing approaches and the observation of Abell 2744 which finds the mass discrepancy. Section 5.3 provides an overview of some of the current state-of-the-art simulations with emphasis placed on their method of determining substructures. The findings are summarized in Section 5.4.

5.1 Measuring Galaxy Clusters, Ground- and Space-based Observations

This section will provide a brief overview of typical observational methods employed to study galaxy clusters and how they have been used to determine their masses. In particular, Section 5.1.1 focuses on the signals from the hot intracluster medium, typically observed in X-ray or via the Sunyaev-Zeldovich (Sunyaev & Zeldovich, 1972) effect's distortions in the CMB. Section 5.1.2 then looks at the method originally used by Zwicky (1933) to first determine the "missing mass" problem as in Section 4.1.1, namely by use of dynamical modeling.

5.1.1 X-Ray and the SZ-Effect

Since its first observations in the late 1970's described in Section 4.1.2, the hot diffuse intracluster medium has provided invaluable insights into many facets of galaxy clusters, such as their dynamical state and mass. The X-ray emission resulting from the ICM is incredibly high, reaching luminosities of $1 \times 10^{43} \, \text{erg s}^{-1}$ to $1 \times 10^{45} \, \text{erg s}^{-1}$ (Cimatti et al., 2019). The following provides a brief overview of the theoretical foundations upon which observational methods are built.

Initially, the source of this X-ray emission was not clear. It could for example be the result of compact sources, or of a diffuse hot intracluster gas (Sarazin, 1988). In the latter case it would follow that the resulting thermal velocities of the protons are then comparable to the velocities of the galaxies within the cluster due to sharing the same gravitational potential, and further that the gas would be heated sufficiently to become a plasma. The charged particles within the plasma would then emit in X-ray as thermal bremsstrahlung, where passing by an ion the electron emits radiation because its velocity changes due to the deflection (Cimatti et al., 2019), and one should thus observe a continuum, in addition to any emission lines of heavier elements should these be contaminating the gas (Sarazin, 1988). It is this case of thermal bremsstrahlung emitted from a hot intracluster plasma which would be found consistent with observations (Davidsen et al., 1975). In the framework of hierarchical structure formation it is then the baryonic mass which collapsed together with the cluster's dark matter halo, being shock-heated in the process before settling into equilibrium (Biffi et al., 2016).

It is through the assumption of hydrostatic equilibrium from which then galaxy cluster masses can be measured by modeling the gas with a spherically symmetric mass distribution, resulting in:

$$M(r) = \frac{k_b \cdot T}{G \mu m_p} \left(\frac{d \log \rho}{d \log r} + \frac{d \log T}{d \log r} \right), \tag{5.1}$$

with m_p the proton mass, k_b the Boltzmann constant and G Newton's gravitational constant (Pellegrini & Ciotti, 2006; Biffi et al., 2016). Knowledge of the radial temperature T and density ρ profiles as well as the mean molecular weight μ thus allow direct inference into the total mass.

One can also derive the form for the electron temperature T_e as:

$$k_b \cdot T_e \approx \frac{GMm_p}{2R_{eff}} \approx 7 \, \text{keV} \cdot \frac{M}{3 \times 10^{14} \, M_\odot} \left(\frac{r_{eff}}{\text{Mpc}} \right)^{-1} \tag{5.2}$$

with R_{eff} as the effective gravitational radius (Birkinshaw, 1999). As can be seen from Equation 5.2, a particularly important feature within the X-ray spectrum is then the 7 keV iron line complex, though it also includes many lower-energy lines from lighter highly-ionized elements (Cimatti et al., 2019).

One of the great advantages of X-ray observations is that they reduce the chance of projection effects. A high X-ray signal indicates a potential well with a depth found only in galaxy clusters, such that for example projected galaxies add nothing to the signal. However, in rare cases it is possible to enhance the signal when instead two *galaxy clusters* are found in projection, as seen for example by Böhringer et al. (2010). Note that there exists a further differentiation between galaxy clusters depending on their central temperature profile. If the temperature decreases towards the center, this indicates that the cooling time is shorter there than the cluster age and they are thus called "cool-core" clusters, with those not exhibiting this feature correspondingly as "non-cool-core clusters" (Cimatti et al., 2019). This can have an

impact on a number of properties, such as for example the relation between the concentration (see Chapter 3) and mass of the galaxy cluster (Ragagnin et al., 2019).

Furthermore, as suggested first by Sunyaev & Zeldovich (1972), the free electrons within the plasma are able to scatter radio emission passing through it via Thomson scattering, which occurs as the low-energy limit of Compton scattering when the wavelength of the photons is much larger than the Compton wavelength of the scattering electrons (Thomson, 1906). The cross section is

$$\sigma_T = \frac{8\pi}{3} \cdot \left(\frac{e^2}{m_e c^2} \right)^2 \tag{5.3}$$

with e and m_e the electron charge and mass, respectively, such that for an electron number density of $n_e \approx 1 \times 10^{-2}\,\mathrm{cm}^{-3}$ persisting through a galaxy cluster of size $R_{\mathrm{eff}} \approx 1\,\mathrm{Mpc}$ the chance of scattering is $\tau_e \approx n_e \sigma_T R_{\mathrm{eff}} \approx 1\%$ (Cimatti et al., 2019). This is particularly interesting as there is a general radio background, namely the CMB. Because the electrons are at significantly higher energies than the CMB photons the scattering shifts the CMB spectrum to higher energies. The net result is a reduction in the CMB intensity at typically measured wavelengths ($\nu < 218\,\mathrm{GHz}$) referred to as "microwave diminution" (Sarazin, 1988; Birkinshaw, 1999; Cimatti et al., 2019). This SZ-effect on the CMB is significantly more intense than other local perturbations, for example of galaxy clusters acting as gravitational lenses, and furthermore has the advantage of being independent of the redshift thus allowing the detection of galaxy clusters at very high redshifts (Birkinshaw, 1999). Note that in addition to the SZ-effect described here resulting from the thermal motions of the electrons (thermal SZ), there arises also a signal from the bulk peculiar motions of the electrons (i.e., of the galaxy cluster itself) called the "kinetic SZ", which is typically around an order of magnitude weaker (Cimatti et al., 2019).

It is through the combined use of X-ray and SZ images that statements about the thermal and density structure can be derived, as they depend on (n_e, T_e) in different ways (Birkinshaw, 1999). To this end, a model for the gas distribution n_e is integrated across the depth of the cluster with the requirement of reproducing both the X-ray $\left(\propto n_e^2 \cdot T_e^{1/2} \right)$ and SZ ($\propto n_e \cdot T_e$) signatures (Myers et al., 1997). Additionally, knowledge of the thermal profile allows the SZE to provide information on the surface baryonic mass density (Myers et al., 1997), which allows direct comparison to other projected mass density measurements such as gravitational lensing (Birkinshaw, 1999) – see Section 5.2. One of the most interesting uses is achieved by comparing the expected SZ effect from X-ray measurements providing the thermal structure (n_e, T_e), where the measurements are dependent on the angular diameter distance, to those of the actual measured SZ which are redshift independent. This allows a measure of the Hubble constant H_0 as described in Section 4.1 of Birkinshaw (1999).

However, important corrections are necessary for the amount of non-thermal pressure present in the galaxy cluster (Biffi et al., 2016). This can originate from merging and accretion events, resulting also in a scatter of galaxy cluster sizes for equal masses depending on the accretion history. As the observations of X-ray and the SZ-effect commonly rely on the thermal portion of the pressure, this can lead to biases resulting from the dynamical state

(Rosati et al., 2014; Walker et al., 2019). One example would be attributing all pressure support to the thermal portion measured by an X-ray observation and then assuming the ICM to be in hydrostatic equilibrium, resulting in a higher mass estimate due to the neglect of pressure support from bulk and turbulent motions of the gas (Shi et al., 2016). Furthermore, a disturbed galaxy cluster's gas profile, or even just a departure from spherical symmetry, is likely not reproduced well by typical models such as the isothermal sphere and can induce uncertainty up to a factor of 2 (Myers et al., 1997). Nonetheless, many properties of the ICM are found to be quite resilient against disruptive processes including accretion, such as the entropy slope ζ (from $K \equiv P/\rho^\gamma \propto M_{gas}^{-\zeta}$), and thus provide an overall excellent tool (Voit et al., 2005; Shi, 2016).

5.1.2 Dynamics

Dynamical modeling can also be used to determine the masses of galaxy clusters, so long as they are assumed to be bound, self-gravitating structures. It is with this assumption and the virial theorem that Zwicky (1933) first demonstrated most of their mass to be present in dark matter, and the assumption of their bound nature has since held firm – see also Section 4.1.3. The derivation of masses via observed dynamics is relatively straightforward. With T and W the total kinetic and potential energies, the condition to be bound is $T + W < 0$. When additionally they are assumed to have reached some degree of equilibrium, their distribution fulfills then the virial theorem as $2 \cdot T + W = 0$, which following Sarazin (1988) gives:

$$0 = 2 \cdot T + W = \sum_i \left(m_i v_i^2 \right) - \frac{1}{2} \sum_{i \neq j} \frac{G m_i m_j}{r_{ij}}$$

$$1 = \frac{1}{G} \left[\sum_i \left(m_i v_i^2 \right) \right] / \left[\frac{1}{2} \sum_{i \neq j} \frac{m_i m_j}{r_{ij}} \right]$$

$$M_{tot} \equiv \frac{R_G \langle v^2 \rangle}{G} \tag{5.4}$$

where the last step defines the mass-weighted velocity dispersion as

$$\langle v^2 \rangle \equiv \frac{\sum_i m_i v_i^2}{M_{tot}} \tag{5.5}$$

and the gravitational radius as

$$R_G \equiv 2 M_{tot}^2 \cdot \left(\frac{m_i m_j}{r_{ij}} \right)^{-1}. \tag{5.6}$$

This may at first seem an odd transformation, yet the new values are easier to deal with. When assuming spherical symmetry, $\langle v^2 \rangle$ has the advantage of being able to be related to projected line-of-sight velocities instead of the full three-dimensional ones, and further then instead simply to the radial velocity dispersion $\langle v^2 \rangle = 3\sigma_r^2$ as described by Limber

& Mathews (1960). Similarly, R_G can be related to a similar variable b_G which however takes the projected distances as well, giving $R_G = (2/\pi)b_G$. When observing a statistically representative sample of the galaxies within the galaxy cluster, then measurements of these values gives an estimate of the total mass present (Sarazin, 1988).

Difficulties can arise for dynamical masses due to substructure and velocity anisotropy (Rosati et al., 2014). These can locally alter the dynamical properties, such as the velocity dispersion, and thus lead to biases in the determined masses (Sarazin, 1988).

5.2 Gravitational Lensing

Foreseen already in the year 1937 as crucially viable for the case of galaxies (and by extension galaxy clusters), due to their larger distortion and greater apparent size, Zwicky 1937 had already realized the potential power of a tool such as gravitational lensing. Not only could its observation serve as another test on the calculations from general relativity, but it would provide the final definitive proof to the "missing mass" problem discussed in Section 4.1 (Zwicky, 1937). Though gravitational arcs could already have been seen in many astronomical images before then (Fort & Mellier, 1994), it would be the advent of more sensitive CCDs that allowed in the later years of the 90's a row of observations of these arcs (Lynds & Petrosian, 1986; Soucail et al., 1987). Initially associated to the galaxy clusters themselves, for example as the result of powerful explosions or galactic cannibalism resulting in a tidally stripped galaxy, it would be Paczynski (1987) who proposed the arcs to be the result of gravitational lensing. He further provided a simple test of the hypothesis, in that if they resulted from the cluster, they should have approximately the same redshift, while if the result of gravitational lensing their redshift should be higher. And indeed, spectroscopic measurements by Soucail et al. (1988) found the arc at $z = 0.724$ and therefore behind the galaxy cluster Abell 370 at $z = 0.374$. This would enable, for the first time, direct probing of the dark matter distribution in galaxy clusters through their distortions on background galaxies (Fort & Mellier, 1994). Furthermore, given sufficient knowledge of the mass distribution of a gravitational lens would allow statements about the redshift of a background source based on the distortion, without the need for spectroscopic measurements (Fort & Mellier, 1994). Indeed, gravitational lensing would prove to be such a powerful tool that within the decade after these first confirmations it would enable the measurement of the Hubble constant H_0, constrain the cosmological constant Ω and, as mentioned, the mass distribution in the centers of galaxy clusters (Seitz et al., 2022).

Recent observations from gravitational lensing have, however, found discrepancies in the mass distributions relative to those from simulations. To understand what these imply, Section 5.2.1 first provides an overview of the basic principles of gravitational lensing. Armed with these basics, the specific procedures and models commonly employed for current lensing observations are described in Section 5.2.2, before describing two current observations finding more mass (Section 5.2.3) and more compact (Section 5.2.4) substructures compared to those from simulations.

5.2.1 Caustics and Critical Lines

The following brief overview of the principle of gravitational lensing is done on the basis of Fort & Mellier (1994), Narayan & Bartelmann (1996) and Seitz et al. (2022). Of central importance is the angular diameter distance typically assigned the letter D when used in gravitational lensing (where more general books on cosmology may define it instead as d_A). D describes the relation between the angular extent $d\theta$ as observed to the proper extent $d\xi$ of the object itself as $D = d\xi/d\theta$ and is defined for example in Equation 2.8a of Seitz et al. (2022). Assuming the size of the lensing mass to be small relative to the total distance between observer and source, it can be approximated as a thin lens (Fort & Mellier, 1994). The picture is then that light from the source travels unperturbed through a flat spacetime described by the Friedmann-Lemaître-Robertson-Walker metric given in Section 2.2, which is then deflected in the lens plane by an angle α given entirely by the project mass distribution Σ, and finally continues again unperturbed to the observer. This is illustrated in Figure 5.1. As seen therein for point sources this alters their apparent position in the source plane from η to ξ.

Generally the deflection angle is calculated assuming a weak perturbation of a Minkwoskian spacetime through the lensing mass and its resulting gravitational potential (Narayan & Bartelmann, 1996). This also requires the peculiar motion of the lensing mass to be non-relativistic, which is the case for practically all cases of interest. The local perturbation from the gravitational potential causes the light to travel slower (its effective speed is reduced) akin to a prism – see Figure 2 from Narayan & Bartelmann (1996) – which results in the deflection. In theory this leads to a line integral over the path of the light which is continuously bent by the potential, while in practice when the assumptions above hold the deflection angle is relatively small and as such the line integral can be evaluated for a straight path of the light, also known as the Born approximation from scattering theory (Narayan & Bartelmann, 1996; Seitz et al., 2022). It follows that:

$$\hat{\alpha} = \frac{2}{c^2} \int_l dl \, \Delta_\perp \Phi = \frac{4G}{c^2} \int_{\mathbb{R}^2} d^2\xi' \, \frac{\Sigma(\xi')\,(\xi - \xi')}{|\xi - \xi'|^2}, \tag{5.7}$$

given as Equations 2.11 and 2.12 in (Seitz et al., 2022) and where the second equality follows from the thin lens approximation. Note that it is only the transverse gradient of the gravitational potential relative to the lights travel path which causes the deflection (left of Equation 5.7), while parallel gradients (for example from sheets of mass perpendicular to the travel path) cause *no* deflection. Consequently it is only the change in projected surface mass density which impacts the lensing signal.

When defining ζ as the apparent position of the source in the source plane, from Figure 5.1 it can be concluded that

$$\theta = \frac{\xi}{D_d} = \frac{\zeta}{D_s}$$
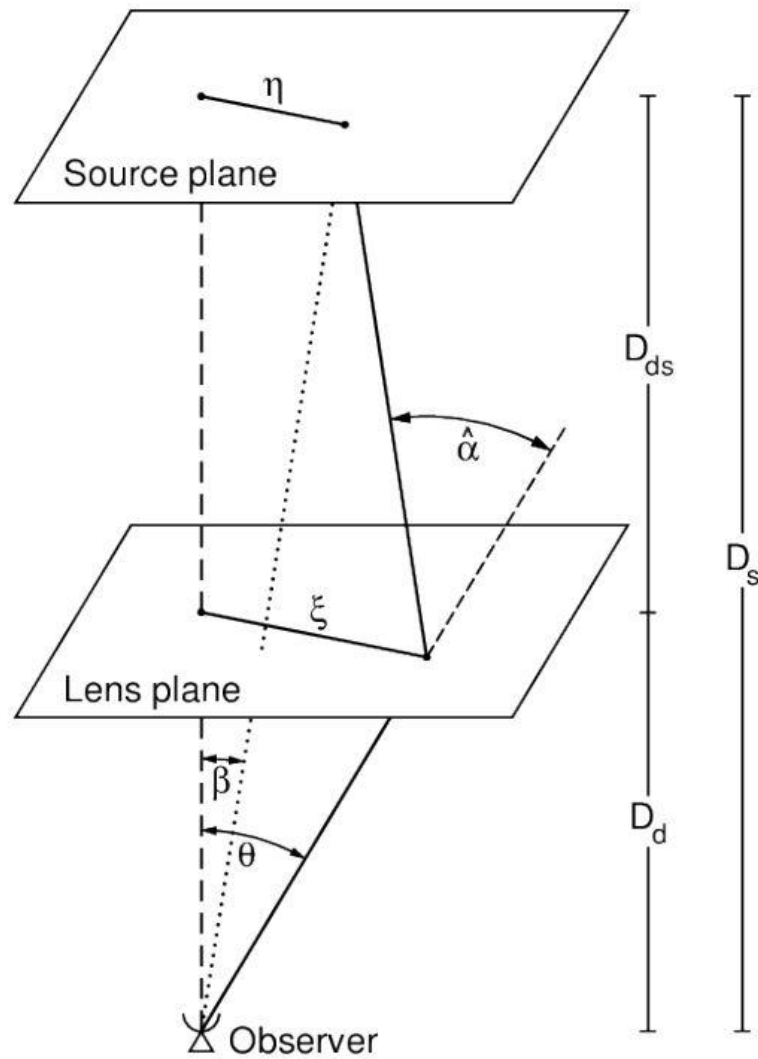
Figure 5.1: The geometric relations between the observed position ξ in the lens plane versus the actual position η in the source plane, and their link through the deflection angle $\hat{\alpha}$. Note that due to the nature of the expanding background metric in general $D_s \neq D_{ds} + D_d$. Figure 1 taken from Seitz et al. (2022).

$$\longrightarrow \hat{\alpha} = \frac{\zeta - \eta}{D_{ds}} = \frac{\frac{D_s}{D_d} \cdot \xi - \eta}{D_{ds}}$$

$$\longleftrightarrow \eta = \frac{D_s}{D_d} \cdot \xi - D_{ds} \cdot \hat{\alpha}(\xi) \tag{5.8}$$

which is the form of the lens equation given as Equation 2.13a from Seitz et al. 2022 and is often also given in forms of angles as

$$\beta = \theta - \alpha(\theta), \tag{5.9}$$

with $\alpha(\theta) = (D_{ds}/D_s)\hat{\alpha}(\theta)$ the reduced deflection angle (Equations 13 and 14 from Narayan & Bartelmann 1996) where the dependency on ξ in Equation 5.7 has been replaced by the equivalent angle θ. There is a beautiful relationship in the behavior of the reduced deflection angle. It can be shown that α can be related to an underlying "deflection potential" ψ which fulfills the condition $\alpha(\theta) \equiv \nabla\psi(\theta)$ by transforming $\xi = D_d \cdot \theta$:

$$\nabla\psi(\theta) \stackrel{!}{=} \alpha(\theta) = \frac{D_{ds}}{D_s} \cdot \hat{\alpha}(\theta) \stackrel{(5.7)}{=} \frac{D_{ds}}{D_s} \cdot \frac{4G \cdot D_s}{c^2} \int_{\mathbb{R}^2} d^2\theta' \frac{\Sigma(\theta')(\theta - \theta')}{|\theta - \theta'|^2}$$

$$\longleftrightarrow \psi(\theta) = \frac{4G}{c^2} \cdot \frac{D_s D_{ds}}{D_s} \int_{\mathbb{R}^2} d^2\theta' \int d\theta \frac{\Sigma(\theta')(\theta - \theta')}{|\theta - \theta'|^2}$$

$$\psi(\theta) \equiv \frac{1}{\Sigma_{crit}} \cdot \frac{1}{\pi} \cdot \int_{\mathbb{R}^2} d^2\theta' \, \Sigma(\theta') \cdot \ln|\theta - \theta'|$$

$$\longrightarrow \psi(\theta) \equiv \frac{1}{\pi} \int_{\mathbb{R}^2} d^2\theta' \, \kappa(\theta') \cdot \ln|\theta - \theta'|, \tag{5.10}$$

where in two steps first the critical surface mass density

$$\Sigma_{crit} \equiv \frac{c^2}{4\pi G} \cdot \frac{D_s}{D_s D_{ds}} \tag{5.11}$$

and then the dimensionless surface mass density

$$\kappa(\theta') \equiv \frac{\Sigma(\theta')}{\Sigma_{crit}} \tag{5.12}$$

were defined. This is then exactly akin to how the electric field is given as a gradient of the electric potential, where here instead the reduced deflection angle is given as a gradient of a deflection potential (Seitz et al., 2022). It can be shown that the lens equation in Equation 5.9 for small angles linearises to a Jacobian matrix as

$$\mathcal{A} = \begin{pmatrix} 1 - \kappa - \gamma_1 & -\gamma_2 \\ -\gamma_2 & 1 - \kappa + \gamma_1 \end{pmatrix} = (1 - \kappa) \cdot \mathbb{I} - \gamma \cdot \begin{pmatrix} \cos(2\phi) & \sin(\phi) \\ \sin(\phi) & -\cos(2\phi) \end{pmatrix} \tag{5.13}$$

as shown for example by Narayan & Bartelmann (1996). κ is known from the above definition and describes the convergence (Ricci focusing), commonly also defined in the form as the the Laplacian of the deflection potential, $2 \cdot \kappa(\theta) = \Delta\psi(\theta)$ (from Equation 5.10). The second

term γ is the complex shear (Weyl focusing) and can be determined as

$$\gamma^2 = \frac{1}{4}\left(\delta_{xx}\psi - \delta_{yy}\psi\right)^2 + \left(\delta_{xy}\psi\right)^2, \tag{5.14}$$

as given by Equations 6 and 7 from Fort & Mellier (1994). κ then describes the isotropic focusing of a bundle of light, while γ results in an anisotropic distortion (Seitz et al., 2022). If the latter is non-zero this will result in extra ellipticity induced in the images, causing the formation of arclets or weak distortion of background galaxies (Fort & Mellier, 1994). Depending on how strong the combined distortion through the deflection potential is, this results in different lensing regimes. If it is strong enough to bundle multiple rays into a single point this is the strong lensing regime resulting in multiple strongly distorted images, while for weaker regimes one sees arclets or just weakly distorted images – see for example Figure 4 from (Fort & Mellier, 1994).

The points in the lens plane θ where the determinant of the Jacobian $\mathcal{A}$ becomes singular describe a so-called "critical curve", which can be related directly via Equation 5.9 to points β in the source plane forming "caustic" (Seitz et al., 2022). As a source crosses a caustic towards the optical axis two additional images are produced within the corresponding critical curve in the lens plane. Note that the number of such critical lines is defined by the mass distribution of the lens, with great examples found in Figures 2 and 3 from Seitz et al. (2022).

For a circularly symmetric lens, it follows from Equation 5.9 and Equation 5.7 that for a source placed at β the resulting image within the lens plane is that of a ring $\hat{\alpha} = \theta$ if the lens is supercritical $\Sigma > \Sigma_{\mathrm{crit}}$ with a radius given by the "Einstein radius":

$$\theta_{\mathrm{E}} = \sqrt{\frac{4GM(\theta_{\mathrm{E}})}{c^2} \cdot \frac{D_{\mathrm{ds}}}{D_{\mathrm{d}}D_{\mathrm{s}}}} \tag{5.15}$$

as given by Equation 20 from Narayan & Bartelmann (1996). This provides a nice scale for the lensed images, with sources closer than θ_{E} to the optical axes typically experiencing strong lensing. This means that galaxy clusters with a larger Einstein radius are expected to exhibit more multiply imaged systems (Limousin et al., 2007). Furthermore, multiple images are generally separated by about $2 \cdot \theta_{\mathrm{E}}$ (Narayan & Bartelmann, 1996). However, it should be noted that one "can never (EVER!) safely neglect the angular structure of the gravitational potential" (Kochanek, 2004), and as such this should merely be taken as a worthwhile scale, while actual lensing models strive instead to account for significantly disturbed profiles. This therefore leads to the need of finding *projected* variants of typical density distributions that are commonly defined as spherically symmetric in three-dimensions – see for example those introduced in Chapter 3. For the particular case of the common Navarro-Frenk-White profile an example derivation of its projected surface mass distribution is given in Appendix A.2, providing an insight into the difficulties that arrive when projecting. More complete analyses including variables such as the resulting shear are given by Takada & Jain (2003) and Lima et al. (2010).

5.2.2   Lensing in Observations

As seen in Section 5.2.1, there exists a direct relationship between the distribution of mass and the resulting images from gravitational lensing. Conversely, it is possible through knowledge of all other variables in Equation 5.9 and Equation 5.10 to deduce the mass distribution $\Sigma(\theta)$ itself. For the case of weak-lensing a thorough statistical analysis must be conducted which then allows a relation of the mean ellipticity of the background galaxies and the mass distribution of the lensing galaxy cluster (Seitz et al., 2022) as proposed by Kaiser & Squires (1993). Meanwhile the multiple images resulting from strong lensing allow for the direct fitting of a mass model, though they require first identifying which images belong to the same objects. To this end, one must construct a mass model for the lens and vary the parameters of the model until the resulting lensed images match those observed, where it is typical the measure the goodness of the fit with the root-mean-square with lower values indicating better fits – see for example the definitions as Equations 1 and 2 from Elíasdóttir et al. (2007) or Jullo et al. (2007). The following outlines the general procedure.

Firstly the final mass distribution is comprised generally of mass models of two separate classes, with one or more large-scale halos and numerous small-scale halos. The former therefore typically has masses of order $1 \times 10^{14} \, M_\odot$ and is associated with the galaxy cluster itself (dark matter and ICL) while the latter is associated with members (dark matter and stars), typically large ellipticals (Jauzac et al., 2015). A typical model used for the surface mass density distributions is the Pseudo Isothermal Elliptical Mass Distribution (PIEMD) introduced by Kassiola & Kovner (1993), which they found to feature greater variability with elongated masses than the restricted Pseudo Isothermal Elliptical Potential (PIEP). The general condition for such a distribution takes the form:

$$\kappa_{\text{PIEMD}} \propto \left(c_0 + c_1^2 \cdot x^2 + c_2^2 \cdot y^2 \right)^{-1/2}, \tag{5.16}$$

with κ the convergence as defined in Equation 5.12 and where c_0 is generally $\neq 0$ and thus allows non-singular (i.e., analytic) behavior at the center. The corresponding density profile takes the form (Kassiola & Kovner, 1993; Limousin et al., 2007)

$$\rho(r) = \frac{\rho_0}{\left(1 + r^2/r_c^2 \right) \left(1 + r^2/r_{\text{cut}}^2 \right)}. \tag{5.17}$$

Defining the ellipticity $\epsilon \equiv (a - b)/(a + b)$ and using two PIEMDs allows for a smoothly truncated elliptical mass distribution, commonly referred to as a dual Pseudo Isothermal Elliptical Mass Distribution, or dPIE in short, to be defined as:

$$\Sigma(x, y) \equiv \Sigma_0 \frac{r_{\text{cut}} \cdot r_c}{r_{\text{cut}} - r_c} \left(\frac{1}{\sqrt{r_c^2 + \rho^2}} - \frac{1}{\sqrt{r_{\text{cut}}^2 + \rho^2}} \right), \tag{5.18}$$

where

$$\rho^2 \equiv \frac{x^2}{(1+\epsilon)^2} + \frac{y^2}{(1-\epsilon)^2}, \tag{5.19}$$

given here in the form by Kneib et al. (1996) (compared to Equation 8.10 from Kassiola & Kovner 1993). r_{cut} is the cut radius beyond which the surface mass density converges to a slope as $\propto r^{-3}$ allowing for finite total masses. Meanwhile for radii with $r < r_{\mathrm{c}}$ there is a cored central region with density ρ_0, while for the transition region the density slope is isothermal $\rho \propto r^{-2}$ (Limousin et al., 2007). As it is typically the larger ellipticals which are modeled by the small-scale PIEMDs this slope matches the slopes found for the inner parts by Koopmans et al. (2006). Note that it is common to transform the central surface mass density to the central velocity dispersion as $\Sigma_0 = \sigma_0^2/(2G \cdot r_{\mathrm{c}})$. The final parameters for each dPIE are thus seven in number, namely the central position (two, one for RA one for DEC), the ellipticity ϵ, the position angle and finally the parameters for the density profile σ_0, r_{cut} and , r_{c} (Limousin et al., 2007).

Some reductions to the necessary parameters can be made. It is typical to fix the center, ellipticity and angle by those observed for the associated light distribution (cf. Kneib et al. 1996; Limousin et al. 2007). This still leaves a large number of free parameters as there are three free ones per galaxy-scale dPIE, though they tend to be less than when instead reconstructing the mass distribution via the fit of a grid of pixels (Jullo et al., 2007). To reduce further the total number of free parameters, it is typical to scale the two of the free parameters of the density profile according to the observed galaxy luminosity (Brainerd et al., 1996) as:

$$\sigma_0 = \sigma_{0,*} \cdot \left(\frac{L}{L_*}\right)^a \qquad r_{\mathrm{cut}} = r_{\mathrm{cut},*} \cdot \left(\frac{L}{L_*}\right)^b \tag{5.20}$$

as done for example by Meneghetti et al. (2020). If one further assumes a mass-to-light ratio, which can be argued through the Faber & Jackson (1976) relation and is done for example by Limousin et al. (2007), this further reduces the variables by linking the slopes a and b. Note that the core radius can further be scaled as the cut radius is, by assuming some fixed initial value relating to a luminosity (Limousin et al., 2007). or instead can be assumed to be negligible (Meneghetti et al., 2020).

Note that there is a significant nuance in the exact application of such lensing models. For example, prescriptions must enable the model to differentiate the case of merging images, where two images overlap into one if the resolution is not sufficient (Kassiola & Kovner, 1993). Furthermore, as lensing is sensible only to the projected mass – see Section 5.2.2 – this can lead to problems with structure along the line of sight being included (Rosati et al., 2014). The degeneracy between the mass of the lens and the source redshift – see Equation 5.10 – requires high accuracy of the distance measurements, which typically necessitates spectroscopy. Common use of the Faber & Jackson (1976) relation additionally constrains the $\sigma_0 - M$ relation by definition, which may however not accurately reproduce the real behavior of the galaxy members. This can be seen by comparing lensing models of the same galaxy cluster once using the Faber & Jackson (1976) relation versus using

the fundamental plane (Dressler et al., 1987), as plotted in Figure 4 from Granata et al. (2022) which leads to an improvement relative to Bergamini et al. (2019). Furthermore, the assumption that the central positions, ellipticity and orientation of the visible mass traces the dark mass as found by Koopmans et al. (2006) was conducted specifically for elliptical field galaxies, and may not hold as well for those within galaxy cluster environments.

Finally, using weak-lensing to construct the large-scale mass distribution relies on the random distribution of orientations (Heavens et al., 2000). However, the presence of shape and spin alignments is found for both observations (Pen et al., 2000; Brown et al., 2002) and simulations (Heavens et al., 2000), with greater alignment across larger scales (Smargon et al., 2012). This can be caused by the tidal fields from local large-scale overdensities (Hoyle, 1949; Doroshkevich, 1970; White, 1984), and can hamper the weak-lensing reconstructions (Porciani et al., 2002).

5.2.3   The Missing Mass and Abell 2744

Gravitational lensing has been very successful in pushing the boundaries of the mass distributions which can be observed. Especially strong lensing has allowed insight into the centralmost regions of galaxy clusters. It is now however in the region of the substructures, modeled by the galaxy-scale dPIEs, where discrepancies are being found to those observed in simulations. In particular, the case of the galaxy cluster Abell 2744 is of utmost interest, finding in the observations performed by Jauzac et al. (2016) extreme substructure masses in excess of an order of magnitude different than those from equivalent simulations (Schwinn et al., 2017).

Abell 2744 is a dynamically disturbed galaxy cluster located at $z = 0.308$, and is one of the current most massive ones known with a mass as $M(< 1.3\,\text{Mpc}) = (2.3 \pm 0.1) \times 10^{15}\,\text{M}_\odot$ (Jauzac et al., 2016). its disturbed nature has been observed also in X-ray through the presence of a shock front in the South, an X-ray emission peak without corresponding galaxy overdensity, most likely resulting from stripped atmospheres, and finally an offset of the X-ray peak to the main mass peak as noted by Owers et al. (2011) and via dynamical studies through finding of a bimodal velocity distribution by Braglia et al. (2009). A particularly striking example of this is its powerful and extended radio halo (Giovannini et al., 1999; Merten et al., 2011).

The observations by Jauzac et al. (2016) are imaged via the Hubble Space Telescope twice, with the latter as part of the Hubble Frontier Fields (Lotz et al., 2017) for the central regions, and probed on the larger scales with the Canada-France-Hawaii Telescope. They supplement photometric redshifts from the Wide Field Imager with spectroscopic redshifts of the Anglo-Australian Telescope (Saunders et al., 2004) produced by Owers et al. (2011), accounting for a total of 343 members within 3 Mpc (Jauzac et al., 2016). In particular for the weak-lensing analysis, the selection of galaxy cluster members via redshift is crucial (Seitz et al., 2022). The criterion defined by Jauzac et al. (2016) is $0.308 - 0.01 < z < 0.308 + 0.01$ for the member galaxies' spectroscopic redshift, with color-color selections additionally

applied. They also extended the latter color selections to the main bulk of galaxies for which no photometric redshift was determined (around 70%).

The resulting mass distribution as determined by Jauzac et al. (2016) consists of two cluster-scale PIEMDs and 733 galaxy-scale dPIEs, with an additional grid for the weak-lensing region consisting of radial basis functions (dPIEs of fixed size and position). Within the mass distribution, they identify eight substructures which have masses in excess of $5 \times 10^{13}\,\mathrm{M}_\odot$ and lie within 1 Mpc. These, according to Jauzac et al. (2016), are in excess of any comparable galaxy clusters' substructure masses found in simulations. Given the direct link between structure formation and the cosmological model – see Section 4.2 – is this then a new iteration of the "missing mass" problem? A comparison of these observational results to those determined within this thesis is found in Section 8.6 to answer the question.

5.2.4 Concentration and Velocity

The question of observed cluster substructure compactness warrants a brief consideration. As discussed in Section 5.2.2, it is common to model a galaxy cluster as one or two large-scale mass distributions with an addition of numerous galaxy-scale models. One typically expects the multiple images to be a result of the large-scale distributions critical lines – however, it is possible in rare cases to have substructures within the cluster produce strong lensing events if they are sufficiently massive and compact, termed galaxy-galaxy strong lensing (GGSL) events by Meneghetti et al. (2020). The resulting scales are much smaller and thus require much higher resolution to observe, but this has become possible in recent years due to projects such as the Hubble Frontier Fields (Lotz et al., 2017) and CLASH (Postman et al., 2012) surveys.

Through use of these newer catalogues, Meneghetti et al. (2020) find a significant increase in the number of GGSL from observations compared to the hydrodynamical simulations by Planelles et al. (2014). This would imply observed substructure to be noticeably more compact than their simulated equivalents. To see this it is commonly the maximum circular velocity which is actually determined. In lensing observations this is achieved through fitting of galaxy-scale dPIE lens models as in Equation 5.18 (Kassiola & Kovner, 1993; Kneib et al., 1996) with core radii tending towards zero (Meneghetti et al., 2020), which then have a density slope of $\rho \propto r^{-2}$ for central radii out to the cut radius – see the descriptions in Section 5.2.2. This in turn is the slope of a singular isothermal density profile as defined in Equation 3.5 and thus translates directly into a circular velocity as:

$$v_{\mathrm{circ}}(r) = \sqrt{\frac{GM(r)}{r}} = \sqrt{\frac{G \cdot 4\pi\sigma_0^2}{2\pi Gr} \cdot \int_0^r dr' r'^2 r'^{-2}} = \sqrt{\frac{2\sigma_0^2}{r} \cdot r} = \sqrt{2\sigma_0^2} \qquad (5.21)$$

As the outer slopes of the dPIE model fall of more steeply $\rho \propto r^{-4}$ it is only the region within the cut radius that determines the maximum circular velocity and as such by extension the concentration: a halo with equal total mass but higher σ_0 will have a small cut radius and is thus more concentrated. Similar behavior between a halo's maximum circular velocity and

concentration are found for the Einasto and Navarro-Frenk-White density profiles, as can be seen in Section 7.1.

It follows that the measurements of high central velocity dispersions by Meneghetti et al. (2020) then directly imply high concentrations. Consequently, observed substructures appear to be more compact than their simulated equivalents. This is discussed further in Section 7.1.

5.3   Simulated Equivalents?

Assuming our understanding of the Universe as given by ΛCDM is correct – see Chapter 2 – and that most relevant physics are implemented into the code, cosmological simulations can be used as a direct comparison to the observations described in Section 5.1. Discrepancies then can be used to refine either the physics employed by the simulations or the observational methods, or both, thus enabling a fruitful cross-checking process.

The simulation used throughout this thesis is the `Magneticum Pathfinder` simulation suite (Dolag, 2022; Hirschmann et al., 2014; Teklu et al., 2015), performed with a fully hydrodynamic smoothed-particle hydrodynamics (Lucy, 1977; Gingold & Monaghan, 1977) code, also known as "SPH", on the basis of `GADGET-2` (Springel, 2005). This type of code relies on the discrete version of the Lagrangian description of fluid flow, where tracer particles mimic the density field. To recover the true density field is "then equivalent to recovering a probability distribution from a sample" (Gingold & Monaghan, 1977), where to avoid the cost of multiple integrals for each particle instead a smoothing kernel method is employed (Bartlett, 1963). As described in Section 2.1, the fundamental equations for the gravitational force calculations are given entirely by the chosen spacetime metric. Due to the common use of the Friedmann-Lemaître-Robertson-Walker metric (Springel, 2005; Vogelsberger et al., 2014; Springel, 2010), this implies that deviations in the observed properties of objects from simulations are given through differences in the chosen cosmology, in the baryonic physics employed (e.g., star formation, cooling, metals, black holes, feedback, magnetic fields) and finally in the way the output is calculated or a mixture of those. Information with respect to the former two are given for `Magneticum Pathfinder` by Hirschmann et al. (2014) and Teklu et al. (2015) and also at www.magneticum.org. The final point raises the question of how a given set of particles from a simulation can be grouped together to identify structures. These structures are of utmost importance, at they are the starting point for the definition of global halo properties, and as such the following will provide a brief insight into the concept of structure finders.

5.3.1   Identifying Structure in Structure

The basic foundation of such linking is the idea of a friends-of-friends (FoF) algorithm, whereby particles are linked together if their separation is smaller than some defined linking length (Davis et al., 1985), which is commonly given in terms of the mean interparticle separation and on the order of 0.2. A group of such linked particles is then for simple

implementations a "halo". This method however poses the problem of how to define a subhalo *within* another halo, where this difficulty is further exacerbated for lower-resolved early simulation codes that would suffer from "overmerging" – seeing infalling halos entirely disrupted and amalgamated (Frenk et al., 1996). Initial solutions were varied in their goals, where for example to ensure the survival of subhalos entirely one method relied on replacing a halo once it has been identified instead by a more massive second type of particle as described by van Kampen et al. (1999), which however runs into the difficulty of entirely preventing natural stripping or merging of the particles. Another solution was by instead setting a sequence of discrete steps of linking lengths and assigning a hierarchy based on which particles link on the smallest steps as employed by hierarchical friends-of-friends (HFOF) algorithms (Klypin et al., 1999), enabling a hierarchy of halos but in turn making the halo definitions entirely dependent on the chosen steps. A third alternative is given through specifically bestowing the most-bound-particle of a dark matter halo with the identity of a galaxy as done by Kauffmann et al. (1999), with the latter two variants more flexibly allowing parts of the dark matter halo to be stripped away during infall while still retaining the subhalo as a galaxy within the larger halo. Building on the last variant, Springel et al. (2001) developed an algorithm they called SUBFIND. While explained in great detail therein, a supplementary overview is given here as the difference between bound and projected structures lies at the heart of the following analyses.

Given an initial set of particles, which in theory could encompass the whole simulation but in practice typically a subset is chosen in form of a FoF group as a starting point, their densities are calculated according to the typical SPH smoothing kernel formalism. They are then sorted according to density, starting the iteration from high to low – this is the first panel in Figure 5.2. The highest density particle is the center of the FoF halo. Going a step in density up, all corresponding particles have their nearest neighbors calculated. Then all neighbors with equal or lesser density are removed and finally the closest two particles fulfilling these conditions kept. This is illustrated in the second panel of Figure 5.2, where the case occurs that the closest two higher density neighboring particles are in fact a single particle, and all three particles of density ρ_1 are assigned to the group that the particle with density ρ_0 belongs to. Going another step down in the third panel, the same occurs, with the particles in the center finding one or two higher density neighbors all belonging to the halo originating from the particle at density ρ_0 – except for the particle on the far left. This particle finds *no* neighbors of higher density, and thus begins growing its own subgroup. This is not a subhalo yet, but rather a group. In the final panel, a particle of a density another step down is illustrated in red, which has the third possible situation occur: its closest neighbors of higher density belong to two different subgroups, so it is considered to be a saddle point and both groups it borders are now considered subhalo candidates. Subsequently, the subgroups are joined to one, the red particle is added, and the procedure carries farther down the list. After all subhalo candidates are then cleaned of any particles not actually bound to them, if the remaining grouping is of sufficient number or mass it is identified as a subhalo (Springel et al., 2001).
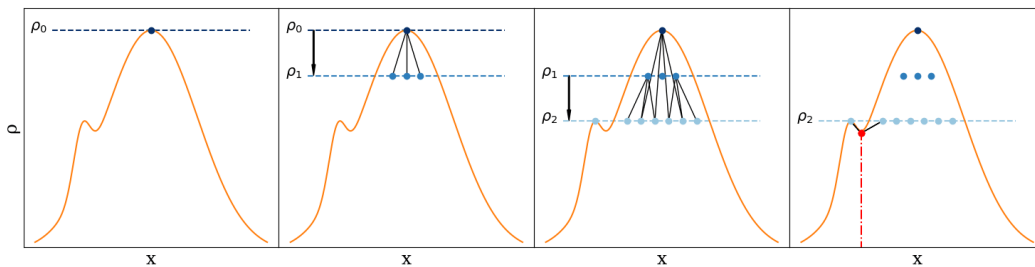
Figure 5.2: Schematic of the `SUBFIND` structure identification algorithm as given by Springel et al. (2001), illustrating the detection of a potential subhalo.

`SUBFIND` was subsequently improved upon by Dolag et al. (2009). Firstly, by considering a cosmology-dependent linking length FoF groups will better reproduce expected overdensities from the spherical collapse model. Secondly and importantly, in its original conception `SUBFIND` was optimized for identifying specifically dark matter halos, while the differing, more compact distributions of the baryons should not be treated in the same way. While this is fine for the initial FoF halo, Dolag et al. (2009) modify the subsequent steps by considering each species separately, using the closest *three* higher density neighbors and also disregarding gas particles when applying the minimum number limit.

This method allows the definition of halos and subhalos, and subsequently of their properties. Some of the main ones considered throughout this thesis are M_{FoF}, the total mass of the friends-of-friends group, GPOS, the position (in code units) of the most-bound-particle which constitutes the center of the halo, M_{vir} and correspondingly r_{vir} as the virial mass and radius as defined through the virial overdensity relative to the critical density. Note that the latter two assume spherical symmetry and thus may not directly correspond to the true extent or mass of a particularly irregular object. Similarly for subhalos the total linked particle mass is called M_{sub}, with the position of the most-bound-particle considered the center of the subhalo as SPOS.

Given the importance of a sophisticated structure finder in simulations, many differing variants have been developed with time. A comprehensive overview is performed by Knebe et al. (2011), finding general behavior to be overall similar between most common structure finders. Larger variations are found for subhalos in halos, with phase-space based structure finder performing slightly better. Therefore, although the findings by Knebe et al. (2011) provide confidence for the identifications of halos, caution must be kept when dealing with more complex and disturbed structures. This is especially the case during major mergers as shown by Behroozi et al. (2015).

5.3.2 The `Magneticum Pathfinder` Simulation Suite

As mentioned previously, the simulation used throughout this thesis is the fully hydrodynamical cosmological simulation `Magneticum Pathfinder` (Dolag, 2022). A comparison of different state-of-the-art simulations can be found in Figure 5.3. The particular box used for most of the following analyses is box 2b (hr), which forms a middle ground between the

larger volume and higher resolution of box 0 (mr) and box 4 (uhr), respectively. This provides a unique opportunity to explore objects of similar mass to those discussed in Section 5.1, something that is practically impossible for boxes of smaller size due to the extremely high masses on the order of $1 \times 10^{15}\,M_\odot$ while still having enough resolution to resolve internal structures. In particular, the inclusion of baryonic physics allows a more direct comparison to the observations. The chosen snapshot is number 31 at a redshift of $z = 0.252$.
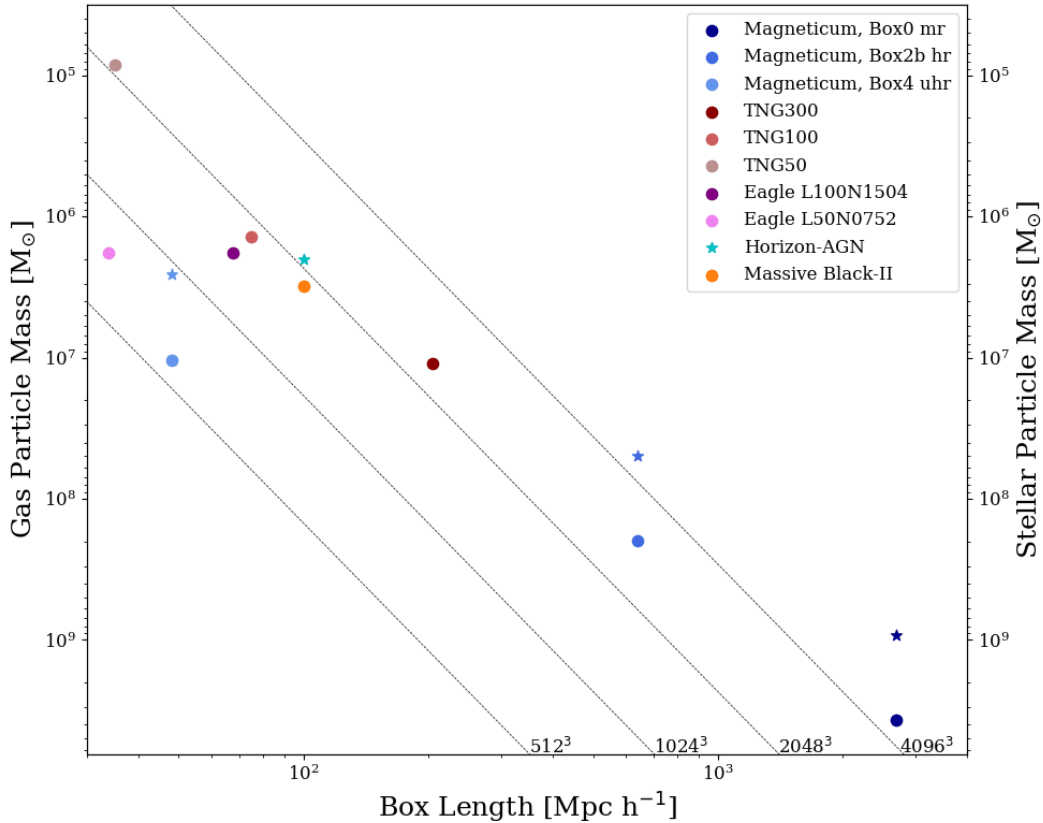
Figure 5.3: A comparison of some of the highest resolution hydrodynamical simulation boxes as of 2022. Simulation parameters are taken from Dolag (2022), Nelson et al. (2018), Schaye et al. (2015), Dubois et al. (2014) and Khandai et al. (2015) for `Magneticum Pathfinder`, `IllustrisTNG`, `Eagle`, `Horizon-AGN` and `MassiveBlack-II`, respectively.

The cosmology employed is that of WMAP-7 (Komatsu et al., 2011) with Hubble constant $H_0 = 70.4\,\mathrm{km\,s^{-1}\,Mpc^{-1}}$, matter and dark energy density fraction at present day of $\Omega_\mathrm{m} = 0.272$ and $\Omega_\Lambda = 0.728$, an index of the primordial power spectrum of $n = 0.963$ and an overall variance at 8 Mpc of $\sigma_8 = 0.809$. The baryonic physics included cover all relevant subgrid physics from star formation recipes to AGN feedback models, metal enrichment and cooling. Details of these physics are presented by Hirschmann et al. (2014), Teklu et al. (2015) and Dolag et al. (2017). The simulations well capture many global galaxy properties (like angular momentum – see Teklu et al. 2015 and Schulze et al. 2018, density distributions – see Remus et al. 2017b and Remus & Forbes 2021), of galaxies in cluster environments (Lotz et al. 2019 and Lotz et al. 2021) as well as general properties of X-ray emission from galaxy clusters (Biffi et al., 2018). Therefore the simulation is well suited for the analysis presented in this thesis.

5.3.3   Comparing Apples to Oranges

An astute reader will have noticed a glaring difference between the output from the observations and the simulations: SUBFIND uses and outputs the full phase-space description of the objects, while observations are (initially) limited to two-dimensional spatial and one-dimensional velocity data, the latter of which is further degenerate for purely photometric data with the recession velocity. While the inclusion of spectroscopic data for the observations enables an increase to approximate three dimensional spatial data, the final mass distribution responsible for the observed lensing signal is still 2-dimensional - that is to say, it is *projected*. This can also be seen immediately by noting that the mass distributions fitted for lensing are 2-dimensional surface densities, and is mentioned also by Jauzac et al. (2016) as a potential source of the discrepancy. However, both they and Schwinn et al. (2017) find only marginal differences from projection when comparing with dark matter-only simulations.

Similarly, the topic of structure finders perhaps cutting too much matter away from massive subhalos far towards the center has been discussed as a possible reason for the discrepancies by Han et al. (2018a). However, though differences still exist for the different structure finders, recent studies find good overall agreement for general properties of subhalos (Gómez et al., 2022). Furthermore, the assumption that the high substructure masses found from lensing are entirely carried by a single bound subhalo within its host galaxy cluster in projection can lead to requiring more mass in the subhalos than is present in the overall halo, as was found by Schwinn et al. (2017) for the particularly extreme case of Abell 2744. There, extrapolating the projected masses within a 150 kpc aperture from lensing (Jauzac et al., 2016) finds a total subhalo mass of $\Sigma_{1-8} M_{\mathrm{sub}} = 7 \times 10^{15}\,\mathrm{M_\odot}$, compared to the main halo with $M_{200} = 3.3 \times 10^{15}\,\mathrm{M_\odot}$ (Schwinn et al., 2017). This result already provides an indication that the found substructure masses are most likely not singular bound subhalos within the larger halo, but rather include a significant amount of mass from other subhalos and the main halo within the projected aperture. It is important here to note the distinction between a real, bound *subhalo* identified by a structure finder within a cosmological simulation to a *substructure*, which here is defined to mean a "structure within a single aperture" – these need not be actual, self-bound structures!

5.4   The State of Affairs and the Future

At this point then all necessary groundwork for the following analysis is laid. First, the observational methods and their findings are discussed in Section 5.1, with a special emphasis placed on gravitational lensing which is discussed in detail in Section 5.2. The same is done for simulations in Section 5.3. The arising discrepancies are topicalized in Section 5.3.3, where the difference between a "substructure" and a "subhalo" is defined. The exact nature of singular projected halos is discussed further in Appendix A.2, where in the following chapters instead the impact of a total projection of a galaxy cluster on its perceived substructure masses is explored. Using the projected simulation output from the method which is described in

detail in the following Chapter 6, the relationship between projected masses within an aperture and bound masses is explored in Chapter 8.

Chapter 6

Finding the Building Blocks

The following chapter will then present a more thorough step-by-step consideration for the construction of a method similar in its behavior to what an observer would have, with the final goal of determining properties of the substructures – in particular their mass – through two-dimensional images instead of the full three-dimensional information.

To provide a brief overview, first the galaxy clusters will be projected into two-dimensional surface density maps and centered on their two-dimensional center-of-mass in Section 6.1. Then present substructures are identified in Section 6.2 and masked such that only the main remains. Afterwards in Section 6.3, a two-dimensional radial density profile is fit to the main halo, based on which its contributions in mass to each substructure are subtracted to finally arrive at their masses.

Four mass bins of 29 galaxy clusters will be considered. The largest, henceforth "giants", is comprised of the most massive galaxy clusters based on their friends-of-friends mass as given by `SUBFIND` with each reaching $1 \times 10^{15}\,\mathrm{M_\odot}$ and above. The three smaller mass bins are chosen instead based on their virial mass (again from SUBFIND), as for the purpose of scaling some degree of spherical symmetry must be assumed (see Section 6.4 for more details) and the friends-of-friends mass can often be significantly elongated in its distribution, to the point where in extreme cases upwards of 15% of the friends-of-friends mass can lie wholly outside of the assigned virial radius (as is for example the case for cluster 3 of the giants). The mass bins used are summarized in Table 6.1.

As the method described in the following relies on projected maps, it is necessary to first specify the gridding employed. For the sake of comparability among the different galaxy clusters of a mass bin, each bin has a fixed pixel size, with the giants having pixels of area $2\mathrm{kpc} \times 2\mathrm{kpc}$ and the other bins being scaled as described in Section 6.4. Galaxy clusters of different sizes can then have different numbers of pixels per image, though aside from the giants the galaxy clusters in the mass bins should vary only slightly in size among each other. Particles used for the map are then gridded into each pixel based on their positions, and their masses are summed into a surface mass density – this is then the "value" of each pixel.

Furthermore, to avoid depicted maps from appearing exceedingly diffuse due to the gridding, any plotted versions of the maps in the following are smoothed via a Gaussion kernel as implemented in the "imshow" function from `matplotlib` (Hunter, 2007). Due

to the large differences in pixel values, plots are displayed with logarithmic surface mass densities. This in turn leads to problems where empty pixels with value "0" become "$-\infty$" in logarithmic space and then when smoothed overwhelm the values of any other nearby pixels. These pixels are instead set to the surface mass density that would result from the mean mass density so as to allow the smoothing kernel to function correctly. This fix is however purely aesthetic in nature to better visualize the plots and is never applied to any values given as results here.

Finally, random orientations are achieved via a distribution of rotation angles resulting in a rotation matrix applied to the data, after which then the projection is done along the third axis. This axis then represents a random projection, and the specifics of the applied rotations are discussed more in Appendix A.3. An example of the resulting projected map via the method employed here as compared to the mock image creation code by Martin et al. (2022) is depicted in Figure A.11 for a galaxy cluster from box 4 (uhr) of `Magneticum Pathfinder`.

Table 6.1: Summary of the mass bins used. Each contains the first 29 galaxy clusters within the specified mass range, as sorted by their friend-of-friends mass. The ranges for "medium" to "tiny" are chosen such that their mean virial mass is tightly distributed around 5, 2 and 1e14 $M_\odot$ respectively.

Mass Bin	Mass Range	Mean Virial Mass in Bin
Giants	$M_{\mathrm{fof}} > 1 \times 10^{15}\,M_\odot$	$\bar{M}_{\mathrm{vir}} \approx 1.313 \times 10^{15}\,M_\odot$
Medium	$5.15 \times 10^{14}\,M_\odot > M_{\mathrm{vir}} > 4.85 \times 10^{14}\,M_\odot$	$\bar{M}_{\mathrm{vir}} \approx 5.002 \times 10^{14}\,M_\odot$
Small	$2.01 \times 10^{14}\,M_\odot > M_{\mathrm{vir}} > 1.99 \times 10^{14}\,M_\odot$	$\bar{M}_{\mathrm{vir}} \approx 2.000 \times 10^{14}\,M_\odot$
Tiny	$1.002 \times 10^{14}\,M_\odot > M_{\mathrm{vir}} > 0.998 \times 10^{14}\,M_\odot$	$\bar{M}_{\mathrm{vir}} \approx 1.000 \times 10^{14}\,M_\odot$

6.1 Beginning at the Start

To construct a projected density map of a selected galaxy cluster, a position to center it on and a size for the projected volume considered around this point are required.

First, the volume is considered. The extent in the plane perpendicular to the line-of-sight is chosen as $r_{\mathrm{2D}} = r_{\mathrm{vir}}$, with r_{vir} as given by SUBFIND. This ensures that the largest part of the cluster's mass is considered, while not being too large. For the projection depth, a result derived from Chapter 2 is applied: assuming the virial mass of the cluster were distributed perfectly spherically, then a test particle at rest at r_{turn} would feel an exactly equal acceleration between the expanding background and the cluster – see Section 2.6.1 – and would thus remain at the same physical distance to the galaxy cluster. This is then a reasonable approximation of the sphere of influence of the cluster and comes out to be around $r_{\mathrm{turn}} \approx 5 \cdot r_{\mathrm{vir}}$ for $z = 0.252$.

The final volume considered for the projected surface density map is then a cylinder of radius r_{vir} and height $Z = 2 \cdot r_{\mathrm{turn}}$, with the factor 2 arising from the consideration that both matter before and behind the cluster is projected. Given the volume, it is then necessary to determine the central point of this cylinder.
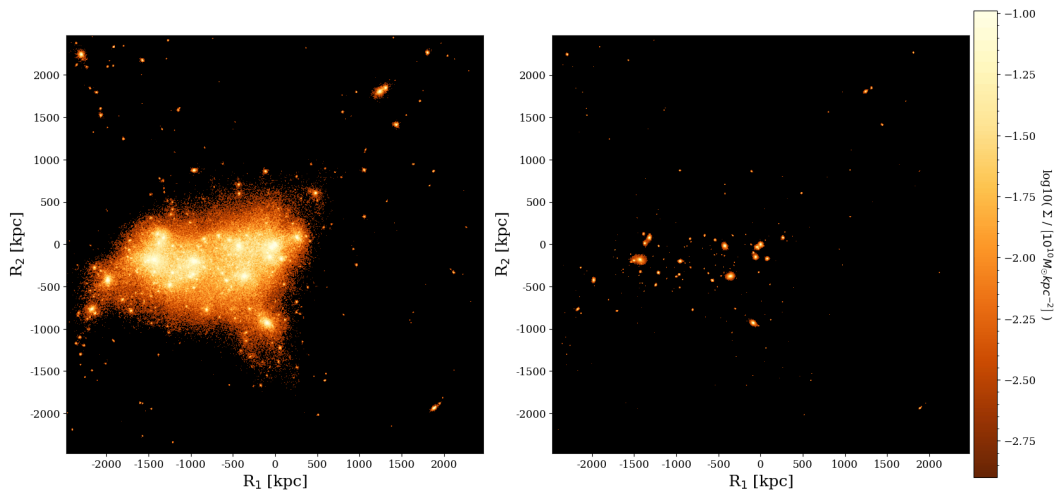
Figure 6.1: The total (left) and stellar (right) surface density map of galaxy cluster 20 of the "giants" in projection centered on its most bound particle. Depicted is a region of boxsize $2 \cdot r_{vir} \approx 2 \cdot 2.47$ Mpc, with the direction of the line-of-sight in code coordinates along $[0.03; 0.99; -0.17]$. It is apparent that an observer would not place the center of mass where the most bound particle resides, but rather on the order of 500 kpc to the left – a shift of around $0.2 \cdot r_{vir}$!

6.1.1 An Initial Position

A good initial position is provided by the location of the cluster's most-bound-particle as given by the SUBFIND output "GPOS". Figure 6.1 depicts the resulting map for an example cluster. This projection is chosen to highlight an arising difficulty when simply using the simulation output without further consideration. Though SUBFIND has determined the three-dimensional position of the minimum of the gravitational potential and is then correctly projected into two dimensions, this most-bound-particle is not necessarily the actual two-dimensional center-of-mass.

6.1.2 And a Better One

As the lensing fits are sensitive to the lensing signal, which in turn are dependent on the total mass (not only the stellar mass) and normally the center of the large-scale cluster mass distribution is left variable, the total mass is used here to determine the center of mass. The method employed is the "shrinking-sphere algorithm", or rather as the particle distribution is projected to 2 dimensions a shrinking-circle method. For this algorithm, provided a sufficiently large initial region, the resulting barycenters are quite independent of the initial parameters (Power et al., 2003). It should be noted that the direct particle data is used for this calculation before any binning into a map is done.

Given an initial set of particle positions x_i and masses m_i, an initial barycenter $\bar{x}_0$ is calculated as

$$\bar{x}_0 = \frac{\sum_i m_i \cdot x_i}{\sum_i m_i}. \tag{6.1}$$

To further refine the center, a fixed shrinking factor $f_{shrink} < 1$ as well as a radius r_1 are chosen for the next step, and the particles are reduced to only those j with $|x_j - \bar{x}_0| < r_1$.

Then the barycenter of these particles is calculated once again via Equation 6.1 as $\bar{x}_1$. The iteration then proceeds for each step n as follows: shrink the radius to $r_n = f_{shrink} \cdot r_{n-1}$, reduce the particles to only those k within $|x_k - \bar{x}_{n-1}| < r_n$ and then from these calculate $\bar{x}_n$. Here, a shrinking factor of $f_{shrink} = 0.975$ as given by Power et al. (2003) is chosen.

To determine when a stable center-of-mass is found, break-off conditions are applied. An important such condition is to ensure sufficient particles within the final circle (to avoid statistical fluctuations) where here a minimum particle number of 1000 is chosen (akin to the limit chosen by Power et al. 2003). If the number of particles were to drop below this value, the algorithm breaks and returns the prior center-of-mass found. Considering, however, that the smallest clusters of the sample still contain on the order of 1×10^6 particles within their initial cylinder, the iteration is very unlikely to break due to this limit.

Instead, there is a further secondary break-off condition: if the center-of-mass varies very little between steps, it can be assumed to be sufficiently stable. As box 2B has a softening length for dark matter of $3.75\,\text{kpc}\,h^{-1}$ at $z = 0$ (Dolag, 2022) – or equivalently $z = 0.252$ $x_{soft} = 2.6\,\text{kpc} - r_{min} = 8\,\text{kpc}$ is chosen as a sufficiently small length for the breaking point. If the center-of-mass shifts on this order or less, so $|\bar{x}_{n+1} - \bar{x}_n| \leq r_{min}$, this shift is negligible compared to the general resolution itself (less than 4·) and thus we break the iteration and output the final two-dimensional center-of-mass.

The final parameters then are an read-in radius of r_{vir} which shrinks with each iteration by a factor of $f_{shrink} = 0.975$, initially centered on the most-bound-particle but then shifting with each step, breaking off if the found center-of-mass is moving very slightly or if too few particles remain. After this new two-dimensional center-of-mass $\bar{x}$ is found, the particles are read out once more but this time within the same cylinder as described above centered instead on $\bar{x}$. Taking the example cluster from Figure 6.1, the resulting surface density map is depicted in Figure 6.2. It should be kept in mind that this step alone can already result in very large differences when considering how close substructures are to the center of the cluster, where in three-dimensional they could be quite far from this center but in projection appear much closer – in the case between Figure 6.1 and Figure 6.2, the shift is on the order of 20% of r_{vir}.

6.2   From Large to Small Structures

We then turn to the primary focus of this thesis: the substructures of the galaxy cluster. It is very important to note here again that "substructures" here means "structures within a single aperture" – these need not be actual, self-bound structures. As these are projected structures the data used transitions from the direct particle data to instead using the gridded maps. Visually speaking, in particular the stellar map allows a relatively straightforward identifying of clear massive substructures due to its more peaked distribution. In comparison, the total mass map is dominated by dark matter, and the flatter density profile of the main halo results in a more diffuse image as can be seen in Figure 6.2. Either map could be used to identify the substructures but for the purpose of this work the stellar mass map is chosen, due to the
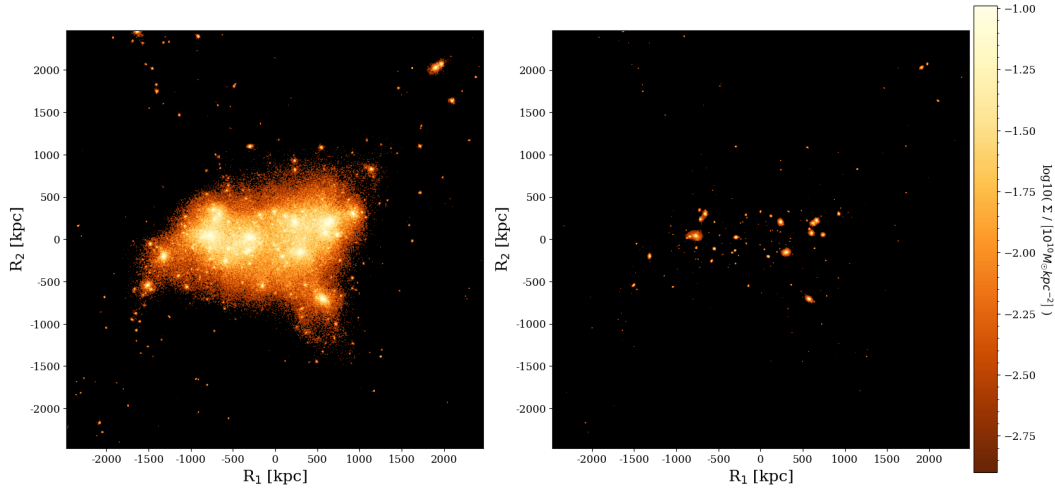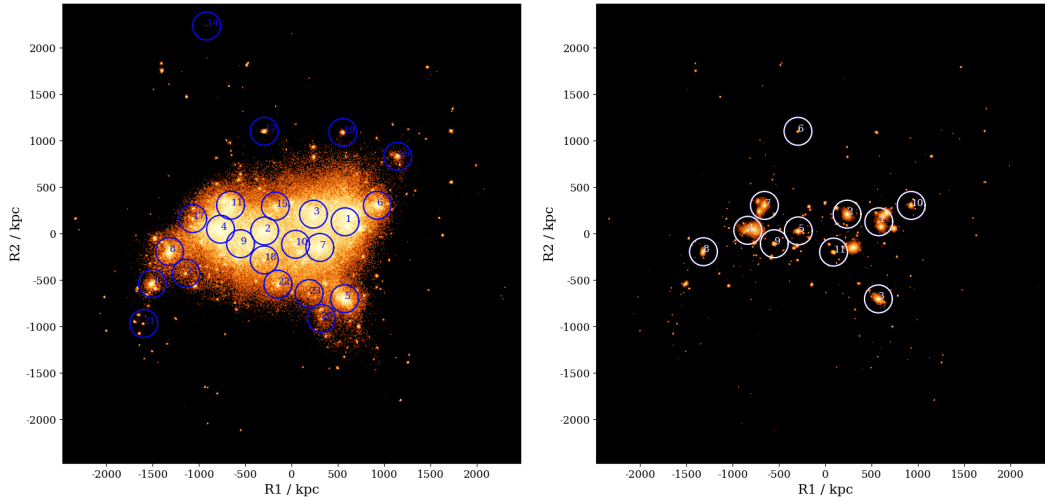
Figure 6.2: The total (left) and stellar (right) surface density map of galaxy cluster 20 of the "giants" in projection centered on its two-dimensional center-of-mass determined from the total mass. As in Figure 6.1, a region of boxsize $2 \cdot r_{\mathrm{vir}} \approx 2 \cdot 2.47\,\mathrm{Mpc}$ is depicted with the direction of the line-of-sight in code coordinates along $[0.03; 0.99; -0.17]$.

fact that when placing the smaller galaxy-scale over-densities for their lensing models, by necessity observers use images to determine the locations, and these images trace the stellar mass – see for example Jauzac et al. (2016), .

6.2.1   Using a Simple Cutoff

An initial simple method to determine these over-densities is to set a cutoff value for the surface mass density of the pixels, and select any that lie above this cutoff. Once a substructure is found, we then assign a surrounding area to it, that is to say an aperture of radius r_{aperture}. This area should be large enough to ensure that most of the massive central area of the substructure is captured, so as to avoid oversampling a single structure with multiple apertures, while not being too large to where it covers multiple distinct substructures. Distinct is taken here to mean separated sufficiently in the plane perpendicular to the line-of-sight, as by the nature of projections it is unavoidable that multiple self-bound structures can and will end up in a single aperture if they are projected on top of each other along the line-of-sight. This is also the case for the results obtained from lensing observations. For sake of simplicity and consistency, a fixed aperture size for each mass bin of the galaxy clusters is chosen.

A further condition is that these apertures should not be overlapping too strongly, as then the same mass contributes multiple times to what should be different structures. However, setting a hard border, that is to say any aperture may not have *any* overlap with former ones, can easily lead to the blocking of what should be two substructures that happen to be separated by a distance that is only marginally less than $2 \cdot r_{\mathrm{ap}}$. An observer may in this case simply choose a smaller aperture for their object, as they could differentiate the two structures, but as a large range of clusters and projections are considered here it is not feasible to manually decide on aperture sizes for each orientation. Furthermore, varying aperture

Figure 6.3: The total (**left**) and stellar (**right**) surface density map of galaxy cluster 20 of the "giants" in projection centered on its two-dimensional center-of-mass determined from the total mass as in Figure 6.2. Circles denote the apertures placed determined via a simple cutoff based on the total (blue) and stellar (white) surface density map, with numbers indicating the order in which the apertures are placed.

sizes would prohibit consistent comparisons between the projections, and as such a marginal overlap of the apertures is allowed to ensure a degree of flexibility in their placements. The hard minimum distance of a new aperture to all former ones is chosen as $d_{min} = 2 \cdot \sqrt{3}/2 \cdot r_{ap}$, ensuring that while two apertures can overlap there will be no point that is simultaneously overlapped by three of them - see Appendix A.4 for a further explanation of the details.

As for the order of placing these apertures, it is then sensible to go from the most massive to least massive pixel, such that the apertures which are placed first are also more massive and therefore of greater importance for the overall mass distribution. The resulting apertures can be seen in Figure 6.3.

6.2.2   SUBFIND Motivated

An alternative method would be to begin with the subhalos identified from SUBFIND, first cutting them based on which subhalos fall into the read-in volume of the cylinder and then utilizing a stellar mass cut to leave only the more massive subhalos, referred to here as the "subhalo" method. The aperture is then placed at the location of the most-bound-particle of each respective subhalo, again in order of their surface mass density values, with higher densities placed first. The subhalo method has the advantage of being able to guarantee that each aperture contains a real, bound subhalo of at least some stellar mass cutoff. This also allows for a consistent number of initial possible aperture positions for each cluster, avoiding a strong dependence on the explicit projections. If a cluster has n subhalos fulfilling the stellar mass cutoff, every projection will start with these n possible initial aperture positions, where in contrast a cutoff may produce any number more or less pixels above the chosen pixel surface mass density cutoff than another, though the final number of apertures placed can still vary for the subhalo method based on how many subhalos are projected sufficiently
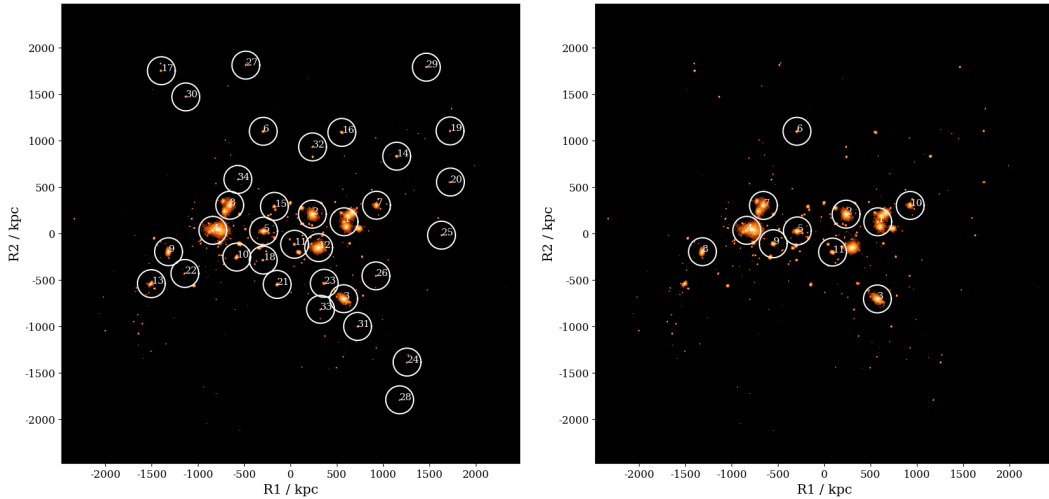
Figure 6.4: The stellar surface density map of galaxy cluster 20 of the "giants", with the apertures placed on the **left** as determined via the subhalo method as well as a convergence radius as described in Section 6.2.2 while on the **right** as in Figure 6.3 via a simple cutoff. Numbers indicate the order in which the apertures are placed. Up until aperture 6 the same apertures are found, where-after for aperture 7 of the simple cutoff (right), the most-bound-particle of the subhalo is apparently not the most massive pixel and thus is placed after other structures, such that a difference in ordering arises. This occurs again for aperture 11 on the right, where the simple cutoff finds a denser pixel in the upper structure (aperture 11 on the right) that must differ from the position of the structures most-bound-particle, such that instead the aperture is placed farther down for the subhalo method. This in turn allows for the subhalo method the placement of aperture 12 around the obvious substructure missed by the simple cutoff. Without an allowed overlap of the apertures, however, this substructure would once again be missed, illustrating both the difficulties arising from using single pixel values to sort the aperture placements (with this large substructure lacking a single very dense pixel and thus being missed) as well those that would arise when using hard borders for the apertures. Aside from the problem for the simple cutoff in identifying the obvious substructure found as aperture 12 for the subhalo method, the coverage of the most obvious substructures is comparable. It is noticeable that the chosen simple cutoff one the right does not produce the same number of apertures here as for the stellar subhalo mass cutoff on the left, as it is difficult to exactly compare a projected surface mass density with a bound absolute stellar mass.

close to where an aperture is not placed for one of them anymore. A comparison between this method and the previous simple cutoff for an example projection is illustrated in Figure 6.4.

It should be noted, however, that the subhalo method runs into the same trouble as with the center-of-mass in Section 6.1, where projection of the subhalo can create orientations with a noticeable distance between the subhalo's two-dimensional center-of-mass (where the aperture should be placed) and its point of least potential (where the most-bound-particle lies). To remedy this offset, instead a combination of both variants is employed. The initial selection of potential pixels is determined by the positions of the most-bound-particles of the SUBFIND subhalos which fulfill a stellar mass cutoff, but is then allowed to move in a second step onto the most massive pixel within a certain radius – more akin to how the simple cutoff finds aperture centers. This radius should be small so as to ensure the selection is still of the same substructure found by SUBFIND, but will be more robust against shifting centers-of-mass from projection effects. This "convergence radius" is chosen as $r_{\mathrm{conv}} = 22\,\mathrm{kpc}$.
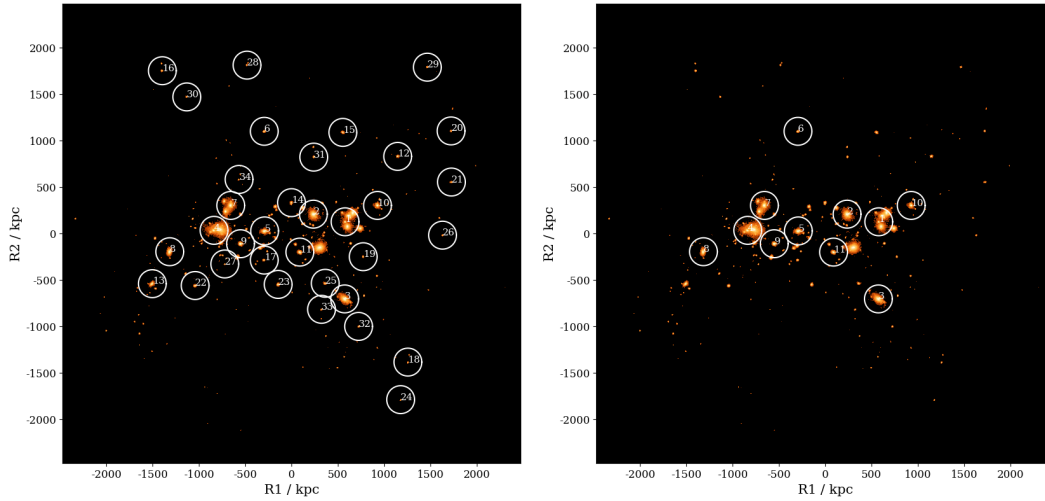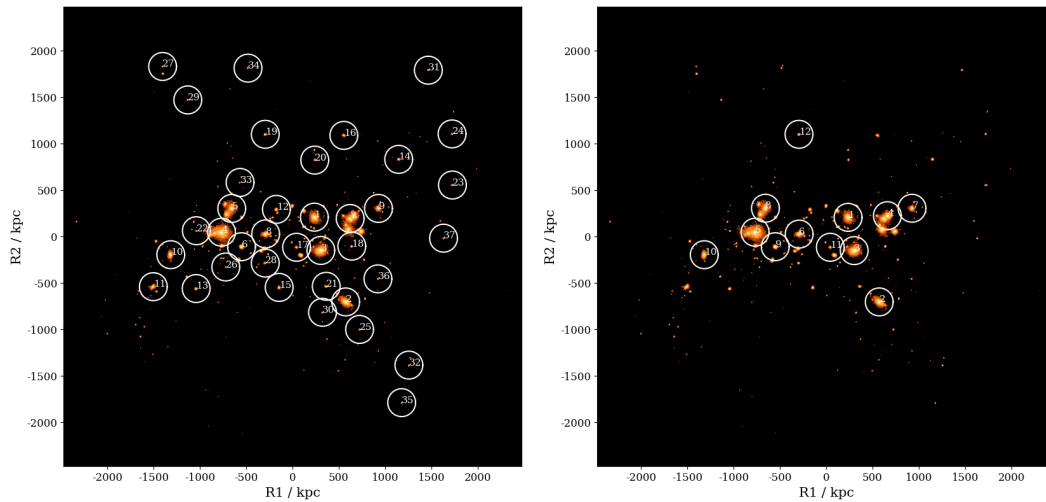
Figure 6.5: The stellar surface density map of galaxy cluster 20 of the "giants", with the apertures placed on the **left** as determined via the subhalo method as well as a convergence radius as described in Section 6.2.2 while on the **right** as in Figure 6.3 via a simple cutoff. Numbers indicate the order in which the apertures are placed. It can be seen that allowing the aperture centers to converge onto the nearby most dense pixel for this projection then leads to exact consistency between the simple cutoff and subhalo method. On one hand this is good as aperture 11 is now placed on a larger object compared to aperture 11 of the subhalo method in Figure 6.4, but on the other hand this aperture blocks the placement of the even larger substructure found there as aperture 12.

Nonetheless, the subhalo method also suffers from the possibility of finding a single very dense pixel of what is actually a less massive substructure and placing it first, which then blocks the placement of a more massive substructure that may by virtue of the projection lack such a singularly dense pixel – as happens when applying the convergence radius for the galaxy cluster depicted in Figure 6.5. To counteract this, instead of placing apertures in the order from most to least dense selected pixel, the summed values of the pixels *and their surrounding pixels* are sorted. The area selected for this summation is chosen as a 9×9 square with the initial pixel at its center. This ensures that even if a smaller substructure happens to have such a single very dense pixel, the larger substructure's selected pixel will have a higher surface mass density over the larger area and thus will be placed first. This summed ordering can be applied both to the simple cutoff and subhalo methods, with the resulting apertures of the example orientation depicted in Figure 6.6.

The final variant employed for the following parts of this thesis is the subhalo method with a convergence radius of $r_{\mathrm{conv}} = 22\,\mathrm{kpc}$ and apertures placed according to their summed surface mass densities in an area of 9×9 pixels.

6.3   The Main Halo

At this point, the center of the galaxy cluster has been found, the volume projected into a surface density map and apertures representing the substructures placed. It is possible with this to determine "aperture masses" by simply summing up all particles within each aperture, where the direct particle data instead of the pixel values are used to both ensure
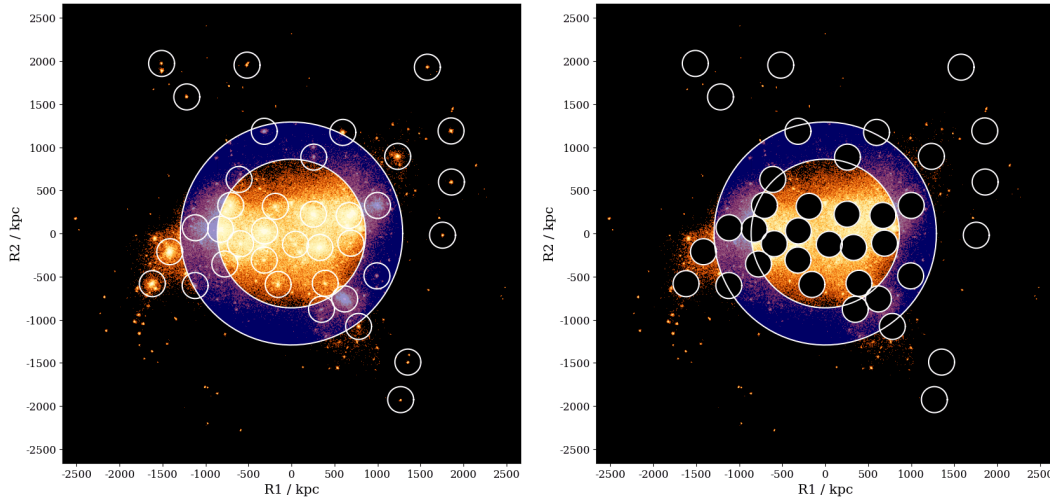
Figure 6.6: The stellar surface density map of galaxy cluster 20 of the "giants", with apertures from the subhalo method on the **left** and the simple cutoff on the **right**. The subhalo method further has a convergence radius applied to each apertures central position, and both methods' apertures are placed in order according to their *summed* surface mass density values as opposed to those of just their central pixel, as described in Section 6.2.2. Numbers indicate this order, with large differences visible compared to Figure 6.5 especially for the first few apertures. Most noticeable is the placement of aperture 3 for both, where indeed the previous difficulties of this massive substructure lacking a single strongly peaked pixel are now avoided. Generally, the ordering now better matches the visual size of the substructures, with both methods finding the same 12 apertures (although interestingly not in the same order).

more accurate masses as well as to avoid difficulties from fitting square pixels into spherical apertures. These "aperture masses", however, are not "substructure masses", as they contain all mass within the full cylinder – including contributions from the galaxy cluster's large dark matter halo as well as intracluster gas. It is therefore necessary to fit a density profile for the galaxy cluster itself and then subtract its contributions to each aperture mass.

As discussed in Section 5.3, many different profiles can be fit to the main halo which is dominated primarily by dark matter, with some of the more typical ones being the NFW- (Navarro et al., 1996) and Einasto-profiles (Einasto 1965 – see Equation 3.22). However, these fits are most commonly done with full three-dimensional data where instead lensing models apply to two-dimensional density profiles (see Section 5.2). As such, for better comparability here the particles are binned based on their two-dimensional, so projected, distance r_{2D} to the center-of-mass determined from Section 6.1.2, and additionally for the NFW profile a projected version considered (see Appendix A.2).

To determine which particles belong to the main halo, all particles within the cylinder are assigned an identifier. Then all particles within any apertures not overlapping the center are removed from the list based on their identifiers, and the remaining array of particles comprises the main halo. Apertures overlapping the center are treated as part of the main halo and subsequently not subtracted to avoid holes at the center-of-mass. This does not guarantee that the resulting aperture will also be the most massive substructure which is later considered the main – see Chapter 8. The remaining particles are then sorted based on

Figure 6.7: Left: The total surface density map of galaxy cluster 20 of the "giants", with apertures from the subhalo method including a convergence radius and summed pixel values. The blue shaded area illustrates an exaggerated radial bin for the main-fit binning where the surface density within equals the total mass divided by the total area, excluding any apertures. The same is depicted on the **right** with apertures blacked out – any remaining mass/area is attributed to the main halo.

their 2-dimensional distances and binned into equal mass bins, that is to say starting from the center the masses of the particles are summed to the each bin until a threshold mass is reached where then the next bin is started. This threshold mass can alternatively also constitute a threshold number of particles, or for both mass or number could be based purely on one of the particle species – i.e., only on dark matter, gas or stellar particles. The bins could also instead be defined purely by radii such that an unequal number of particles falls into each bin. Some of these considerations are further discussed in Section 7.3, where here instead the focus lies on the density profile chosen to be fitted to the output of the binning.

For the chosen case of equal-mass bins the selection criterion is mass based, but to determine densities it is necessary for each bin to know their radial extent. Further, subsequent bins should touch to be volume-filling but their natural borders defined by the particles within them do not unless particles from neighboring bins have the same radii. That is to say, there is initially some "empty space" between the maximum radius $r'_{n-1,\max} = \max(||x_{n-1}||_{2D})$ of the particles within a bin $n-1$ and the minimum radius $r'_{n,\min} = \min(||x_n||_{2D})$ of the particles within the next bin n. To remedy this, bin borders are placed in the middle of these two bordering particles,

$$r_{n-1,\max} = r_{n,\min} = (r'_{n-1,\max} + r'_{n,\min})/2.$$

For each bin n then a mass-weighted mean radius $\bar{r}_{2D,n}$ can be determined via Equation 6.1, which is then the first necessary part for the fitting to a main halo density profile. Using further the bin borders as well as the summed mass $M_n = \sum_i m_i$ in the bin and considering that each bin represents cylinder shells with volume $V_{cyl,shell} = V_{cyl,r_{max}} - V_{cyl,r_{min}}$, these values

can be converted into a density profile via

$$\rho(\bar{r}_\text{n}) = \frac{M_\text{n}}{V_{\text{cyl},r_\text{max}} - V_{\text{cyl},r_\text{min}}} = \frac{M_\text{n}}{z \cdot \pi \cdot (r_\text{max}^2 - r_\text{min}^2)}, \tag{6.2}$$

with z the total depth of the cylinder. As this depth is constant for every radius this simply adds a scaling factor to the density, which is to say the density and surface density profiles $\rho(r) \cdot z$ are identical in their form.

A further consideration must be made for this main halo density profile. Given that each aperture cuts out the particles, which are then not considered for the main halo density profile, the corresponding *area* should also not be considered when calculating the density as is illustrated in Figure 6.7. The exact calculation of this corrected area in each ring (or equivalently the volume of each cylinder shell) ascribed to each mass bin is given by Appendix A.4.

Figure 6.8 depicts the resulting radial density profile for two example clusters from the "giants" chosen to illustrate two extremes of the types of projected profiles that arise, with galaxy cluster 20 (on the top) going from a very flat profile into a steep drop-off while galaxy cluster 5 (on the bottom) transitions at a noticeably smaller projected radius into a more shallow outer slope. As can be seen from the two plots on the left, for galaxy cluster 20 the discrepancy between the total and main halo density profiles is significantly more noticeable than for galaxy cluster 5, indicating that the apertures mask noticeable overdensities for the former case while the latter contains most of its mass in a smoothly distributed large dark matter halo such that the density within the masked apertures is comparable to the density outside. The uncorrected masked density profile indicates the clear need of correctly accounting for both the masked mass *as well as* area, with up to half an order of magnitude in difference.

The two plots on the right of Figure 6.8 illustrate possible fitting functions to the corrected masked density profile, i.e., to the main halo profile. As can be seen, the Einasto-profile performs the best overall – though the projected NFW-profile fit is of comparable quality for the case of galaxy cluster 5 – which is attributable to its three free parameters allowing for a greater flexibility including a varying of the slope, something which both the three-dimensional and projected NFW-profiles cannot. The form of the projected NFW-profiles are given by Takada & Jain (2003) for a projection depth of r_vir and further discussed in Appendix A.2. It can also be seen that the fit projected NFW-profiles can result in strongly different concentrations to those determined through the concentration-halo mass relation given by Ragagnin et al. (2019), though they still lie within the possible scatter (in figure 2 therein). The same cannot be said for the concentrations for the three-dimensional NFW-profile fit of 1 and 0.7 for galaxy cluster 20 and 5, respectively, which simply demonstrates the projected nature of the main profile.

Given the Einasto fit for the main halo, the contribution in mass is calculated from the projected distance d_l between the center-of-mass to the center of each aperture l with a radius
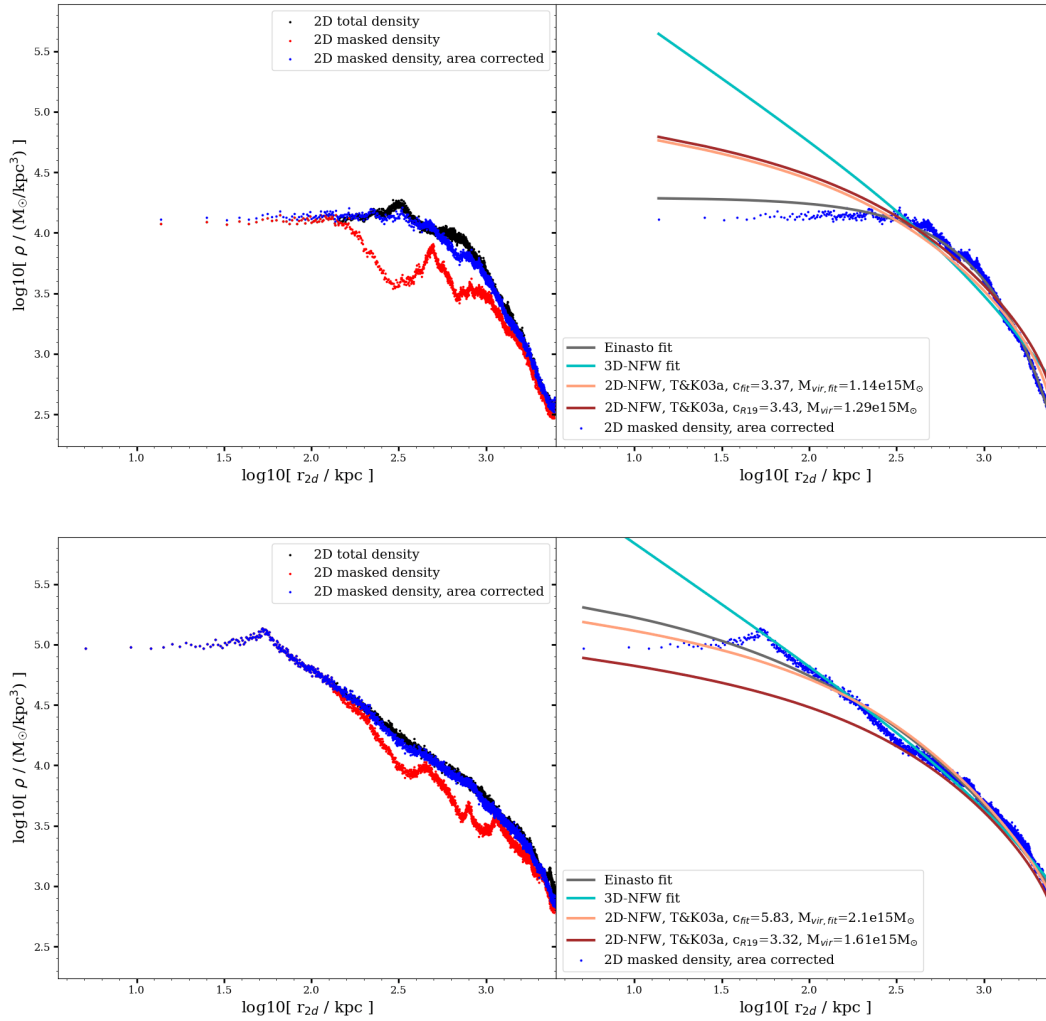
Figure 6.8: Left: The total (black) as well as masked (red) and corrected (blue) main halo two-dimensional density profiles for galaxy cluster 20 (**top**) and 5 (**bottom**) of the "giants" with the orientation as depicted in Figure 6.7 and Figure A.12, respectively. **Right:** Einasto (gray), three-dimensional (cyan) and projected (orange) NFW-density profiles fit to the corrected main halo density profile, as well as the projected NFW-density profile (red) expected from the concentration-halo mass relation (Ragagnin et al., 2019).

r_{ap} as

$$M_{\mathrm{main,l}} = \rho_{\mathrm{Ein,fit}}(d_l) \cdot \pi r_{\mathrm{ap}}^2 \cdot z. \tag{6.3}$$

Additionally, the contribution from the mean density within the box to each aperture is subtracted, such that the final mass of an aperture is given as:

$$M_{\mathrm{ap,l}} = M_l - \left[\rho_{\mathrm{Ein,fit}}(d_l) + \rho_{\mathrm{mean}} \right] \cdot \pi r_{\mathrm{ap}}^2 \cdot z, \tag{6.4}$$

where M_l is the summed mass of all particles within the aperture. Further considerations accounting for the extended nature of the apertures – i.e., determining the contribution from the main halo according to the area-weighted mean radius of the aperture as opposed to simply its center – are discussed in Section 7.3.

6.4 Values and Scaling With Mass

As mentioned in the beginning of Chapter 6 for the purpose of this thesis four mass bins are considered, each containing 29 galaxy clusters. To ensure consistent behavior within each bin, constant values for the necessary parameters of the method are used. These parameters are the aperture radius r_{ap}, the convergence radius r_{conv}, the pixel size of the maps r_{pix} and the stellar mass cutoff of the subhalos used for the subhalo method $M_{*,\mathrm{sub,cut}}$. Furthermore, to compare the individual aperture masses to a projected total mass of the halo, as the aperture radii are also fixed per mass bin, a fixed radius r_{tot} is chosen centered on the projected center-of-mass where all mass within it is summed up as a measure of the projected galaxy clusters total mass M_{tot}.

For scaling between the different mass bins, given the choice in cylinder radius of r_{vir} all other parameters should scale in a similar fashion, where then M_{vir} is used as the basis for this scaling factor. As the giants constitute the highest mass range of the box they have a significant unavoidable scatter in mass. For the other mass bins, however, there are sufficient galaxy clusters within the mass ranges such that it is possible to tightly constrain the virial masses to ensure that using a single set of parameters for the medium, small and tiny mass bins, respectively, is reasonable. Finally, given the mass dependence of the turnaround radius r_{turn} as defined by Equation 2.43, the depth of the projection is already intrinsically scaled.

Then the set of parameters used as the basis for scaling are those of the giants, with mass parameters scaling for the medium, small and tiny mass bins proportional to

$$f_{\mathrm{m,scale}} = \bar{M}_{\mathrm{vir,i}}/\bar{M}_{\mathrm{vir,giants}}, \tag{6.5}$$

while the length-scale parameters then scale as

$$f_{\mathrm{r,scale}} = \sqrt[3]{f_{\mathrm{m,scale}}}. \tag{6.6}$$

The resulting parameters are listed in Table 6.2, with the only exception being the scaling of the stellar mass cutoff for the mass bin "tiny" as here the correctly scaled mass, $M_{\mathrm{sub,cut,tiny}} \approx 3 \times 10^9 \, \mathrm{M}_\odot$ is near the box resolution of box 2b. This can be seen from considering the mean stellar mass given by Dolag (2022), accounting for the fact that each gas particle can spawn up to four stellar particles, such that $\bar{M}_* = 1.4 \times 10^8 \, \mathrm{M}_\odot \, h^{-1}/4 = 4.97 \times 10^7 \, \mathrm{M}_\odot$. To constitute a reliable halo, at least 100 stellar particles should be contained within as can be seen in Figure 7.3, and consequently a hard lower cutoff of $M_{*,\mathrm{sub,cut,tiny}} = 5 \times 10^9 \, \mathrm{M}_\odot$ is chosen.

6.5 Taking Inventory

This chapter has extensively developed a method to determine properties of substructure within galaxy clusters while accounting for projection effects. To this end, Section 6.1 has discussed how the projections are made, finding a significant difference between the projected

Table 6.2: Overview of the relevant parameters for each mass bins used. Each mass bin is scaled relative to the "giants" according to their relative mean virial mass. The stellar mass cut used throughout is $M_{*,\mathrm{sub,cut}}$, with the alternative cut discussed more in Section 7.2. Note that the hard minimum for distances between aperture centers, $d_{\min} = 2 \cdot \sqrt{3}/2 \cdot r_{\mathrm{ap}}$ as discussed in Section 6.2.1, scales automatically with r_{ap}.

	Giants	Medium	Small	Tiny
$f_{\mathrm{m,scale}}$	1	0.381	0.152	0.076
r_{tot} [Mpc]	1.3	0.942	0.694	0.551
r_{ap} [kpc]	150.0	109	80.1	63.6
r_{conv}[kpc]	25.0	18.1	13.4	10.6
r_{pix} [kpc]	2.0	1.45	1.07	0.848
$M_{*,\mathrm{sub,cut}}$ [$10^{10}\mathrm{M_\odot}$]	4.0	1.524	0.609	0.5
$M_{*,\mathrm{sub,altcut}}$ [$10^{10}\mathrm{M_\odot}$]	11.233	5.663	2.636	0.593

and three-dimensional centers-of-mass. Using the projected maps, Section 6.2 defines the method of substructure identification via initial positions from the structure finder SUBFIND (Dolag et al., 2009), which are then locally varied to maxima in the projected stellar mass map. Substructures found like this are then masked, and the remaining mass in projection is found in Section 6.3 to best fit an Einasto density profile (Einasto, 1965). The subtraction of the main halo mass contributions then results in the final substructure masses. As multiple galaxy cluster bins across a magnitude of mass are considered, Section 6.4 summarizes the scaling of the method and the chosen input parameters.

Chapter 7

To Build a Castle, a Crane Has To Lift

Since this study strongly relies on identifying substructures a more thorough study of the identification process is necessary. This quantification is of great importance to understand the impact of the choices made on the final resulting properties. Therefore, this chapter will quantify some of the questions arising in Chapter 6 by illustrating finer details, with important sanity checks for the employed method. First, Section 7.1 will focus on the property of halos known as the maximum circular velocity, which on one hand comprises an alternative tracer for the subhalos that form the foundation of the subhalo method as described in Section 6.2. On the other hand, it is of particular interest as well for the discrepancy found in subhalo concentration Chapter 5. The latter is discussed in Section 7.1.1 and the former in Section 7.1.2. Section 7.2 will then further quantify the chosen tracer of stellar subhalo mass for the final method through consideration of two differing scalings, with a curious finding in the slopes of the cumulative subhalo abundances discussed in more detail in Section 7.2.1. Finally, the impact of different binning methods on the main halo fits, as well as the difference between bound and projected mass are discussed in Section 7.3.

7.1 The Maximum Circular Velocity

The natural choice of the stellar mass as a tracer for the substructures, due to it also coinciding with the placement of galaxy-scale lensing models – see Section 5.2 – may not actually be the best tracer of the total mass due to the large scatter in the stellar-mass halo-mass relation. Thus, it is interesting to consider the maximum circular velocity v_{max} of subhalos with two-fold purpose: first, to compare the values in the `Magneticum Pathfinder` simulation to those from observations, in particular from lensing, as there seems to exists a discrepancy as mentioned in Section 5.2.4. Second, for the sake of determining the initial positions of apertures, instead of using a stellar mass cutoff as described in Section 6.2.2, it is possible to use other tracers for the subhalo masses, one of which is v_{max}. This is especially interesting as v_{max} is found to trace the mass at infall, as opposed to the current mass of the halo (Boylan-Kolchin et al., 2012; Moliné et al., 2017), with the relation between the retained halo mass

versus retained maximum circular velocity found by Peñarrubia et al. (2010) being slightly more shallow than the $v_{\max} \propto M^{1/3}$ advocated for by Hayashi & Navarro (2003).

It is relevant for both cases to see how the substructure density profile relates to the circular velocity, as for the former the actual measurements made are of central velocity dispersions, not maximum circular velocities, while for the latter it is this correlation between the circular velocity and density profiles that gives insight into the overall compactness of the initial infalling halo. As shown by Klypin et al. (2016), both the Einasto and NFW profiles find a direct correlation between the concentration of a halo and its maximum circular velocity. In the simpler case for an NFW, the relation becomes, as per equation 20 from Klypin et al. (2016):

$$|v_{\text{circ}}|_{\max} \approx \sqrt{0.2162} \cdot v_{\text{vir}} \cdot \sqrt{\frac{c}{\ln(1+c) - \frac{c}{1+c}}}. \tag{7.1}$$

This means that the maximum circular velocity of an NFW halo of fixed M_{vir} has a minimum for a concentration of $c = 2.163$, and increases towards both higher and lower concentrations. As per the concentration-mass relation (Comerford & Natarajan, 2007; Ragagnin et al., 2019), this is equivalent to $v_{\max}$ increasing with concentration as very few halos have concentrations below 2. Given that Remus et al. (2013) find a total density slope of $\rho \propto r^{-2}$ to be a stable attractor, this behavior is expected to hold more generally. However, it is important to emphasize that the relationship between $v_{\max}$, c and M_{vir} is of a three-parameter form, such that generally with increasing halo mass the concentration decreases yet overall $v_{\max}$ increases. This is further complicated by the formation time of the halo, with earlier formation times generally corresponding to higher initial concentrations, as shown in Equations 6 and 7 by Jiang & van den Bosch (2016).

7.1.1   Comparing Compactness

As discussed in Section 5.2.4, recent lensing observations of substructure within massive galaxy clusters have found higher circular velocities, and thus higher concentrations, than those found in simulations (Meneghetti et al., 2020). One of the possible explanations could be the presence (or lack) of baryons. The inclusion of baryonic physics can lead to strong spikes in the central density due to a problem known as "overcooling", whereby cold gas accumulates towards the centers of halos leading to extreme stellar masses (Teyssier et al., 2011; Dubois et al., 2010). This leads to steeper slopes of the density profile even for the dark matter, as found for example by Remus et al. (2013) when comparing a set of 39 galaxies from Oser et al. (2010) between dark-matter only and hydrodynamic simulations, which in turn can then become steeper than those from observations. This can be regulated by including in particular AGN feedback (Teyssier et al., 2011), which lowers the central total density slope substantially to better align again to observations. This can be seen for massive early-type galaxies in Figures 2 to 4 by Peirani et al. (2019), where in particular the gas density flattens noticeably towards the center. As noted by Peirani et al. (2019), the inclusion of AGN feedback can however significantly extend the halo sizes, that is to say it is possible to

overquench the central cold gas and then produce too shallow density slopes. Similarly, even with AGN feedback depending on the implementation, it can occur in very gas-rich mergers that the baryonic density slopes will still strongly peak towards the center, as seen in Figure 7 of Remus et al. (2013).

For the case of subhalos in `Magneticum Pathfinder` the v_{max} values are given by the `SUBFIND` implementation by Dolag et al. (2009). Of note here is that v_{max} is determined purely from the dark matter particles, and does not correspond to an actual particle's velocity. Rather, in spherical shells originating from the most-bound-particle of each subhalo, the circular velocity is determined and finally its maximum stored as v_{max} (private corroboration). This therefore avoids any of the possible strong dependencies of v_{max} on the included baryonic physics (Dubois et al., 2010). On the other hand, as the baryons dominate the central mass distribution, they are responsible for higher v_{max} even when including AGN feedback (Bahé, 2021; Peirani et al., 2019). It is thus expected that the maximum circular velocities will lie under the observed values when determining them purely by the dark matter.

To test this, boxes 2b (hr), 3 (hr) and 4 (uhr) of the `Magneticum Pathfinder` simulation are used (Dolag, 2022). The chosen snapshot for boxes 3 and 4 is number 128 at $z = 0.137$, which is at a lower redshift than the galaxy clusters observed by Meneghetti et al. (2020), though considering that halos become more concentrated with time (Ragagnin et al., 2019) this should at most overestimate the maximum circular velocities in comparison. For box 2b, the latest available snapshot is number 31 at $z = 0.252$. The minimum mass M_{sub} for each box is chosen to be at least equal to 100 dark matter particles.
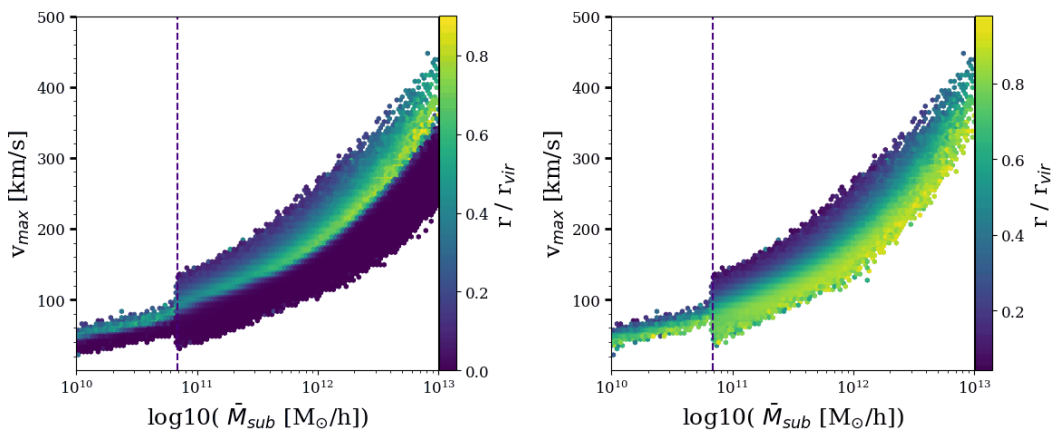
Figure 7.1: *Left*: The dependence of the maximum circular velocity on the total subhalo masses for boxes 2b (hr), 3 (hr) and 4 (uhr) of the `Magneticum Pathfinder` simulation. *Right*: The same, but with main halos removed. The vertical line in both represents the mass of 100 dark matter particles for boxes of resolution "hr". The higher resolution box 4 has a limit to the left of the borders of the depicted M_{sub} range. For both, the subhalos are binned and colored according to the mean distance to the host halo center.

As can be seen in Figure 7.1, v_{max} lies noticeably below the values of the observations, instead matching the distribution of the clusters from the Planelles et al. (2014) simulations analyzed by Meneghetti et al. (2020) as in Figure 4 therein. They are further comparable with values found in dark matter-only zoom simulations by De Lucia et al. (2004), as shown

in Figure A.13. The general behavior with radius is comparable to that found by Meneghetti et al. (2020), in that subhalos generally exhibit larger maximum circular velocities towards the center of their host halo, or alternatively that subhalos of equal v_{max} generally have less mass the closer they are to the center. Given that the main halos also lie where the subhalos with large radii are, this indicates that halos which fall into a larger halo experience stripping of their masses through processes such as tidal and ram pressure stripping (Hester, 2006), while at the same time largely keeping their v_{max}, mirroring the findings of Angulo et al. (2009). Subhalos farther out have yet to experience significant stripping, and lie in the relation akin to where a field galaxy would lie: on the purple lower track of the mains (Peñarrubia et al., 2008; Springel et al., 2008; Moliné et al., 2021). This is also the expected result from analytic models which, when considering just tidal stripping, find a decreasing subhalo mass with halo-centric distance (Han et al., 2016), and also from dark matter-only simulations, which find increased subhalo concentrations towards the center of the main halo (Diemand et al., 2007). However, Cautun et al. (2014) find that SUBFIND generally identifies less high v_{max} galactic-mass subhalos than the full phase-space structure finder ROCKSTAR (Behroozi et al., 2013), as per Figure B1 therein on the order of 10%. This clearly shows the need for a more thorough analysis of the impact of the structure finder on the properties determined for the substructures, to test the origin of the v_{max} tension between simulations and observations – be it physical or methodological.

7.1.2   Baryons and The Mass at Infall

The advantage of the chosen v_{max} definition lies in the ability to compare the dark matter-only and fully hydrodynamic simulation runs central dark matter density slopes, providing a more rigid tracer of the overall infall mass of a subhalo that is not as strongly dependent on the chosen baryonic feedback processes (Boylan-Kolchin et al., 2012). Furthermore, Muldrew et al. (2011) find that structure finding codes such as SUBFIND can struggle in recovering the full number of particles of a subhalo passing through or near the center of its main halo. It is by construction that density-based halo finders are strongly dependent on the local density, and subsequently will have more and more difficulty in identifying subhalos the closer these are to the center of their host halo. Conversely, v_{max} is found to be better conserved due to the fact that this velocity is reached at sufficiently small radii – at around $1.4 \cdot R_{1/2}$ as found for Magneticum Pathfinder at $z = 0$ by Teklu et al. (2018) and a significant amount of matter must be lost before it is affected (Muldrew et al., 2011; Peñarrubia et al., 2008).

In the following, the boxes 1a (mr), 3 (hr) and 4 (uhr) are analyzed, chosen to have a representative box for each resolution level commonly used by Magneticum Pathfinder. Snapshot number 128 at $z = 0.137$ is chosen for the comparison as this is a late snapshot where all boxes and their dark matter-only counterparts have data. To be able to then compare the fully hydrodynamical boxes to their dark matter counterparts, a halo matching algorithm is run.
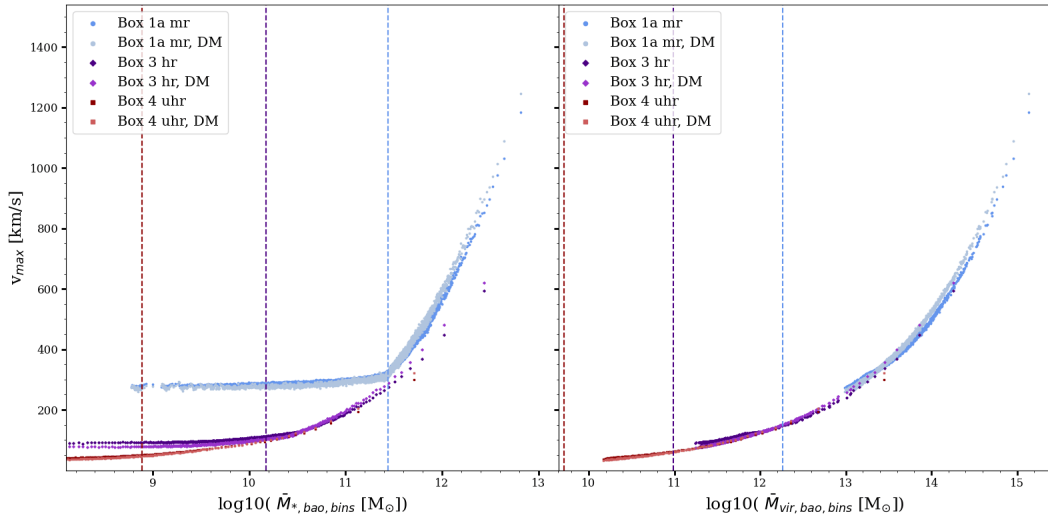
Figure 7.2: The maximum circular velocities of main halos for boxes of differing resolutions and sizes of the `Magneticum Pathfinder` simulation, plotted against the halo's stellar (*left*) or virial masses (*right*). Dark matter velocities are binned according to their virial mass matched hydrodynamical equivalents.

The algorithm reads every main halo's virial mass M_{vir} as well as its first subhalo's – its BCG's – maximum circular velocity. For the boxes containing baryons, the total stellar mass of the main halo is also read. The halos from the dark matter-only runs are then matched according to their virial mass to the halo with the nearest virial mass from the hydrodynamical simulation. Finally, the halos are binned according to either the stellar or virial mass of the matched halo into equal number bins of 100 halos each. The resulting distribution is plotted for all halos in Figure 7.2, with the maximum circular velocity on the y-axis and the stellar or virial mass on the x-axis with a logarithmic scale. The vertical lines denote the respective mass cutoffs for each resolution level, which are 100 gas or dark matter particles for the stellar or virial mass, respectively. As stellar particles do not have the same mass as gas particles, because a single gas particle can spawn up to 4 stellar particles, the vertical lines here then denote up to 400 stellar particles. It is best to mainly rely on the values above these cutoffs to ensure a statistically sound number of particles. There are a total number of 176 000 (319 900), 18 400 (46 100) and 8000 (18 300) halos which fulfill the stellar (dark matter) resolution-based mass cutoffs for Box 1a mr, Box 3 hr and Box4 uhr respectively.

The first observation of note is the overall good convergence between the boxes for the dependence on the virial mass on the right. There is no noticeable resolution-based effect taking place for the v_{max} measurements. A similar behavior is found for the relation between the dark matter-only and hydrodynamical simulations, although there does appear a trend towards higher v_{max} for the dark matter-only halos with increasing halo mass. More precisely, the relation $v_{max} - M_{vir}$ has a steeper slope for the dark matter-only boxes. It is unclear whether this is a real trend due to minor variations in the dark matter density slopes from the baryonic mass distribution, but it is found systematically for all boxes, i.e., also over

all resolutions. Given that the halos considered are all main halos, this minor discrepancy cannot be explained by differences in the amount of stripped matter.
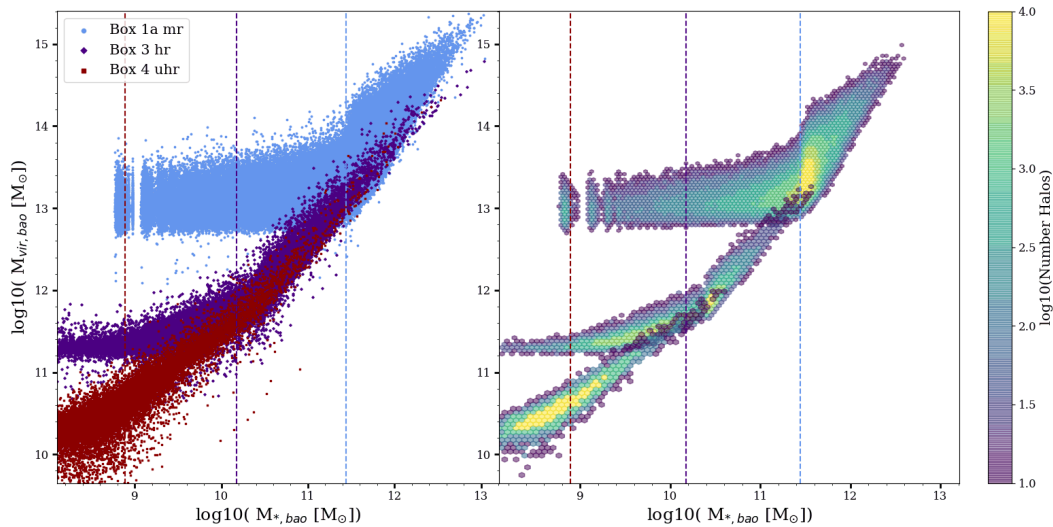
Figure 7.3: The relation between the stellar and halo mass for the main halos of boxes of differing resolution, with the *left* plotting each individual halo to better visualize the overall scatter while the *right* shows the binned number density.

This is found similarly for the $v_{\max} - M_*$ relation, as expected as the matching occurs through the virial masses. Here, however, a discrepancy between the boxes themselves is noticeable, with the higher mass end of the relation being steeper with decreasing resolution. Given the behavior of the virial mass, it stands to reason that this is entirely due to a change in the stellar-to-halo mass relation. To test this, the virial mass is plotted against the stellar mass for the hydrodynamical simulations in Figure 7.3. Indeed, there appears a discrepancy between the resolutions, with slight differences in the slope of the distribution beyond the vertical lines denoting the 400 stellar particle limit. Particularly striking is the almost vertical distribution for box 1a just beyond the blue line, as well as the angle of the break decreasing with increasing resolution. This demonstrates that subhalos containing less than 400 stellar particles are not resolved well enough to be included in any further analysis.

Overall, it can be seen that the $v_{\max}$ values in the hydrodynamical boxes in `Magneticum Pathfinder` are comparable to their dark matter-only counterparts, and furthermore that by considering only the dark matter component in their calculation, in case of fully hydrodynamical simulations, baryonic effects leave a negligible impact on them. They therefore can be used as a tracer for the total subhalo mass at infall as described by Peñarrubia et al. (2008) and Springel et al. (2008), and will be discussed in this context relative to the other possible tracer of the subhalo stellar mass $M_{*,\mathrm{sub}}$ in the following Section 7.2.

7.2   Cutting the Subhalos at the Right Point

The number of subhalos that are expected in a cluster from a given stellar mass cut is of great importance, as these halos are to serve as the origin for the placement of the apertures.

Undersampling of the subhalos would lead to overestimation of the main halo mass and subsequent reduction in the real subhalo masses, while noticeable oversampling would have the opposite effect. The number of massive subhalos relative to the main halo mass is plotted in Figure 7.4 for the chosen box 2b (hr), as well as for the most massive clusters of the higher resolution box 4 (uhr) for comparison. It can be seen that the number of massive subhalos steadily increases with virial mass from $1 \times 10^{13} \, \mathrm{M_\odot}$ to $2 \times 10^{14} \, \mathrm{M_\odot}$. Interestingly, this trend begins to flatten out approximately beyond $2 \times 10^{14} \, \mathrm{M_\odot}$, beginning a marginal decrease after around $3 \times 10^{14} \, \mathrm{M_\odot}$. The upper right portion of the distribution is rectangular in nature, which perhaps indicates that a larger box would find the trend continue towards the upper right unabated. Curiously, the highest number of subhalos that are massive relative to their host halo is found between $2 \times 10^{14} \, \mathrm{M_\odot}$ to $5 \times 10^{14} \, \mathrm{M_\odot}$.
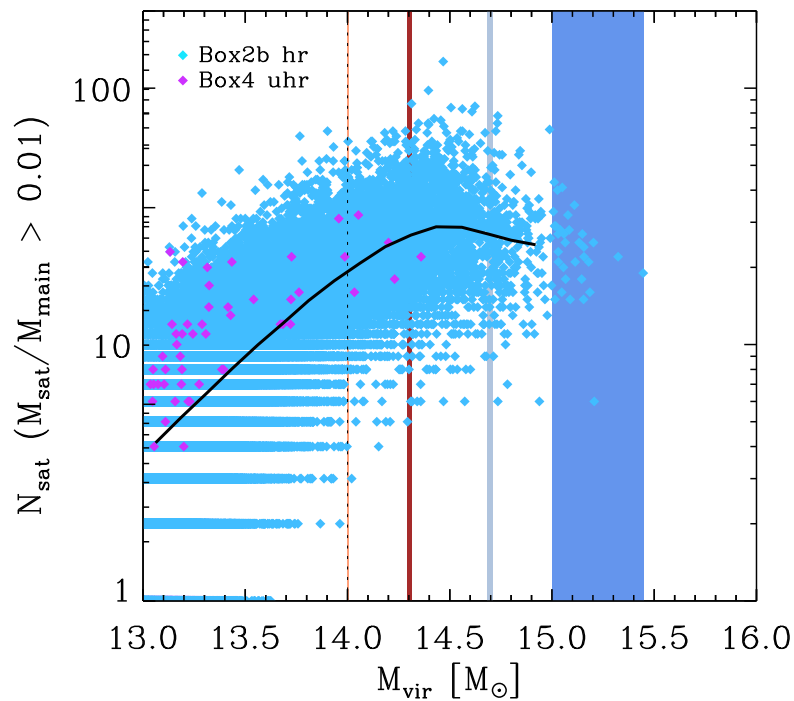
Figure 7.4: The number of subhalos with a mass above 1% of the main halo mass plottet against the virial mass of the galaxy cluster. The chosen box 2b (hr) is plotted in light blue and box 4 (uhr) is plotted in magenta. The black line denotes the running mean number, and shaded areas indicate the mass ranges of the four galaxy cluster mass bins chosen for the study. Plot courtesy of Rhea-Silvia Remus.

The chosen four mass bins for the galaxy clusters are depicted through the shaded areas. One can see that the expected variation in total number of massive subhalos is smaller compared to the overall scatter among each mass bin itself, with the more massive bins finding anything between 5 to 80 subhalos. The scatter in M_{sat} is slightly lessened for the smallest bin of the "tinies", which also have a slightly lower number of subhalos on average. The most massive bin, in turn, sees the most noticeable scatter in virial masses, owing to the fact that it comprises the 29 most massive objects in the box.

Another property to consider is the self-similarity of the subhalo tracers in the four mass bins. The possible tracers in question to identify apertures are the stellar mass $M_{*,\text{sub}}$ as per Section 6.2 and the maximum circular velocity $v_{\text{max,sub}}$ as discussed in Section 7.1. In Figure 7.5 the cumulative number of subhalos per cluster is plotted against the relative fraction of either tracer property to the main halo for the four mass bins. It is apparent that the cumulative subhalo abundance dependence on stellar mass fraction is very self similar between around 2% to 30% of the main halo stellar mass, with the lower mass bins bending off the self-similar line at earlier mass fractions. This is due to the resolution limit of the box, as can be seen in the stellar-mass halo-mass relation in Figure 7.3 – for box 3 with the same resolution (hr) the relation bends below around $2 \times 10^{10}\,\text{M}_\odot$. For the "tiny" mass bin $M_* \approx 2.4 \times 10^{12}\,\text{M}_\odot$, such that $1\% M_* \approx 2.4 \times 10^{10}\,\text{M}_\odot$, hence the bend. The higher mass bins subsequently bend off at a similar absolute stellar mass, ergo at a smaller stellar mass fraction.
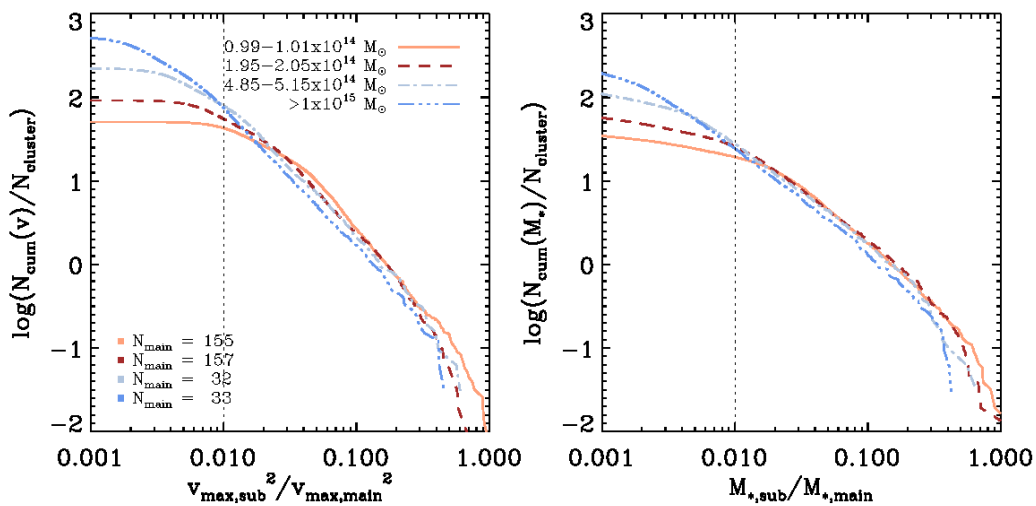
Figure 7.5: The cumulative subhalo abundance per main halo depending on the squared subhalo maximum velocity (*left*) or stellar mass (*right*) fraction of the main halo. The different lines represent the four mass bins. Plots courtesy of Rhea-Silvia Remus.

The maximum circular velocity on the left of Figure 7.5 behaves similarly, with the lower mass bins hitting the bend at higher fractions relative to the main halo v_{max}. As v_{max} traces the mass of the infalling halo (Peñarrubia et al., 2008; Springel et al., 2008), this flattening indicates a minimum halo mass below which there are no halos present in the simulation. The overall shape and values of the cumulative subhalo abundances for the "tinies" and "smalls" as a function of v_{max} are comparable to the ones found in dark matter-only simulations for a similar mass range by Jiang & van den Bosch (2016), with around $10^{1.7} = 50$ subhalos per main halo for $v_{\text{max,sub}}/v_{\text{max,main}} \geq 0.1$. Of note here is that the slope is initially steeper and then more shallow when going from high to low v_{max}, due to the presence of a bend in the distribution prior to the complete flattening. This appears also not to be present in other cumulative subhalo distributions of the maximum circular velocity, see for example Figure 10 from Springel et al. (2008). Consequently, these findings warrant a deeper look into the exact

composition of these halos at the low v_{max} end, which is done in Section 7.2.1, while here for now it can then be concluded that both $M_{*,\mathrm{sub}}$ and $v_{\mathrm{max,sub}}$ are adequate tracers for all mass bins. To better mirror the procedures employed for lensing analyses, for the further analysis the subhalo stellar masses will be used as a tracer for overdensities on which to place the apertures, as described in Section 6.2. This is because the locations of galaxy-scale overdensities in the lensing models are usually placed according to the visual positions (see Section 5.2), that is to say due to luminosity and color of the galaxies as done for example by Jauzac et al. (2016).

Given the choice of tracer, to better understand the direct number of halos fulfilling the stellar mass cut as defined in Section 6.4, the cumulative subhalo abundance is depicted in Figure 7.6 as a function of stellar mass. A noteworthy property is that for a given stellar mass the more massive galaxy clusters have a higher number of subhalos equal to or exceeding it, as can be expected. The left depicts as vertical lines the subhalo stellar mass cutoff for each mass bin scaled according to the virial mass of the objects in the bin following Equation 6.5. Due to the bend in the distribution caused by the resolution limit, this type of scaling leads to an unequal number of subhalos between the mass bins, with approximately 90, 80, 45 and 27 expected subhalos for the "giants" to "tinies", respectively.

The vertical lines in the right plot of Figure 7.6 in turn denote an alternative scaling for the subhalo stellar mass cut which will result in an approximately equal number of apertures for the galaxy clusters between each mass bin. Given a horizontal cut as $N_{\mathrm{cum}}(M_*)/N_{\mathrm{cluster}} = 10^{1.4} \approx 25$, the resulting stellar mass cuts are summarized in Table 6.2 as $M_{*,\mathrm{sub,altcut}}$. These stellar masses are generally higher than those scaled with the virial mass, the highest difference being for the "giants".
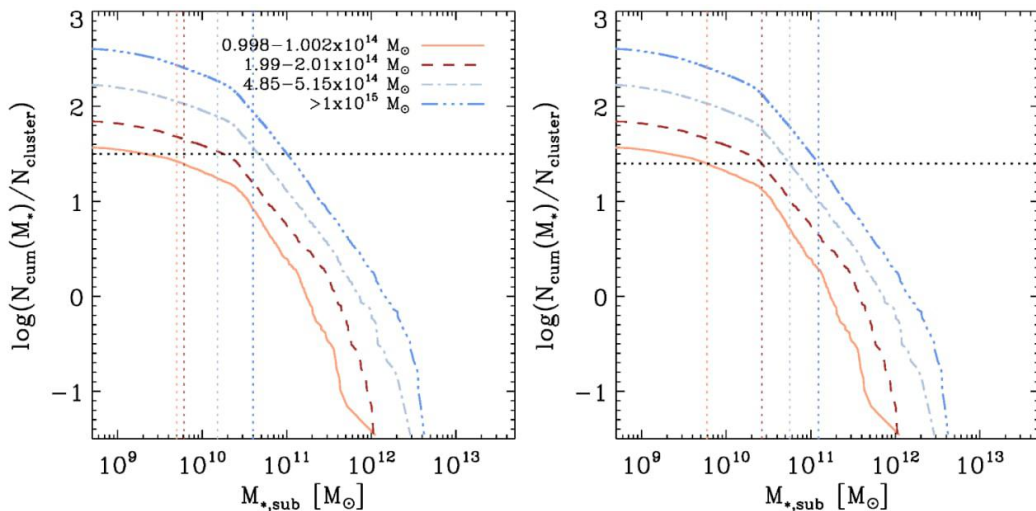
Figure 7.6: The logarithm with base 10 of the cumulative subhalo abundance per main halo in dependence of the subhalo stellar mass. Different colored lines represent the four mass bins. *Left:* Vertical lines denote the chosen stellar mass cuts scaled with the main halo virial mass between the four mass bins via Equation 6.5. *Right:* Here an alternative scaling for the stellar mass cuts is depicted by the vertical lines, scaled to guarantee an equal number of subhalos (around 25, as given by the black dotted horizontal line) between the mass bins on average. Plots courtesy of Rhea-Silvia Remus.

The actual resulting number of apertures must not, however, directly correlate to the number of initial positions. Due to the nature of the projection, should two subhalos fulfilling the stellar mass cut be close enough to have their apertures overlap, only one will be placed. The number of resulting apertures would thus on average be smaller than or equal to the number of subhalos fulfilling the stellar mass cut. This is complicated by the possibility of other massive halos being projected into the cylinders. The resulting number of apertures for either subhalo stellar mass cut are pictured in Figure 7.7, with the left depicting those scaled with the virial mass and the right depicting the alternative cut. A total of 200 random projections are run for each cluster, resulting in 5800 total orientations per mass bin.
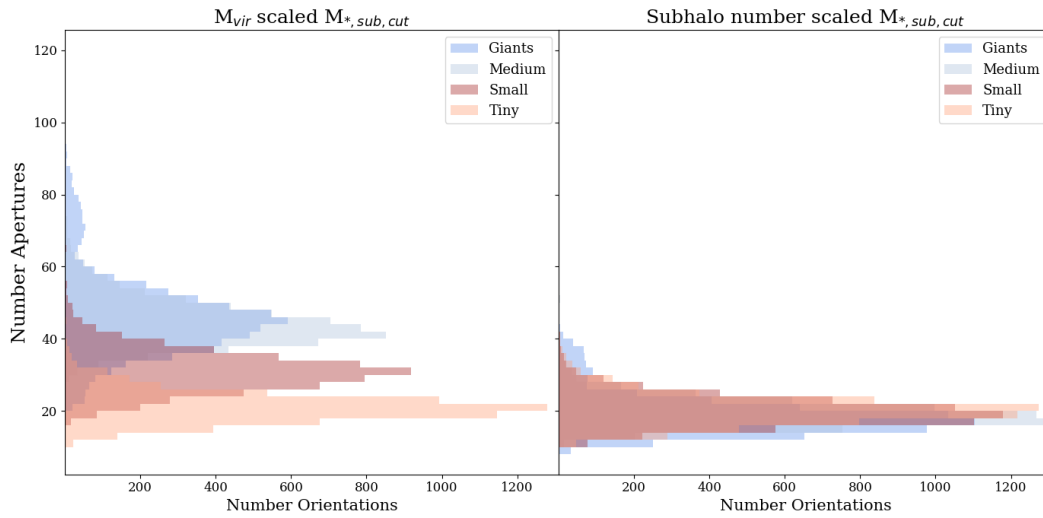
Figure 7.7: *Left:* The resulting number of orientations as a function of the number of apertures for each mass bin when applying the virial mass scaled subhalo stellar mass cut. *Right:* The same when using the alternative subhalo stellar mass cuts, scaled to find an equal number of initial aperture positions.

The number of apertures mirror the behavior in Figure 7.6, with the average number increasing towards the higher mass bins for the standard cut. Furthermore, the "giants" mass bin exhibits a noticeable second peak at around 70 apertures in a single projection which is absent for the other mass bins. This is caused by the two most massive clusters in the box, which for all 200 of their random orientations never finds less than 60 apertures. The next highest numbers of orientations with at least 60 apertures are found for "giants" galaxy clusters 9 and 5, with 43 and 14 such orientations, respectively. For the alternative mass cut the number of apertures found for the mass bins is rather similar from "giants" to "tinies", albeit it that the former once again exhibit a second peak at around 40 mostly comprised by clusters number 1 and 2. The resulting mean, minimum and maximum number of apertures are summarized in Table 7.1 for each mass bin and the differing subhalo stellar mass cuts.

As seen in Figure 7.7, the number of apertures per orientation is distributed approximately normal around the means for both cuts, with the maximum and minimum numbers of apertures for the virial mass scaled cuts being around double and half the mean, respectively. It is further apparent that the alternative cut succeeds in having an approximately equal number of apertures for each mass bin, though the fluctuations upwards can reach up to three times

Table 7.1: The number of resulting apertures per random orientation for the different subhalo stellar mass cuts, rounded to whole numbers.

	Giants	Medium	Small	Tiny
N_{ap}	M_{vir} scaled			
Mean	46	44	31	21
Minimum	19	28	16	10
Maximum	99	104	76	50
N_{ap}	N_{sub} scaled			
Mean	18	19	19	20
Minimum	8	10	9	10
Maximum	43	65	61	45

the average number as given in Table 7.1. Matching expectations, the overall number of apertures (19) is lower than the number of subhalos fulfilling the cut (25 by design) due to overlapping apertures. It is however doubtful if ensuring an equal number of apertures is even sensible, as by their nature more massive halos have a higher number of subhalos (van den Bosch et al., 2005).

7.2.1 What Halos Are These?

The curious double slope transition seen in the cumulative maximum circular velocity for each mass bin in Figure 7.5, where the v_{max} slope transitions into a more shallow slope first before entirely flattening out towards the lower v_{max} end can potentially have a simple explanation. As v_{max} is calculated from purely the dark matter, but the definition of a halo in SUBFIND requires a minimum *summed* number of dark matter and stellar particles (Dolag et al., 2009), it could be the result of a transition from sufficiently dark matter rich toward more stellar mass dominated halos. While there is a lower limit on the necessary number of dark matter particles to calculate a value for v_{max} above 0, namely at least 7, this is sufficiently small to where the potential well can be strongly influenced by the presence of baryons. Figure 7.8 shows on the left the mean number of dark matter (bold) and stellar (dashed) particles for the halos in each mass bin as a function of v_{max}, where this minimum number of dark matter particles to calculate v_{max} can be seen as the lower border. Above approximately $v_{\mathrm{max,sub}} = 100\,\mathrm{km\,s^{-1}}$ the number of dark matter particles present in a subhalo scales according to a powerlaw, which transitions into a more shallow slope once it falls below and then fluctuates strongly due to low number statistics at the lowest end. Interestingly, it is also around this point where the number of stellar particles begins to decline with increasing maximum circular velocity.

The right panel of Figure 7.8 clearly highlights that below 100 dark matter particles ($v_{\mathrm{max,sub}} = 100\,\mathrm{km\,s^{-1}}$) the number of substructures rapidly declines, indicating that stripping but also dynamical friction and harassment processes (see Section 4.3.1) can easily destroy subhalos with less particles. Thus such low particle-number subhalos cannot be considered
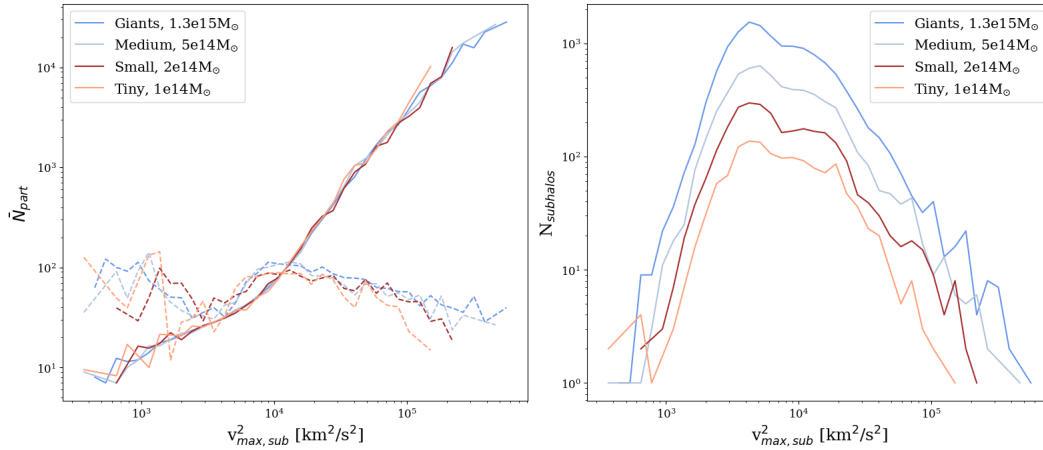
Figure 7.8: *Left:* The mean number of dark matter (bold) or stellar (dashed) particles in a halo as a function of the absolute maximum velocity of the subhalo for each of the four mass bins. The stellar particle numbers are determined from the stellar mass and as such to be treated with caution, as the actual numbers should be higher due to the mass loss with time of the stellar particles. *Right:* The absolute number of subhalos in dependence of the same. Both distributions are binned into 50 bins equally spaced in log-space.

complete number-wise in numerical simulations. The reliability of those which remain is questionable.

To see this impact resulting in the double transition of the slopes immediately in the cumulative subhalo abundance, Figure 7.9 plots the behavior for the "smalls" also split up into three types of subhalos: those with less dark matter particles than the minimum number 20 of particles required for a halo (i.e., halos that cannot be purely dark matter), those with at least 20 but below 100 dark matter particles which is the transition point into the steeper slope, and those with above 100 dark matter particles. As can be seen on the left, the high v_{max} end is completely dominated by the third subhalo type and their number of subhalos flattens out at a relative squared maximum circular velocity around 3% to 4%, which is exactly where the total subhalo slope transitions to the intermediate steepness. This intermediate slope is caused by the second group of subhalos which fall of less strongly in number with increasing v_{max} than the third group. The first group interestingly never reaches the same number of subhalos as the second, and all groups then flatten out towards the resolution limit on the far left, causing the flattening of the total subhalo slope and thus the second bend. As can be seen on the right of Figure 7.9, the behavior for the cumulative subhalo abundance based on the stellar mass is quite comparable, albeit it also becomes apparent that for the first and second subhalo type many subhalos at the low mass end are completely dominated by stars as their numbers do not flatten out as quickly as the total subhalo slope.

7.3   Alternative Main Halo Fits

Given the importance of a correct main halo mass distribution, this section will briefly analyze the impact of different binning methods on the projected main halo density profile, as well
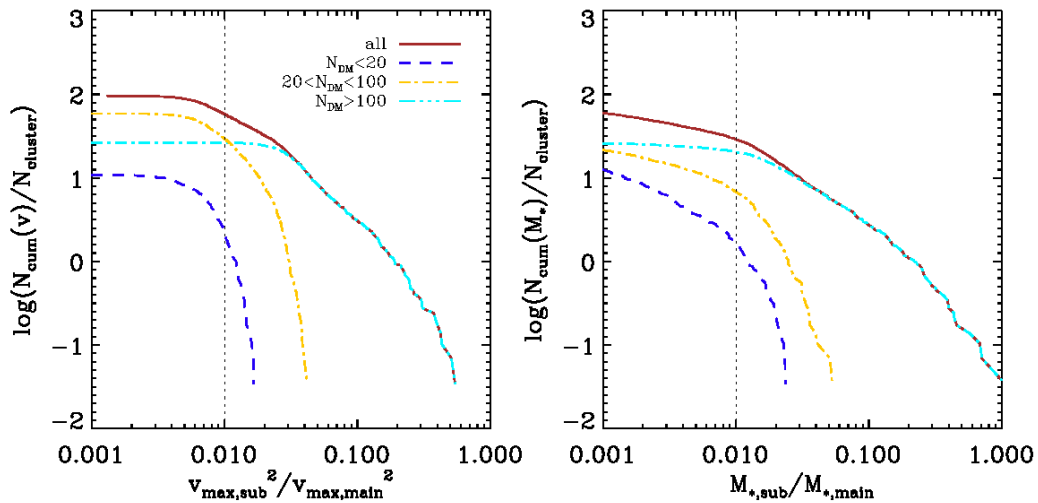
Figure 7.9: The cumulative subhalo abundance per main halo depending on the squared subhalo maximum velocity (*left*) or stellar mass (*right*) fraction of the main halo. Additionally, the subhalos are split into three groups based on their number of dark matter particles, and it can be seen that the overall behavior of the groups is similar between either tracer. Plots courtesy of Rhea-Silvia Remus.

as compare it with the profile determined purely from particles classified as part of the main halo by SUBFIND. Beginning with the binning methods, there are three variants which will be considered. The first is that of "equal-number" bins, where the radii and masses of the particles are sorted, typically from lowest radius to highest, and then grouped into bins by subsequently filling every bin with n particles before starting the next. Here the final bin can have a differing number of particles if the total number is not evenly divided by n. The second option, "equal-radius" bins, instead sets the bin borders at equidistant radii from the center, and sums up any particles within the borders of each bin. This can result in large fluctuations in the number of particles within each bin, with the center typically having a much higher number for density profiles such as the NFW-profile. The final option considered here are "equal-mass" bins, similar to the equal number bins except summing up the masses until a certain threshold mass is reached, instead of the particle numbers. For particles with equal mass, the methods are equivalent, but as there are gas, dark matter and stellar particles present this is not the case and the number of particles can vary per bin. Regions with more stellar particles will then have a higher number of particles, while regions with more dark matter have less.

For the cluster number 20 of the "giants", the three binning methods are plotted on the left in Figure 7.10 for the main halo surface density profile, with all being corrected for the masked area. The equal mass bins for the top left are the same as the blue profile shown in the top plots of Figure 6.8, plotted here in surface mass density to emphasize the point that the shape of the profile does not vary between density and surface density due to the fixed cylinder depth as mentioned in Section 6.3. It can be seen that these equal-mass bins in blue scatter the least overall for this case, with comparable scatter for all binning types between $\log(r_{2d}) = 2.6 - 3.2$. The equal-radius bins in red scatter the most at low and high radii, most

likely due to the large variances in number of particles in the bins there, while equal-number bins are generally comparable to the equal-mass bins. For a lower number of bins, that is to say a higher number of particles per bin for all methods, these statistical fluctuations become negligible and the binning methods converge.
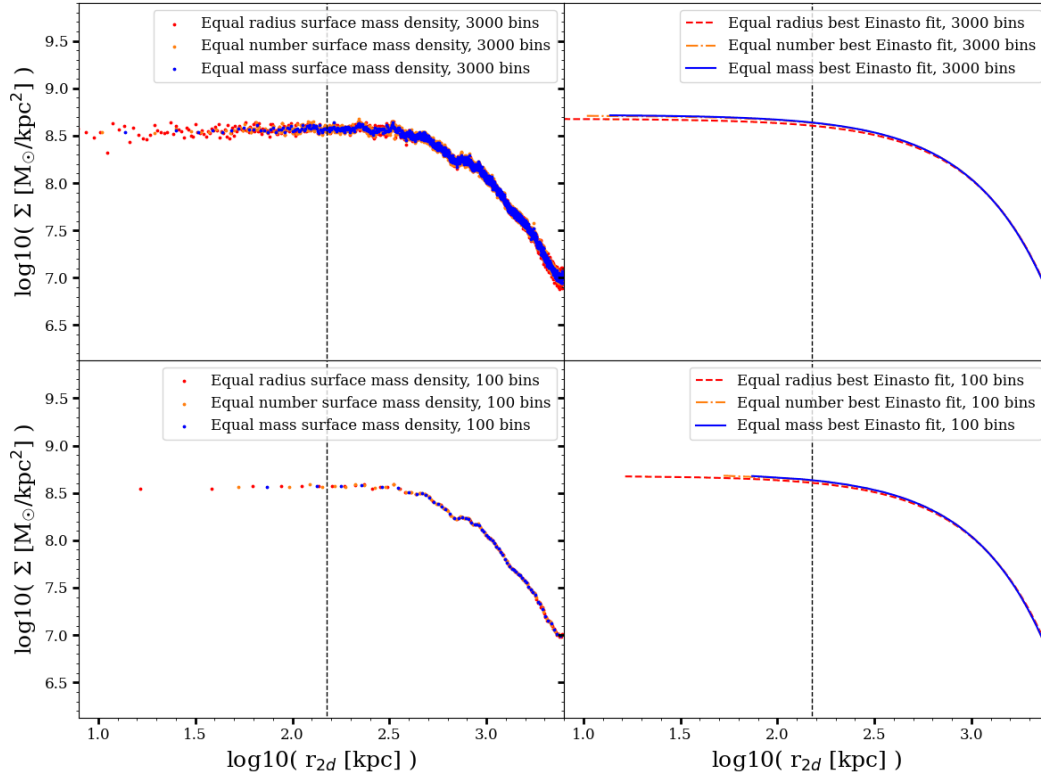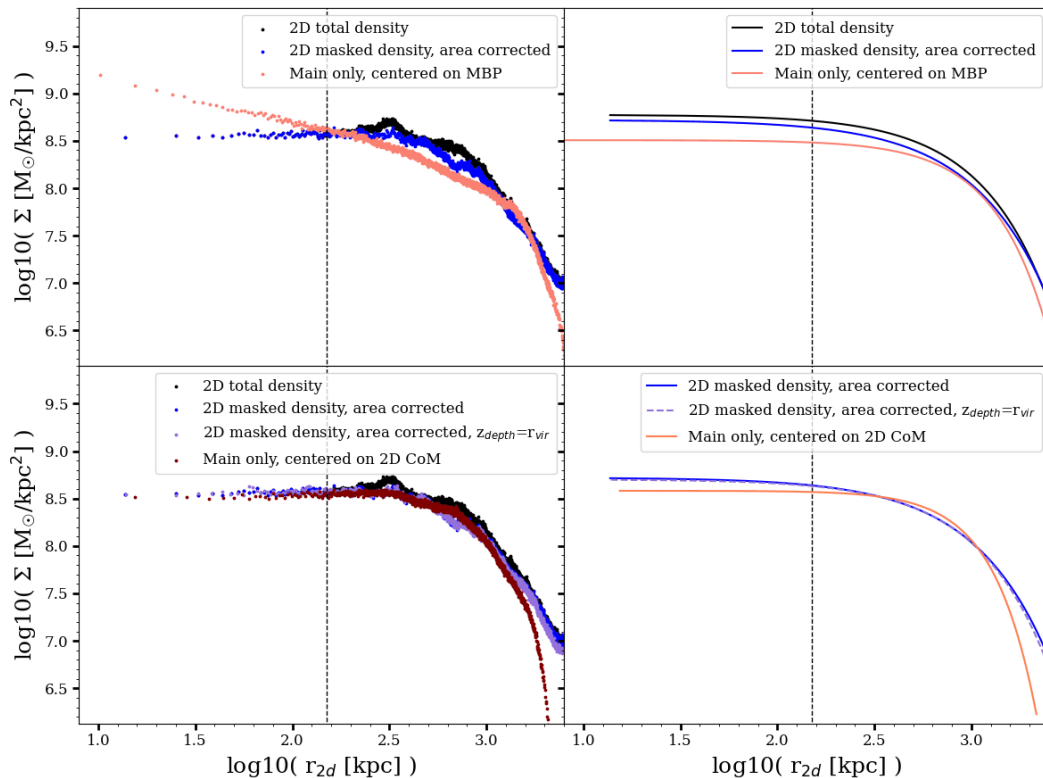

Figure 7.10: *Top:* The radial profile of the main halo surface density for different binning methods for 3000 bins, and the resulting best Einasto fits. The methods show very minor fluctuations for the surface density profile, with the fits being barely distinguishable except for the central region for the equal-radius bins. *Bottom:* The same, but for 100 bins. This removes the statistical fluctuations, showing practically no difference between the methods. The aperture radius of 150 kpc is denoted as a dashed black line.

As can be seen from the Einasto fits to the bins on the right panel of Figure 7.10, the global behavior is similar for all binning methods for both the 3000 and 100 bins, with the equal-radius bin lying marginally below the others toward the center. The main halo profile however only has a real impact for the "giants" beyond $r_{2d} > 150$ kpc, as any aperture lying within this range will be classified as the main and have no mass subtracted, and the minor differences in the binning methods become even smaller beyond this radius. The chosen binning method is then that of equal mass bins, though it is apparent that any of the methods would suffice.

It is then interesting to consider the impact that projection has on the number of additional particles being projected into the bin. To this end a projection is done once out to the usual depth of r_{turn}, as well as only out to r_{vir}. Additionally, this raises the question on the difference between the density calculated from the projected particles assigned to the main halo after the masking of the apertures and those actually bound to it. As such, for comparison, the

bound particles of the main halo as given by `SUBFIND` are also projected and binned into a surface density, once centered around the most-bound-particle and once centered on the projected barycenter. The resulting distributions and Einasto fits are plotted in Figure 7.11.

The profile of the bound particles centered on the most-bound-particle is found to be noticeably steeper towards the center than all the profiles centered on the projected barycenter. This shows that the choice of center is very significant to the shape of the resulting profile. More interesting is the profile of the bound particles centered on the same barycenter as the profiles determined via the method described in Chapter 6. Here, overall good agreement of the shape of the profiles is found, with the hump of increased surface density at $\log_{10}(r_{2d}[\mathrm{kpc}]) = 2.5$ being correctly masked by the method. In turn, the region at $\log_{10}(r_{2d}[\mathrm{kpc}]) = 2.8$ finds the masks also removing a portion of particles which `SUBFIND` assigns to the main halo. The largest difference, however, is in the outermost regions where the profiles of the bound particles have a stark drop-off which is not present in the projected profiles from the method from Chapter 6. This also results in the much more strongly curved Einasto fits on the right. This clearly shows that the choice of projected depth and subhalo masking as presented in Chapter 6 and used in the following analysis is reliable and therefore the results do not depend on the implemented binning and fitting method.

Figure 7.11: *Top:* The radial profile of the main halo surface density as determined once via the method as described in Chapter 6 and once for those assigned to the halo via `SUBFIND`. The latter are binned radially relative to the most-bound-particle as opposed to the projected barycenter. *Bottom:* The same but with the `SUBFIND`-assigned particles binned relative to the projected barycenter instead.

7.4   Tying up Loose Ends

This chapter has finalized the method as given in Chapter 6, discussing the maximum circular velocity v_{max} as an alternative tracer for the subhalo mass in Section 7.1. The radial behavior of v_{max} was found in Section 7.1.1 to agree with that found by Peñarrubia et al. (2008) and Springel et al. (2008), although the discrepancy in subhalo compactness noted by (Meneghetti et al., 2020) remains. Good convergence between the dark-matter only and hydrodynamical simulations was found in Section 7.1.2, confirming the usability of v_{max} as a stable mass tracer as found for dark matter only simulations by (Muldrew et al., 2011). Building on this, the behavior of both of the possible tracers $M_{*,\mathrm{sub}}$ and v_{max} within the galaxy clusters chosen was discussed in Section 7.2, finding both to be self-similar across the mass bins. $M_{*,\mathrm{sub}}$ was then chosen as the final tracer as this is found to be reliable and closer to observations (see Section 5.2), and the resulting number of apertures analyzed. The curious appearance of the double slope transitions found in the cumulative subhalo abundances in v_{max} was given a deeper look in Section 7.2.1, finding it to be due to a breaking point in the dependence of v_{max} on the number of dark matter particles present in a subhalo. Finally, Section 7.3 finds that the largest impact on the shape of the main profile is the choice of the center, with negligible differences between binning methods and only a marginal dependence of the profile on the projection depth. Furthermore, the masking of substructures leads to comparable fits for the Einasto profiles in the central regions to those determined by purely bound particles from SUBFIND, with the largest differences appearing due to the outermost regions beyond 1 Mpc.

Chapter 8

A Tale of Two Cities – Projected and Bound Masses

The recent observational findings by Jauzac et al. (2016) for the massive galaxy cluster Abell 2744 and the subsequent analysis by Schwinn et al. (2018) indicate that there exists a disconnect between substructure mass definitions from gravitational lensing to those of structure finders commonly used in cosmological simulations. For the sake of future joint investigations into substructures, which can provide insights into the dynamical state (Neto et al., 2007) and accretion history (Jiang & van den Bosch, 2016) of galaxy clusters as well as enabling tests for different potential dark matter variants (Bhattacharyya et al., 2021), it is therefore necessary to understand the relationship between three-dimensional and projected substructure masses.

After having laid the groundwork in Chapter 6 and Chapter 7, this chapter will cover the resulting differences using the cosmological simulation `Magneticum Pathfinder`. First, the language employed is defined in Section 8.1. Section 8.2 then provides an overview of subhalos' mass and radial distribution. These are compared to the projected behavior in Section 8.3 with an additional discussion on the impact of varying projection depths. Typical measures of the dynamical state of galaxy clusters are explored in Section 8.4. Section 8.5 then analyzes the behavior of individual substructures and their underlying bound subhalos. Using the findings as a basis, a conversion function between the two is derived and potential degeneracies with other parameters debated. Section 8.6 discusses reproducing Abell 2744 with Section 8.7 providing future outlooks concerning mass accretion and filaments. Finally, the findings are summarized in Section 8.8.

8.1   Defining A Language

For the sake of clarity, this section will cover commonly used terms. First, the output values are split into two groups: those originating from calculations based on the method in Chapter 6 and those originating directly from the structure finding algorithm `SUBFIND` (for details see Section 5.3). Common parameters from the latter are for the galaxy clusters themselves

the virial radius and mass, denoted as r_{vir} and M_{vir}, as well as the total friends-of-friends mass M_{FoF} and the particle at the deepest potential, the most-bound-particle, "MBP", that represents the center of the galaxy cluster. The primary subhalo property of interest is its mass, referred to throughout as M_{sub}, with indexes i indicating the subhalo number by mass defined in the following. A subhalo's position is given by its most-bound-particle through the SUBFIND parameter "SPOS", and is representative for the entire halo.

Properties for the overall galaxy cluster determined via the method in Chapter 6 are the projected barycenter denoted as "CoM", as well as the total mass within the large scale cylinder M_{tot}. Note that this is *not* the friends-of-friends mass from SUBFIND, which is often also assigned this designation. The masses of individual substructures, i.e., the masses in the apertures, are denoted either as M_{cyl}, $M_{cylinder}$ or M_{ap}, again with indexes i indicating the subhalo number by mass. Finally, $M_{subfind\ in\ cyl}$ is the mass of the most massive subhalo as found by SUBFIND whose "SPOS" in projection falls within the area of the aperture. Every aperture thus has a well-defined value $M_{subfind\ in\ cyl} > 0$, as the SUBFIND positions of subhalos fulfilling the stellar mass cut discussed in Section 7.2 are used as the origins of the apertures (see Section 6.2). The value is also sometimes defined as $M_{subfind}$ wherever greater brevity is necessary. Distances given are projected, 2-dimensional distances unless otherwise stated.

As a final note on the naming convention, halos or substructures within a galaxy cluster are numbered according to their mass to enable direct comparisons between the bound and projected masses. By this definition, for the SUBFIND masses the main halo is considered number 1 and the most massive subhalo is then number 2. Note that when plotted, for convenience the main halo is at the position "Subhalo #1". Similarly for apertures, the substructure with the highest mass is considered the "main halo" and subsequently the total subhalo mass fraction for both cases, f_{sub} or f_{cyl} respectively, is then the sum of all masses excluding the structure with number 1. A case can be made that for the projected masses instead the substructure at the center-of-mass should be considered the main, or alternatively the substructure which includes the most-bound-particle (i.e., which is overlapping the main halo as defined by SUBFIND). Both of these definitions can and also can not be equivalent to the most massive substructure. The chosen definition is used to enable a consistent differentiation of sub- versus main halos between the two methods, so that a subhalo mass content can be compared, even though the fixed size of the apertures by nature lead to more rigid definitions of mass compared to the variable extents of bound mass from SUBFIND.

8.2   A SUBFIND Consideration

To get an understanding of the clusters in each mass bin, a first impression of their substructure mass content can be gained by working with the SUBFIND output. Summing all subhalo masses as provided by the SUBFIND value MSUB and dividing by the total mass, the resulting distribution gives a measure of the mass contained in bound substructures versus that in the main halo. This is shown in Figure 8.2 for subhalos within one virial radius from the center of the cluster, defined by the most-bound-particle. There exists no clear trend between
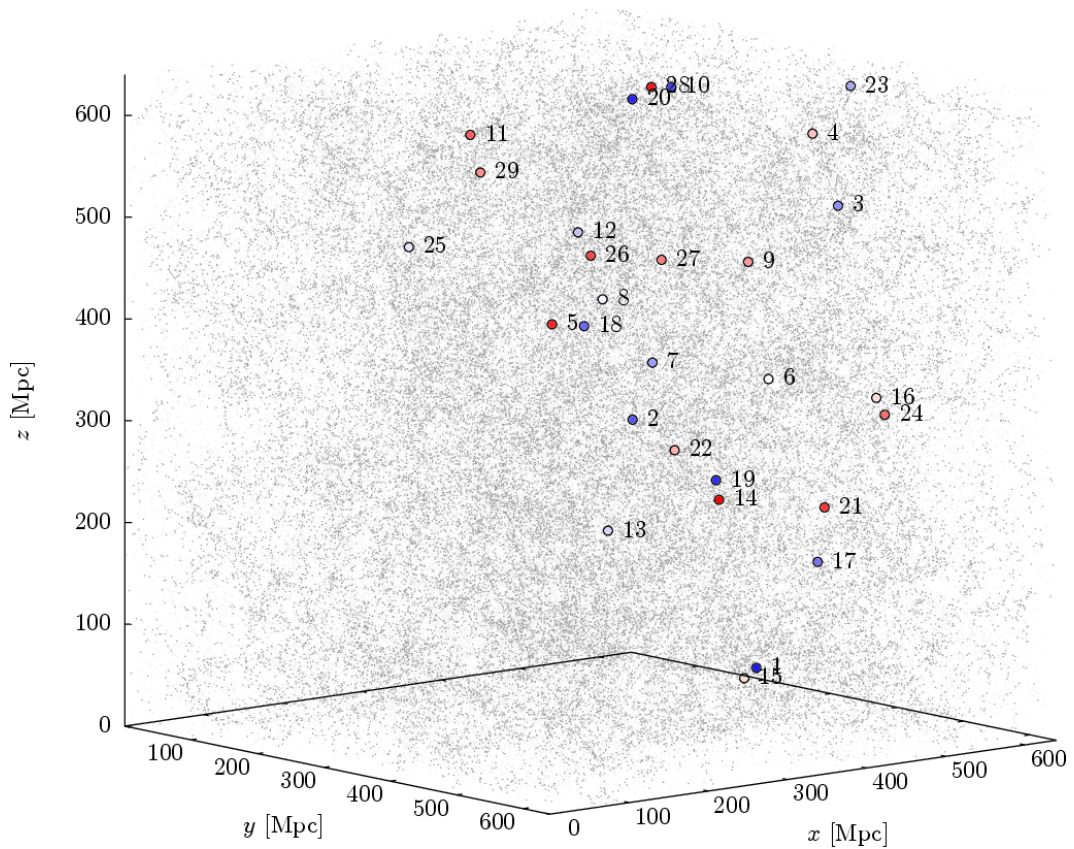
Figure 8.1: The positions of the 29 giants in the volume of box 2b. Plot courtesy Rhea-Silvia Remus.

the main halo mass and the summed subhalo masses for any of the mass bins. Though the outliers with very high subhalo mass fractions increase toward the smaller mass bins, most galaxy clusters of each mass bin have a summed subhalo mass between 5% to 10% of M_{vir}, somewhat lower than the values of 10% to 16% found by Jiang & van den Bosch (2017) for the dark matter-only simulations `Bolshoi` (Klypin et al., 2011) and `MultiDark` (Prada et al., 2012).

Instead, as seen from the left four plots in Figure 8.3, for all mass bins except the "giants", the total subhalo mass within r_{vir} is strongly dominated by that of the most massive subhalo, with extreme cases – galaxy clusters number 2, 2 and 4 of the "medium", "small" and "tiny" mass bins, respectively – having half of their total subhalo mass contained in this single subhalo. The case is not as clear for the "giants", where the distribution is more cloud-like in nature, that is to say the total subhalo mass is not carried as strongly by one subhalo for the most massive clusters in the box. This can also be seen from the median mass fraction of the subhalos by subhalo number on the right of Figure 8.3. The most massive subhalo for the "tiny" and "small" mass bins comprises a higher fraction of the total mass than for the "medium" and "giant" mass bins, a trend which holds true until the fourth subhalo. As can be seen on the right of Figure A.14, for higher subhalo numbers the mass bins converge to very similar subhalo mass fractions.

Taking a closer look at the subhalo mass fractions for galaxy clusters in the "giants" bin, the subhalos within the total friends-of-friends group are compared to those within a sphere
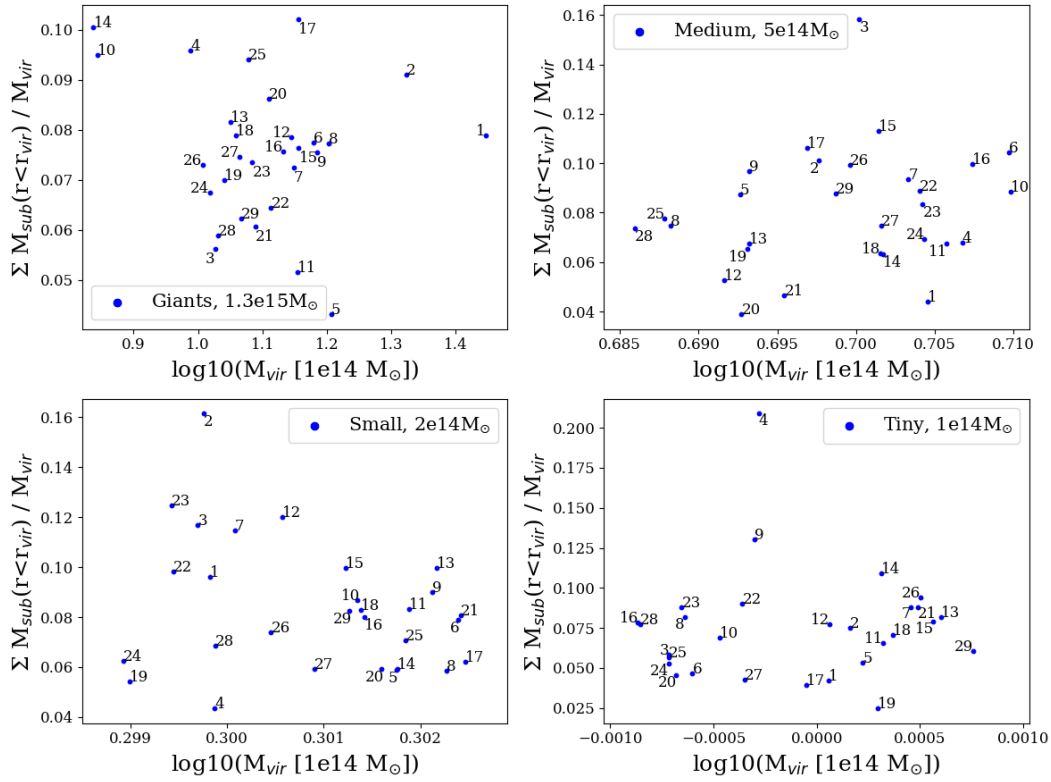
Figure 8.2: Relation between the fractional summed mass of all subhalos f_{sub} within one virial radius and the host galaxy cluster's virial mass for the four mass bins.

of radius r_{vir} in Figure 8.4. Subhalo mass fractions are quoted against the relevant mass of the galaxy cluster, either M_{FoF} for the former or M_{vir} for the latter. A stark contrast can be found between the two, with a splitting up of the total subhalo distribution on the left into galaxy clusters dominated by either one or two halos. On the right-hand side, all subhalos within r_{vir} have a mass of no more than $5\% \cdot M_{vir}$. This implies that for the extreme cases highlighted on the left, the massive subhalo is linked to the galaxy cluster's main halo through a bridge of sufficient density to be considered a single object by the friends-of-friends linking length discussed in Section 5.3, while being far enough away to where very little of its dark matter halo is stripped or misattributed to the main halo as can commonly occur (Muldrew et al., 2011). For example, the most massive subhalo of galaxy cluster number 3 with a mass of $M_{2,sub} = 16.4\% \cdot M_{FoF}$ lies at a distance of $r_{2,sub} = 2.1 \cdot r_{vir}$.

Interestingly, there is a slight difference between which galaxy clusters have the highest summed subhalo mass for the two ranges. Though there is general agreement, with the galaxy clusters 4, 10 and 14 having one of the highest four subhalo mass fractions for either case, the ordering is not the same as well as the fourth galaxy cluster being different, clearly demonstrating that the surrounding structure can be indicative of though not directly linked to the dynamical state.
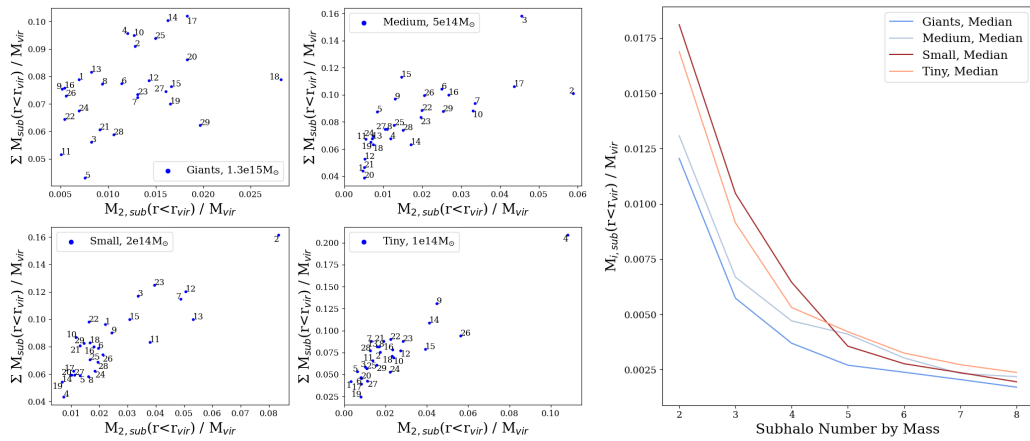
Figure 8.3: *Left:* The dependence of the total subhalo mass fraction on the mass fraction of the most massive subhalo for all four mass bins. *Right:* The median mass fractions of the most massive subhalos within r_{vir} as a function of their subhalo number as defined in the beginning of the chapter.

8.2.1 The Radial Trends

To further investigate the behavior of the subhalo masses, one important parameter to consider is a subhalo's distance to the main halo center. Due to dynamical friction (Chandrasekhar, 1943), more massive subhalos sink more quickly towards the center, where in turn, as already discussed in Section 7.1.1, processes such as tidal stripping more rapidly reduce the subhalo masses. This can be derived when considering both analytic models of tidal stripping (Han et al., 2016) as well as when analyzing directly the output of dark matter-only simulations (Peñarrubia et al., 2008; Springel et al., 2008). The result is that more massive subhalos more quickly lose mass, as found for example by Diemand et al. (2007) and Giocoli et al. (2008), with models of the mass loss given for example by Jiang & van den Bosch (2016) – though the mass loss also strongly depends on the orbit of the subhalo (Peñarrubia et al., 2010).

For all galaxy clusters in each mass bin, the subhalo total (top row) and stellar masses (bottom row) are plotted against their distance to the most-bound-particle in Figure 8.5 for all subhalos within r_{vir}. The thick black line of the top row denotes the best-fit line of the total subhalo mass as a function of subhalo barycentric distance to all subhalos, excluding the mains, and shows that the mass increases on average towards the outskirts. Furthermore, a plateau can be seen, becoming more prominent towards the outskirts. This plateau lies at a mass equivalent to 20 dark matter particles, and thus forms the lower bound below which the required 20 stellar or dark matter particles are increasingly provided by the stellar particles. The number of these halos increases towards the center as the dark matter of the subhalo is more easily stripped than the more dense stellar core. Surprisingly, when excluding these halos with less than 20 dark matter particles, the curve instead flattens out to find approximately equal subhalo masses at all radii, shown by the dashed line.

To further demonstrate that the stellar portion of the subhalo is less prone to being tidally stripped, the bottom row of Figure 8.5 depicts the stellar mass of the subhalos. The thick black line denotes the best-fit line for all subhalos and finds a much flatter behavior with radius than for the total subhalo mass, even slightly decreasing toward the outside. For halos
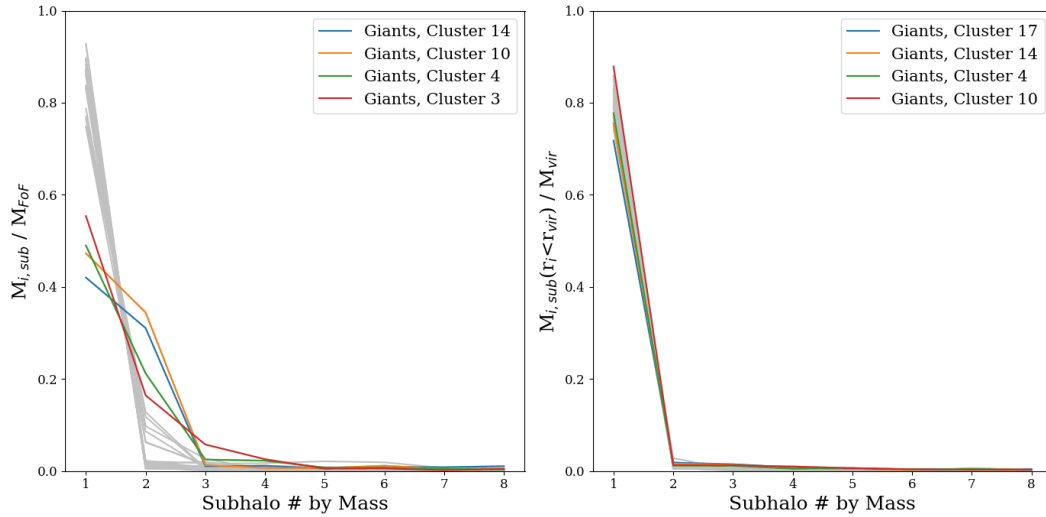
Figure 8.4: The mass fractions of the most massive subhalos within the FoF group (*left*) and within r_{vir} in three dimensions (*right*) as a function of their subhalo number for the 29 galaxy clusters of the "giants" bin. Mass fractions are relative to the friends-of-friends and virial masses, respectively. Highlighted clusters are in descending order the four with the highest total subhalo mass fraction, and the main halo is plotted as #1.

with at least 100 stellar particles, which is motivated as a lower bound for reasonably resolved halos from the findings in Section 7.1.2 and Section 7.2, the subhalo stellar mass stays almost constant with subhalo radius, seen from the dashed line. This further indicates that $M_{*,\mathrm{sub}}$ can be used as a reasonably consistent mass tracer for the subhalos at any radii (Niemiec et al., 2017) in addition to the arguments raised in Section 7.2.

The discrepancy between the behavior for the total matter on the top, which is usually dominated by dark matter, versus the purely stellar mass on the bottom, is indicative of the fact that the stellar mass is stripped significantly less than the dark matter, with the result that subhalos have an increased stellar mass toward the center relative to their halo mass. This can also be seen explicitly in Figure 8.6, where the ratio between the two is plotted for all galaxy clusters in each mass bin. Noteworthy is the relatively flat behavior from 1 to $0.5 \cdot r_{\mathrm{vir}}$ with a subhalo stellar- to halo-mass ratio of around 10%, comparable to the 10% to 20% found for the general stellar mass-halo mass relation of galaxies with $M_{\mathrm{tot}} = 1\times10^{11}\,\mathrm{M}_\odot$ to $1\times10^{12}\,\mathrm{M}_\odot$ in lensing observations (Hudson et al., 2015), while for the central regions stripping begins to have a severe impact – see also Figure A.13.

8.3   The Projection Section

Here, the results from the projected method are presented and compared to those obtained from SUBFIND. For every galaxy cluster, 200 orientations are done, for a total of 5800 orientations per mass bin. The statistics on the amount of substructures identified on average per orientation are summarized in Table 7.1. First, for every galaxy cluster, the substructure masses are ordered from large to small and the most massive substructure then classified as the main. Then, the masses of all substructures within the projected radius of the large
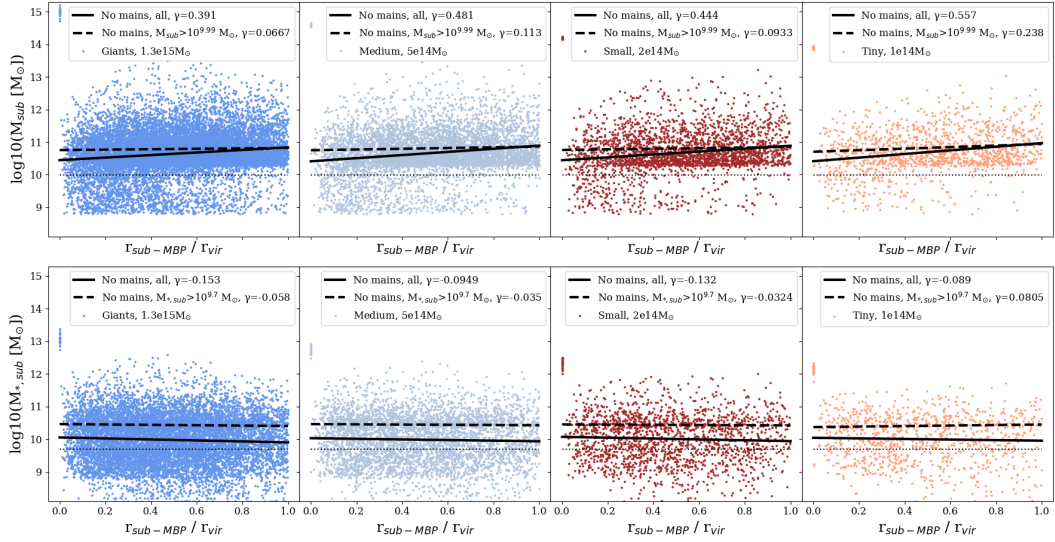
Figure 8.5: Subhalo total (*top*) and stellar mass (*bottom*) for all subhalos within r_{vir} in three dimensions for the 29 galaxy clusters of each mass bin. The thin dotted lines denote the equivalent mass of 20 dark matter (*top*) and 400 (*bottom*) stellar mass particles. It can be seen that the stellar component more closely resembles the radial behavior of the maximum circular velocity as depicted in Figure A.15 than the subhalo mass does.
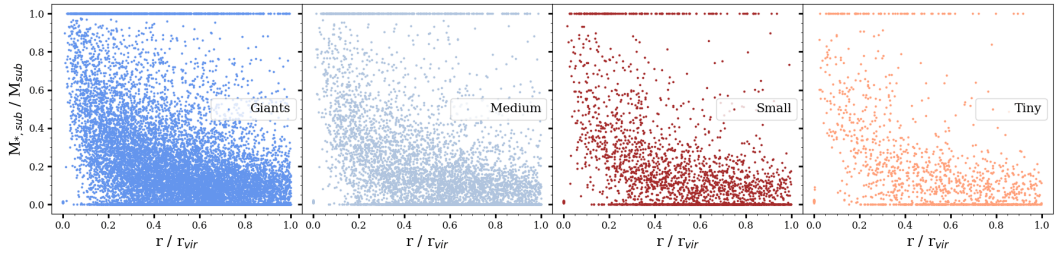
Figure 8.6: The subhalo stellar-mass to halo-mass ratio for all subhalos within r_{vir} in three dimensions for the 29 galaxy clusters of each mass bin. Note the decreasing number of purely stellar halos ($y = 1$) toward the outskirts, while the converse can be seen for dark matter only halos ($y = 0$) which are noticeably less present toward the centers of the galaxy clusters.

cylinder r_{tot} are summed and the resulting substructure mass fraction $f_{\mathrm{cyl}} \equiv \Sigma_2^N M_{\mathrm{i,cyl}}/M_{\mathrm{tot}}$ plotted against the total projected mass within the large cylinder, M_{tot}, in Figure 8.7. Though r_{tot} is smaller than r_{vir} – on the order of half – if anything this would normally decrease the subhalo mass fraction as shown by Jiang & van den Bosch (2017) in Figure 4 therein, even in projection. Nonetheless, most likely due to the use of the projected particle distribution (see Chapter 6) as opposed to using the SUBFIND output in projection, the fractional substructure mass f_{cyl} is noticeably higher than the fractional subhalo mass f_{sub} in Figure 8.2. This is particularly extreme for the "giants", where the lowest substructure mass fraction in projection is a factor 1.7 times higher than the highest for the SUBFIND case.

This discrepancy between the projected and three-dimensional values is of significant physical importance when classifying the dynamical state of a galaxy cluster between obser-vations and simulations: As time passes, the subhalos within a host halo slowly lose mass due to tidal stripping, slowly being amalgamated. This is in contest with the accretion of
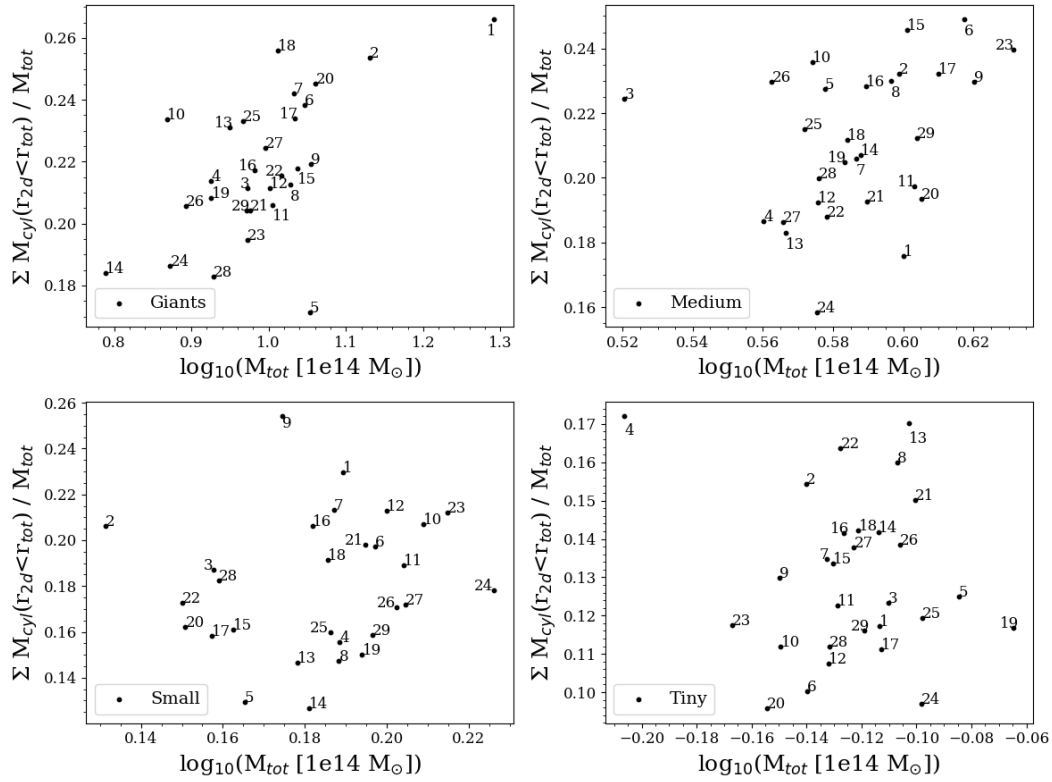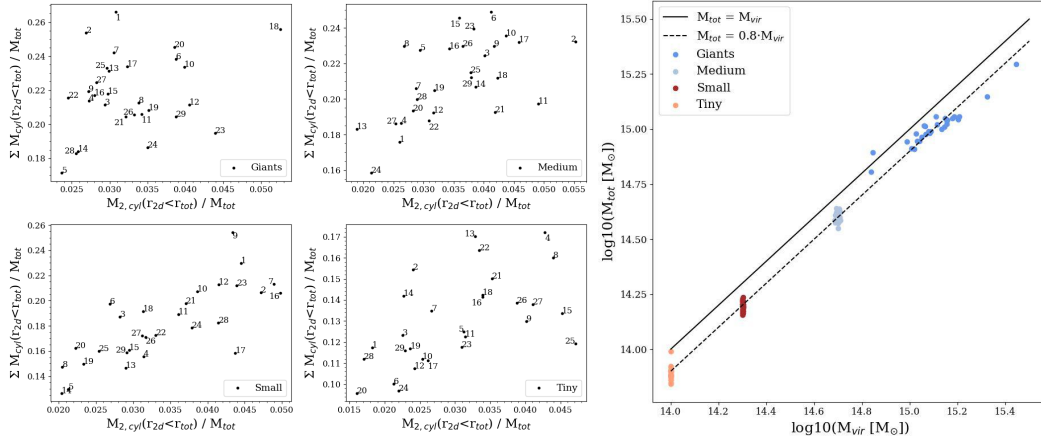
Figure 8.7: Relation between the relative summed mass of all substructures f_{cyl} excluding the main within r_{tot} of the 2-dimensional center-of-mass to the total projected mass in the larger cylinder M_{tot}.

additional mass into the halo, where at present times there is a net loss of mass due to the longer timescales of the accretion processes as discussed in Section 4.3.1. Subsequently, a higher subhalo mass fraction implies that there were many recent accretions onto the main halo (Jiang & van den Bosch, 2016), which in turn means that it is more dynamically active and therefore f_{sub} is commonly used as a tracer to relaxedness (Neto et al., 2007; Biffi et al., 2016; Jiang & van den Bosch, 2017). Thus knowing the effect of projection on this fraction is of high importance when interpreting observational results.

A further trend found in Figure 8.7 is that f_{cyl} tends toward higher values with higher total mass, both marginally within the mass bins themselves as well as more noticeably between them, in line with findings for dark matter-only simulations in Figure 2 of Jiang & van den Bosch (2017). Additionally, for the mass bins with tight SUBFIND virial masses the overall scatter of the total mass in projection M_{tot} is of comparable size in log-space, something which can be seen more clearly also on the right in Figure 8.8.

The dependency of the substructure mass fraction f_{cyl} on the most massive substructure (excluding the main) is plotted on the left in Figure 8.8 to test whether it behaves similarly to f_{sub}. While there may be a marginal correlation for the "medium" and "small" mass bins, it is not nearly as noticeable as it was for f_{sub} in Figure 8.3. That is to say, the projected substructure mass fractions are less dependent on a single massive subhalo and rather have more mass spread over multiple apertures. Furthermore, there are no cases of extreme outliers, with the mass fractions $M_{2,\mathrm{cyl}}$ all lying in a more compact range of 1.5% to 5.5%.

Figure 8.8: *Left:* The total substructure mass fraction f_{cyl} as a function of the mass fraction of the most massive substructure for all four mass bins. *Right:* The relation between the median projected mass M_{tot} versus M_{vir} for every galaxy cluster. The outlier upwards for the "tinies" is galaxy cluster number 19, while the four noticeable outliers of the "giants" are from bottom to top on the left numbers 14 and 10 and on the right 2 and 1.

To get a better idea of the mass distribution of individual substructures, the median mass fraction of the eight most massive substructures, $M_{i,cyl}/M_{tot}$ is plotted in Figure 8.9, with a column for each mass bin, respectively. The median is determined for an individual galaxy cluster from the obtained substructure masses sorted by mass over the 200 orientations. Highlighted substructure mass functions are for the galaxy clusters with the highest (blue) and lowest (red) substructure mass fraction. This is determined once in the top row via the median value for the orientations, f_{cyl}, and once on the bottom row via the SUBFIND values. It is apparent that while individual clusters with a high/low f_{sub} can also have a high/low f_{cyl}, for example galaxy cluster number 5 of the "giants" having the lowest for both cases, this is not the expectation. Rather, the ordering among each mass bin is remarkably uncorrelated between the two methods, with matches being the exception instead of the norm. This can also be seen when comparing individual clusters between Figure 8.2 and Figure 8.7.

Additionally, although the overall mass fraction f_{cyl} has increased as noted earlier, this increase is not as extreme as the increase in fractional mass for the individual substructures here. That is to say, while f_{cyl} has on average doubled to tripled relative to f_{sub}, the substructure fractional mass $M_{i,cyl}/M_{tot}$ is around an order of magnitude higher than $M_{i,sub}/M_{vir}$ for the first eight substructures. The result is that in projection more mass in substructures overall is further distributed across a smaller number of structures. The converse is true for the main, where instead due to the localized nature of the aperture in projection it is assigned noticeably less mass than the main halo in SUBFIND, which is depicted clearly in Figure A.16. Further interesting is the difference in slopes of the substructure fractional mass distribution between galaxy clusters of a given mass bin. As can be seen from the top row of Figure 8.9, those with overall higher substructure mass also have more shallow slopes and less massive mains, while those with a very dominant first mass have curves which fall off steeply and continue relatively flat afterwards, more reminiscent of those found for the "giants" in Figure 8.4 on the right. Furthermore, having a high second substructure mass is not sufficient to have the
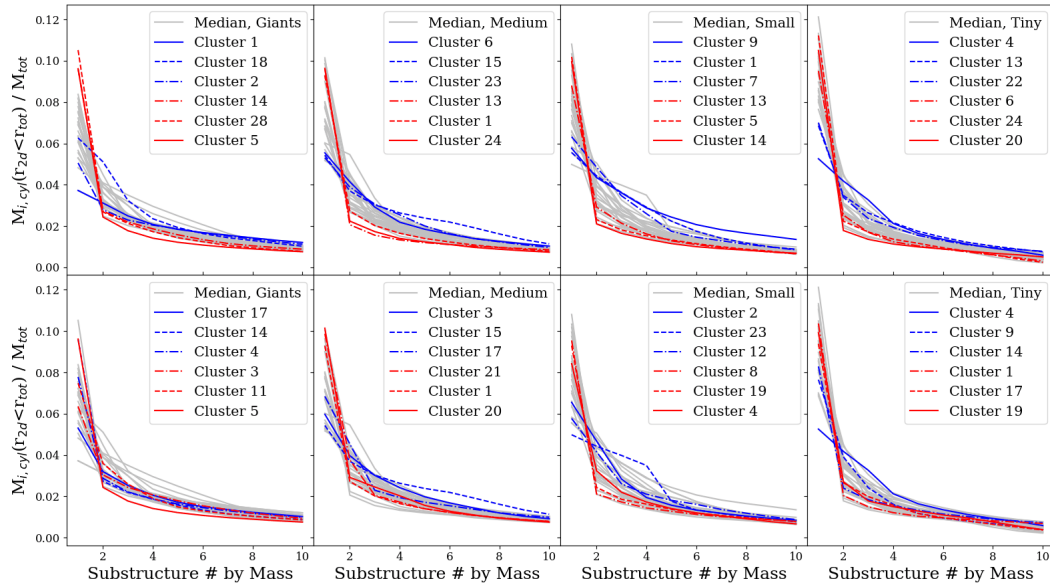
Figure 8.9: The median mass fractions for the eight most massive substructures within r_{tot} as a function of their substructure number. Columns are for each of the mass bins. Highlighted galaxy clusters are those with the highest (blue) and lowest (red) three f_{cyl} (*top row*) or f_{sub} (*bottom row*), with bold to dash-dotted going from most to least extreme.

highest total substructure mass, as can be seen from multiple gray lines lying above blue ones at low substructure numbers 2 to 3 in the top row of Figure 8.9.

This also raises the question of whether or not there is a correlation between the mass fractions of individual substructures and f_{cyl} at a higher substructure number, as the correlation was not very clear for the most massive substructure as shown in Figure 8.8. To this point, the dependence of f_{cyl} on the substructure mass fractions of substructures number 1 (the main), 2, 4 and 8 is plotted in Figure 8.10 for every orientation in each mass bin. Here the point made for Figure 8.9 is further demonstrated, with orientations of high f_{cyl} having generally lower first and higher second to eighth substructure masses. The trend is not as clear for the second or fourth substructure mass as it is for the eighth, which is to say there exist orientations with up to two or four massive substructures that do not have an overall high substructure mass fraction, while this occurs noticeably less frequently for those with a high eighth mass. It appears that the eighth substructure has a lower overall mass fraction for the lower mass bins, though the trend is not very strong.

To summarize this behavior in the slopes of the substructure mass with number it is useful to consider the parameter d_8, defined as the difference between the mass fraction of the first (main) to the eighth substructure, $d_8 \equiv (M_{1,\text{cyl}} - M_{8,\text{cyl}})/M_{\text{tot}}$. This then defines the shallowness of the slope, with lower/higher d_8 having a flatter/steeper substructure mass distribution. Considering again the importance of the total substructure mass for insight into a galaxy cluster's dynamical state (Neto et al., 2007; Jiang & van den Bosch, 2017), it can be seen that d_8 clearly correlates with f_{cyl} in Figure 8.11.

There exists a general downwards trend, further confirming that a more shallow slope in Figure 8.9 corresponds to an overall higher substructure mass fraction. Curiously, the slope
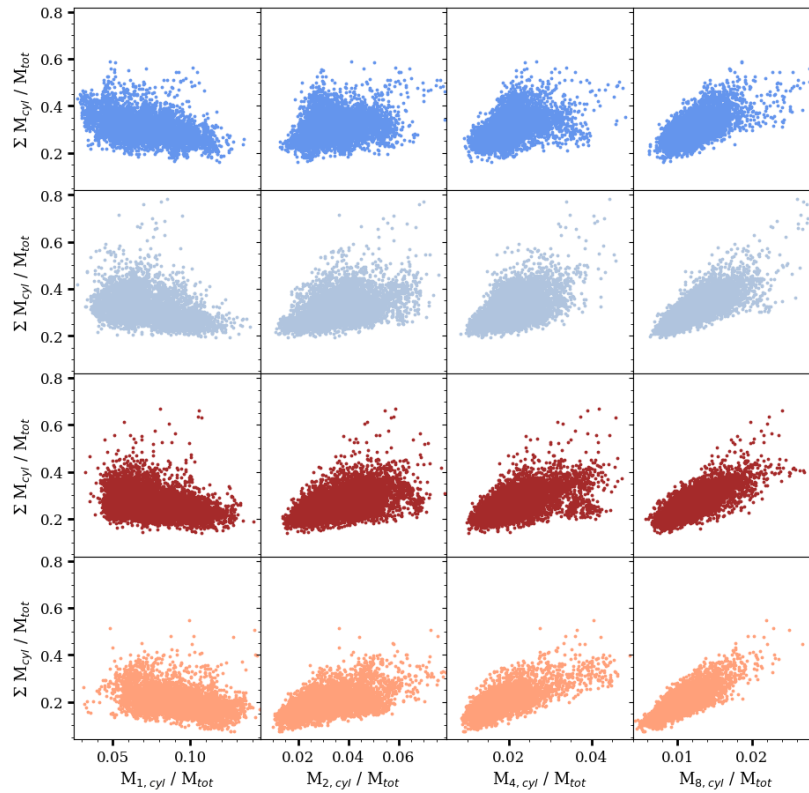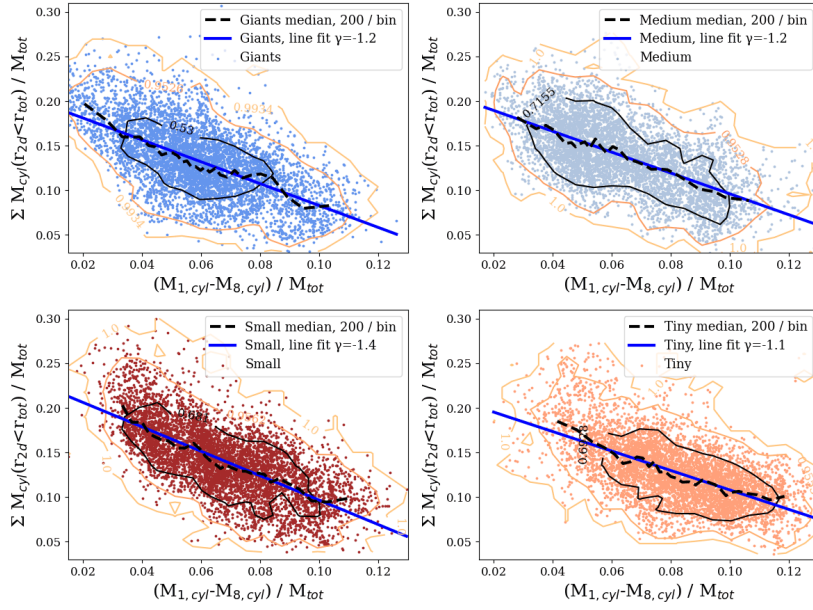
Figure 8.10: The total substructure mass fraction f_{cyl} as a function of the fractional mass of substructure 1, 2, 4 and 8 in the columns from *left* to *right*. Rows each represent a mass bin, going from the "giants" to the "tinies" from *top* to *bottom*.

of the best fit line for the relation varies relatively little between the mass bins, while generally the lower mass bins tend towards a larger d_8, indicating steeper slopes of the substructure mass fractions with decreasing main halo mass.

8.3.1 How Far Does Projection Go?

In Figure 8.12, for two different projection depths, two galaxy clusters, number 5 (left) and 20 (right) of the "giants" mass bin, are then chosen for a deeper look, as they represent the steepest and one of the flattest slopes in the mass bin, respectively. Their fractional substructure mass for their eight most massive ones is depicted through a violin plot, with the blue error bars denoting the overall spread in the 200 projections while the frequency of mass fractions for each substructure number is represented through the blue shaded area. The black line denotes the mean mass over all orientations. First the top row with the typical projection depth $Z = 2 \cdot r_{turn}$ is considered.

Galaxy cluster 5 exhibits a noticeably more peaked distribution, with orientations being quite similar in their substructure mass fractions especially for the higher numbers, while in contrast number 20 has a generally flatter slope and a larger variance in the mass fractions of higher number substructures. This can also be seen with regards to the black dotted line representing a value slightly above 2% of the total mass, which for galaxy cluster 5 is only achieved very rarely for substructure number 5 and is common only for substructure 2, while

Figure 8.11: The total substructure mass fraction f_{cyl} as a function of the first to eighth mass difference d_8. Dashed black lines are the median values binned into sets of 200 orientations. The blue line denotes the best line fit, and contours contain the fraction of orientations as written.

galaxy cluster 20 has this occur even more frequently for substructure numbers as high as 8 and regularly makes this threshold for substructures up to number 5. It is interesting to note the bi-modal behavior in the frequencies of mass fractions which appears for galaxy cluster 20 especially noticeably in the first and third substructure. Here, two distinct peaks are visible, indicating that there exists two classes of orientations for this galaxy cluster: one more commonly with a lower first substructure mass and another more rarely with a nearly 1.5 times as high first mass. Even for the seventh and eighth substructures, there is still a significant spread possible between the masses, unlike for galaxy cluster 5. This distinct behavior will be of central importance later in Section 8.6.

The bottom row of Figure 8.12 depicts the same for a projection depth of $Z = 2 \cdot r_{vir}$ to test how relevant fore-/ background structures are. Little difference overall is found to the usual projection depth depicted in the top row. The first substructure mass for both clusters rises marginally, with the most noticeable difference being the absence of orientations with a small value for galaxy cluster 5. This implies that there exists in some projections a fore- or background structure which shifts the center-of-mass, thus reducing the first apertures mass in some cases, while the cluster itself is entirely dominated by its BCG. However, this does not strongly impact the distribution of the higher substructure masses except for reducing the overall maxima marginally. This can be seen also for galaxy cluster 20, where the number of orientations lying above the black line is 3 and 1 for the top and bottom row, respectively. It follows that a deeper projection depth (i.e., less resolved redshift space) does marginally allow for larger peak masses of substructures in the cases where some additional objects are projected into the image, but the overall effect of projection of the galaxy cluster is significantly larger than the impact from these additional structures.
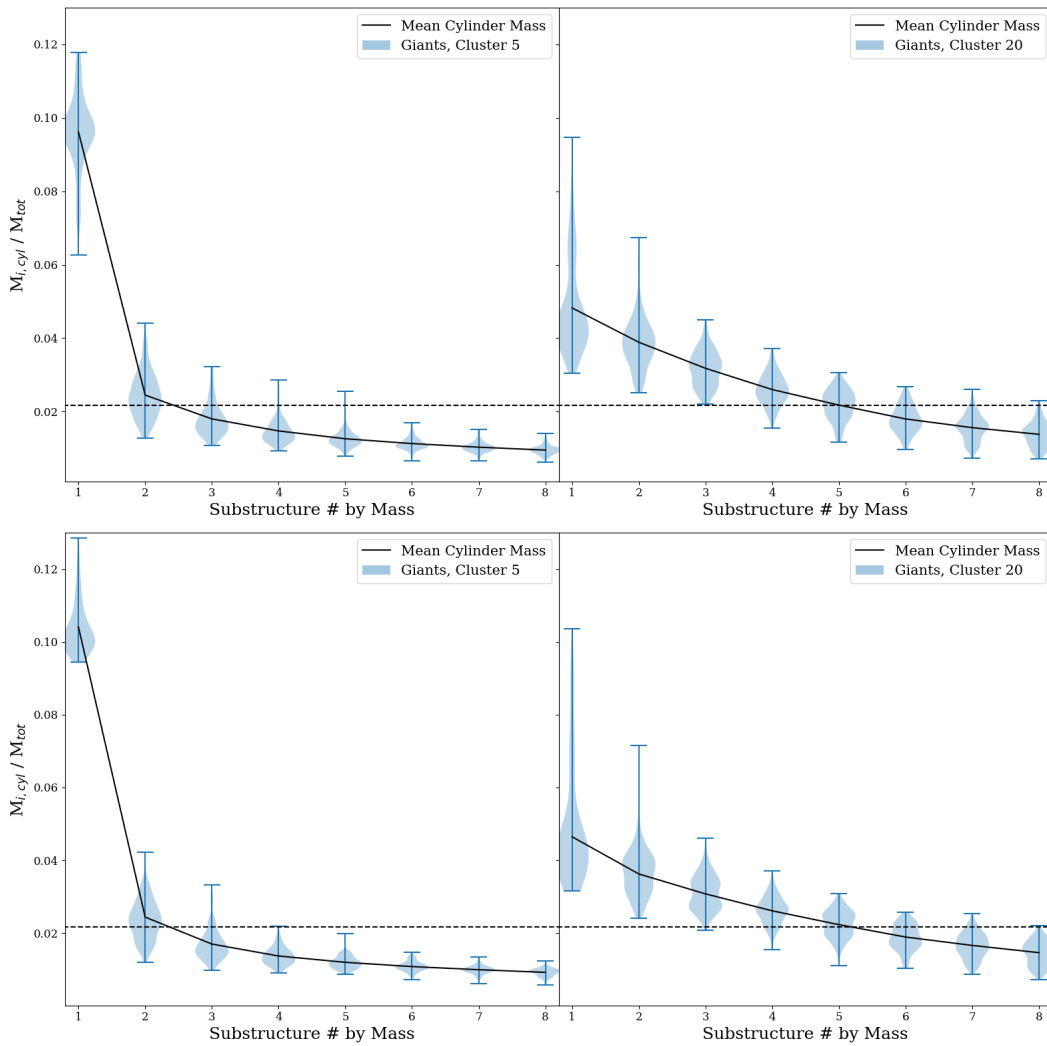
Figure 8.12: The distribution of the mass fractions for the eight most massive substructures within r_{tot} as a function of their substructure number for galaxy clusters 5 (*left*) and 20 (*right*) of the "giants" mass bin for all 200 orientations out to the typical projection depth r_{turn} (*top row*) and out to r_{vir} (*bottom row*). Blue error bars denote the overall spread while the blue shaded area represents the percent number of orientations at each mass fraction, with a larger bulge meaning a larger percentage. Dashed black line equals a mass fraction of around 2.2%.

8.3.2 The Radial Trends in Projection

As discussed in Section 8.2.1, there exist some general trends for the subhalo masses with three-dimensional radius. Here the projected radial behavior of the substructures is discussed. Taking the "giants" mass bin as a representative, the substructure masses and the masses of the most massive subhalos within each aperture are plotted on the left and right in Figure 8.13 as a function of the respective aperture's distance to the center-of-mass.

It can be seen that the substructure masses generally *decrease* with increasing projected distance to the center-of-mass, in stark contrast to the behavior found for the bound subhalos identified by `SUBFIND` in Figure 8.5. Immediately visible is also the outcropping of higher substructure masses below the vertical dashed black line, denoting the size of an aperture $r_{\text{ap}} = 150\,\text{kpc}$. This is because any substructure lying closer than that radius overlaps the center-of-mass, thus does not have part of its mass subtracted as belonging to the main halo
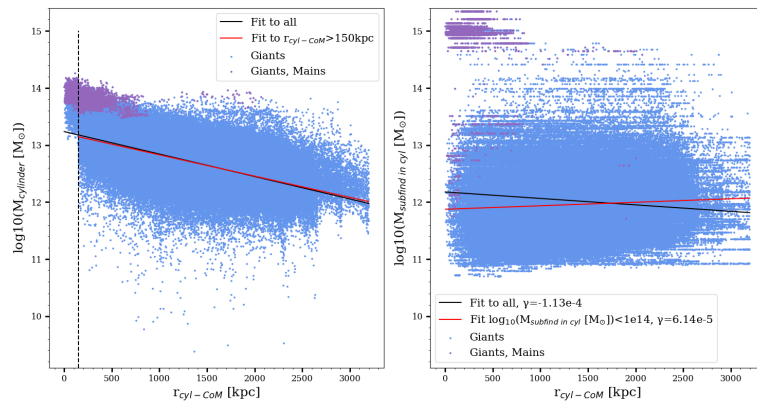
Figure 8.13: The projected radial dependence of the mass of substructures M_{cyl} (*left*) and the most massive subhalos within each aperture $M_{subfind\ in\ cyl}$ (*right*) for the "giants" mass bin. For each orientation, the most massive substructure is plotted in purple. Bold black lines denote the best-fit lines to all data, with red lines representing the best-fit for all apertures not overlapping the center-of-mass (*left*) or all `SUBFIND` masses below $1 \times 10^{14}\,M_\odot$ (*right*). The vertical dashed line on the *left* is $r_{ap} = 150\,kpc$.

(see Section 6.3). A good portion of these central apertures (around 55% for the "giants", see Figure 8.21) also end up being the most massive ones – the mains which are colored in purple. However, the presence of these more massive central apertures does not noticeably alter the slope of the best-fit line (black versus red), indicating that not subtracting any mass has a negligible impact on the overall distribution of substructure masses.

For the masses from `SUBFIND` of the most massive subhalos lying within apertures a downwards trend is also found when fitting to all present. However, when excluding those with $M_{sub} > 1 \times 10^{14}\,M_\odot$, which are predominantly the masses of the `SUBFIND` main halos – and in turn correspond overwhelmingly to the apertures which are the most massive substructures colored in purple, see Figure 8.21 – the trend instead becomes very slightly increasing with radius which is then more comparable to the behavior found in Figure 8.5, though not nearly as strong. The difference is not unexpected, as the radial projected distribution of the most massive subhalo masses within exclusive apertures does not need to correspond to the general distribution in three dimensions of those subhalo masses. The visible strings of equal values for $M_{subfind\ in\ cyl}$ appear due to the same subhalo M_{sub} being found within apertures for multiple orientations.

Narrowing the scope of the radial behavior to that of the mass of a single substructure, Figure 8.14 depicts the mass fraction of the eighth substructure as a function of its distance to the center-of-mass. There exists overall very little dependence, with the strongest trend found for the "giants" while for the "tinies" there exists practically no radial trend at all. This is indicative of the fact that the substructure number is a fluid variable: if an aperture lies farther in, it will have more mass on average and is thus more likely to have a lower substructure number.

To better illustrate this point, Figure 8.15 plots the distribution of radii for the first eight substructures. There exists a clear trend toward lower radii for higher substructure numbers,
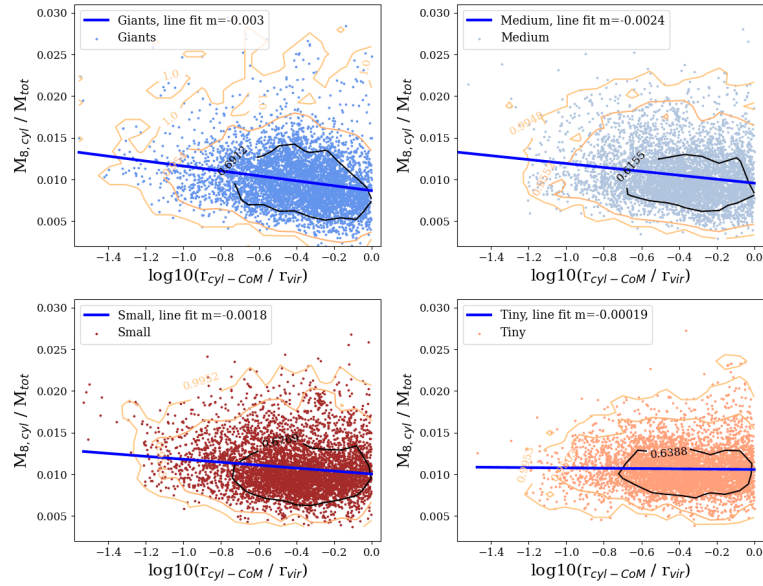
Figure 8.14: The mass fraction of the eighth substructure as a function of the logarithm of the separation between the center of the substructure and the projected center-of-mass for every mass bin. Bold blue lines denote the best-fit line with slopes given in the legend, while the contours contain the fraction of total orientations as written.

as argued. Furthermore, the radial distribution of the sixth to eighth substructure becomes flatter for the lower mass bins, with especially those in the "tiny" mass bin lying noticeably farther out on average. It is also the mass bin where the main most dominantly lies within $0.1 \cdot r_{\mathrm{vir}}$, interestingly with a second very shallow peak forming around $0.8 \cdot r_{\mathrm{vir}}$. All bins find the most significant radial offset between two sequential substructures for the first to second ones, with the average separation being larger than $0.1 \cdot r_{\mathrm{vir}}$. Though it follows that the predominant number of orientations have the most and second-most massive substructure at the nearest radii to the center-of-mass, there still exist a noteable portion of orientations where any of the first eight substructures can fall within $0.1 \cdot r_{\mathrm{vir}}$, with decreasing probability for higher substructure numbers but even for the eighth staying above zero.

Given the importance of the total substructure mass fraction in determining a galaxy clusters dynamical state (Neto et al., 2007), the radial behavior of this parameter is analyzed next. Here, f_{cyl} is defined to be the fraction of mass contained within substructures relative to only the main halo mass, as opposed to its usual definition relative to all mass. The Einasto profile determined for the main as in Section 6.3 is integrated numerically up to radius x, and the masses of all substructures with a projected distance to the center-of-mass that is less than or equal to that, $r_{\mathrm{cyl-CoM}} \leq x$, are added together (excluding the main) and divided by the main halo mass. This total substructure mass fraction as a function of radius is then plotted in Figure 8.16 and compared to the curve for $z = 0.2$ obtained for a projected model as given by Jiang & van den Bosch (2017), comparable to the redshift $z = 0.252$ used here. There, subhalos are positioned according to the semi-analytical model and then summed up by their projected radius as a fraction of the integrated mass of the main halo, approximated by an NFW-profile. Note that the distribution of the subhalos is isotropic, and further that
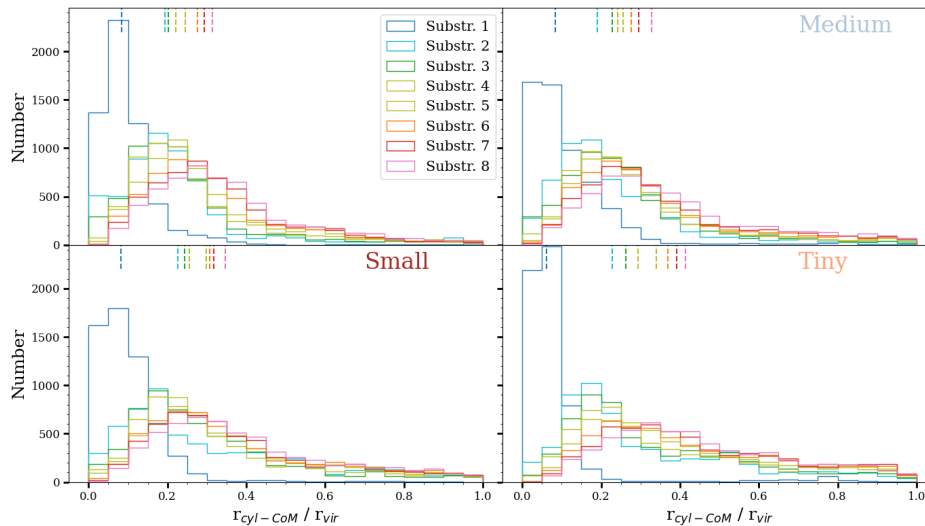
Figure 8.15: The radial distribution of substructures. Dashed lines at the top indicate the median radii, with colors denoting the substructure number by mass. The top left plot displays the distribution for the "giants" mass bin.

the rescaled higher main halo mass (dotted black line in Figure 8.16) is scaled according to $f_{sub} \propto M_0^{0.12}$ as given therein, converting their mass given in units of h^{-1} $M_\odot$ with the Hubble parameter used for the `Magneticum Pathfinder` simulations, $h = 0.704$ (Dolag, 2022), in accordance with WMAP-7 (Komatsu et al., 2011).

The black vertical lines represent r_{ap} (dashed) and r_{tot} (dash-dotted). At large radii the behavior found for `Magneticum Pathfinder` is similar to the model by Jiang & van den Bosch (2017), while towards small radii the results diverge. The lack of substructure mass within $r < r_{ap}$ results from the fact that when an aperture exists which overlaps the center-of-mass, $r_{cyl–CoM} < r_{ap}$, this is also commonly the main (see Figure 8.21). Consequently, on average there is no aperture overlapping the center which is not a main, and as apertures have a minimum separation of $d_{min} = 2 \cdot \sqrt{3}/2 \cdot r_{ap}$ between each other (see Section 6.2.1) this means that the first radius with substructure mass on average is larger than the aperture radius, r_{ap}. This is why the steep initial jump is observed farther out than the one just outside the extent of the BCG for the model from Jiang & van den Bosch (2017). As can be seen from the 1σ ranges depicted in Figure A.17, there do exist orientations with substructures found quite far toward the center, hence the increasing substructure mass fraction at $x = r_{ap}/r_{vir}$ for the upper bounds for those cases where no aperture is placed within r_{ap}. Nonetheless, the 1σ upper bound of the substructure mass fraction drops to zero once the aperture actually overlaps the center. Curiously, the "tiny" mass bin does not exhibit this increase. Additionally, it can be seen that the crosses, indicating the median total subhalo mass as a fraction of the total mass within r_{tot}, lie lower than the curves for the fraction relative to the integrated main halo mass. This is as expected, as a portion of the total mass lies within the substructures themselves.

Albeit the small number of observations on this matter, two substructure mass fractions from lensing observations are shown for comparison: The purple diamond is from a weak-lensing measurement of the Coma cluster at $z = 0.0236$ for the substructure mass as a
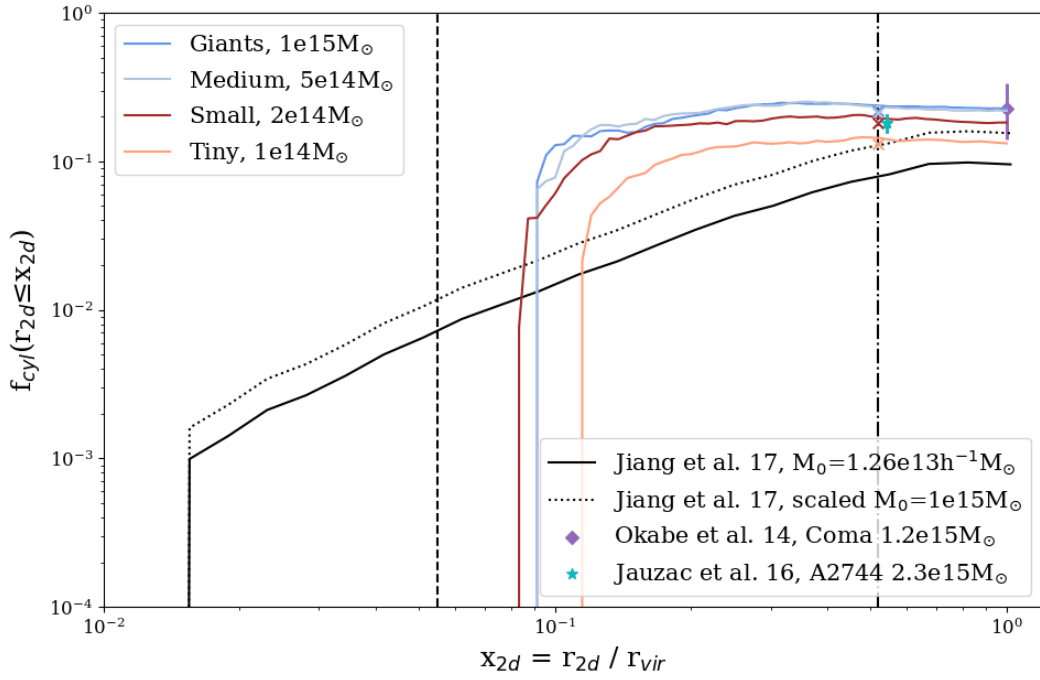
Figure 8.16: The median running substructure mass fraction of the integrated main halo mass as a function of projected distance to the center-of-mass for the four mass bins with colored solid lines, as well as in the dotted and solid black lines (for differing main halo masses as given) the dark matter-only model from Jiang & van den Bosch (2017) which well match the re-scaled results from the BOLSHOI simulation (Klypin et al., 2011). Vertical lines denote the approximate relative aperture size r_{ap}/r_{vir} (dashed) and large cylinder size r_{tot}/r_{vir} (dash-dotted). The colored crosses represent the substructure mass fraction of the *total* mass at that radius M_{tot}, not just the main halo. Similarly, the purple diamond denotes the substructure mass as a fraction of the *total* mass within the virial radius r_{vir} for the Coma cluster performed by Okabe et al. (2014), with the quoted total mass stemming from their tangential fit. The cyan diamond is from extrapolations of the substructure mass data for Abell 2744 as given by Jauzac et al. (2016).

fraction of the total mass within r_{vir} as performed by Okabe et al. (2014), with the total mass quoted as determined from their tangential fit. With a final value of $f_{sub} = 0.226$, the measurement agrees well with the curves of the "giants" and "mediums", the former of which have comparable masses to the Coma cluster but less well with the model from Jiang & van den Bosch (2017). Meanwhile, the strong- and weak-lensing combined analysis for Abell 2744 at $z = 0.308$ as done by Jauzac et al. (2016) finds eight massive substructures within 1 Mpc of the galaxy cluster center. Assuming the substructure labeled as "core" to be the main and as such excluding it from the sum, the total substructure mass is then $4.16 \times 10^{14} \, M_\odot$, which compared to the total mass within 1.3 Mpc, $M_{tot} = 2.3 \times 10^{15} \, M_\odot$, then gives $f_{sub} = 0.181$. x_{2d} is determined by assuming the virial radius to be approximately at r_{200}, and then using the value of 2.4 Mpc given by Boschin et al. (2006) to get $x_{2d} = 1.3/2.4$. This point lies somewhat below the most comparable mass bin of the "giants", but generally agrees well with the results found for the `Magneticum Pathfinder` clusters, especially given that the value for the total substructure mass fraction calculated should be understood as a lower bound, as the eighth substructures as determined by Jauzac et al. (2016) do not

necessarily constitute all substructure mass, especially considering that all lie within 1 Mpc while the total mass is measured within 1.3 Mpc.
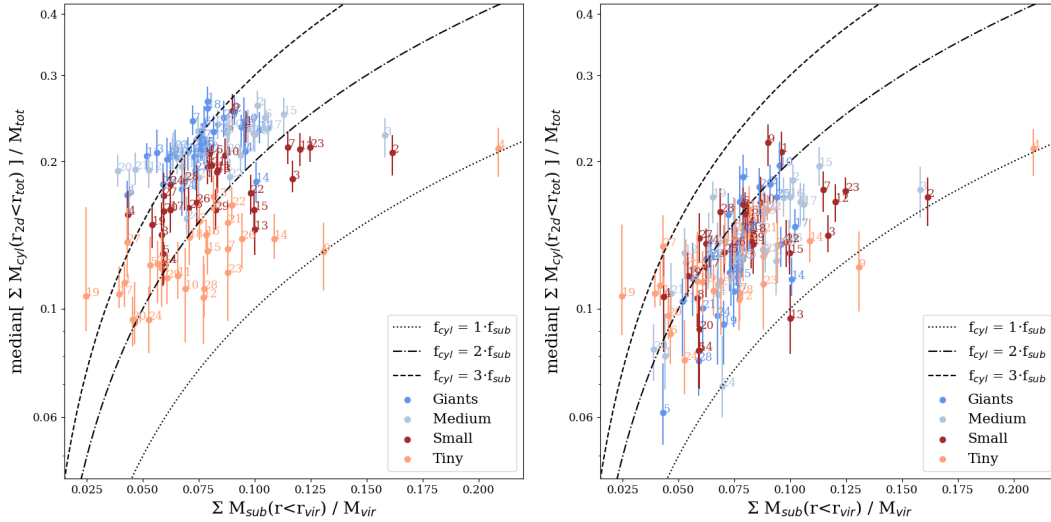
Figure 8.17: For every galaxy cluster individually the median substructure mass fraction f_{cyl} as a function of the subhalo mass fraction f_{sub} for the primary scaling method with virial mass (*left*) and the alternative with fixed subhalo numbers (*right*), colored by mass bins (see Section 7.2). f_{cyl} is determined from all substructures within r_{tot}. Vertical colored lines denote 50% bounds, while the dotted, dash-dotted and dashed black curves give factors 1, 2 and 3 between the projected and bound mass fractions.

Figure 8.17 depicts the relationship of the measured substructure mass fractions between projected and bound values for the individual galaxy clusters of all mass bins for both the main scaling method considered throughout ($\propto M_{vir}$ of the galaxy cluster, left) as well as the alternative given in Section 7.2 (constant N_{sub}, right), with general values for the bins summarized in Table 8.1. There is unsurprisingly a trend towards larger substructure mass fractions for a higher number of apertures placed, with this effect being stronger for galaxy clusters which start out with little bound subhalo mass – see for example number 5 and 11 of the "giants", or number 1 and 20 of the "mediums". Even for the low number of total apertures placed on the right (around 19 on average, see Section 7.2) the mean increase is still around $f_{cyl}/f_{sub} \approx 1.75$, with very few clusters ending up with 1-to-1 relations. Interestingly, these do not occur only for high values of f_{sub} but rather are spread across all mass bins and bound subhalo mass fractions. Furthermore, even with just 19 apertures, there exist some galaxy clusters which in projection exhibit consistently higher substructure mass fractions between 2 to 3 times larger.

8.4 Other Measures of Dynamical State

Another important parameter for a galaxy cluster is that of the centershift, which is the distance between the point of least potential and the center-of-mass, the latter of which is typically defined in three dimensions for all particles within the virial radius. Together with the total

Table 8.1: The relation between projected and bound substructure mass f_{cyl}/f_{sub} for the different mass bins and scaling methods (see Section 7.2).

	Giants	Medium	Small	Tiny
f_{cyl}/f_{sub}		M_{vir} scaled		
Mean	2.94	2.77	2.27	1.93
Minimum	1.81	1.43	1.29	1.00
Maximum	3.97	4.92	3.59	4.31
f_{cyl}/f_{sub}		N_{sub} scaled		
Mean	1.74	1.75	1.75	1.88
Minimum	1.14	1.00	0.96	0.93
Maximum	2.35	2.60	2.44	4.31

subhalo mass fraction f_{sub}, these parameters can be used as a tracer for the relaxedness of the galaxy cluster itself (Neto et al., 2007; Biffi et al., 2016).
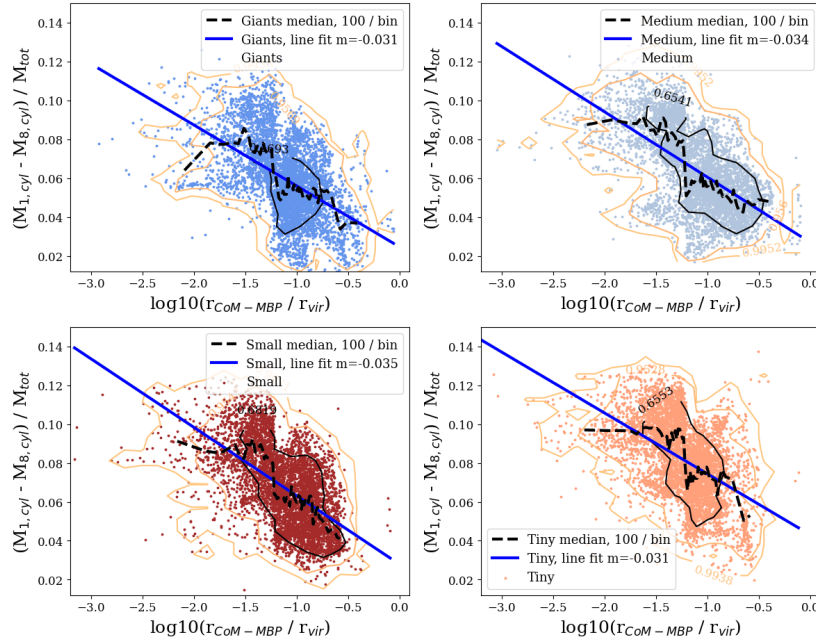
Figure 8.18: d_8 as a function of the centershift. Dashed black lines denote the running median, and best-fit lines are given in solid blue. Contour lines enclose the fraction of orientations as given.

First, given the behavior observed for the slopes of the substructure mass distribution in Figure 8.9, the question arises whether it can be linked to the centershift. Using again the d_8 parameter for comparison, the resulting relation is depicted in 8.18. Indeed, there is a general trend towards more shallow slopes (smaller d_8) with increasing centershift, so more massive substructures are found for orientations where the point of deepest potential is not the center-of-mass. These are then dynamically active galaxy clusters, with sufficient infalling mass – identified as many substructures – which shifts the center-of-mass away from the main halo center. It is interesting to note that the slopes for the relations are generally comparable between the mass bins. Furthermore, it is apparent that most orientations exhibit

decently large centershifts, with the median values from the most to least massive mass bins being 209.55, 154.25, 107.71 and 65.95 kpc, which means that for all bins on average $r_{\mathrm{CoM-MBP}} > r_{\mathrm{ap}}$.
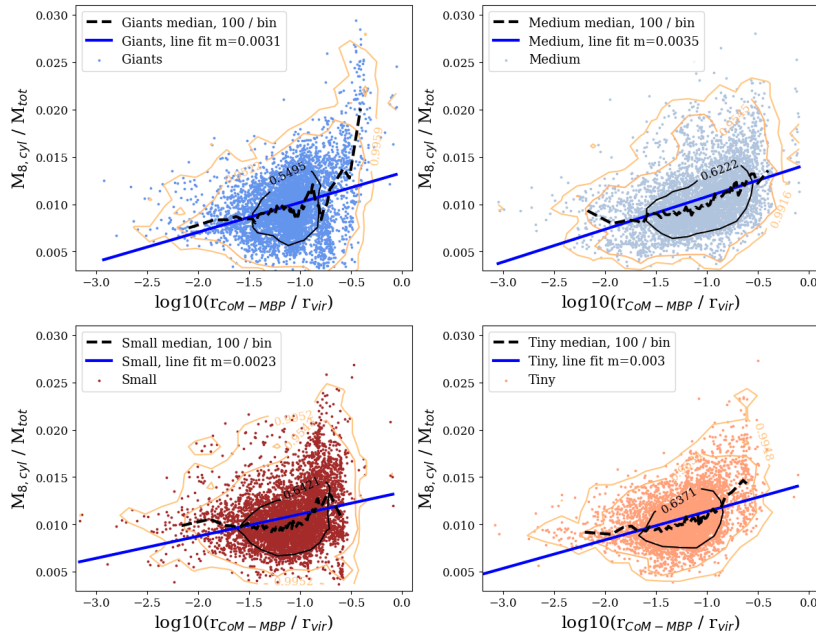
Figure 8.19: The dependence of the eighth substructure mass on the orientations centershift. Dashed black lines denote the running median, and best-fit lines are given in solid blue. Contour lines enclose the fraction of orientations as given.

But what impact does the centershift have on single substructure masses? Recalling that little correlation is found between the mass of the eighth substructure with projected distance to the center-of-mass in Figure 8.14, which there is due to the fluidity of the definition of an eighth substructure mass, this implies that to have a more massive eighth substructure requires all substructures of higher number to equally rise in mass (as a consequence of the relatively shallow substructure mass slopes of all galaxy clusters in Figure 8.9 for numbers beyond 3). Plotting the eight mass fraction against the centershift in Figure 8.19, there appears little correlation for $\log_{10}(r_{\mathrm{CoM-MBP}}/r_{\mathrm{vir}}) < -0.1$, which can be seen from the flat course of the median. However, at sufficiently high centershifts of around $r_{\mathrm{CoM-MBP}} \approx 0.3 r_{\mathrm{vir}}$ there is a distinct rise in frequency of high $M_{8,\mathrm{cyl}}$ values. Especially for the "giants" and "tinies", it is noticeable that the strongest outliers are not present for lower centershifts. These then are unique orientations with numerous very massive substructures, where for some of the most extreme examples found for the "giants" the first seven non-main substructures account for at least $7 \cdot 3\% = 21\%$ of the total mass within r_{tot}. As is discussed further in Section 8.6, these are the orientations which give rise to the extreme projected substructure masses found from lensing observations, or example by Jauzac et al. (2016).

Finally, to tie together both of the here considered parameters indicative of the dynamical state of a galaxy cluster, Figure 8.20 plots both the total substructure mass fraction and centershift against their values determined in 3 dimensions. The dashed black lines represent typical limits for both parameters, namely $f_{\mathrm{sub}} = 0.1$ and $s_{\mathrm{shift}} = 0.07$, where higher values
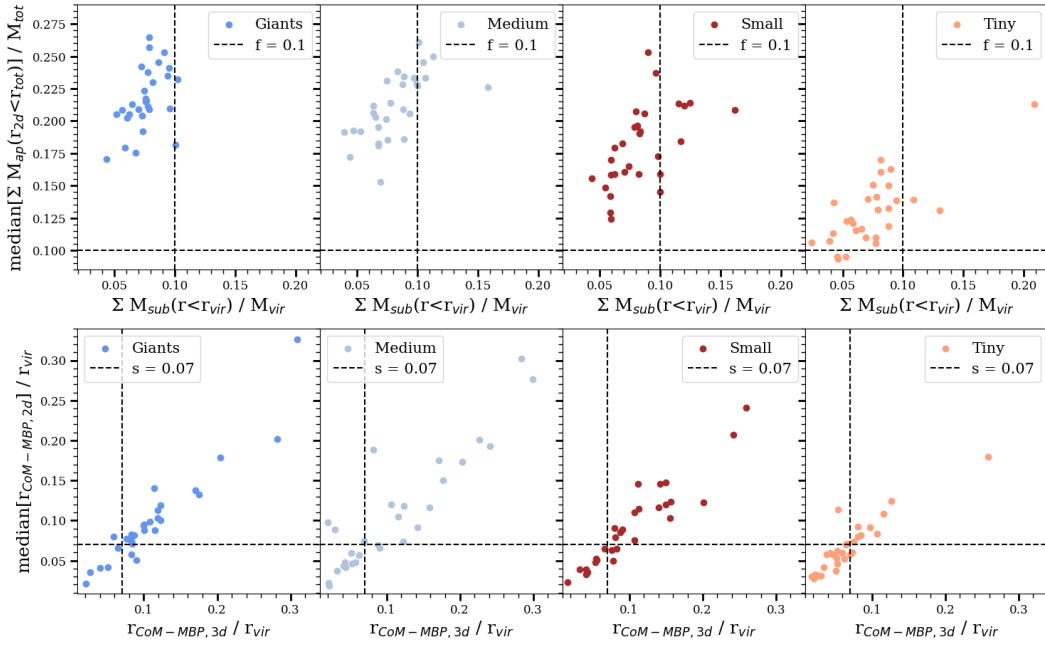
Figure 8.20: *Top row:* The median projected substructure mass fraction within r_{tot} as a function of the bound value determined from SUBFIND. *Bottom row:* The median projected centershift versus the value in three dimensions. Dashed black lines denote typical bounds between relaxed and dynamically active galaxy cluster, with lower values indicative of the former (Neto et al., 2007; Biffi et al., 2016). Explicit galaxy cluster numbers within the mass bins are given in Figure A.18.

indicate a galaxy cluster which is dynamically active (Neto et al., 2007). As is already shown in Figure 8.17, there is a significant discrepancy between the substructure mass fractions f_{cyl} and f_{sub}, with the former falling in the range of "dynamically active" for nearly all galaxy clusters of all mass bins. Contrarily, very few galaxy clusters have sufficient f_{sub}. This implies that determining the dynamical state via the substructure mass fractions will strongly depend on considerations of projection, with potentially significant discrepancies in classification.

The converse is true for the centershift, which exhibits a very tight correlation between the projected and 3-dimensional methods. Sufficient mass to disturb the center-of-mass away from the point of deepest potential therefore does so similarly in projection, while the mass being assigned to these substructures is not as comparable. This is most likely due to the centershift being a more global parameter, determined from the large-scale mass distribution as opposed to from individual smaller-scale overdensities. Interestingly, similar stability in projection is found for the centershift w as determined by X-ray emission in simulations performed by Böhringer et al. (2010), there given as the distance between the X-ray peak and centroids of increasing radius. Note, however, that their w is measured within r_{500} (not r_{vir}) and the border between dynamically disturbed to regular is much lower as well, being at $w = 0.01$.

## 8.5   It is Bound to be Projected

Given the differences found between projected and bound masses in the preceding sections, it is sensible to seek a method of converting one into the other. This section will develop such a model to construct expected masses in projection M_{cyl} as a function of the underlying subhalo mass $M_{\text{subfind in cyl}}$ and projected distance to the two-dimensional center-of-mass $r_{\text{cyl–CoM}}$ for the four mass bins. The great benefit lies in the ability to, for a given observed mass in projection, be able to take a sample of galaxy clusters from simulations and then predict confidence bounds with which an orientation exists that can reproduce it. As a great deal of the following analysis will focus on the dependence of substructure masses on $M_{\text{subfind in cyl}}$ and $r_{\text{cyl–CoM}}$, for brevity's sake, the two parameters will be shortened to M_{s} and r_{c} throughout. The final form of the model is that of a Gaussian probability distribution, where the probability for a given projected substructure mass of M_{cyl} resulting from a bound subhalo of mass M_{s} at projected distance r_c within a galaxy cluster of comparable mass to one of the mass bins is given by:

$$p_{\text{bin}}\left(x = M_{\text{cyl}}; \sigma(M_s, r_c), \mu(M_s, r_c)\right) = \frac{1}{\sqrt{2\pi\sigma^2}} \exp\left(-\frac{(x-\mu)^2}{2\sigma^2}\right). \tag{8.1}$$

8.5.1   The General Behavior of Individual Apertures

To get an initial impression for the relationship between the apertures and bound subhalos as determined in three dimensions via SUBFIND, two choice correlations are plotted in Figure 8.21. On the left, for the orientations that have an aperture overlapping the projected center-of-mass, the frequency of this central aperture ending up as the first to eighth most massive substructure is shown. For the cluster mass bins from "giants" to "tiny", this central aperture exists in around 55.5%, 59.4%, 58.2%, and 58.7% of all orientations, which end up being comparable frequencies, and for those where it does the most massive substructure is in over half. Given the large amount of mass at the original center of the galaxy clusters, the most-bound-particle, to fail placing an aperture on the center-of-mass for nearly half of all orientations requires on average centershifts that are larger than the aperture size, which is exactly what is found in Section 8.4.

In turn, the right of Figure 8.21 depicts the correlation between the order of substructure masses to the order of the bound subhalo masses within, where for example if $x = 3$, the most massive three substructures also contain the most massive three subhalos in the same order. As can be seen, an aperture containing the first/second most massive bound subhalo has very high/good chances of also being the first/second most massive substructure, while already for the third most massive subhalo the correlation to the substructure number of the aperture containing it is on average between the bins only 10%. This is because a significant portion of the projected mass contained in the apertures comes from the main halo, such that only overwhelmingly massive subhalos can guarantee high final aperture masses.
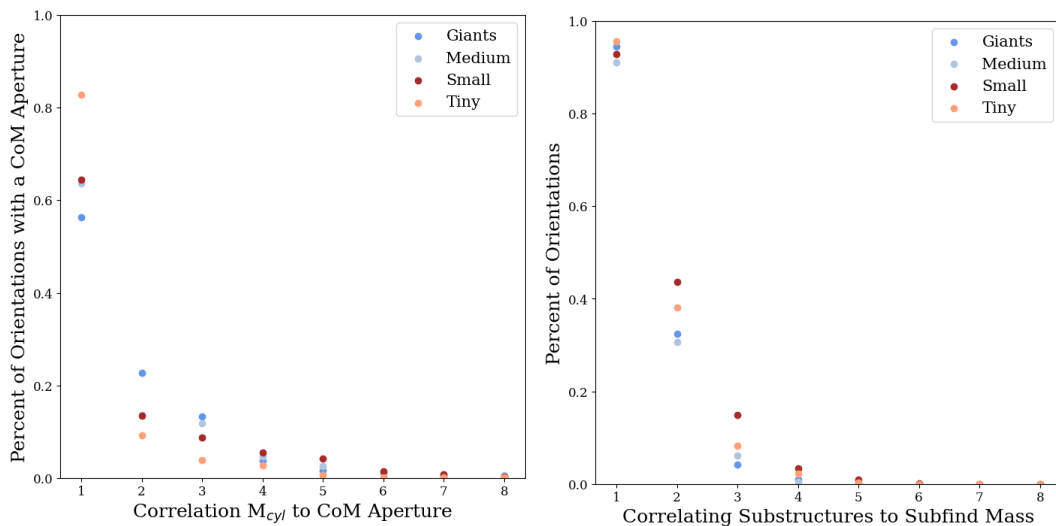
Figure 8.21: *Left:* The fraction of orientations where the center-of-mass lies within the "x"-th most massive aperture. Note that this considers only orientations which have an aperture containing the center-of-mass, which represent approximately 33, 44, 55 and 41% for the "giants" to "tinies", respectively. *Right:* The fraction of orientations where the first "x" substructures also contain the first "x" subhalos in order, as sorted by mass. The frequency for $x = 1$ is equivalent to the frequency of the most massive aperture containing in projection the most-bound-particle, as it is the center of the most massive halo.

The correlation for $x = 1$ is of particular interest, as it describes the correlations between the point of deepest potential which forms the center of the galaxy clusters in three dimensions, so the most-bound-particle, and the most massive substructure (i.e., the main in projection). It demonstrates that the aperture containing the `SUBFIND` main is also subsequently the main in over 90% of the orientations. As an example, cases where this does not happen for the "giants" mass bin occur more than 20 times (i.e., in at least 10% of the total orientations) only for four clusters: numbers 20, 10, 1 and 18 have 152, 68, 58 and 25 orientations where the most massive substructure does not contain the most-bound-particle. It is apparent then that most galaxy clusters in projection directly correlate the most massive substructure to the most-bound-particle, and that there are only few exceptions to the rule. Interestingly, these extreme cases correspond somewhat to the galaxy clusters with those of high centershift, which is discussed more in Figure A.19.

Similarly, it can be considered whether having a high initial projected mass within an aperture is a guarantee for a resultingly high final mass after subtracting the contribution of the main halo or not. Generally, some halos may gain significant mass initially from the main halo by lying far towards the center, but then correspondingly have an equally significant fraction subtracted. Nonetheless, as seen in Figure A.20, having a high initial mass is correlated significantly more strongly with the final projected substructure mass than containing one of the most massive bound subhalos.

Figure 8.22 exactly depicts the relationship between the projected substructure mass to the most massive bound `SUBFIND` mass within the corresponding aperture. All mass bins exhibit the same triangular form, with a large scatter in M_{cyl} at lower values of M_s reducing to very little scatter at higher values, although the overall distribution exhibits the general trend
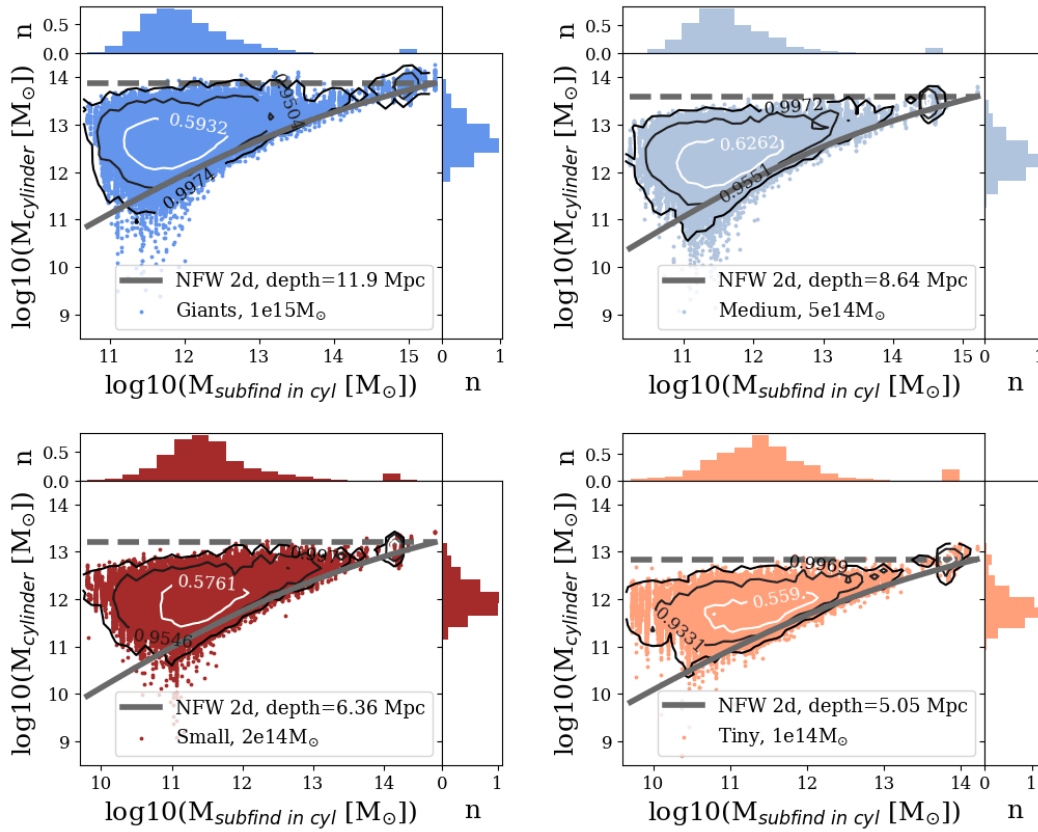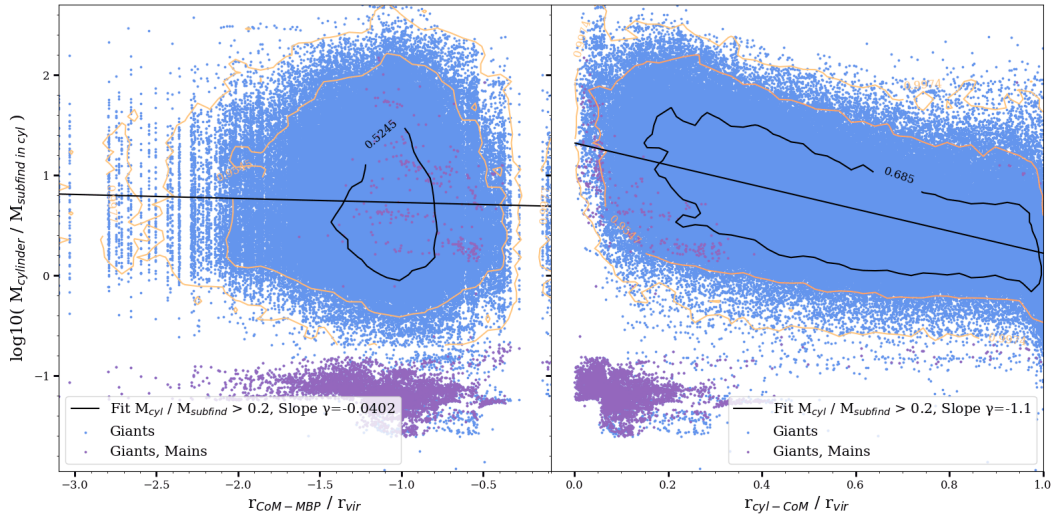
Figure 8.22: The aperture mass as a function of the most massive bound subhalo within it given by `SUBFIND`. The curved solid gray line denotes the projected mass within r_{ap} at constant depth r_{turn} as given in the legends for a given bound subhalo mass M_s assuming the subhalo to approximate an NFW-profile (such that Equation A.8 can be used) with concentration given by the $c - M$ relation from Ragagnin et al. (2019). Horizontal dashed gray lines denote this projected mass for the most massive M_s, with histograms depicting the number density n distribution of either M_s (*top*) or M_{cyl} (*right*). Contour lines contain the fraction of total orientations as written.

of higher substructure masses with higher bound masses, as can be seen from the contours nonetheless. Furthermore, the histograms show that the `SUBFIND` masses exhibit a second peak where the mains lie, which the aperture masses do not have (except very slightly for the "tiny" mass bin).

The solid gray line represents what the projected mass of a single isolated NFW-halo with the corresponding M_s would have when projected out to the depth of r_{turn}, as given by Equation A.8. Consequently, the fact that the main bulk of substructure masses lie on or above this line implies that the projected mass is in general *not* carried by a single subhalo! Instead, portions of the main halo mass as well as other subhalos are projected within the aperture. These effects become less relevant for increasing mass of M_s, where at the highest values the substructure masses lie rather close to what would result from a single halo in projection.

To disentangle the effects which lead to this scatter of $M_{cyl} - M_s$, when assuming that a portion of this increased mass is due to the main halo, it follows that those apertures closer to the center-of-mass should experience stronger increases. Also of interest is a follow-up on the

Figure 8.23: The ratio between a substructure's mass and its most massive bound subhalo M_{cyl}/M_s as a function of the centershift (*left*) and distance to the center-of-mass (*right*). Black solid lines are the linear best fits for all apertures with ratios above 0.2, to avoid the effects of the main halos depicted in purple. Contours contain the fraction of total orientations as written. The vertical lines of points appearing on the *left* are due to multiple substructures of one orientation having the same centershift, as it is a global property.

findings of Figure 8.19. Given that most extreme masses of the eighth substructure are found at high centershifts, are these masses being more strongly increased relative to their bound masses than those at lower centershifts? To this point, Figure 8.23 depicts the ratio between the substructure and maximal `SUBFIND` mass within apertures as a function of the centershift (left) and distance of the aperture to the center-of-mass (right) for the "giants" mass bin. This finds little dependence on the centershift, with contours exhibiting no distinct shape. Consequently, it can be concluded that a larger centershift does not imply that substructure masses will be increased more relative to their contained bound masses than is the case for lower centershifts. Conversely, for the apertures' distance to the center-of-mass a dependence is found. Apertures closer to it tend to have more substructure mass compared to the bound subhalo mass within them – aside from the mains lying at the bottom, which due to the localized extent of apertures lose a substantial amount of mass relative to what is assigned to them by `SUBFIND`.

Given the findings in Figure 8.23, the distance of substructures to the center-of-mass is of further interest as it impacts the ratio M_{cyl}/M_s. To better understand the general behavior, Figure 8.24 plots the relation from Figure 8.22 colored by the distance, where the trend from Figure 8.23 is found to persist for all mass bins. Those apertures farther in lie at overall higher projected masses, relatively independent from the actual underlying bound subhalo mass. The mains from `SUBFIND` also lie close to the center, as expected from Figure 8.21. Interestingly, the "arm" connecting the mains to the overall bulk of the substructures is made up primarily of apertures lying farther out, mirroring the findings in Figure 8.4 that very massive bound subhalos generally lie at larger distances from the galaxy cluster center. Though some projections can exist where these massive subhalos will appear close to the
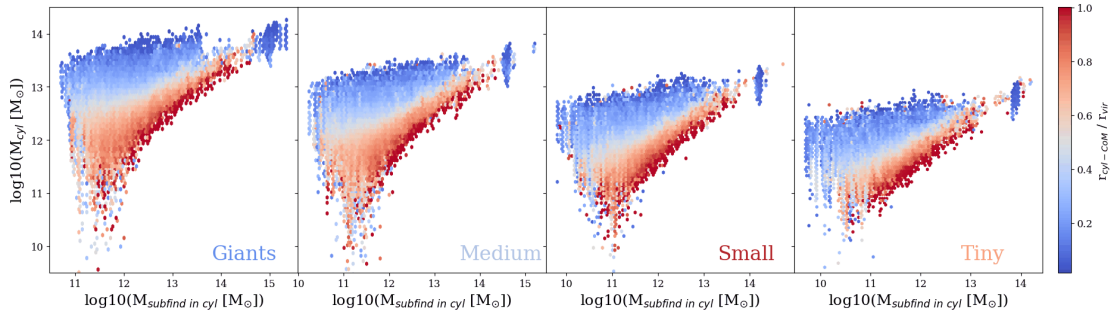
Figure 8.24: The aperture mass as a function of the most massive bound subhalo within it given by `SUBFIND`, binned and colored by the projected distance of the aperture to the center-of-mass. Binning is done via `hexbin` from Hunter (2007).

center, as shown in Appendix A.3, on average larger distances in three dimensions also result in larger distances in projection, explaining the trend towards larger radii. Overall, it is found that slopes of equal radii become more/less steep and thus $M_{\rm cyl}$ is more/less dependent on $M_{\rm s}$ for higher/lower projected distances.
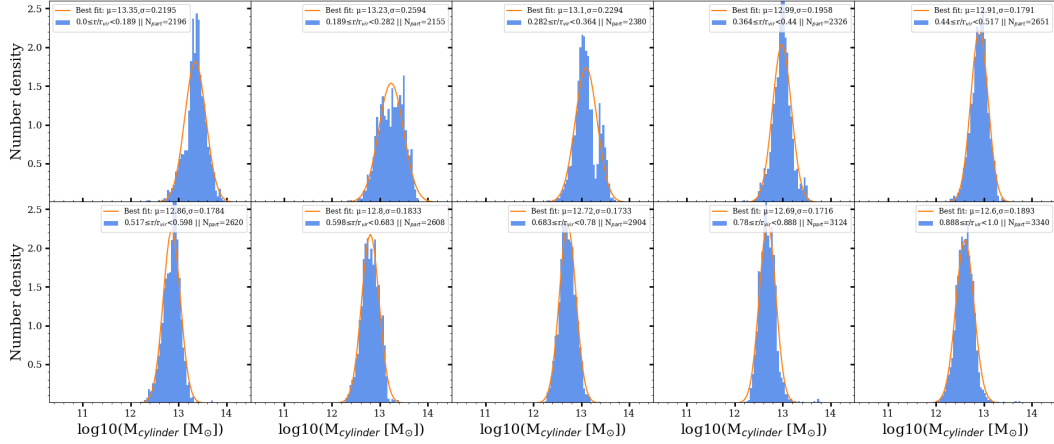
8.5.2   Modeling the Masses
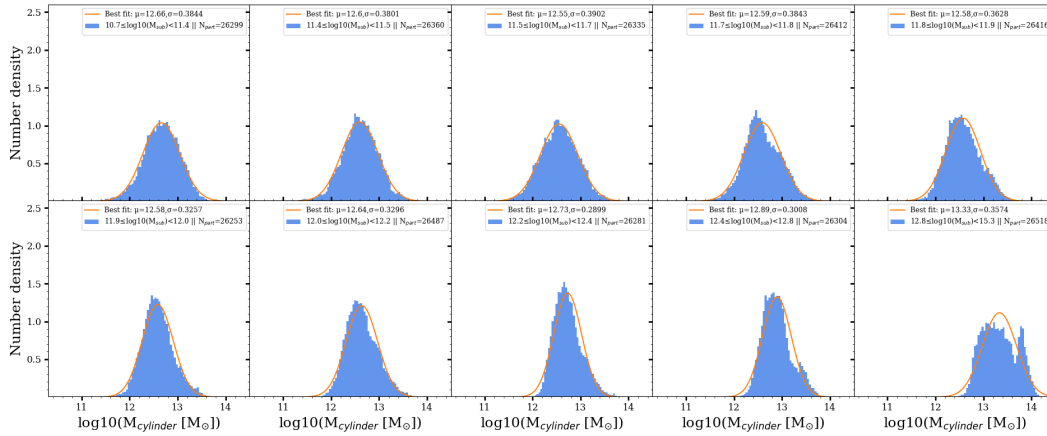
Figure 8.25: The distribution of substructure masses $M_{\rm cyl}$ for 10 different ranges of $M_{\rm s}$ as written in the legend, going from lowest to highest mass as *left* to *right*, then *top* to *bottom*. Orange lines are the best-fit single Gaussian models performed using the `Julia` "Distributions.jl" package by Besançon et al. (2021), with mean and variance as given in the legend.

Figure 8.25 depicts the initial step towards the model, where the range of $M_{\rm s}$ is split into 10 bins containing an equal number of orientations for the "giants". The distributions of substructure masses $M_{\rm cyl}$ take the form of an approximate single Gaussian, though especially for the bins at the high mass end of $12.2 \leq \log_{10}(M_{\rm s}[M_\odot])$ there is significant deviation in the distributions from the best-fit single Gaussian models shown in orange. Given the overall shape however, the model $M_{\rm cyl}(M_{\rm s}, r_{\rm c})$ will take the form of a single Gaussian, with the radial dependence from Figure 8.24 used to further disentangle the distribution. Taking for example the 9th mass bin, $12.4 \leq \log_{10}(M_{\rm s}[M_\odot]) < 12.8$, and splitting it further into 10

radial distance bins, the single Guassian fits better match the resulting distributions – see Figure 8.26. Nonetheless, there are still deviations present with some apparent double peaks; these will be discussed later in Section 8.5.3.

Figure 8.26: The distribution of substructure masses M_{cyl} of the second most massive M_s bin from Figure 8.25 for different ranges of r_c as written in the legend going from lowest to highest mass as *left* to *right*, then *top* to *bottom*. Orange lines are the best-fit single Gaussian models performed using the `Julia` "Distributions.jl" package by Besançon et al. (2021), with mean and variance as given in the legend.

The total range of apertures is split into 50 bins each for the two parameters, being the maximum `SUBFIND` mass in the cylinder M_s and the projected distance to the center-of-mass r_c, and single Gaussians are fit. This gives a set of 2500 pairs of (μ, σ). To construct the model $M_{cyl}(M_s, r_c)$, functional forms for μ and σ in dependence of the two parameters are required.

First, the variances σ of the Gaussian fits turn out to be dependent primarily on the `SUBFIND` mass, and not on the radial distance of the aperture to the center-of-mass. This can be see from Figure 8.27, where on the left σ goes noticeably from higher to lower values with increasing M_s, but stays approximately constant with varying r_c. The explicit dependence on M_s is plotted on the right, with the best-fit line for all bins in solid blue chosen as the model form of the variance, i.e.,

$$\sigma(M_s, r_c) = \sigma(M_s) = \gamma_0 \cdot \log_{10}(M_s[M_\odot]) + \sigma_0. \tag{8.2}$$

This is the same functional form used for σ for every individual mass bin.

The behavior of the means $\mu_{\rm fit}$ of the single Gaussians, however, exhibits a dependence on both r_c and M_s. This can be seen again for the representative mass bin of the "giants" in Figure 8.28, with the left depicting each of the 50 radial bins as a colored solid line in the $\mu_{\rm fit} - M_s$ plane. Overall, there is a tendency for all radial bins towards higher mean substructure masses of the fits $\mu_{\rm fit}$ with increasing M_s, where the values of r_c for the bins impacts both the slope and y-intercept of the relation – apertures farther in lie at higher values of M_{cyl} and subsequently $\mu_{\rm fit}$, and also make the slope more shallow as also seen in Figure 8.24. On the right in turn the same is depicted for the 50 M_s bins in the $\mu_{\rm fit} - r_c$
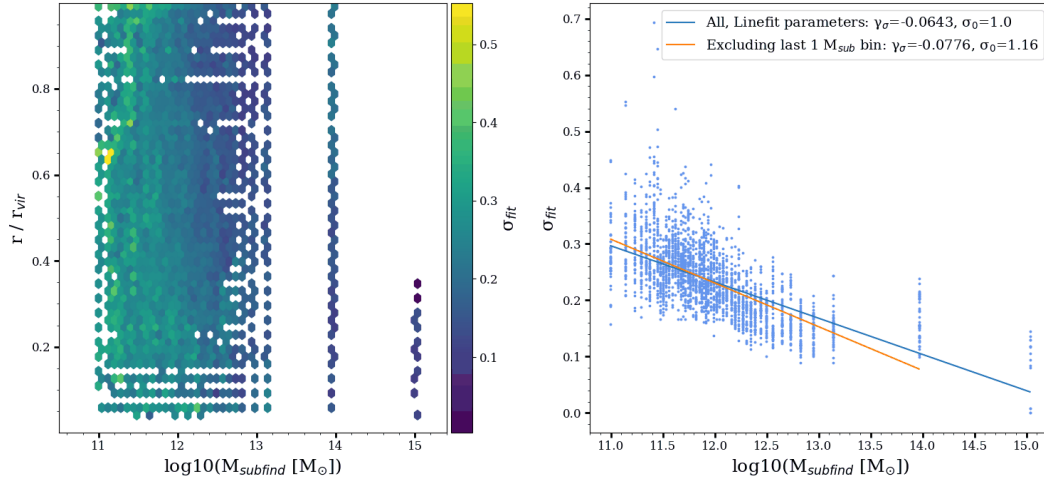
Figure 8.27: *Left:* The dependence of the variances σ of the Gaussian fits to the "giants". *Right:* σ from the single Gaussian fits as a function of M_{subfind}. The best-fit line for all points is given in solid blue, while that for all except the last mass bin (i.e., except the main halos) is solid orange, with slope γ_0 and y-intercept σ_0 for both as in the legend.

plane with the same behavior found. Noticeably, the highest M_s bin (the top cyan curve) has no orientations where the apertures containing these subhalo masses lie farther out than $35\% \cdot r_{\text{vir}}$.

For the curves both on the left and right generally good agreement is found with a simple line-fit, but the overall best fit was found for a parabolic functional form:

$$\mu_{\text{fit}}(a, b) = \alpha_b \cdot a^2 + \beta_b \cdot a + \mu_{0,b}, \tag{8.3}$$

with $(a, b) \in \{(M_s, r_c), (r_c, M_s)\}$ for the fits on the left/right sides of Figure 8.28.
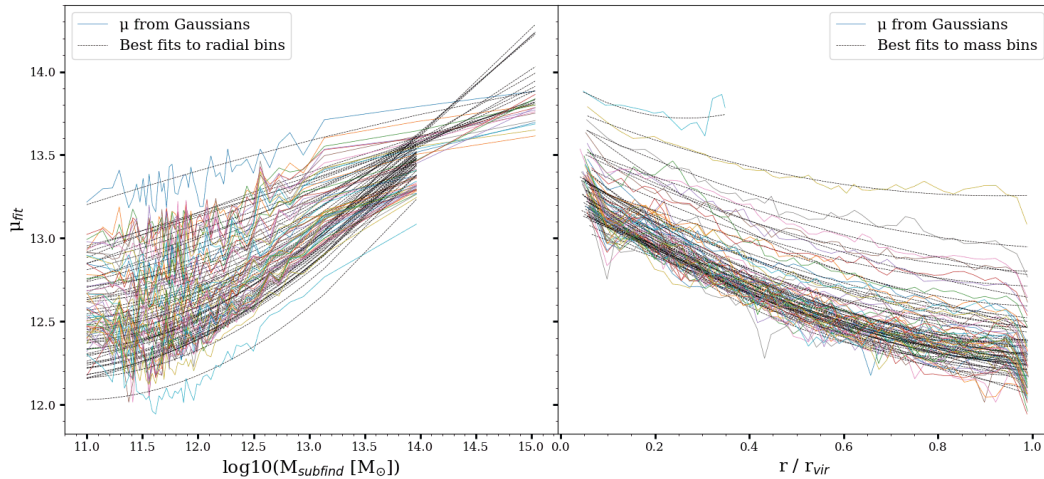

Figure 8.28: The dependence of the means μ_{fit} of the Gaussian fits to the "giants" for the different radial/subfind mass bins as a function of the subfind mass/radius on the *left/right* are plotted as colored solid lines, with the best fit parabolas of the form in Equation 8.3 as dashed black lines.

Continuing with the fits on the left of Figure 8.28, the behavior of the fit-parameters $\alpha_{r_c}, \beta_{r_c}, \mu_{0,r_c}$ if plotted as a function of the mean aperture distance r_c of each of the 50 radial
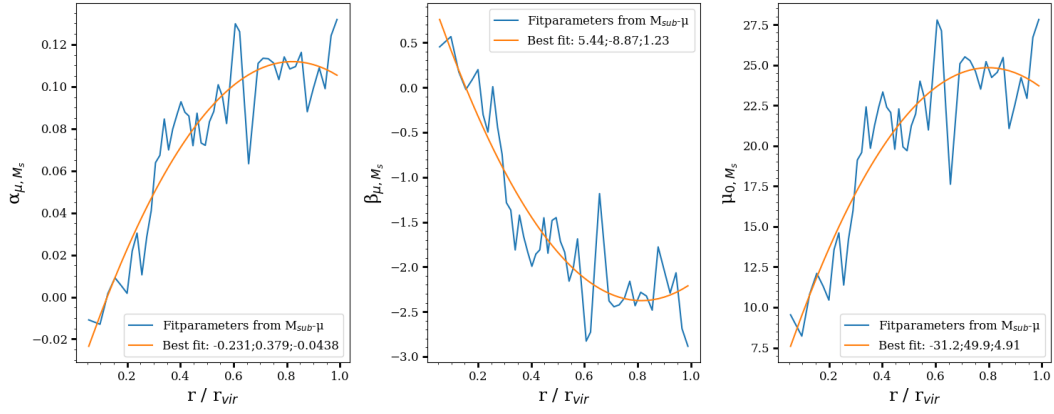
Figure 8.29: The behavior of the fit parameters of the parabolas from the $\mu_{\text{fit}} - M_s$ plane on the left in Figure 8.28 as a function of the mean aperture distances r_c of each radial bin. From *left* to *right* in order are α_{r_c}, β_{r_c} and μ_{0,r_c}. The orange solid lines represent the best-fit parabolas, with fitparameters A, B, M as written in the order of their lower-case occurrence in Equation 8.3. Note that these final nine parameters are *constants* for the entire mass bin, i.e., carry no further dependence as for example α_{r_c} has.

bins in Figure 8.29. Interestingly, α_{r_c} and μ_{0,r_c} follow very similar curves, while β_{r_c} does so with an inverted sign. The common behavior could indicate that the parabolic fits to the radial bins are constrained by a further, third parameter which gives a dependence as $\alpha, \beta, \mu_0 \propto f(r_c, p)$, though this goes beyond the scope considered here.
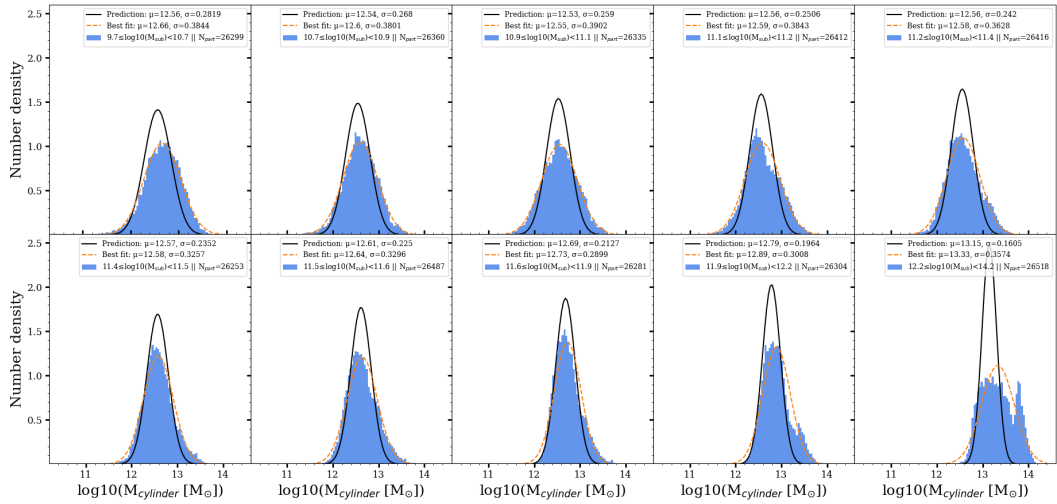
Figure 8.30: The predicted distribution of substructure masses M_{cyl} in black solid lines against the real values in blue, for 10 different ranges of M_s as written in the legend, going from lowest to highest mass as *left* to *right*, then *top* to *bottom*. Orange dashed lines are the best-fit single Gaussian models performed using the `Julia` "Distributions.jl" package by Besançon et al. (2021), with mean and variance as given in the legend.

Fitting the curves found in Figure 8.29 also with a parabolic function as in Equation 8.3 then gives the final functional form for the mean μ_{fit} of the predicted Gaussians when starting from the $\mu_{\text{fit}} - M_s$ relation as:

$$\mu_{\text{fit}}(M_s, r_c) = (A_\alpha \cdot (r_c/r_{\text{vir}})^2 + B_\alpha \cdot (r_c/r_{\text{vir}}) + M_\alpha) \cdot \log_{10}(M_s[M_\odot])^2$$

$$+(A_\beta \cdot (r_c/r_{\text{vir}})^2 + B_\beta \cdot (r_c/r_{\text{vir}}) + M_\beta) \cdot \log_{10}(M_s[M_\odot])$$
$$+(A_{\mu_0} \cdot (r_c/r_{\text{vir}})^2 + B_{\mu_0} \cdot (r_c/r_{\text{vir}}) + M_{\mu_0}), \tag{8.4}$$

where A, B, M are the parabola fit parameters for the orange solid lines from Figure 8.29 for the parameter in their subscript, and are constants for each mass bin. Figure A.21 then shows how well the so-calculated means μ_{fit} agree with all aperture values, though this does not yet account for the variance. The total prediction then depends on 11 fixed parameters, nine for μ_{fit} and the two (γ_0, σ_0) from the line-fit as in Equation 8.2.

The resulting predictions for the 10 initial M_s bins in Figure 8.25 are depicted with the model's predicted distribution as solid black lines in Figure 8.30. The values fed to the model are the mean r_c and median M_s for each bin, where for M_s the median is chosen due to the greater range of possible values where the jump to the values of the mains can lead to overestimation of the general behavior of the bin. Generally, the predicted distributions are found to match well to the actual ones. On the lower mass end the variance is predicted to be somewhat smaller than it actually is, as the M_s values within the bin scatter over a large range such that a single value for M_s is not sufficiently representative. The highest mass bin experiences similar problems which are exacerbated by the fact that it is clearly not comprised of a single Gaussian. Furthermore, the information contained in r_c is largely lost here for all bins as splitting the distribution only by M_s finds all possible values for r_c and the mean is then consequently $\approx 0.5 \cdot r_{\text{vir}}$, as can be seen from Figure 8.24.
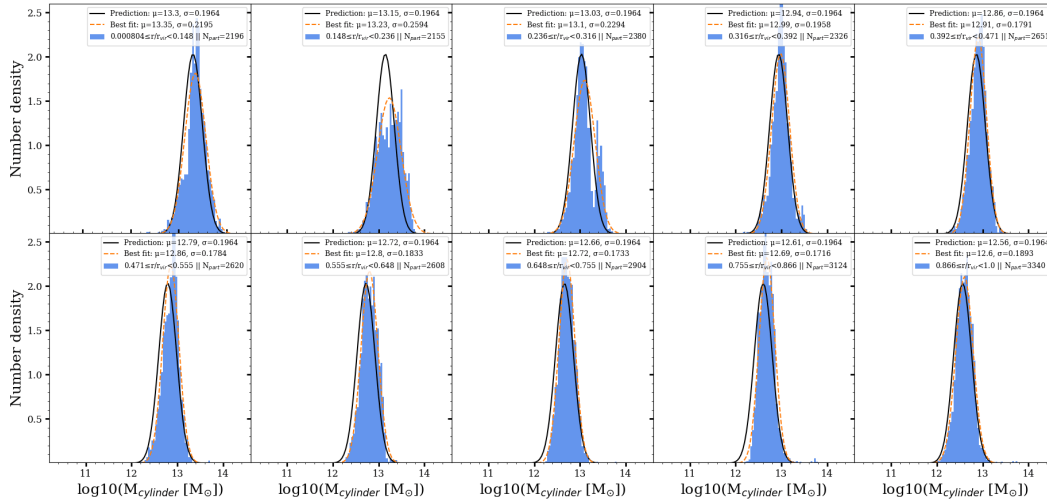
Figure 8.31: The predicted distribution of substructure masses M_{cyl} in black solid lines against the real values in blue, for the second most massive M_s bin from Figure 8.25 for different ranges of r_c as written in the legend going from lowest to highest mass as *left* to *right*, then *top* to *bottom*. Orange dashed lines are the best-fit single Gaussian models performed using the `Julia` "Distributions.jl" package by Besançon et al. (2021), with mean and variance as given in the legend.

Including the information contained in r_c strongly refines the model's performance, as can be seen when taking again the ninth M_s bin and splitting it into 10 r_c bins. The resulting distributions are plotted in Figure 8.31, where the predicted distribution in black very tightly matches the underlying real values of M_{cyl}. In particular the mean values of the predicted

versus explicitly fit Gaussians (black to orange dashed) match very closely, while the σ is comparable for most even though it is calculated only from the median value of M_s of the total bin.

Table 8.2: The fit parameters for σ and μ_{fit} in Equation 8.2 and Equation 8.4, providing the basis for the model in Equation 8.1.

	Giants			Medium		
(γ_0, σ_0)	-0.06430	1.004		-0.06274	0.9643	
$A_\alpha, B_\alpha, M_\alpha$	-0.2308	0.3790	-0.04376	-0.1726	0.2820	-0.02980
$A_\beta, B_\beta, M_\beta$	5.443	-8.866	1.233	3.922	-6.341	0.8907
$A_{\mu_0}, B_{\mu_0}, M_{\mu_0}$	-31.21	49.87	4.913	-21.492	33.88	6.607
	Small			Tiny		
(γ_0, σ_0)	-0.05690	0.8481		-0.05179	0.7549	
$A_\alpha, B_\alpha, M_\alpha$	-0.2910	0.2967	-0.01105	-0.1730	0.1307	0.02490
$A_\beta, B_\beta, M_\beta$	6.642	-6.537	0.4500	3.673	-2.419	-0.4200
$A_{\mu_0}, B_{\mu_0}, M_{\mu_0}$	-37.14	34.32	8.873	-18.54	9.010	13.87

Some general trends between the fits of the different mass bins can be found. For example, both parameters of the variance fits (γ_0, σ_0) decrease toward the lower mass bins, meaning that the variance becomes lower and more shallow in its dependence on M_s. Conversely, all y-intercepts of the parabola fits M_x increase toward the lower mass bins. In the future, possible trends of the model with the mass of the bins could perhaps allow for a more generalized form, $p(M_{\text{cyl}}, M_s, r_c; M_{\text{gc}})$, incorporating the mass of the galaxy cluster itself as the third parameter.

8.5.3 Subhalos: What do the Numbers Mean?

As found in Figure 8.26, even after the split-up according to M_s and r_c bins there exist some deviations from singular Gaussians. Though it is possible that these may be further reduced by choosing more fine bins, here the alternative is considered that further parameters play a role. Given the usage of the maximum bound subhalo mass M_s throughout, it is not unreasonable to assume that the total number of subhalos within the aperture has an impact on the final projected mass. For the high mass end of M_s, this is unlikely to make much of a difference as minor additional subhalos carry comparatively little mass, but this may not be the case for other less massive subhalos. To this end, the relation $M_s - M_{\text{cyl}}$ is plotted for apertures with 1, 2, 3 and 4 or more in Figure 8.32.
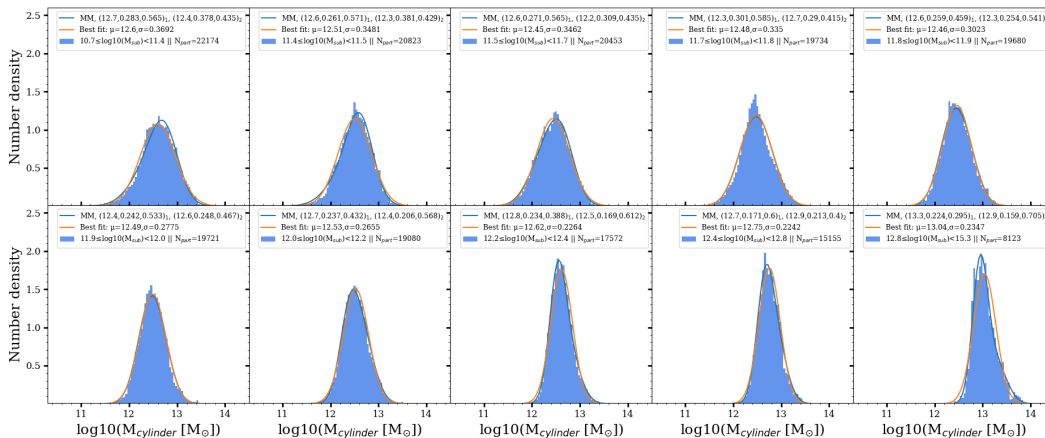
Apertures with higher numbers of bound subhalos tend up and to the right in the $M_{\text{cyl}} - M_s$ relation. The trend of the lower bound going to increasingly higher M_{cyl} with increasing subhalo numbers interestingly implies that higher numbers of subhalos within a single aperture are found predominantly at lower distances from the center-of-mass, as they lie at similar positions in the $M_{\text{cyl}} - M_s$ relation (see Figure 8.24). It is unclear here if the masses of the subhalos themselves push the projected masses upwards, or if conversely other properties of
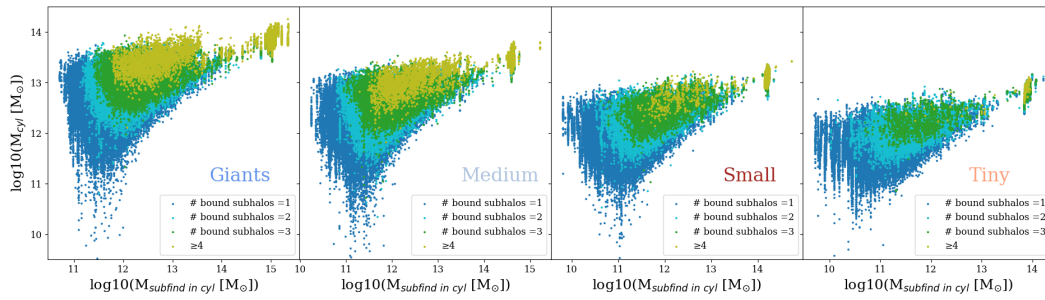
Figure 8.32: The aperture mass as a function of the most massive bound subhalo within it M_s, with apertures with increasing numbers of bound subhalos plotted over each other. Note that apertures with just one bound subhalo are by far the most numerous, such that to see the placement of those with higher numbers they are plotted on top. This does not imply that no halos are found within the overplotted regions with lower numbers.

the more massive projected apertures lead to increased numbers of bound subhalos within them. Given that little difference is found between the general form of $M_{\mathrm{cyl}} - M_s$ relation between M_s being the single most massive subhalo in Figure 8.22 versus being the total summed subhalo mass within the apertures in Figure A.22, the latter reasoning seems more likely.

The second trend to higher M_s with increasing subhalo numbers is curious, as it implies that to find multiple subhalos in the same aperture one of them must be of an increasing mass. This may, however, be simply statistical in nature, where for a random sample of a higher number of subhalos it is more likely to find one having a higher mass.

Figure 8.33: The aperture mass as a function of the most massive bound subhalo within it M_s, with apertures with increasing numbers of bound subhalos plotted over each other. Note that apertures with just one bound subhalo are by far the most numerous, such that to see the placement of those with higher numbers they are plotted on top. This does not imply that no halos are found within the overplotted regions with lower numbers.

Nonetheless, when splitting all substructures by their number of bound subhalos and then taking only those with exactly one, Figure 8.33 shows that the split up into 10 bins according to M_s finds behavior in the distribution of substructure masses M_{cyl} closer to single Gaussians than when not pre-selecting apertures as in Figure 8.25. Especially the most massive M_s

bin becomes noticeably more regular, losing its second peak. To emphasize this point, mixture models of two overlayed Gaussians are also fitted to the distribution as a blue line to compare to the orange line fitted for a single Gaussian, and little difference between the two is found, indicating little presence of secondary peaks. The mixture models are fitted via the `GaussianMixtures.jl` package (van Leeuwen, 2022). Given the findings here, as well as the correlated behavior of the fit parameters found in Figure 8.29, it is then of great interest in the future to further explore potential additional parameters and their impact on the projected masses of substructures in relation to the underlying bound subhalo masses. For example, in addition to the number of subhalos discussed here, one could consider separating apertures into bins based on the curvature of the main-halo fit from Section 6.3, or instead based on the large-scale dynamical state of the galaxy cluster, for example via the centershift discussed in Section 8.4.

8.6   Reproducing Abell 2744

This section will answer the fourth question posed in Chapter 1: Can the extreme substructure masses found in observations be explained in the paradigm of ΛCDM when also including baryonic physics? In particular, the focus is placed on the eight massive substructures found by Jauzac et al. (2016) within galaxy cluster Abell 2744 through the use of weak- and strong-lensing, discussed in more detail in Section 5.1. First, the specific orientation found to best reproduce the masses in Abell 2744 is discussed, before moving on to more generally quantify *when* orientations become host to such large masses, identifying one parameter in particular to correlate strongly to such cases.

Figure 8.34 depicts the projection of galaxy cluster number 20 of the "giants" mass bin, with the method from Chapter 6 summarized in four steps. Depicted in order from top to bottom and left to right are the initial read-in with subsequent center-of-mass determined as a blue cross (Section 6.1), the second read-in around this center (Section 6.2), the main halo fit after masking the apertures (Section 6.3) and finally the resulting first eight substructure masses. It is important to note that the orientation exhibits a noticeable centershift (top left) and that the resulting substructures are all quite close to the center-of-mass, which can be seen also more clearly in Figure 8.35, similar to Abell 2744 where all eight substructures are within 1 Mpc of the most massive substructure (Jauzac et al., 2016).

Most interesting, however, are the resulting mass fractions of the eight substructures relative to the total mass within 1.3 Mpc plotted in the bottom right as orange crosses. Aside from the less massive first, the remaining substructure mass fractions match those found by Jauzac et al. (2016) for Abell 2744 remarkably well, in stark contrast to the mass fractions for subhalos from `SUBFIND` plotted as cyan stars. This provides strong evidence that such masses are the result of projection effects, and that they are reproducible for the WMAP-7 cosmology (Komatsu et al., 2011) used by `Magneticum Pathfinder`. The substructure masses and mass fractions are summarized in Table 8.3.
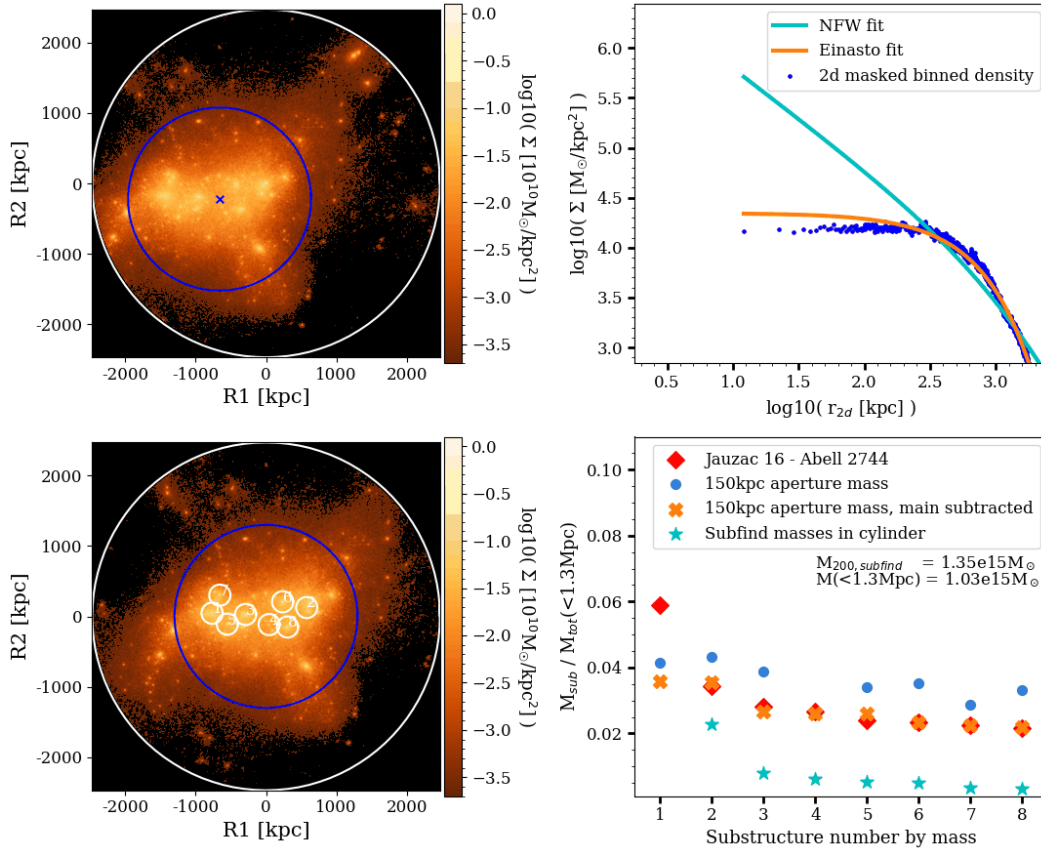
Figure 8.34: *Top left:* The initial $1 \cdot r_{\mathrm{vir}}$ read-in centered on the most-bound-particle in projection used to determine the center-of-mass, indicated by the blue cross. The blue circle represents 1.3 Mpc around the center-of-mass, and colors are the smoothed surface mass density as described in Chapter 6. *Bottom left:* Final projected area of $1 \cdot r_{\mathrm{vir}}$ localized on the center-of-mass, with while circles denoting the positions of the eight massive substructures identified. *Top right:* The main halo surface density profile after masking (blue dots) and the chosen Einasto fit (solid orange line) as well as a fit to an NFW-profile for comparison (solid cyan line). *Bottom right:* Aperture masses before (blue dots) and after (orange crosses) subtracting the mass contribution from the main halo, given as a fraction of the total mass within 1.3 Mpc M_{tot}. Red diamonds denote the substructure mass fractions as listed by Jauzac et al. (2016). The masses of the eight most massive subhalos (cyan stars) within r_{vir} are plotted for comparison as a fraction of M_{vir}, which is comparable in mass to M_{tot}.

It should be noted here however that the total mass present within 1.3 Mpc for the projection of galaxy cluster 20 of the "giants" is around a factor of 2 smaller than that of Abell 2744, namely $1.03 \times 10^{15}\,\mathrm{M_\odot}$ versus $2.3 \times 10^{15}\,\mathrm{M_\odot}$ (Jauzac et al., 2016). This

Table 8.3: The 8 substructure masses determined within 150 kpc apertures for galaxy cluster 20 of the "giants" as well as Abell 2744, with values for the latter as determined by Jauzac et al. (2016).

|	1	2	3	4	5	6	7	8
Abell 2744 identifiers	Core	NW	S3	N	S4	S2	W_{bis}	S1
$M_{\mathrm{A2744}}/M_{<1.3\,\mathrm{Mpc}}$ [%]	5.9	3.4	2.8	2.7	2.4	2.3	2.3	2.2
$M_{\mathrm{Cl20,cyl}}/M_{<1.3\,\mathrm{Mpc}}$ [%]	3.6	3.5	2.6	2.6	2.6	2.3	2.2	2.2
M_{A2744} [$10^{13}\mathrm{M_\odot}$]	13.55	7.9	6.5	6.1	5.5	5.4	5.2	5.0
M_{Cl20} [$10^{13}\mathrm{M_\odot}$]	3.7	3.7	2.7	2.7	2.7	2.4	2.3	2.3
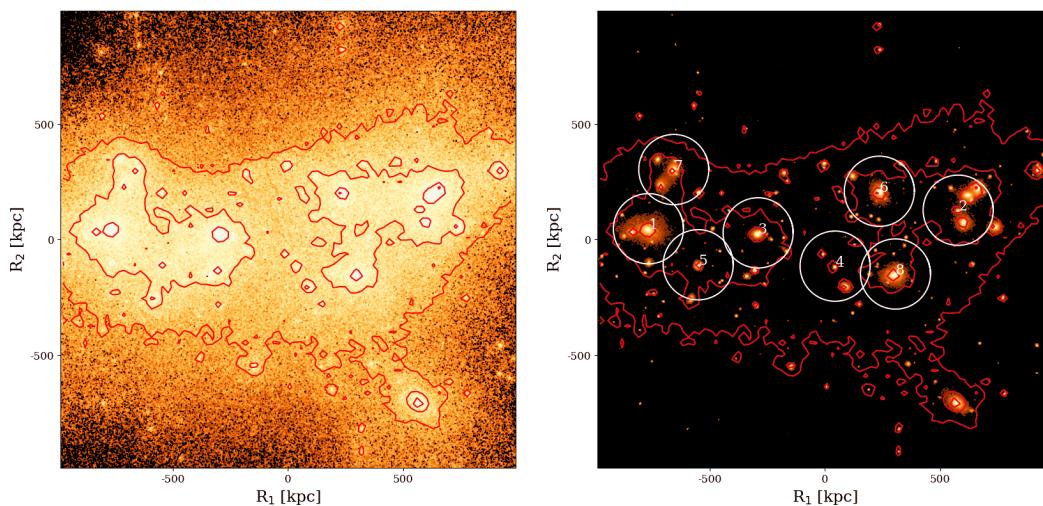
Figure 8.35: The total (*left*) and stellar (*right*) surface mass density maps of the central 1 Mpc^2 region in the bottom left of Figure 8.34. White circles on the *right* denote the 150 kpc apertures enclosing the eight substructures, with numbers denoting their order by mass. Red curves denote isodensity contours, increasing by factor 2 between each.

subsequently is also the case for the absolute masses of the substructures, as seen in Table 8.3. However, as can be seen in Section 8.3 and in particular Figure 8.9, the mass fractions scale self-similarly between different mass ranges for the employed projection method, such that it can be assumed with some certainty that Abell 2744 can be reproduced also in absolute terms when using a larger simulation box volume. This is thus in agreement with the findings by Schwinn et al. (2018) in that a significant portion of the mass in projection is contributed by the main halo.

Given that the substructures of Abell 2744 can be reproduced, the question then becomes under which conditions this can occur. Beginning with the example of the substructure masses for galaxy clusters number 5 and 20 of the "giants", Figure 8.12 is updated to include the eight most massive subhalo mass fractions within r_{vir} as given by SUBFIND in Figure 8.36. The horizontal dashed black line represents the mass fraction of the eighth most massive substructure of Abell 2744 as given in Table 8.3.

As seen on the left of Figure 8.36, galaxy cluster 5 never manages to produce even a sixth substructure with the mass of the eighth of Abell 2744, instead falling below it by a factor of 2. The overall distribution falls off steeply, with especially the subhalo mass fractions from SUBFIND reaching negligible values very rapidly. On the other hand, although the mean substructure mass fraction of galaxy cluster 20 lies below the values for Abell 2744, they lie within the bounds, with up to the sixth also occurring with relative frequency. The extreme values for the seventh and eighth are, however, rare overall. Nonetheless, this provides clear rationale for the difference between galaxy clusters which can and which cannot reproduce orientations with high substructure masses, namely the dynamical state. Galaxy cluster 5 is one of the most relaxed clusters of the "giants" while the converse holds for 20, as can be seen in Figure 8.20. In particular there is a noticeable difference in the centershift. This is consistent with the findings in Figure 8.19, where it is observed that to achieve high numbers
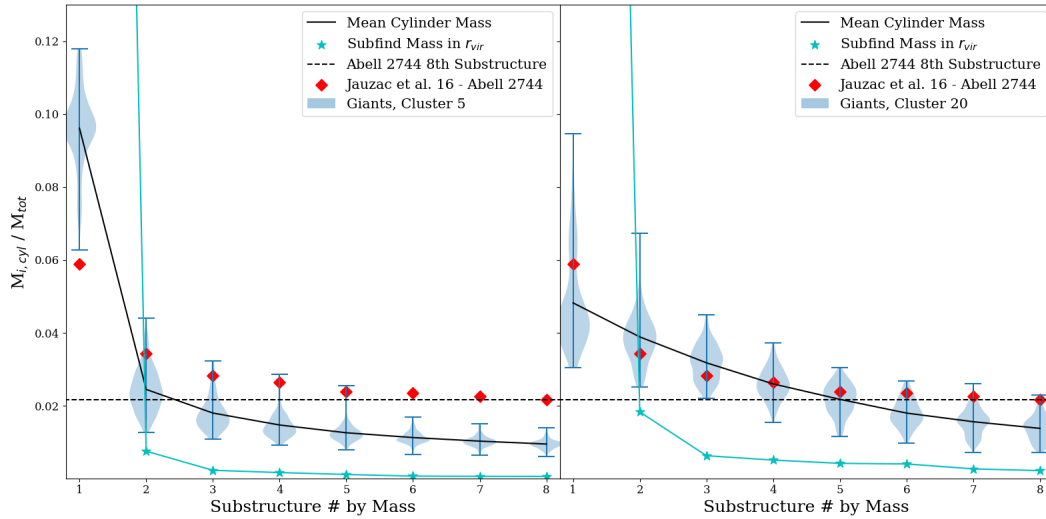
Figure 8.36: The distribution of the mass fractions for the eight most massive substructures within r_{tot} as a function of their substructure number for galaxy clusters 5 (*left*) and 20 (*right*) of the "giants" mass bin for all 200 orientations. Blue error bars denote the overall spread while the blue shaded area represents the percent number of orientations at each mass fraction, with a larger bulge meaning a larger percentage. Red diamonds denote the substructure mass fractions as listed by Jauzac et al. (2016), with the black dashed line equal to the mass fraction of the eighth. The masses of the eight most massive subhalos (cyan stars) within r_{vir} are plotted for comparison as a fraction of M_{vir}.

of substructure with the highest apertures masses, the projection considered must exhibit a high centershift.
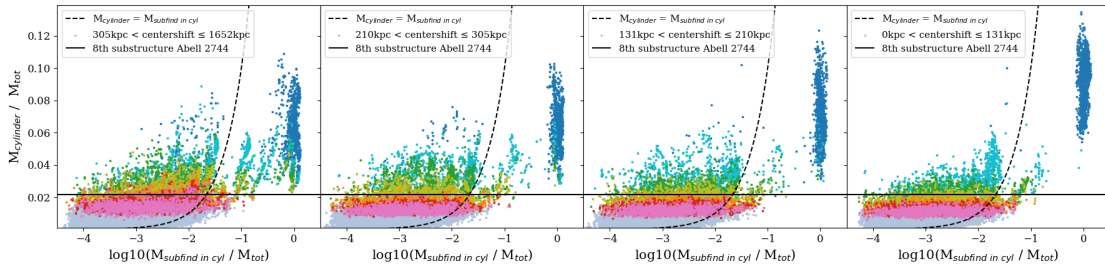

Figure 8.37: The mass fractions of substructures as a function of the mass of the most massive bound subhalo within them, split into four bins going from the orientations with the highest (*left*) to lowest (*right*) centershifts. Substructures are colored according to their position within the orientation based on mass, where the most massive substructure of a given orientation is colored in blue and the second most massive in cyan. This continues until the eighth in the sequence of: green, olive, drab olive, orange, red, pink, with all remaining apertures colored in silver.

Figure 8.37 demonstrates this point even more clearly, where all substructures of the "giants" are split into four bins based on the centershift of the orientation from which they stem. Furthermore, substructures are colored according to their ordering by mass for a given orientation, with the most massive apertures in blue and the eighth most massive apertures in pink. The solid black line denotes the mass of the eight substructure of Abell 2744, such that any pink point lying above this line is part of an orientation with eight similarly massive substructures to Abell 2744. There are 58 such orientations out of 5800 total, so 1%, of which 57 lie in the left most bin – at the highest orientations with highest centershift. The
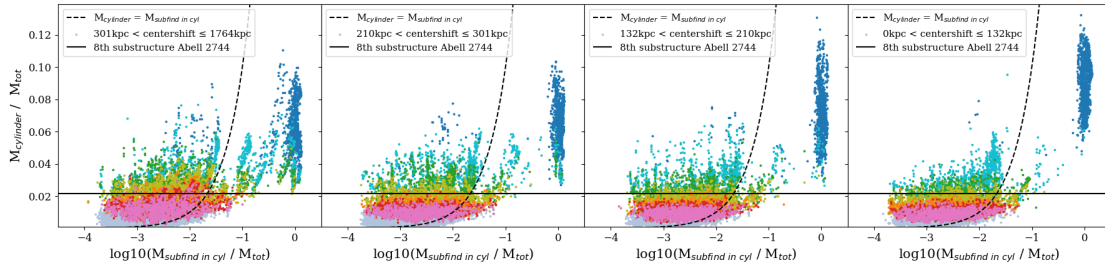
Figure 8.38: As in Figure 8.37, but done for the alternative stellar mass cut based on equal numbers of apertures (see Section 7.2).

one exception lies in the second centershift bin from the left, with none in the right two. It can be concluded then that to reproduce such high substructure masses, a large centershift is a necessary condition. As for the general behavior, it is found that for decreasing centershift, the mass fractions contained within the mains in blue steadily increases, while simultaneously the mass fractions of higher substructure numbers decrease, where for the lowest centershifts on the right even the fourth substructure (olive dots) rarely manages values above 2%.
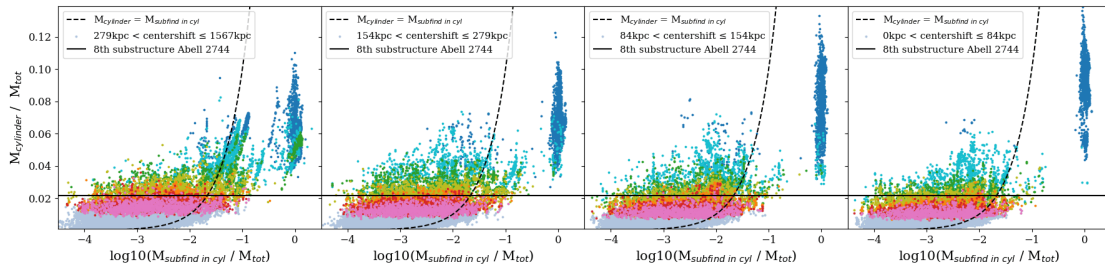
Figure 8.39: As in Figure 8.37, but for the "medium" mass bin with the default stellar mass cut scaled with virial mass (see Section 7.2).

This is also found to be the case for the other scaling method from Section 7.2, as shown in Figure 8.38 for the same "giants" mass bin. The lower number of apertures placed for the method (around 19 on average, see Table 7.1) still allows for orientations where the eighth substructure reaches a mass fraction equal to or above that for Abell 2744, namely 39 of 5800 total. All of these lie in the bin on the far left for the highest centershift. Furthermore, the behavior is also consistent with that found for other cluster mass bins, with the substructures from galaxy clusters of the "medium" mass bin depicted in Figure 8.39. Here 46 such orientations are found, with a broader spread than for the "giants". From left to right, there are 30, 4, 9 and 3 cases per centershift bin. Nonetheless, the overall majority are again within the bin of highest centershift. An overview of all such cases for the different mass bins is given in Table 8.4.

This constitutes the first reproduction of these extreme substructure masses with a hydrodynamical simulation, and is consistent with the findings by Schwinn et al. (2018) who employed the dark matter-only simulation `Millenium-XXL` (Angulo et al., 2012). It is of note that similar

Table 8.4: The number of orientations with eighth substructure mass fractions relative to M_{tot} in excess of 2.17% split up for each of the four mass bins based on the centershift into four bins containing a quarter each of the total 5800 orientations.

|	Giants	Medium	Small	Tiny
centershift	M_{vir} scaled			
Top 25%	57	30	30	10
Third quartile	1	4	5	0
Second quartile	0	9	3	0
Lowest 25%	0	3	2	0
centershift	N_{sub} scaled			
Top 25%	39	12	19	10
Third quartile	0	4	0	1
Second quartile	0	3	0	0
Lowest 25%	0	0	0	0

In summary, galaxy clusters with comparable substructure masses to Abell 2744 in projection are found within box 2b of the `Magneticum Pathfinder` simulation (Dolag, 2022). For the largest 29 galaxy clusters, such orientations occur for around 1% of all cases, making them rare but not impossible. The parameter found to correlate most strongly to a very high eighth substructure mass is the centershift, with higher values being generally necessary for the most extreme masses. It is exceedingly rare to simultaneously have an eighth substructure mass fraction in excess of 2.17% and centershift in the range of the lowest 25% overall, occurring for only 0.02% of all projections. Note, however, that Jauzac et al. (2016) themselves stipulate W_{bis} to be a background structure, such that it is not impossible for the projection to be one such rare case.

It should be noted further that the mass-to-light ratios, determined through the method from Jauzac et al. (2015), of the four least massive substructures, $S1$, $S2$, $S4$ and W_{bis} are in excess of 100, which for the close projected proximity to the cluster center, in particular of $S1$, appears curious. These could perhaps be indicative of significant mass from the main halo being included, which would coincide with the present findings. It can be concluded that at any rate accounting for projection effects is of utmost importance.

8.7   Filaments and Accretion

Though the preceding sections have provided in-depth analyses of the projected and three-dimensional properties of simulated galaxy clusters over a broad mass range, these objects are much too complex to consider every interesting aspect they posses. There are numerous further avenues to consider for future research with too many to list here, but this section will provide at least a brief outlook on two such considerations: the large-scale structure as well as the usage of the accretion history as potential tracers for the dynamical state of a galaxy cluster. Furthermore, as one of the key findings of this thesis is that the way objects

are observed has a large impact on their determined properties, some alternatives to the conditions for the placement of apertures are discussed at the end.
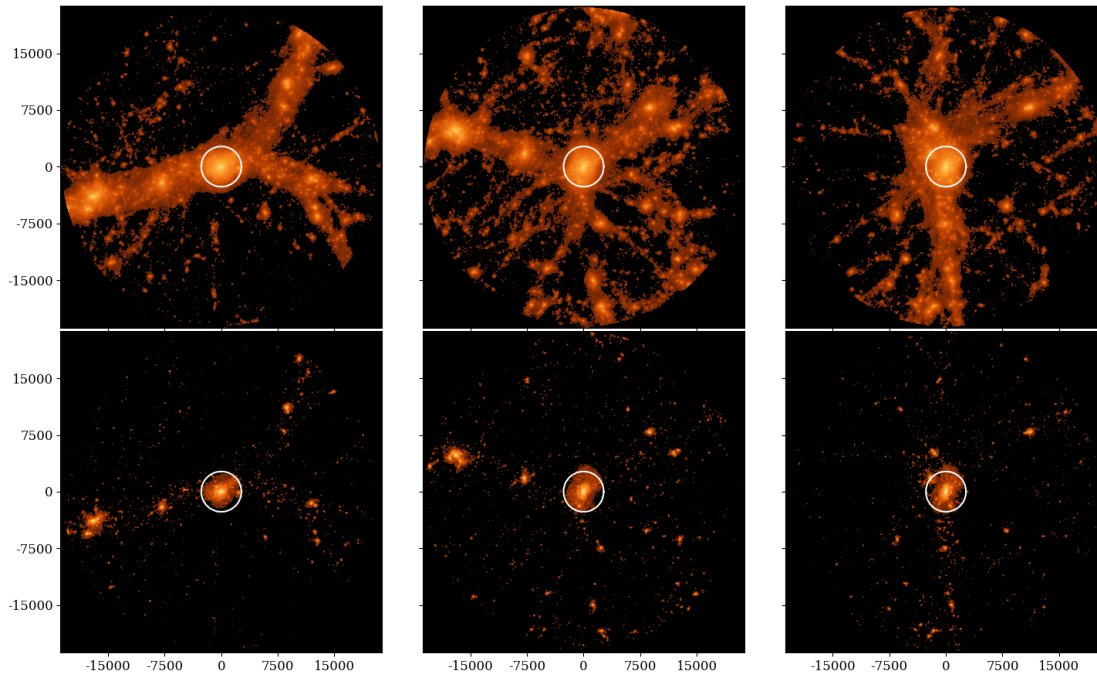
Figure 8.40: The large scale structure surrounding galaxy cluster 5, projected out to a depth of r_{turn} once for the total mass (*top row*) and for the stellar mass (*bottom row*). Columns depict the projection along the z-, y- and x-axis, respectively, and the cutout shows an area of $8 \cdot r_{vir}$. The central white circles denote $1 \cdot r_{vir}$ centered on the galalxy clusters most-bound-particle.

Beginning with the large-scale structure, it can be argued that the surroundings of galaxy clusters have yet to fall in, and structures which have fallen in are not in the surroundings anymore. Therefore, the large-scale structure should only provide information about the future evolution of galaxy clusters, as opposed to making statements about its current or past state. It should be noted that even in this case, the surrounding large-scale structure will still have an impact on some of the typical observational measures such as for lensing (see Section 5.2) and Compton-distortion because these have little line-of-sight resolution (White et al., 2010). Thus, when comparing properties determined from observations and simulations this impact must be taken into account – as demonstrated throughout this thesis for the case of substructure masses. Furthermore, as shown by White et al. (2010), in the case of the large-scale filaments feeding galaxy clusters the velocities of galaxies within the cluster do generally trace the large scale anisotropy. The large-scale properties are further interesting as they can provide insight into the "missing baryons" problem (Cen & Ostriker, 1999), where for the specific case of Abell 2744 Eckert et al. (2015) find a substantial amount of gas present as a warm hot intergalactic medium (WHIM). Similar analyses could be conducted in the simulations, and perhaps even linked to the dynamical state of the galaxy clusters – compare Figure 8.41 to Figure 1 from Eckert et al. (2015). The large-scale structure for galaxy cluster 1 of the other three mass bins is found in Appendix A.6.
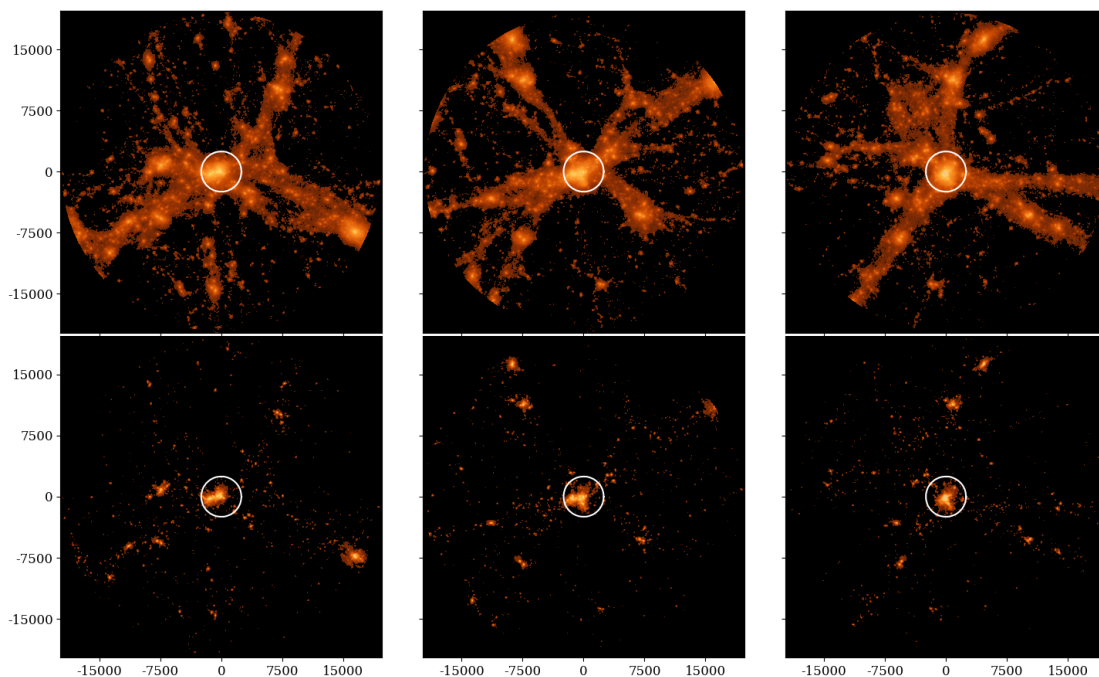
Figure 8.41: The large scale structure as in Figure 8.40, but for galaxy cluster 20 of the "giants".

Turning then to the second parameter, the accretion history, first recall that as discussed in Section 4.3.1 and Section 8.3 one of the typical tracers for the dynamical activity is that of the total subhalo mass fraction. This is as the balance between accreted subhalos and tidal stripping for later times tips in favor of the latter, meaning that the presence of large amounts of substructure is indication of recent merging events as were they farther back stripping would have removed significant portions (Neto et al., 2007; Jiang & van den Bosch, 2017). One of the great advantages of simulations, however, is that the accretion history *is known* and can be traced. For eight galaxy clusters from the "giants" mass bin the main halo mass M_{200} is depicted as a function of redshift on the right of Figure 8.42, while the left shows the correlation between the amount of accreted mass and the eighth substructure mass fraction at $z = 0.252$.

Solid lines mark the accretion history of the highly relaxed cluster according to the centershift and d_8, especially galaxy cluster 5. Dashed lines mark the same for dynamically active galaxy clusters, in particular of number 20. As can clearly be seen, the latter half just recently accumulated large fractions of their mass, especially 20 and 10, while the former have accreted most of their mass already at higher redshifts. This clearly supports the previous conclusion that galaxy clusters with multiple substructures have only recently accreted significant amounts of their present-day mass.

Finally, some alternative to determining the placements of apertures are considered. Recall that for the placement of apertures, as described in Section 6.2, the centers of subhalos from SUBFIND fulfilling a stellar mass cut are used as potential origins. Around these origins, using the stellar mass map, the nearby most massive pixels are searched out within r_{conv} and then sorted based on the total stellar mass within a 9×9 grid of pixels, which means this grid
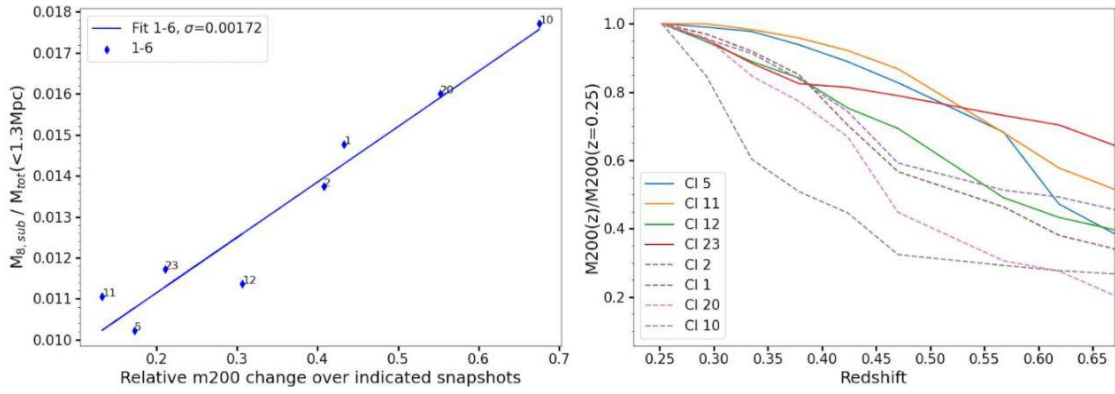
Figure 8.42: *Left:* The eighth substructure mass fraction determined at $z = 0.252$ for the four galaxy clusters of the "giants" with the highest and lowest d_8 as a function of the amount of accreted mass over five previous snapshots relative to M_{200}, i.e., $x = 1 - M_{200}(z = 0.252)/M_{200}(z = 0.47)$. The best-fit line is depicted in solid blue, where σ is the standard deviation of the fit as given in the legend. *Right:* The mass accretion history for the same eight clusters.

of pixels includes the central pixel and extends a distance of $s_{\mathrm{pix}} = 4$ out in each direction. Apertures are then placed from going from high to low masses.
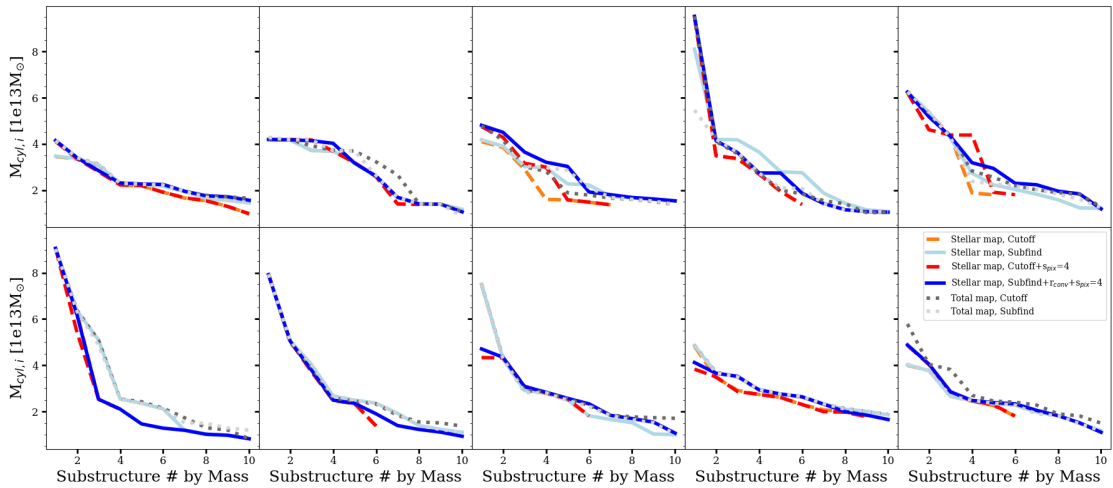
Figure 8.43: The substructure mass for ten random orientations of galaxy cluster 20 of the "giants" as determined for six different methods of aperture placement. Dashed lines are for usage of a stellar map with a simple cutoff for pixel values, sorted by the single pixel masses (orange) or by their summed mass in a 9×9 grid (red). Solid lines are for beginning with the centers of subhalos above a stellar mass cut, again sorting either by single pixel masses (light blue) or by the summed grid mass surrounding the highest mass pixel within r_{conv} (blue). The latter is the method used throughout. Finally, dotted lines correspond to using the total mass map, sorting by the masses of single pixels either determined through a cutoff (dark gray) or by subhalo positions (light gray).

As the first alternative, the initial positions from `SUBFIND` could be used immediately, sorted purely by the mass value of the pixel in which they lie. Secondly, instead of beginning with subhalo positions the stellar mass map itself can be used directly, where the potential origins for apertures are then simply all pixels with a mass above some cutoff. The origins from this cutoff can then be sorted directly or by the summed grid with $s_{\mathrm{pix}} = 4$. Finally, instead of the stellar mass map, the total mass map can be used, with initial positions given

either by the cutoff or by `SUBFIND` subhalo positions. These variants are applied to ten random orientations of galaxy cluster 20 of the "giants", with the resulting first ten substructure masses plotted in Figure 8.43.

Generally, the methods find substructure masses that are more comparable among themselves for a single orientation than to the same method applied to other orientations of the galaxy cluster, demonstrating that all methods trace the overdensities in a similar fashion. The largest difference overall is found for the stellar mass map with a simple cutoff, both when sorting by single pixel as well as by summed pixel masses, where the resulting substructures tend to lie at lower masses. Furthermore, often not more than six apertures are identified. This could, however, imply that the cutoff should be placed lower for the stellar map. An interesting conclusion is that the usage of the total mass map versus the stellar mass map makes little difference, implying that within galaxy clusters stars trace mass. This is consistent with the findings by Bahcall & Kulier (2014) for weak-lensing observations, where the mass-to-light profile remains practically constant for radii beyond the BCG.

8.8   The Lessons Learned

Section 8.2 has discussed subhalo mass fractions when using `SUBFIND` in `Magneticum Pathfinder`, finding generally $f_{\text{sub}} \approx 5\%$ to 10% for all four mass bins. f_{sub} is shown to strongly correlate especially for the lower mass bins with the second subhalo mass, which usually contains between 1.2% to 1.8% of the galaxy cluster virial mass by itself. Stellar subhalo masses are seen to be relatively constant across all radii, contrasted to the total subhalo mass which increases outwards. This indicates that the dark matter component of subhalos is more prone to stripping (see Section 4.3.1) than the stars. In Section 8.3, the projected substructures mass fraction is shown to be noticeably higher than its three-dimensional counterpart, reaching $f_{\text{cyl}} \approx 10\%$ to 27% with increasing values for the more massive galaxy clusters. The dependency on the second substructure mass is considerably less stringent than for the subhalos, instead finding the mass fractions of substructures number 4 and above to be better indicators for high substructure mass fractions. Furthermore, there appear systematic differences between galaxy cluster substructure mass distributions, with some having significantly more shallow slopes compared to others with more strongly falling distributions. This behavior can be characterized by the slope between substructures number 1 and 8, defined as d_8, and is found to correlate with f_{cyl}. Section 8.3.1 illustrates for the example of two strongly differing galaxy clusters from the "giants" that the projection depth beyond r_{vir} has only a marginal impact on the resulting substructure masses. For the case of individual bound versus projected masses, Section 8.3.2 finds the projected distance to the center-of-mass to strongly determine the increase of the latter from the former and demonstrates that the resulting substructure mass fraction is consistent with lensing observations. Generally, the total mass contained within substructures increases substantially in projection by a factor of 2 to 3. Section 8.4 then analyzes the centershift s as another typical tracer for the dynamical

state of the galaxy cluster and finds it to be significantly more stable between projection and three dimensions than the total substructure mass fraction.

On the basis of these findings, Section 8.5 developed a conversion function from bound to projected masses. It was first seen that the lower limit of the possible projected masses M_{cyl} is approximately given by a simple projection of the bound mass M_s when assuming an NFW profile. Similarly, the general behavior finds a direct correlation between bound and projected masses, while the upper limit is largely independent of bound mass. The responsible degenerate parameter was found to be the projected distance r_c, such that when an aperture lies closer to the center-of-mass it can gain significant amounts of mass irrespective of the actual bound mass present within it. Consequently, the apertures were binned according to M_s and r_c and the resulting distributions of M_{cyl} identified as Gaussian in nature. The analysis of the fit parameters of the Gaussians found a parabolic dependency of the mean μ_{fit} on M_s and r_c, while the variance σ_{fit} is given only by M_s. This can be understood as smaller bound masses being able to exhibit a greater range of potential projected masses, while larger bound masses have an increased lower boundary without a significantly increased upper limit and thus a lower overall spread. The derived conversion function is shown to well reproduce the actual projected masses.

Section 8.6 has shown Abell 2744 to be reproducible within `Magneticum Pathfinder`, and identified the necessary condition of particularly extreme substructure masses to be the centershift s – only when a large s occurs for a given projection can the masses reach the extreme fractions present in Abell 2744. This is found to be true across all mass ranges. Even then, Abell 2744 represents a particularly rare case overall. Finally, Section 8.7 discussed potential future research avenues, with the accretion history shown to correlate with the mass fractions of projected substructures. Those galaxy clusters which accreted more mass more recently also find larger substructure masses, consistent with the usage of f_{cyl} as indicators for dynamical activity.

Chapter 9

Gazing from the Towers

This work has shed light on physical processes influencing the largest scales within the Universe. It is the evolution of structure which provides insights into yet unresolved questions such as the nature of dark matter or the impact. This evolution, however, occurs on timescales so large that they are unfortunately impossible to directly observe. Furthermore, many of the relevant processes are already difficult to analyze in isolation with analytical models and quickly become highly non-linear once the scope considered is extended. Consequently, cosmological simulations which allow insight into the full phase-space evolution with time have quickly become irreplaceable.

Based on the current understanding of the concordance cosmology of ΛCDM, the Universe is expanding and comprised of baryons, dark matter and dark energy. This expansion does not occur at a constant rate but rather is accelerating. As a consequence, a force term arises in the equation of motion, which is consistently implemented in all major cosmological simulations. This work has studied the consequences of this additional force term on the orbits of bound objects for a ΛCDM cosmology with $\Omega_m = 0.272$ and $\Omega_\Lambda = 0.728$. It extends the findings in the literature for circular orbits around a point mass to the behavior of general orbits, demonstrating that the resulting perturbation from expansion is dependent only on the enclosed density contrast relative to the critical density. Orbits enclosing higher density are perturbed less, irregardless of the absolute scales as some of the typical interpretations suggest. Differences between the impact of expansion on galaxy clusters and galaxies thus arises entirely through differences in the distribution of mass, as galaxies are more centrally concentrated than clusters. Furthermore, it is shown that the expanding force is highest during the matter-dominated phase of expansion when it points inwards, disappears briefly at redshift $z = 0.751$ and then points outwards during dark energy-domination. Consequently, the effective potential felt by an orbiting particle is found to go from a steep slope pointing inwards at high z to a flat and then decreasing slope at lower z. It is derived that this results in a particle at fixed total energy being able to make more eccentric orbits at later times. Noticeably, though the minimum of the effective potential and consequently potential circular orbits exist for all times, the corresponding total energies vary with time. Thus, before complete dark energy-domination, there can exist no fixed circular orbits within an expanding

Universe – though corrections become smaller the higher the mean density contained within the orbit.

Using a reduced code based on Gadget 2 (Springel, 2005) with a symplectic KDK integrator (Binney & Tremaine, 2008), simulated orbits are compared to the analytically derived extent of the orbits. Good agreement is found when particles are initialized at the pericenter of their orbits. Curiously, a discrepancy is found when instead initializing at the apocenter for particles which are at far distances to the central mass. This is interpreted as being due to the changing nature of the expanding force term: those particles starting farther out have their total energy reduced as the potential they are lying on is lowered by expansion with time, while those starting at the center experience the opposite, briefly gaining energy as they move outwards. This results from the non-zero orbital period, such that those far out cannot actualize the potential to kinetic energy quickly enough before expansion has transitioned to dark energy-domination, lowering the potential. It follows that, for a particle initially at rest, $\dot{r} = 0$, separated by a fixed physical distance r to a central mass M, different orbits arise when initialized at different redshifts z.

The analysis was then further expanded to extended density profiles, which more accurately represent real objects. This was found overall not to have a large impact, with the same general behavior as seen before for the point masses. To ensure that N-body interactions do not alter the analytical results for the extended profiles, spheres following a Plummer (1911) and Hernquist (1990) density profile were simulated with a reduced code. The simulation was run once with a Newtonian and once with an expanding background. Practically no quantifiable difference is found, consistent with the previous findings, as the density profiles of the spheres are strongly centrally peaked and thus should find little impact from expansion.

The results mentioned so far all arise from the specific choice of ΛCDM cosmology. Recent observations, however, have found difficulties in reconciling the properties of substructures within galaxy clusters with those from simulations. In particular, they appear too concentrated (Meneghetti et al., 2020) as well as too massive (Schwinn et al., 2017). Using the fully hydrodynamical cosmological simulation `Magneticum Pathfinder` (Hirschmann et al., 2014; Teklu et al., 2015; Dolag, 2022) both questions are explored. For the first one, the boxes 2b (hr), 3 (hr) and 4 (uhr) are used. For all subhalos within the mass range $10^{10} < M_{\mathrm{sub}}[M_\odot] < 10^{13}$ the maximum circular velocities, as a tracer for compactness, were compared to those from observations, finding the reported discrepancy present as well. To analyze whether baryonic effects significantly altered the dark matter density slopes – and thus maximum circular velocities – the halos within boxes 1a (mr), 3 (hr) and 4 (uhr) were matched to those within the dark matter-only counterparts to the boxes. Consistent values were found across the varying resolutions between the baryonic and dark matter only boxes.

To explore the second question of absolute masses, a method for constructing projected masses of substructures was developed. Subsequently, it was shown that the large values from the gravitational lensing observation of Abell 2744 by Jauzac et al. (2016) can be reproduced within `Magneticum Pathfinder`, and that they are the result of projection effects with significant contributions in mass from the main halo. This constitutes the first reproduction

of these extreme substructure masses with a hydrodynamical simulation and is consistent with the findings by Schwinn et al. (2018) who employed the dark matter-only simulation `Millenium-XXL` (Angulo et al., 2012). It is of note that `Magneticum Pathfinder`'s mass resolution for the dark matter is over an order of magnitude higher, which is made use of by finer gridding and by not smoothing. Additionally, the redshift for the snapshot used here is slightly closer to that of Abell 2744, and an Einasto density profile is fit to the main halo which closer resembles the projected form of an NFW while also better accounting for shifts of the center-of-mass away from the potential minimum. This demonstrates the power of `Magneticum Pathfinder` when tackling the largest scales and correspondingly rarest objects within the Universe, while also including baryonic physics with a high mass resolution.

The impact of projection on galaxy cluster and substructure properties were then further explored across four cluster mass bins covering a magnitude in mass, from $1 \times 10^{14} \, \mathrm{M}_\odot$ to $10^{15} \, \mathrm{M}_\odot$. It was found that the total mass contained within substructures increases substantially in projection by a factor of 2 to 3. This mass is further distributed over a smaller number of substructures compared to those in three-dimensions, thus resulting in the largest exhibiting increases in mass of up to an order of magnitude. Furthermore, the increase is more severe the closer the substructure lies to the galaxy cluster center in projection. The dynamical state of the galaxy cluster is shown to play a vital role in these increases, with the most extreme masses occurring only when there is a significant difference between the most-bound-particle and projected center-of-mass, i.e., when the centershift is large. It is shown that for the two typical tracers of the dynamical state, the centershift and total substructure mass fraction, the former stays approximately constant in projection while the latter finds a large discrepancy.

To quantify the differences of substructure masses in projection and three dimensions, a conversion function is developed. The projected aperture masses were first extensively compared to the masses of the subhalos as identified in three dimensions via `SUBFIND` that were lying within the same aperture. Interestingly, most apertures are found to be dominated by a single subhalo in mass. Furthermore, while the most massive aperture also hosts the most-bound-particle in nearly all cases, the second most massive aperture contains the second most massive subhalo in only less than half the cases. The projected masses were then binned according to their projected distance as well as the most massive subhalo mass within them, and the resulting distribution found to be approximately Gaussian. While the mean of the Gaussians was found to be dependent on both the distance and subhalo mass, the variance was interestingly only dependent on the latter. These fit parameters were then shown to follow a parabolic form. Finally, the conversion function, which takes as parameters the projected distance and subhalo mass, was shown to well reproduce the resulting projected masses of the apertures. This will allow in the future a direct conversion to the expected distribution of projected masses from typical simulation output.

As understanding of the Universe continues to grow, many more new questions arise in the process. This is also the case for the present work, where the behavior of the orbits in

the expanding frame has raised interesting future prospects. One could consider significantly downscaled systems to masses far below those of galaxies or galaxy clusters. This would result in an orbital period for a particle which is sufficiently small to complete during matter-domination when the expanding force is largest, even when initialized far outside of r_{200}. Based on the present findings, it is expected that one could then observe the orbit of the particle varying with time as the expanding force changes. Furthermore, analyses of particles initially at rest could provide insight on whether the inflowing velocities change with time, perhaps leading to increasingly slower infall velocities. These findings can in the future lead to a more thorough understanding of the early phases of structure formation, allowing more refined approaches to models of the earliest objects while accounting for expansion effects. This coincides with exciting new opportunities in direct deep observations of these early structures by the new James Webb telescope (Glazebrook et al., 2021).

Similarly, the conversion function between bound to projected masses could be further explored. One could extend the formalism to account for any range of main halo masses, or perhaps even consider if a generalized scaled form exists. Considering the findings that the most extreme masses occur for dynamically disturbed galaxy clusters, it would be interesting to consider if including a dependency on the dynamical state of the cluster could assist in more tightly constraining the distributions. Furthermore, possible correlations of the relaxedness to the accretion history and large scale structure could offer insight into a broader picture of structure formation.

Finally, while the masses of substructures are shown here not to be in tension with ΛCDM even when including baryonic physics, the tension with their concentrations still remains between simulations and observations. As shown just now by (Ragagnin et al., 2022) a greatly reduced AGN energy feedback can in principle lead to more efficient star formation and consequently a strongly peaked central stellar core with a concentration matching that from observations. This, however, comes at the cost of increased stellar masses, which then in turn do not match the observations anymore, exchanging one problem for another. The consequences are far-reaching, not just for galaxies within galaxy clusters but also down to galaxies of Milky Way masses and below. More refined star formation and feedback models together with potential alternatives to ΛCDM are all feasible candidates to solve this issue from a combined approach of simulations and observations, with many fascinating insights and much deeper understanding to be gained into the complex puzzles and mysteries of structure formation within the Universe.

Appendix A

Appendix

A.1 Expansion and Fun with Taylor

Our current understanding of the Universe provides an image of an expanding background metric within which bound objects reside. However, to understand the impact of expansion on orbits of bound particles, as discussed in Section 2.4, it is necessary to understand the form of the term $a/\ddot{a}$. The general flat ΛCDM cosmology, which is used in simulation codes such as `Magneticum Pathfinder` (Dolag, 2022), finds that $a(t)$ has no finite series form, instead resulting in a hypergeometric function. To nonetheless see if it is feasible to construct a functional form, here the left side integrand of Equation 2.20 is expanded as a Taylor series around $a_0 = 1$ for $t_0 = 0$ up to order three, resulting in:

$$
\frac{1}{\sqrt{\Omega_{0,m} \cdot a^{-1} + \Omega_{0,\Lambda} \cdot a^2}} \approx 1 + (a-1)\left(\frac{\Omega_m}{2} - \Omega_\Lambda\right) + (a-1)^2\left[\frac{3}{2}\left(\frac{\Omega_m}{2} - \Omega_\Lambda\right)^2 - \frac{1}{2}\right]
$$

$$
+ (a-1)^3\left[\frac{5}{4}\left(\frac{\Omega_m}{2} - \Omega_\Lambda\right)^3 - \frac{3}{2}\left(\frac{\Omega_m}{2} - \Omega_\Lambda\right) + \frac{\Omega_m}{2}\right]
$$

$$
+ O\left((a-1)^4\right)
$$

$$
\equiv f_1 + b \cdot f_2 + b^2 \cdot f_3 + b^3 \cdot f_4. \tag{A.1}
$$

where $b \equiv a - 1$ was defined and the terms are summarized in the sequence f_i for easier use. This is then integrated such that Equation 2.20 becomes:

$$
H_0 \cdot (t - t_0) \approx \int db \left(f_1 + bf_2 + b^2 f_3 + b^3 f_4\right) = bf_1 + \frac{b^2}{2}f_2 + \frac{b^3}{3}f_3 + \frac{b^4}{4}f_4 \tag{A.2}
$$

This provides a pretty good approximation around $a_0 = 1$ for the form of $t(a)$, however, to get the form for $a(t)$ it must be inverted. Taking the terms up to order $O(b^3)$ allows a rephrasing of the problem into a cubic:

$$
bf_1 + \frac{b^2}{2}f_2 + \frac{b^3}{3}f_3 - H_0 \cdot (t - t_0) = 0, \tag{A.3}
$$

which can be solved analytically. Either three real or one real and two complex roots are found depending on the values of $(\Omega_m, \Omega_\Lambda, t)$. For the case of $\Omega_m = 0.272$ and $\Omega_\Lambda = 0.728$, in accordance with the WMAP-7 parameters (Komatsu et al., 2011), the root which provides the best overall form to the numerical solution (taking $a_0 = 1$ and $t_0 = 0$) is found to have the functional form:

$$L(t) \equiv \left(\sqrt{(0.02905 + 0.001981 \cdot H_0 t)^2 - 0.0009496} + 0.02905 + 0.001981 \cdot H_0 t \right)^3,$$

$$b(t) = (-15.444 + 26.750i) \cdot L(t) - \frac{1.518 + 2.629i}{L(t)} + 11.519,$$

$$a(t) = (-15.444 + 26.750i) \cdot L(t) - \frac{1.518 + 2.629i}{L(t)} + 12.519. \tag{A.4}$$

This approximates the form of $a(t)$ quite well between $-0.45 < H_0 t < 0.5$, as can be seen in Figure 2.2. It is then feasible to derive analytical approximations of $a/\ddot{a}$ for this range, however, the derivative $\ddot{a}$ quickly becomes unreasonably cumbersome and as such is beyond the scope of this thesis.

A.2 "For it all depends on how we look at things"

Though the quote would continue with "and not how they are in themselves." (Jung, 1933), for the case of galaxy clusters *both* are important! The latter, as it dictates what the former becomes, and the former as it is used to make statements about the latter. As such, understanding how typical density profiles of galaxy clusters behave in projection is of utmost importance to understand what is actually being observed – because observation is *always* in projection. Unfortunately, most density profiles are most commonly defined in three dimensions, which makes sense given their assumed spherical symmetry. Given that projection treats the line-of-sight axis differently, instead it is sensible to convert those profiles here to a cylindrical coordinate system.

The density profile used for the fit to the projected main halo density profile is the Einasto profile – see Section 6.3. As much as it would be insightful to go through the effects of projection on it here, this turns out to be tedious enough to warrant a paper all by itself due to the integration being non-analytical in nature. Consequently, the general form of the approximated projected mass can be found in Equation 23 of one such paper written by Dhar (2021). Nonetheless, the simpler analytical properties of another typical profile, namely the NFW-density profile, allow for such integration. As such, a brief derivation of the projected mass is given here to illustrate some of the finer nuances between projected and spherical properties, as well as to allow for a varying cylinder projection depth z, as typically a fixed variant of either $z = r_{\text{vir}}$ (Takada & Jain, 2003) or $z - > \infty$ is chosen for the integration.

Taking (x, ϕ, z) as the variable of the cylindrical coordinate system, the mass in a cylinder of depth $2 \cdot z_l$ and radius x_A for an NFW-profile is equal to:

$$
\begin{aligned}
M(x_A, z_l) &= \int_{\text{Cylinder}} \rho_{\text{NFW}}(r) = \int_C \mathrm{d}r\mathrm{d}\theta\mathrm{d}\phi \; r^2 sin(\theta) \cdot \rho_{\text{NFW}}(r) \\
&= \int_C \mathrm{d}x\mathrm{d}\phi\mathrm{d}z \; x \cdot \rho_{\text{NFW}}\left(\sqrt{x^2 + z^2}\right) \\
&= 2\pi\rho_0 \int_0^{x_A} \mathrm{d}x \int_{-z_l}^{z_l} \mathrm{d}z \; \frac{x}{\frac{\sqrt{x^2+z^2}}{R_s} \cdot \left(1 + \frac{\sqrt{x^2+z^2}}{R_s}\right)^2} \\
&\overset{\substack{x'=x/R_s \\ z'=z/R_s}}{=} 2\pi\rho_0 R_s^3 \int_0^{x_A/R_s} \mathrm{d}x' \int_{-z_l/R_s}^{z_l/R_s} \mathrm{d}z' \; \frac{x'}{\sqrt{x'^2 + z'^2} \cdot \left(1 + \sqrt{x'^2 + z'^2}\right)^2}.
\end{aligned}
\tag{A.5}
$$

The final step utilizes a simple substitution for both variables to simplify the form of the equation. Given the integrals in Equation A.5, we must choose which to integrate over first. It proves to be significantly easier if we integrate first over $\mathrm{d}x'$, as the x' up top appears naturally from the derivative of the bottom terms $\propto \sqrt{x'^2 + z'^2}$. Thus, defining $x_s \equiv x_A/R_s$, $z_s \equiv z_l/R_s$, $x_f \equiv \sqrt{x_s^2 - 1}$, $r_f \equiv \sqrt{x_s^2 + z_s^2}$ and $M_s \equiv 4\pi\rho_0 R_s^3$, we have then:

$$
\begin{aligned}
M(x_A, z_l) &\overset{\text{Equation A.5}}{=} 2\pi\rho_0 R_s^3 \int_0^{x_A/R_s} \mathrm{d}x' \int_{-z_l/R_s}^{z_l/R_s} \mathrm{d}z' \; \frac{x'}{\sqrt{x'^2 + z'^2} \cdot \left(1 + \sqrt{x'^2 + z'^2}\right)^2} \\
&= 2\pi\rho_0 R_s^3 \int_{-z_s}^{z_s} \mathrm{d}z' \left[-\frac{1}{\sqrt{x'^2 + z'^2} + 1} \right]_0^{x_s} \\
&= 4\pi\rho_0 R_s^3 \int_0^{z_s} \mathrm{d}z' \left(\frac{1}{1 + |z'|} - \frac{1}{\sqrt{x_s^2 + z'^2} + 1} \right) \\
&= M_s \cdot \left[\ln(1 + z') - \ln\left(\sqrt{x_s^2 + z'^2} + z'\right) - \frac{\arctan\left(\frac{z'}{\sqrt{x_s^2+1}\sqrt{x_s^2+z'^2}}\right)}{\sqrt{x_s^2 - 1}} + \frac{\arctan\left(\frac{z'}{\sqrt{x_s^2+1}}\right)}{\sqrt{x_s^2 - 1}} \right]_0^{z_s} \\
&= M_s \cdot \left[\ln\left(\frac{1 + z'}{\sqrt{x_s^2 + z'^2} + z'}\right) + \frac{\arctan\left(\frac{z'}{x_f}\right) - \arctan\left(\frac{z'}{x_f\sqrt{x_s^2+z'^2}}\right)}{x_f} \right]_0^{z_s} \\
M(x_A, z_l) &= M_s \cdot \left(\ln\left(\frac{x_s \cdot (1 + z_s)}{r_f + z_s}\right) + \frac{\arctan\left(\left(1 - \frac{1}{r_f}\right)/\left(\frac{z_s}{x_f r_f} + \frac{x_f}{z_s}\right)\right)}{x_f} \right).
\end{aligned}
\tag{A.6}
$$

One can then further use some properties of the NFW-profile to simplify the final result. If additionally assuming a concentration-mass relation $c - M$, the input parameters can be reduced because the scaling radius is then given by (assuming the virialized overdensity to

be around 200):

$$R_s(M_{vir}, \rho_m) = \frac{R_{vir}}{c(M_{vir})} = \frac{\sqrt[3]{M_{vir}/\left(\frac{4\pi}{3} \cdot 200\rho_m\right)}}{c(M_{vir})}. \tag{A.7}$$

The full final form of the projected mass within an aperture of radius x_A for depth out to z_l of a single dark matter halo of virial mass M_{vir}, with a mean mass density of ρ_m, is then:

$$M(x_A, z_l) = \frac{M_{vir}}{\ln(1+c) - \frac{c}{1+c}} \left(\ln\left(\frac{x_s \cdot (1+z_s)}{r_f + z_s}\right) + \frac{\arctan\left(\left(1 - \frac{1}{r_f}\right)/\left(\frac{z_s}{x_f r_f} + \frac{x_f}{z_s}\right)\right)}{x_f} \right). \tag{A.8}$$

A deeper look at all relevant properties for lensing of the NFW profile (for example the resulting shear – see Section 5.2.1) is given for the case $z = r_{vir}$ by (Takada & Jain, 2003).

A.3 Considering all Angles

This section provides a brief overview of the way random orientations are made, as well as some comparisons between different sampling methods. To create the orientations, a rotation matrix $\mathcal{R}_{\alpha,\beta}$ is used to rotate all data points into a random direction as

$$\begin{pmatrix} x' \\ y' \\ z' \end{pmatrix} = \mathcal{R}_{\alpha,\beta} \begin{pmatrix} x \\ y \\ z \end{pmatrix}, \tag{A.9}$$

where

$$\mathcal{R}_{\alpha,\beta} = \begin{pmatrix} \cos(\beta) & \sin(\alpha) \cdot \sin(\beta) & \sin(\alpha) \cdot \sin(\beta) \\ 0 & \cos(\alpha) & -\sin(\alpha) \\ -\sin(\beta) & \sin(\alpha) \cdot \cos(\beta) & \cos(\alpha) \cdot \cos(\beta) \end{pmatrix} \tag{A.10}$$

and then z' is used as the projected random direction, with distances being determined in the $x' - y'$ plane.

Generally, to achieve random orientations isotropically distributed across the surface of a sphere one can sample uniformly distributed random variables u, v on $(0, 1)$, where then

$$\theta = 2\pi u$$
$$\phi = \arccos(2v - 1) \tag{A.11}$$

are the spherical coordinates – see Weisstein (2022b). However, assuming the simulation boxes to have no favored direction, it is also possible to uniformly sample directly (θ, ϕ) on $[0, 2\pi)$ as any sampling bias would then preferentially sample what corresponds to a random direction. From these random angles, the average relation between the projected and 3d distances can be determined by integrating the projected radius $r_{2d} = \sqrt{x'^2 + y'^2} = r_{3d} \cdot \sin(\phi)$

over the surface of the sphere by transforming to the coordinates (u, v):

$$\bar{r}_{2d} = \frac{1}{\Omega} \int d\Omega \, r_{2d} = \frac{1}{4\pi} \int d\theta d\phi \, \sin(\phi) \, r_{2d} = \frac{1}{4\pi} \int d\theta d\phi \, \sin(\phi) \, r_{3d} \cdot \sin(\phi)$$

$$\bar{r}_{2d} \overset{(A.11)}{=} \frac{r_{3d}}{4\pi} \int_0^1 du \, 2\pi \int_0^1 dv \, \frac{\sin^2[\arccos(2v-1)]}{\sqrt{v-v^2}}$$

$$\bar{r}_{2d} = \frac{r_{3d}}{4\pi} \cdot 2\pi \cdot \frac{\pi}{2} = \frac{\pi}{4} r_{3d}. \tag{A.12}$$

The mean projected radii resulting from the different samplings and the analytical version
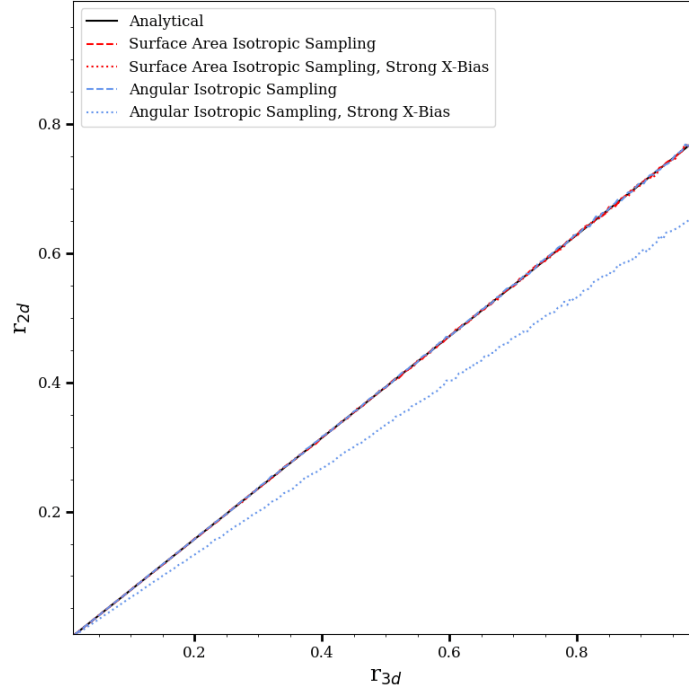
Figure A.1: The mean projected radius over 10 000 random orientations as a function of the 3d-distance for different samplings – the uniform sampling in (θ, ϕ) used throughout (blue dashed) and the isotropic sampling on the spherical surface from Weisstein (2022b) (red dashed) – compared to the analytical solution (black dashed). Additionally, the impact of a strong directional bias (here in x-direction) of the projected distribution on the samplings is shown by the dotted lines.

in Equation A.12 for comparison are plotted in Figure A.1 for 10 000 random orientations. There, the projection is performed on a sample of 200 points evenly distributed between radii of 0 and 1 in three dimensions, once for isotropic placements where $\bar{v} = [1, 1, 1]/\sqrt{3}$ and once with a strong bias in the x-direction, i.e., with points lying along that axis more commonly as $\bar{v} \approx [0.99, 0.099, 0.099]$. For the isotropic points, either sampling method (colored dashed lines) reproduces the analytical line (black dashed) as the isotropy is already guaranteed from the point distribution and sampling biases in the projection directions do not matter. The case is different should there be a bias in the point distribution itself, as then the projection must occur isotropically. If instead then a preferred sampling direction exists, the alignment between the preferred axis of the points and of the sampling dictates the slope of the resulting projected radii – parallel alignment leads to overall lower projected radii (as is the case for the implementation here), while perpendicular alignment will find higher projected radii.

A.4   Overlap of Apertures

As all throughout the thesis apertures around substructures play a central role, perhaps unsurprisingly when working with projected maps, one of the central questions is if and to what degree apertures should be allowed to overlap. This section provides an overview both of the typical overlap of apertures, as well as the prescription used to correct for the missing area when masking apertures (see Section 6.3). While the latter may not initially appear to have much to do with overlapping circles, the connection will be clear by the end.

Starting then with the first question, some overlap is allowed to avoid undersampling of dense central regions of the galaxy clusters (as argued in Section 6.2.2), but a minimum hard border is necessary. The chosen minimum distance of two apertures is defined as $d_{\min} = 2 \cdot \sqrt{3}/2 \cdot r_{\mathrm{ap}}$, as this avoids a triple overlap, which can be seen when considering the case in Figure A.2. From the image depicting the closes overlap possible without triple overlap, the minimum separation of apertures must then be $d_{\min} = 2 \cdot x$. Considering that by symmetry the black central triangle has angles of $2 \cdot \alpha = 60°$ it follows as posited that

$$d_{\min} = 2 \cdot x = 2 \cdot \cos(30°) \cdot r_{\mathrm{ap}} = 2 \cdot \frac{\sqrt{3}}{2} \cdot r_{\mathrm{ap}}, \tag{A.13}$$
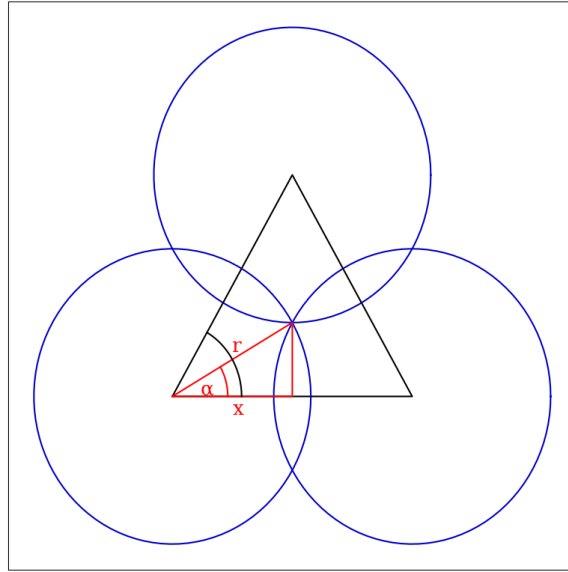
Figure A.2: The geometric reasoning for the choice of $d_{\min}$, as it allows no overlap of three apertures at any point.

Having set a minimum distance that is smaller than twice the aperture radius, it follows logically that apertures can overlap. To quantify how much they do this, the cumulative fraction of all apertures with minimum overlap $x_{\min}$ is shown in Figure A.3 for all mass bins and both considered stellar mass cuts (see Section 7.2). Note that the "giants" bin apparently extends beyond the hard minimum $d_{\min}$, which is due to the large differences in r_{vir} of the mass bin, where for the most extreme cases there (galaxy clusters number 1 and 2) $d_{\mathrm{min,giants}}/r_{\mathrm{vir}} = 130\,\mathrm{kpc}/r_{\mathrm{vir}} \approx 0.08$. Due to the tighter mass ranges, the other bins share

a correspondingly tight relative minimum aperture separation x_{min}. Overlapping halos are those which have a minimum separation below $2 \cdot r_{\text{ap}}$, which aside from the "giants" then lies between the two vertical black lines.
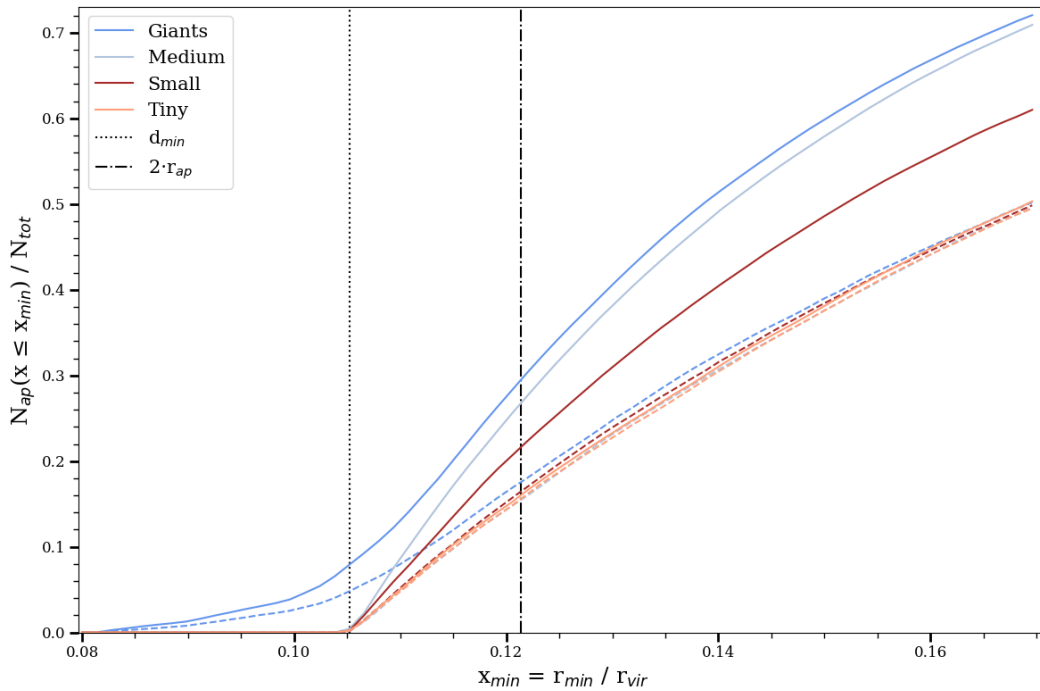
Figure A.3: The cumulative fraction of apertures with minimum aperture separation r_{min}, given in units of r_{vir}. Solid colored lines are for the virial mass scaled cut used throughout, with dashed colored lines for the subhalo number scaled cut. Vertical black lines denote d_{min} (dotted) and $2 \cdot r_{\text{ap}}$ (dash dotted) respectively.

It can be seen that the fraction of overlapping halos increases with the raw number of apertures placed, where consequently the equal subhalo number scaled cuts (dashed colored lines) lead to overall very comparable aperture separations (and hence also overlap fractions) between all mass bins. The most extreme overlap occurs for the "giants" with the virial mass scaled cut, where about 5% of the apertures overlap as much as allowed, though the value is not exact due to the variance in r_{vir}. Generally, however, the great majority of 70% and above experience no overlap whatsoever. In future work an estimation of the substructure mass overestimated as a result is of interest, by for example approximating the substructures based on their mass as NFW-profiles and integrating the overlapping area.

Turning then to the corrected area of the main halo fits, the first thing to consider is that the area being cut out by the apertures is that of a circle. Similarly, the density profile in projection extends spherically outwards, with a given bin between two radii $[r_1, r_2]$ potentially overlapping a portion of one or more apertures. Defining $A_{\text{ap,bin}}$ as the overlapping area and $M_{\text{ap,bin}}$ as the shared mass, the surface density of the main halo in the bin would then be:

$$\rho_{\text{bin}} = \frac{M_{\text{bin}} - M_{\text{ap,bin}}}{\pi \cdot (r_2^2 - r_1^2) - A_{\text{ap,bin}}}. \tag{A.14}$$

Masking the mass is simple, as it is given by particles in the simulation and therefore can be done simply removing all particles which lie within apertures from consideration. The area, however, must be considered separately. This situation is shown in Figure A.4 on the left, with the two radii of the main halo density bin in dark blue and an example aperture in black. The area which is masked and must be subtracted from the density calculation, $A_{\mathrm{ap,bin}}$, is shaded in dark blue. It can be seen that this area is simply equal to the intersected area for the outer radius of the ring, $A_{\mathrm{ap,r_2}}$ in the middle in blue, minus the intersected area for the inner radius, $A_{\mathrm{ap,r_1}}$ on the right in light blue. That is to say, $A_{\mathrm{ap,bin}} = A_{\mathrm{ap,r_2}} - A_{\mathrm{ap,r_1}}$. These other two areas are much easier to calculate, as they are simply the area intersected by two circles, for which elegant considerations exist – see for example Equation 14 from Weisstein (2022a). Note that there are three additional limiting cases:

1. r_2 overlaps the area of the aperture but not r_1, then $A_{\mathrm{ap,bin}} = A_{\mathrm{ap,r_2}}$
2. r_1 overlaps the area of the aperture but not r_2, then $A_{\mathrm{ap,bin}} = \pi \cdot r_{\mathrm{ap}}^2 - A_{\mathrm{ap,r_1}}$
3. Neither overlap, so $A_{\mathrm{ap,bin}} = 0$

A more complex limiting case, where two apertures overlap each other as well as the radial bin, is not considered here as the overall corrections to the area in each ring should be minor.
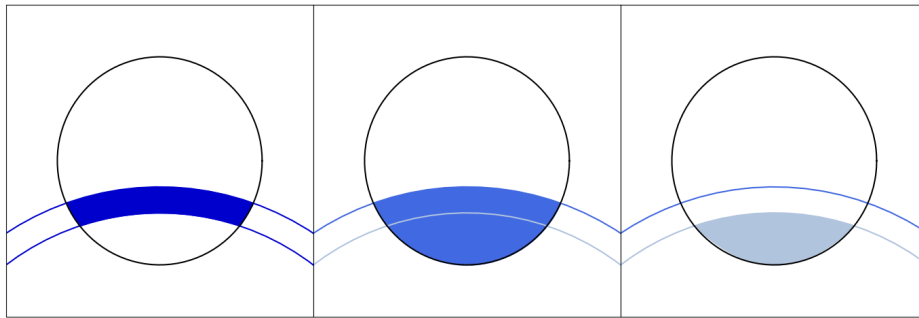

Figure A.4: The geometric argumentation to calculate the masked area due to the presence of apertures in the rings extending outwards for the main halo surface density calculations. From *left* to *right*, the masked area, the circle-circle intersect between the outer ring radius and the aperture, and the same for the inner radius.
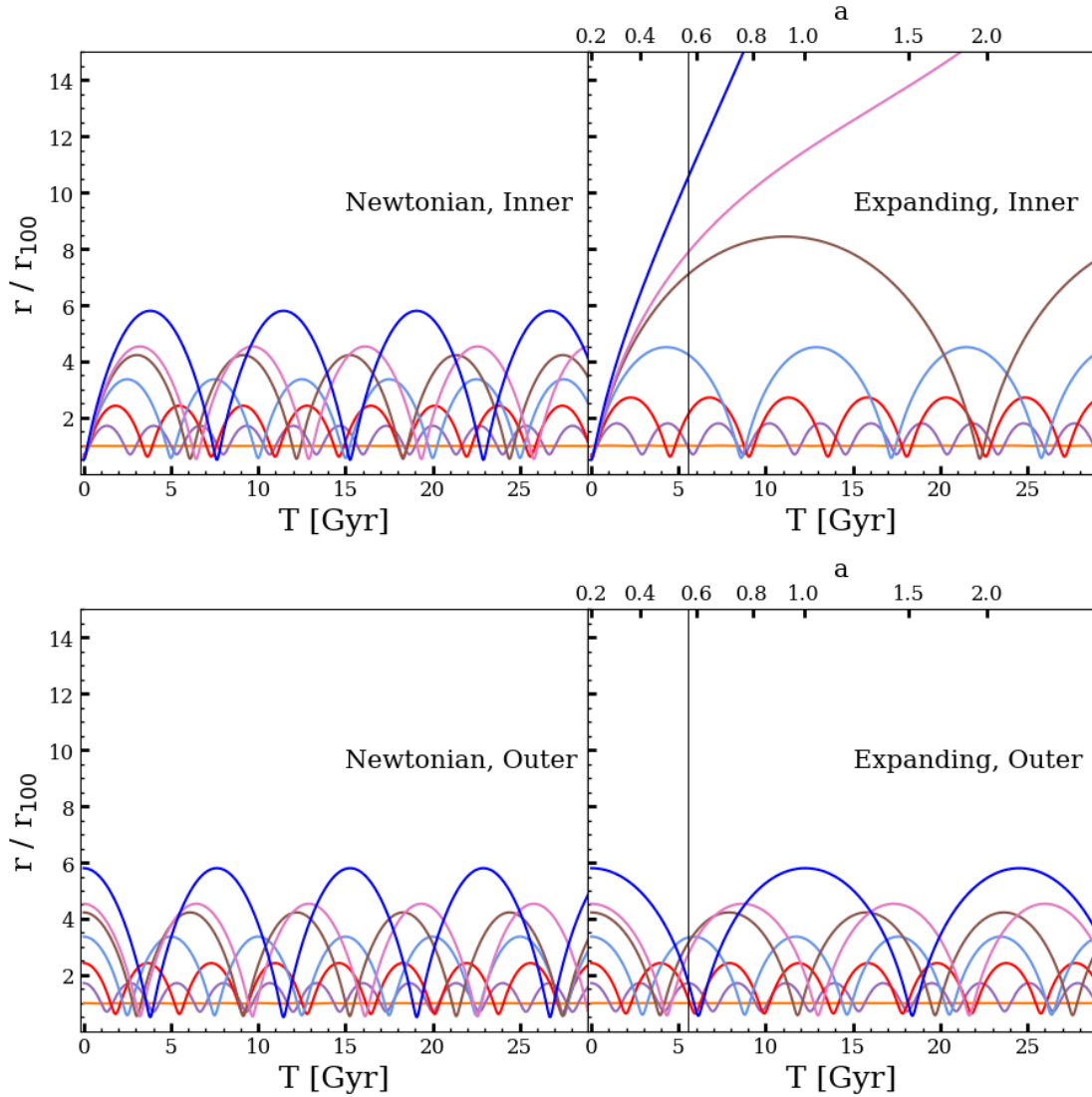
A.5   Expanding the Image Library
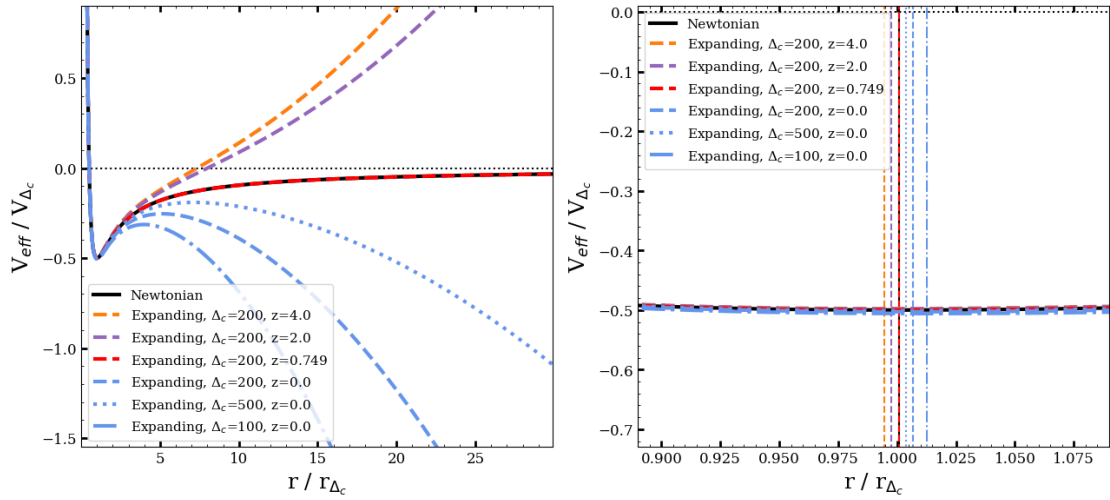
Figure A.5: *Left:* The effective potential at varying times scaled with $V_{\Delta_c}(a)$ resulting from a point mass for the purely Newtonian (black) versus expanding (colored) cases as a function of distance r. *Right:* A zoomed in region around the minima of the effective potentials, demonstrating how the equivalent radii of circular orbits increase with time due to expansion, passing by the Newtonian values at $a = a_{\mathrm{NT}}$.
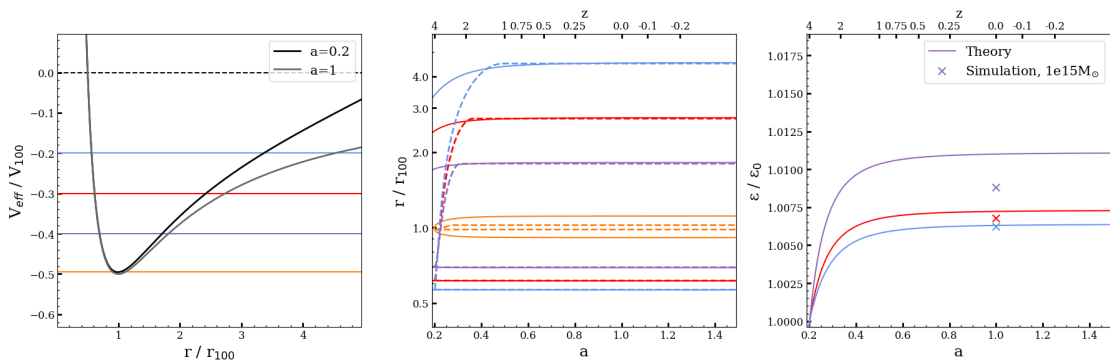

Figure A.6: *Left:* The effective potential scaled with a fixed $V_{100}(a = 0.2)$ resulting from a point mass for the expanding case at two times, $a = 0.2$ and $a = 1$, as a function of distance r. Horizontal colored lines indicate each chosen particle's energy. *Center:* The theoretical evolution (solid lines) of the inner and outer radii of an orbit with total energy as given for the same color on the *left*. Dashed lines are the minimum and maximum radii of the simulated equivalent orbits around a central mass $M = 1 \times 10^{15}\,\mathrm{M_\odot}$, with the initial rise occurring as the particle makes it's first orbit outwards. *Right:* The theoretical evolution (solid lines) of the eccentricity of the orbits as a function of scalefactor, given as a ratio to the original eccentricity. Crosses denote the eccentricity of the last full orbit at $a = 1$ of the simulated equivalents.
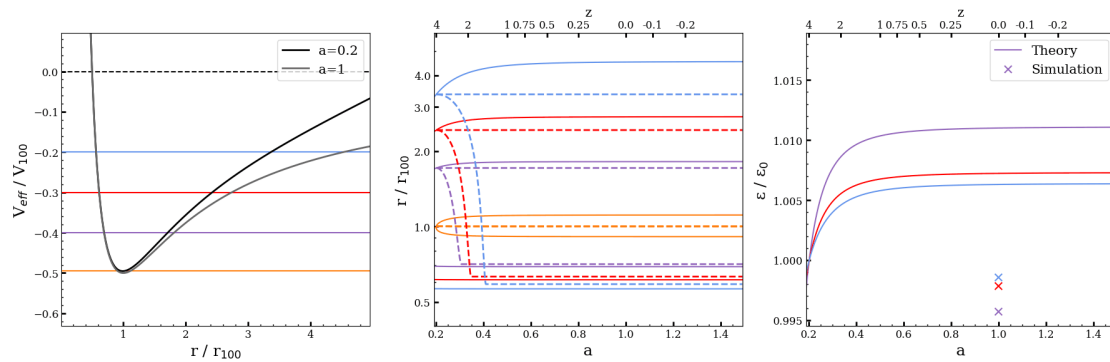
Figure A.7: *Left:* The effective potential scaled with a fixed $V_{100}(a = 0.2)$ resulting from a point mass for the expanding case at two times, $a = 0.2$ and $a = 1$, as a function of distance r/r_{100}. Horizontal colored lines indicate each chosen particle's energy. *Center:* The theoretical evolution (solid lines) of the inner and outer radii of an orbit with total energy as given for the same color on the *left*. Dashed lines are the minimum and maximum radii of the simulated equivalent orbits around a central mass $M = 1 \times 10^{12}\,\mathrm{M}_\odot$, with the initial rise occurring as the particle makes it's first orbit outwards. *Right:* The theoretical evolution (solid lines) of the eccentricity of the orbits as a function of scalefactor, given as a ratio to the original eccentricity. Crosses denote the eccentricity of the last full orbit at $a = 1$ of the simulated equivalents.

Figure A.8: Radii as a function of time of orbits with equal angular momentum $l = 1$ (as defined in Section 2.6) for varying total peculiar energies. The *top* row is initialized at the periapsis and the *bottom* row at the apoasis. The *left* depicts the "Newtonian" potential, where simply an additional force term is added to mimic the effective potential during expansion at $a = 0.2$ but no comoving frame used, while the *right* is for the fully comoving implementation. There the corresponding scalefactor is given for the latter, with a_{NT} highlighted as a thin vertical black line. Crucially, the pink and brown line are initialized at only slightly different energies where pink successfully crosses the threshold, becoming unbound, while brown manages to stay on a bound orbit.
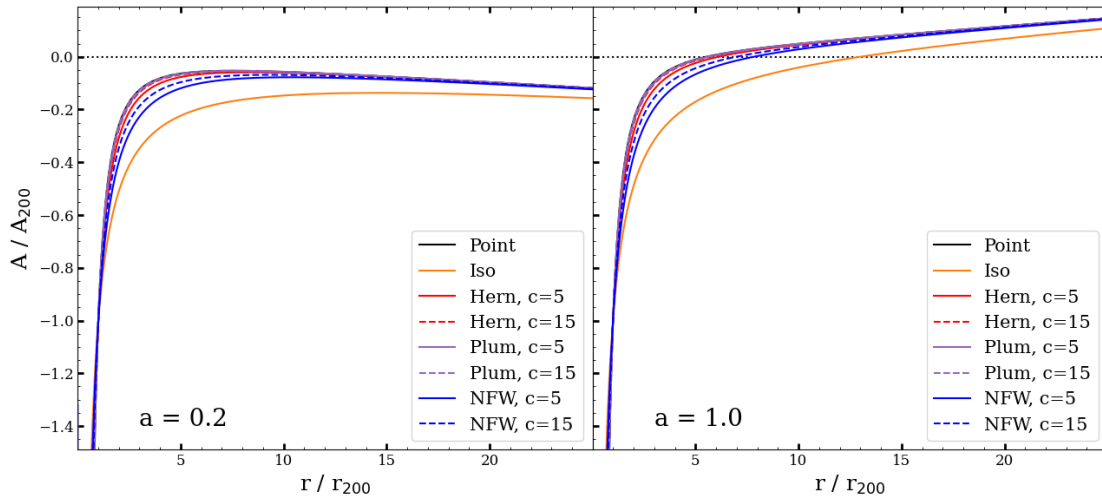
Figure A.9: The acceleration scaled according by A_{Δ_c} resulting from a point mass for varying extended density profiles (colored) versus a point mass (black) as a function of distance r. The overdensity is chosen as Δ_c, with the *left* shown for $a = 0.2$ and the *right* for $a = 1$. All extended profiles are found to behave generally as the point mass does, in particular for large radii. It follows that the results for the acceleration from Section 2.6 can be translated to extended spherically symmetric profiles.
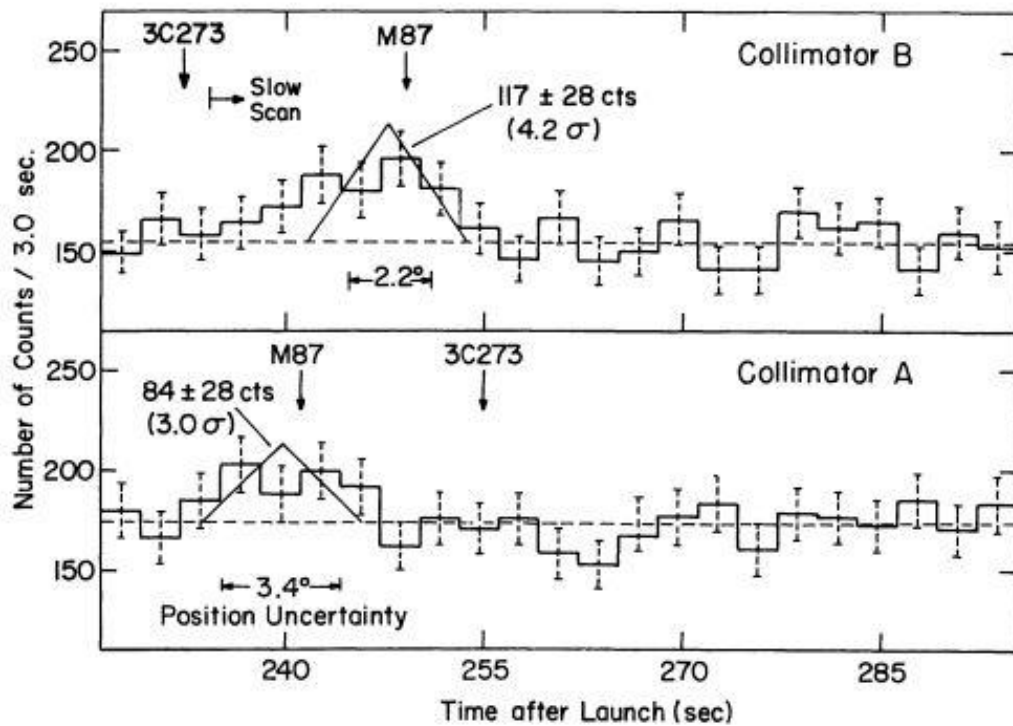

Figure A.10: The X-ray signal measured by Bradt et al. (1967) originating from the M87 at the center of the Virgo cluster.
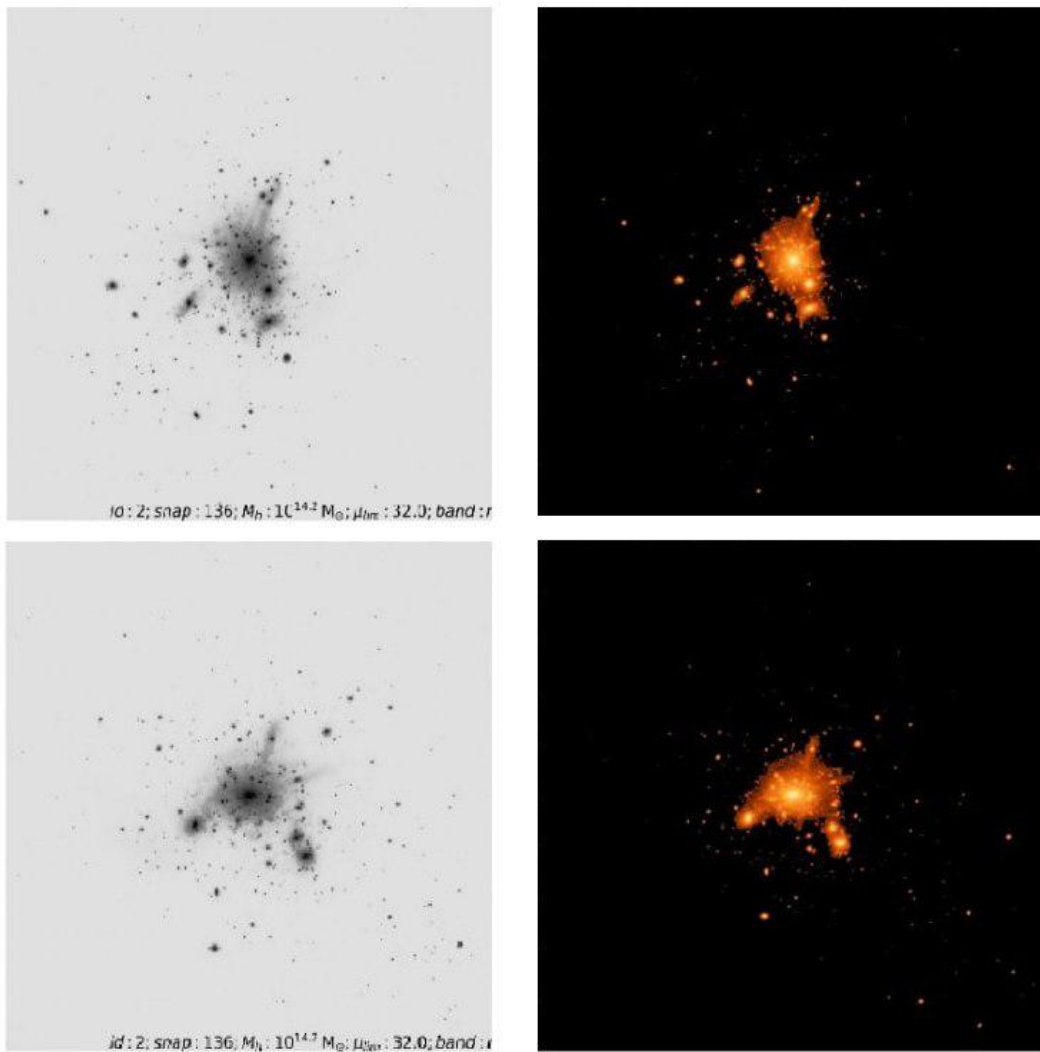
Figure A.11: The mock image created with the code by Martin et al. (2022) (*left*) versus the stellar surface density map created via the method in Chapter 6 (*right*) of a galaxy cluster from box 4 (uhr) for two projections (*top* and *bottom*) centered on its most bound particle. Depicted is a region of boxsize 5 Mpc. The mock image depicts the r-band surface brightness down to 32 mag.
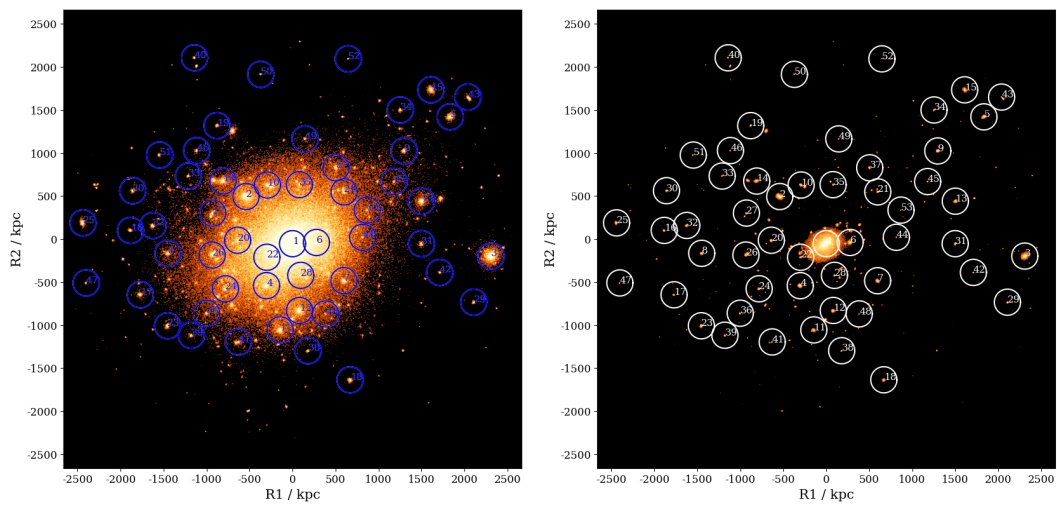
Figure A.12: The total (**left**) and stellar (**right**) surface density map of galaxy cluster 5 of the "giants", with apertures from the subhalo method including a convergence radius and summed pixel values.
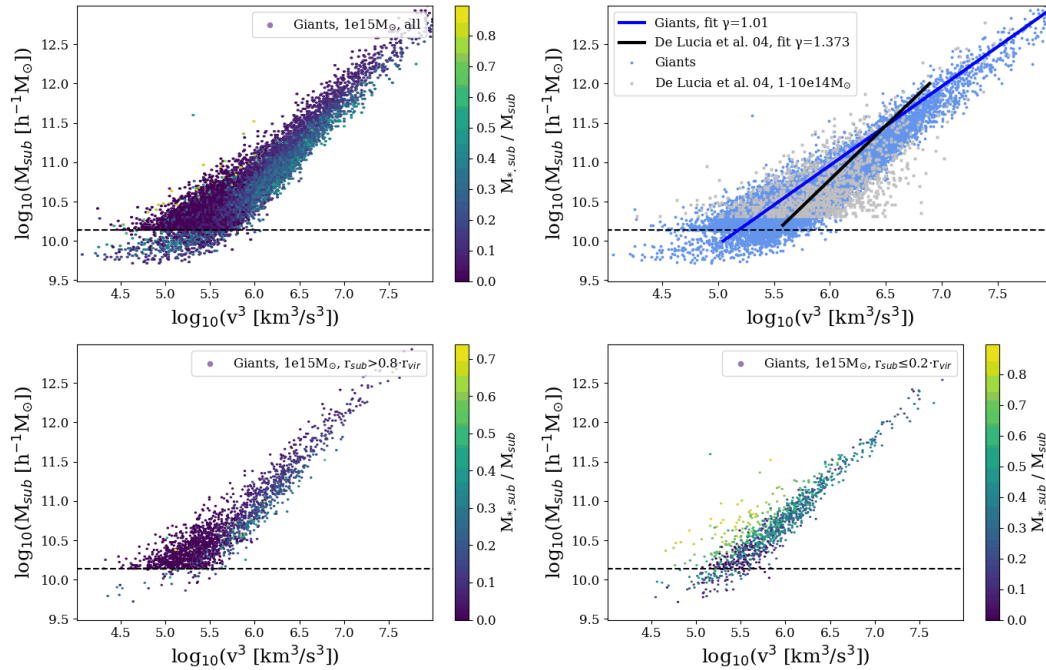
Figure A.13: The subhalo mass as a function of the cubed maximum circular velocity of subhalos within the "giants" mass bin (see Section 6.4). For all fields the dashed horizontal line represents the mass of 20 dark matter particles as a lower resolution bound. The *top left* depicts all subhalos within r_{vir} of all "giants" galaxy clusters, colored according to the stellar mass fraction. Generally, at equal v_{max} (which traces the infalling mass, see Section 7.1) halos with higher total mass tend to have lower stellar mass fractions than those with lower M_{sub}. Plotted in the *top right* for comparison in black are the values found in the dark matter-only zoom simulation by De Lucia et al. (2004), performed on select galaxy clusters from two parent simulations, the GIF-ΛCDM model (Jenkins et al., 2001) and Very Large Simulation (Kauffmann et al., 1999). It can be seen that there is general agreement between the two, though for lower values of v_{max} the subhalos of the "giants" appear to have more total mass than those from De Lucia et al. (2004). The high v_{max}, in turn, is hard to judge due to the lower number statistics. The *bottom left* depicts all subhalos farther out, with the *bottom right* depicting those close to the center. For equal v_{max}, subhalos closer to the center have somewhat lower masses, though the trend is not very clear. Interestingly, for equal v_{max} subhalos on the left subhalos of lower M_{sub} tend to have higher $M_{*,\mathrm{sub}}/M_{\mathrm{sub}}$, while for the right the trend is revered, with the highest stellar mass fractions being found also at the highest total masses with constant v_{max}. Furthermore, farther toward the center subhalos with high dark matter mass fractions are increasingly unlikely.
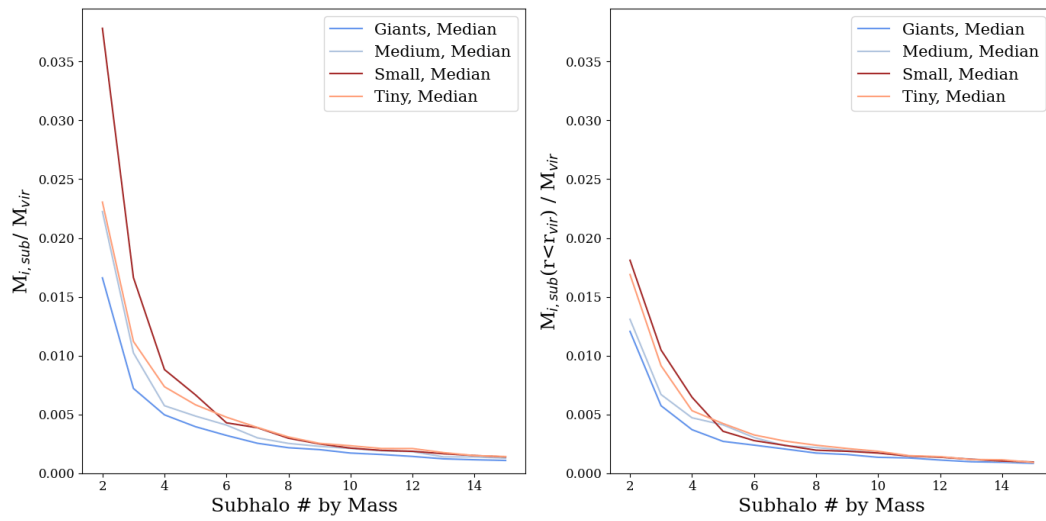
Figure A.14: The median mass fractions of the most massive subhalos within the FoF group (*left*) and within r_{vir} (*right*) as a function of their subhalo number as defined in the beginning of Chapter 8.
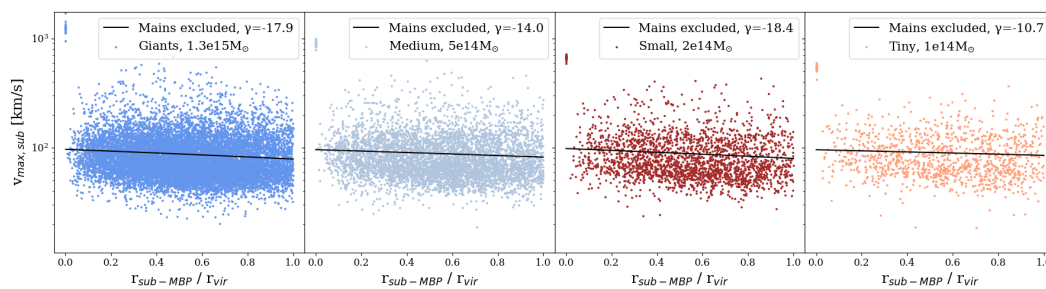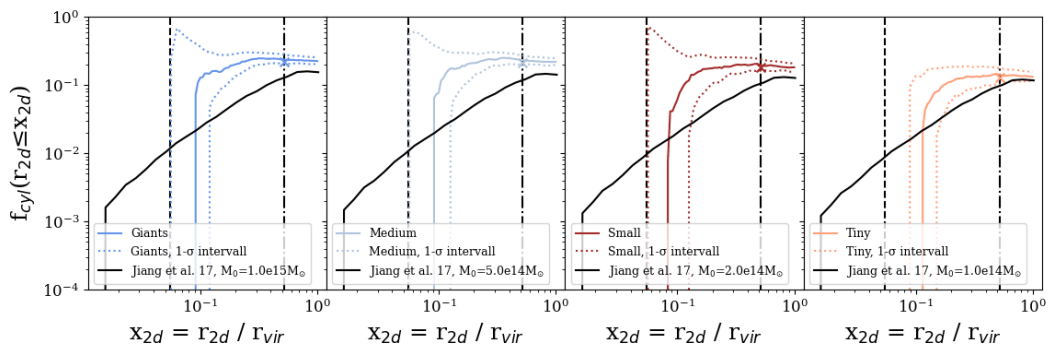

Figure A.15: The median mass fractions of the most massive subhalos within the FoF group (*left*) and within r_{vir} (*right*) as a function of their subhalo number as defined in the beginning of Chapter 8.
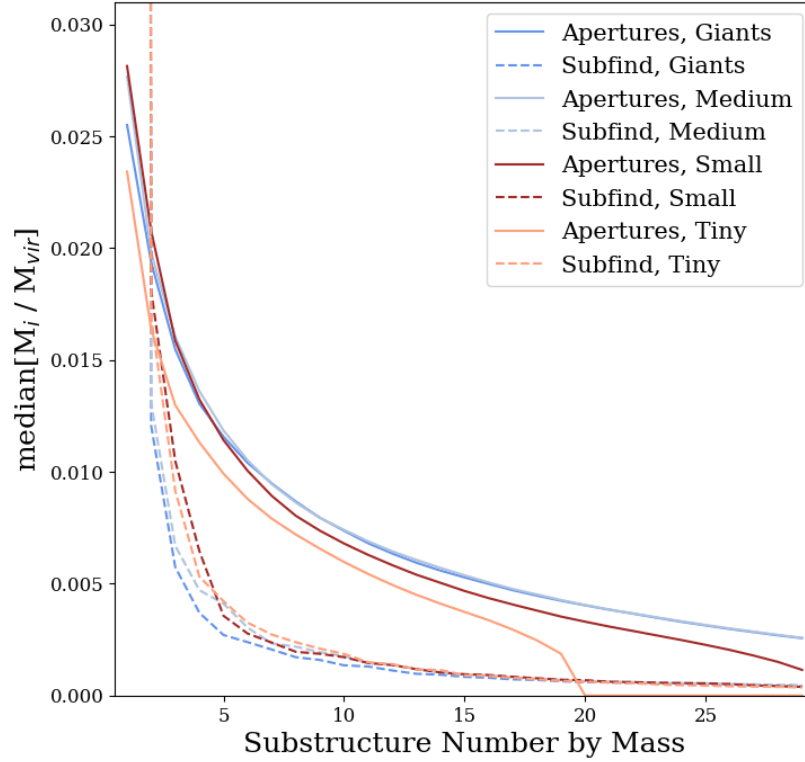
Figure A.16: The substructure mass fraction of the first 29 substructures for all mass bins, once from the `SUBFIND` output and once from projection. Generally, the mass of the main (1) is significantly higher in `SUBFIND`, with the converse being true for any higher substructure numbers. The median values break off to 0 where on average no more apertures are found, as can be seen for the "tinies" and somewhat for the "smalls". Overall, the mass bins find similar curves among themselves for either method, aside from the slight offset downward for the projected masses of the "tiny" mass bin which may simply be the result of having an overall lower number of apertures than the other bins.

Figure A.17: The median running substructure mass fraction of the integrated main halo mass as a function of projected distance to the center-of-mass for the four mass bins with colored solid lines, with $1 - \sigma$ bounds indicated with colored dotted lines, as well as in a solid black line the dark matter-only model from Jiang & van den Bosch (2017) which well match the results from the `BOLSHOI` simulation (Klypin et al., 2011). Vertical lines denote the approximate relative aperture size $r_{\mathrm{ap}}/r_{\mathrm{vir}}$ (dashed) and large cylinder size $r_{\mathrm{tot}}/r_{\mathrm{vir}}$ (dash-dotted). The colored crosses denote the substructure mass fraction of the *total* mass at that radius M_{tot}, not just the main halo.
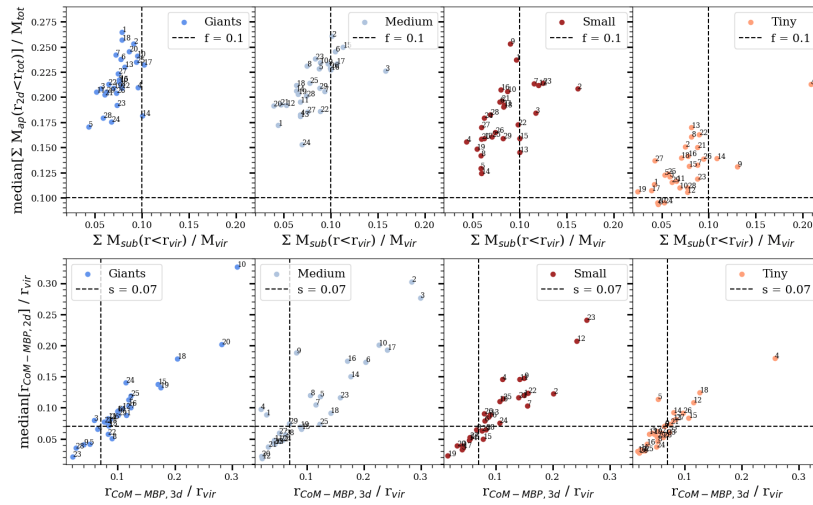
Figure A.18: The same as Figure 8.17 but numbered to allow for explicit comparisons between the centershift and total substructure mass of individual galaxy clusters.

Figure A.19: . This is especially true for the "giants", where the three galaxy clusters with highest centershift also have the highest number of most massive substructure which do not include the most-bound-particle.
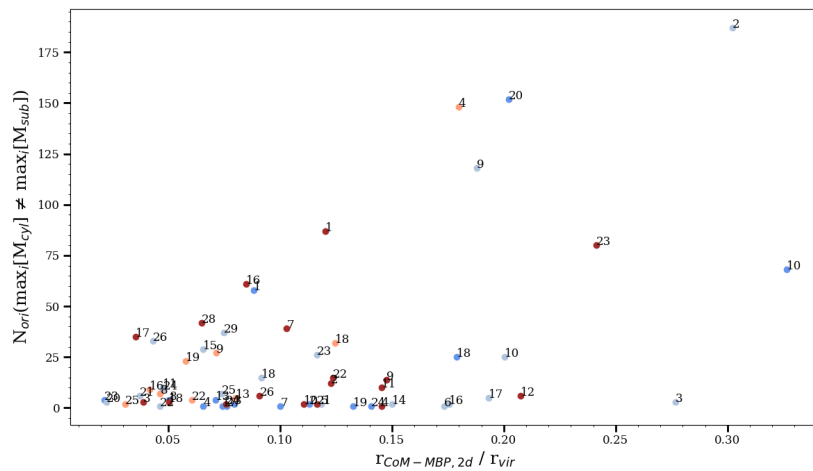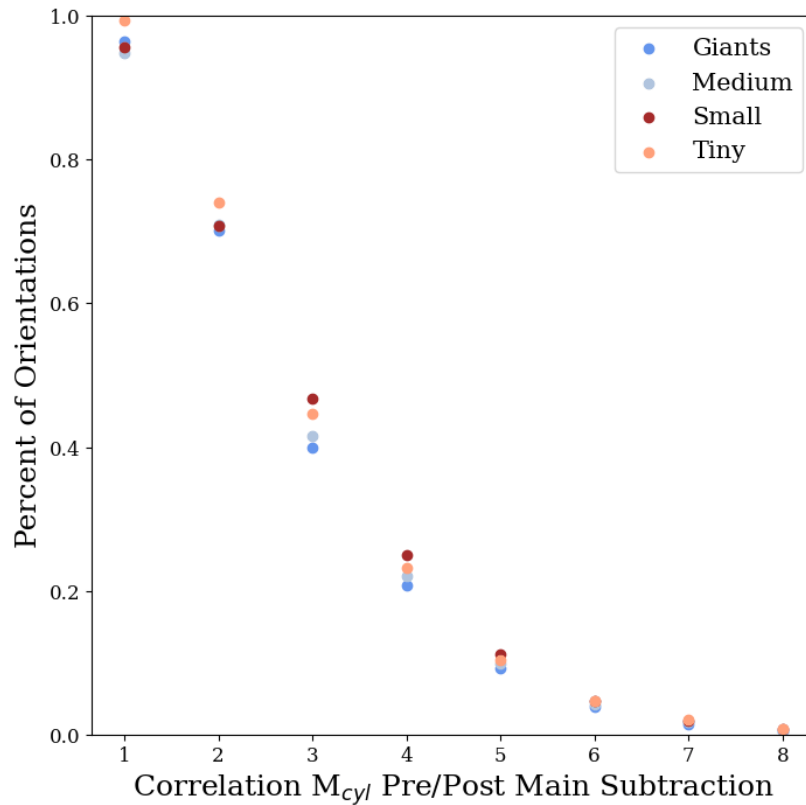
Figure A.20: The substructure mass fraction of the first 29 substructures for all mass bins, once from the SUBFIND output and once from projection. Generally, the mass of the main (1) is significantly higher in SUBFIND, with the converse being true for any higher substructure numbers. The median values break off to 0 where on average no more apertures are found, as can be seen for the "tinies" and somewhat for the "smalls". Overall, the mass bins find similar curves among themselves for either method, aside from the slight offset downward for the projected masses of the "tiny" mass bin which may simply be the result of having an overall lower number of apertures than the other bins.
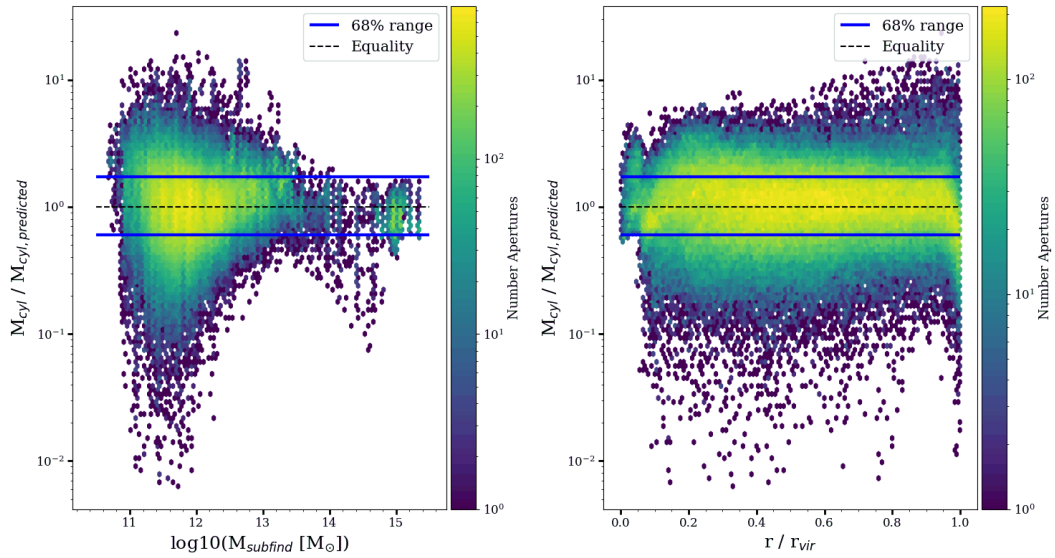
Figure A.21: The ratio between the predicted means μ_{fit} calculated from the individual aperture's properties (subhalo mass contained M_s and distance of the aperture to the center-of-mass r_c) and the actual aperture's mass as a function of M_s (*left*) and r_c (*right*) for the "giants", colored by the number of apertures. Blue solid lines denote the $1 - \sigma$ range, indicating that 68.2% of all apertures lie within a factor 2 of the predicted means. For the most massive subhalos, their projected masses are generally well estimated with a mild tendency toward lower values, while for the smaller subhalo masses the scatter both towards over- and underestimation are comparable, ranging up to factor 10 in a few extreme cases. This does not account for the variance of the Gaussians, and doing so finds better agreement with the found distribution of aperture masses – see Figure 8.31.
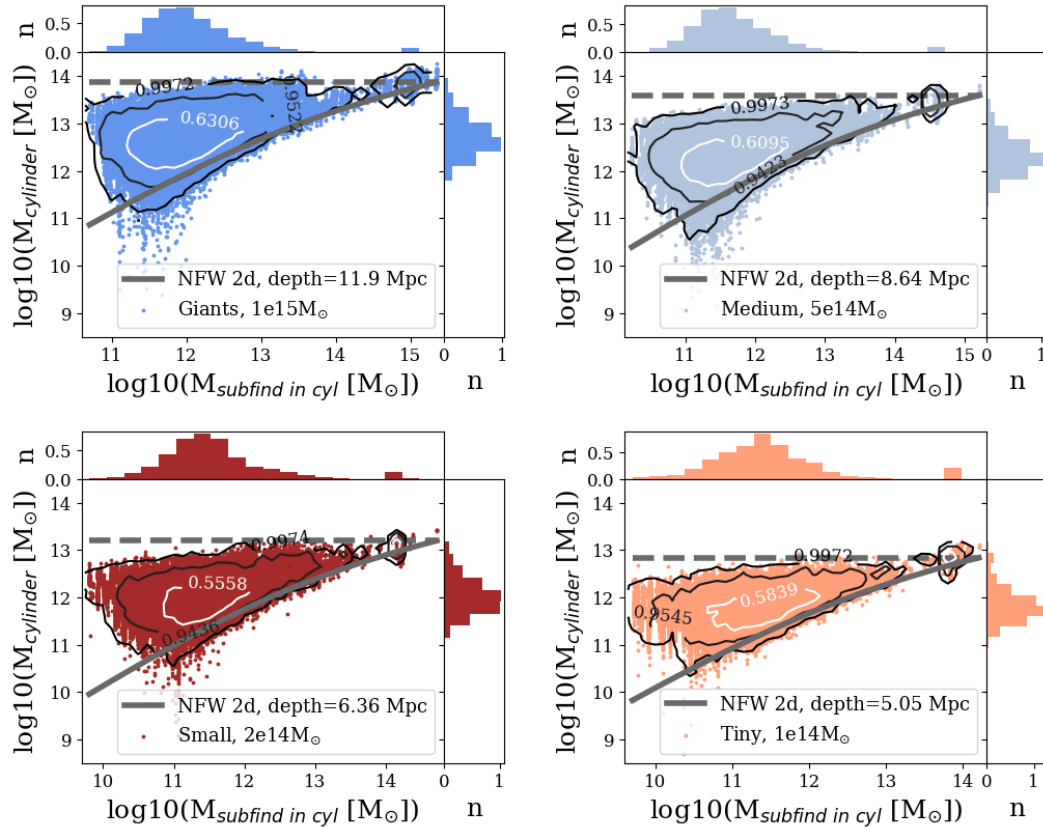
Figure A.22: The aperture mass as a function of the sum of all bound subhalos within it given by SUBFIND. The curved solid gray line denotes the projected mass within r_{ap} at depth $r_{\text{turnaround}}$ for a given bound subhalo mass M_{s} assuming the subhalo to approximate an NFW-profile (such that Equation A.8 can be used) with concentration given by the $c - M$ relation from Ragagnin et al. (2019). Horizontal dashed gray lines denote this projected mass for the most massive M_{s}.

A.6   Examples of Other Mass Bins
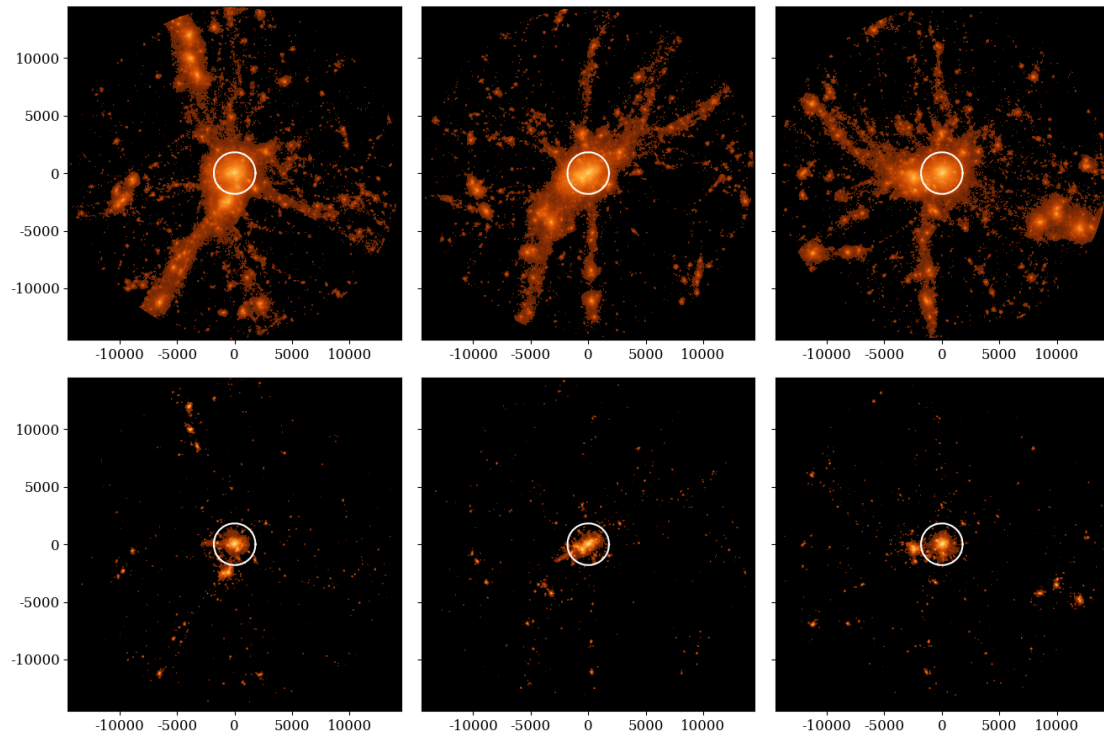
Figure A.23: The large scale structure surrounding galaxy cluster 1 of the "mediums", projected out to a depth of r_{turn} once for the total mass (*top row*) and for the stellar mass (*bottom row*). Columns depict the projection along the z-, y- and x-axis, respectively, and the cutout shows an area of $8 \cdot r_{\text{vir}}$. The central white circles denote $1 \cdot r_{\text{vir}}$ centered on the galalxy clusters most-bound-particle.
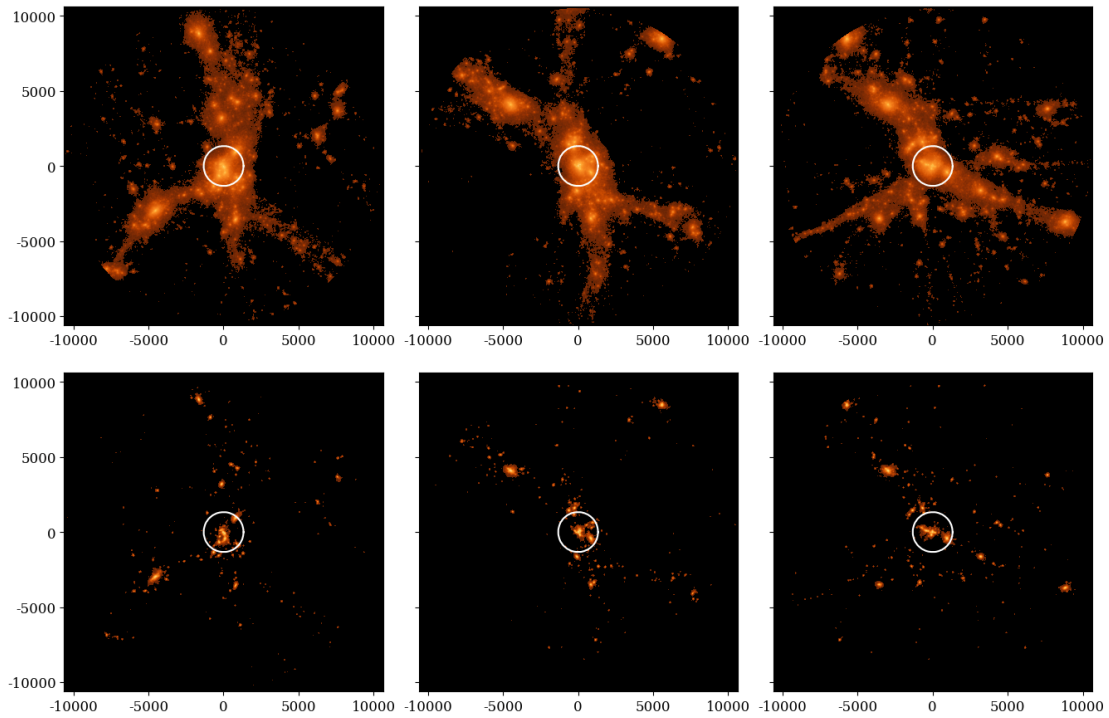
Figure A.24: The large scale structure surrounding galaxy cluster 1 of the "smalls", projected out to a depth of r_{turn} once for the total mass (*top row*) and for the stellar mass (*bottom row*). Columns depict the projection along the z-, y- and x-axis, respectively, and the cutout shows an area of $8 \cdot r_{\text{vir}}$. The central white circles denote $1 \cdot r_{\text{vir}}$ centered on the galalxy clusters most-bound-particle.
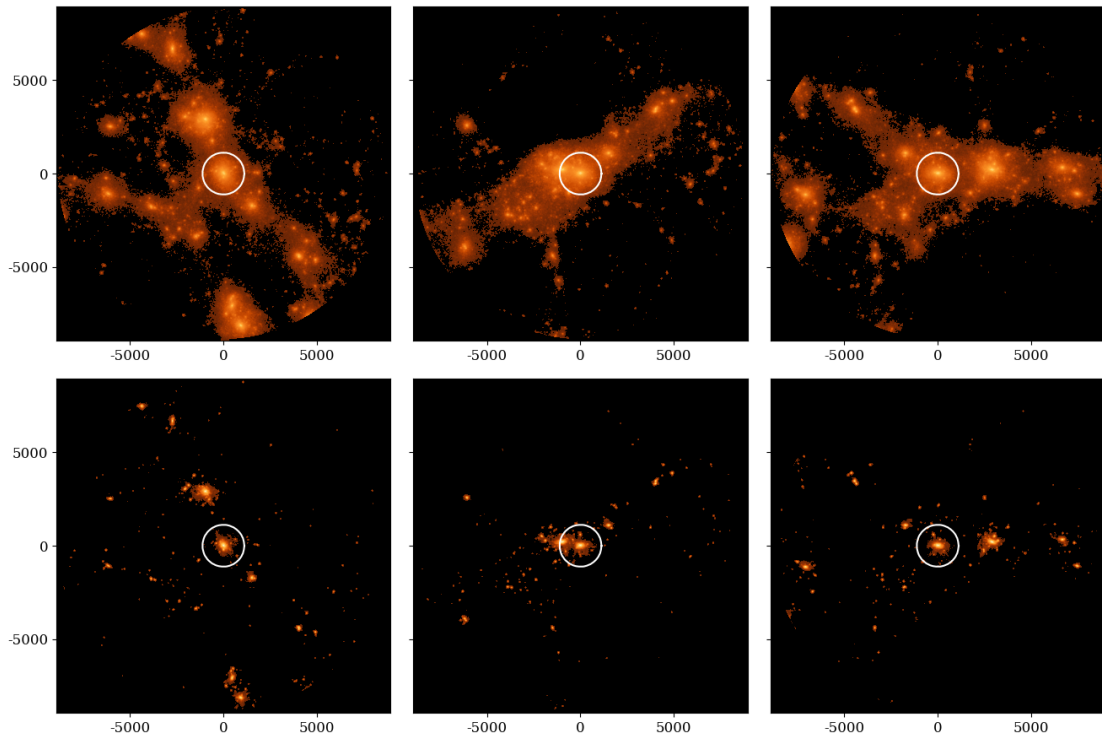
Figure A.25: The large scale structure surrounding galaxy cluster 1 of the "tinies", projected out to a depth of r_{turn} once for the total mass (*top row*) and for the stellar mass (*bottom row*). Columns depict the projection along the z-, y- and x-axis, respectively, and the cutout shows an area of $8 \cdot r_{\text{vir}}$. The central white circles denote $1 \cdot r_{\text{vir}}$ centered on the galalxy clusters most-bound-particle.

References

Abell, G. O. (1965). Clustering of Galaxies. *ARA&A*, *3*, 1.

Allen, S. W., Evrard, A. E., & Mantz, A. B. (2011). Cosmological Parameters from Observations of Galaxy Clusters. *ARA&A*, *49*(1), 409–470.

Ambartsumian, V. A. (1958). On the Evolution of Galaxies. In *La structure et l'évolution de l'universe*, (pp. 241–249).

Angulo, R. E., Lacey, C. G., Baugh, C. M., & Frenk, C. S. (2009). The fate of substructures in cold dark matter haloes. *MNRAS*, *399*(2), 983–995.

Angulo, R. E., Springel, V., White, S. D. M., Jenkins, A., Baugh, C. M., & Frenk, C. S. (2012). Scaling relations for galaxy clusters in the Millennium-XXL simulation. *MNRAS*, *426*(3), 2046–2062.

Arnau Romeu, J. (2014). Derivation of friedman equations. Last accessed: 02.04.2022. URL http://diposit.ub.edu/dspace/handle/2445/59759

Bahcall, N. A., & Kulier, A. (2014). Tracing mass and light in the Universe: where is the dark matter? *MNRAS*, *439*(3), 2505–2514.

Bahé, Y. M. (2021). Strongly lensed cluster substructures are not in tension with ΛCDM. *MNRAS*, *505*(1), 1458–1463.

Bartlett, M. S. (1963). Statistical estimation of density functions. *Sankhya: Indian J. Statistics*, *25*(3), 245–254.

Behroozi, P., Knebe, A., Pearce, F. R., Elahi, P., Han, J., Lux, H., Mao, Y.-Y., Muldrew, S. I., Potter, D., & Srisawat, C. (2015). Major mergers going Notts: challenges for modern halo finders. *MNRAS*, *454*(3), 3020–3029.

Behroozi, P. S., Wechsler, R. H., Lu, Y., Hahn, O., Busha, M. T., Klypin, A., & Primack, J. R. (2014). Mergers and Mass Accretion for Infalling Halos Both End Well Outside Cluster Virial Radii. *ApJ*, *787*(2), 156.

Behroozi, P. S., Wechsler, R. H., & Wu, H.-Y. (2013). The ROCKSTAR Phase-space Temporal Halo Finder and the Velocity Offsets of Cluster Cores. *ApJ*, *762*(2), 109.

Bergamini, P., Rosati, P., Mercurio, A., Grillo, C., Caminha, G. B., Meneghetti, M., Agnello, A., Biviano, A., Calura, F., Giocoli, C., Lombardi, M., Rodighiero, G., & Vanzella, E. (2019). Enhanced cluster lensing models with measured galaxy kinematics. *A&A*, *631*, A130.

Besançon, M., Papamarkou, T., Anthoff, D., Arslan, A., Byrne, S., Lin, D., & Pearson, J. (2021). Distributions.jl: Definition and modeling of probability distributions in the juliastats ecosystem. *Journal of Statistical Software*, *98*(16), 1–30.
URL https://www.jstatsoft.org/v098/i16

Bhattacharyya, S., Adhikari, S., Banerjee, A., More, S., Kumar, A., Nadler, E. O., & Chatterjee, S. (2021). The Signatures of Self-Interacting Dark Matter and Subhalo Disruption on Cluster Substructure. *arXiv e-prints*, (p. arXiv:2106.08292).

Bianconi, M., Smith, G. P., Haines, C. P., McGee, S. L., Finoguenov, A., & Egami, E. (2018). LoCuSS: pre-processing in galaxy groups falling into massive galaxy clusters at z = 0.2. *MNRAS*, *473*(1), L79–L83.

Biffi, V., Borgani, S., Murante, G., Rasia, E., Planelles, S., Granato, G. L., Ragone-Figueroa, C., Beck, A. M., Gaspari, M., & Dolag, K. (2016). On the Nature of Hydrostatic Equilibrium in Galaxy Clusters. *ApJ*, *827*(2), 112.

Biffi, V., Dolag, K., & Merloni, A. (2018). AGN contamination of galaxy-cluster thermal X-ray emission: predictions for eRosita from cosmological simulations. *MNRAS*, *481*(2), 2213–2227.

Binney, J., & Tremaine, S. (2008). *Galactic Dynamics: Second Edition*.

Birkinshaw, M. (1999). The Sunyaev-Zel'dovich effect. *Phys. Rep.*, *310*(2-3), 97–195.

Biviano, A. (2000). From Messier to Abell: 200 Years of Science with Galaxy Clusters. In F. Durret, & D. Gerbal (Eds.) *Constructing the Universe with Clusters of Galaxies*, (p. 1).

Blumenthal, G. R., Faber, S. M., Primack, J. R., & Rees, M. J. (1984). Formation of galaxies and large-scale structure with cold dark matter. *Nature*, *311*, 517–525.

Böhringer, H., Pratt, G. W., Arnaud, M., Borgani, S., Croston, J. H., Ponman, T. J., Ameglio, S., Temple, R. F., & Dolag, K. (2010). Substructure of the galaxy clusters in the REXCESS sample: observed statistics and comparison to numerical simulations. *A&A*, *514*, A32.

Boldt, E., McDonald, F. B., Riegler, G., & Serlemitsos, P. (1966). Extended Source of Energetic Cosmic X Rays. *Phys. Rev. Lett.*, *17*(8), 447–450.

Bond, J. R., Cole, S., Efstathiou, G., & Kaiser, N. (1991). Excursion Set Mass Functions for Hierarchical Gaussian Fluctuations. *ApJ*, *379*, 440.

Bond, J. R., Kofman, L., & Pogosyan, D. (1996). How filaments of galaxies are woven into the cosmic web. *Nature*, *380*(6575), 603–606.

Bond, J. R., Szalay, A. S., & Turner, M. S. (1982). Formation of Galaxies in a Gravitino-Dominated Universe. *Phys. Rev. Lett.*, *48*(23), 1636–1640.

Boschin, W., Girardi, M., Spolaor, M., & Barrena, R. (2006). Internal dynamics of the radio halo cluster Abell 2744. *A&A*, *449*(2), 461–474.

Boylan-Kolchin, M., Bullock, J. S., & Kaplinghat, M. (2012). The Milky Way's bright satellites as an apparent failure of ΛCDM. *MNRAS*, *422*(2), 1203–1218.

Boylan-Kolchin, M., Springel, V., White, S. D. M., Jenkins, A., & Lemson, G. (2009). Resolving cosmic structure formation with the Millennium-II Simulation. *MNRAS*, *398*(3), 1150–1164.

Bradt, H., Mayer, W., Naranan, S., Rappaport, S., & Spada, G. (1967). Evidence for X-Radiation from the Radio Galaxy M87. *ApJ*, *150*, L199.

Braglia, F. G., Pierini, D., Biviano, A., & Böhringer, H. (2009). Multi-wavelength study of X-ray luminous clusters at z ∼0.3. I. Star-formation activity of cluster galaxies. *A&A*, *500*(3), 947–963.

Brainerd, T. G., Blandford, R. D., & Smail, I. (1996). Weak Gravitational Lensing by Galaxies. *ApJ*, *466*, 623.

Brimioulle, F., Seitz, S., Lerchster, M., Bender, R., & Snigula, J. (2013). Dark matter halo properties from galaxy-galaxy lensing. *MNRAS*, *432*(2), 1046–1102.

Brooks, A. M., Kuhlen, M., Zolotov, A., & Hooper, D. (2013). A Baryonic Solution to the Missing Satellites Problem. *ApJ*, *765*(1), 22.

Brown, M. L., Taylor, A. N., Hambly, N. C., & Dye, S. (2002). Measurement of intrinsic alignments in galaxy ellipticities. *MNRAS*, *333*(3), 501–509.

Butcher, H., & Oemler, J., A. (1978). The evolution of galaxies in clusters. I. ISIT photometry of Cl 0024+1654 and 3C 295. *ApJ*, *219*, 18–30.

Byram, E. T., Chubb, T. A., & Friedman, H. (1966). Cosmic X-ray Sources, Galactic and Extragalactic. *Science*, *152*(3718), 66–71.

Carroll, S. M. (2001). The Cosmological Constant. *Living Reviews in Relativity*, *4*(1), 1.

Cautun, M., Hellwing, W. A., van de Weygaert, R., Frenk, C. S., Jones, B. J. T., & Sawala, T. (2014). Subhalo statistics of galactic haloes: beyond the resolution limit. *MNRAS*, *445*(2), 1820–1835.

Cavaliere, A., Menci, N., & Tozzi, P. (1998). Diffuse Baryons in Groups and Clusters of Galaxies. *ApJ*, *501*(2), 493–508.

Cavaliere, A. G., Gursky, H., & Tucker, W. H. (1971). Extragalactic X-ray Sources and Associations of Galaxies. *Nature*, *231*, 437–438.

Cen, R., & Ostriker, J. P. (1999). Where Are the Baryons? *ApJ*, *514*(1), 1–6.

Chandrasekhar, S. (1943). Dynamical Friction. I. General Considerations: the Coefficient of Dynamical Friction. *ApJ*, *97*, 255.

Chiang, Y.-K., Overzier, R., & Gebhardt, K. (2013). Ancient Light from Young Cosmic Cities: Physical and Observational Signatures of Galaxy Proto-clusters. *ApJ*, *779*(2), 127.

Cimatti, A., Fraternali, F., & Nipoti, C. (2019). *Introduction to Galaxy Formation and Evolution: From Primordial Gas to Present-Day Galaxies*.

Comerford, J. M., & Natarajan, P. (2007). The observed concentration-mass relation for galaxy clusters. *MNRAS*, *379*(1), 190–200.

Contini, E. (2021). On the Origin and Evolution of the Intra-Cluster Light: A Brief Review of the Most Recent Developments. *Galaxies*, *9*(3), 60.

Cooperstock, F. I., Faraoni, V., & Vollick, D. N. (1998). The Influence of the Cosmological Expansion on Local Systems. *ApJ*, *503*(1), 61–66.

Cowie, L. L., & Songaila, A. (1977). Thermal evaporation of gas within galaxies by a hot intergalactic medium. *Nature*, *266*, 501–503.

Cowley, W. I., Caputi, K. I., Deshmukh, S., Ashby, M. L. N., Fazio, G. G., Le Fèvre, O., Fynbo, J. P. U., Ilbert, O., & Milvang-Jensen, B. (2019). The Stellar-to-halo Mass Ratios of Passive and Star-forming Galaxies at z ~ 2-3 from the SMUVS Survey. *ApJ*, *874*(2), 114.

Dalal, N., White, M., Bond, J. R., & Shirokov, A. (2008). Halo Assembly Bias in Hierarchical Structure Formation. *ApJ*, *687*(1), 12–21.

Davidsen, A., Bowyer, S., Lampton, M., & Cruddace, R. (1975). The soft X-ray spectrum of the Perseus cluster. *ApJ*, *198*, 1–6.

Davis, M., Efstathiou, G., Frenk, C. S., & White, S. D. M. (1985). The evolution of large-scale structure in a universe dominated by cold dark matter. *ApJ*, *292*, 371–394.

Davis, T. M., Lineweaver, C. H., & Webb, J. K. (2003). Solutions to the tethered galaxy problem in an expanding universe and the observation of receding blueshifted objects. *American Journal of Physics*, *71*(4), 358–364.

De Lucia, G., Kauffmann, G., Springel, V., White, S. D. M., Lanzoni, B., Stoehr, F., Tormen, G., & Yoshida, N. (2004). Substructures in cold dark matter haloes. *MNRAS*, *348*(1), 333–344.

Dhar, B. K. (2021). Erratum: High-accuracy analytical solutions for the projected mass (counts) and surface density (brightness) of Einasto profiles. *MNRAS*, *505*(4), 5468–5468.

Dhoke, P., & Paranjape, A. (2021). Mass accretion rates and multiscale halo environment in cold and warm dark matter cosmologies. *MNRAS*, *508*(1), 852–867.

Diemand, J., Kuhlen, M., & Madau, P. (2007). Formation and Evolution of Galaxy Dark Matter Halos and Their Substructure. *ApJ*, *667*(2), 859–877.

Dolag, K. (2022). Simulations - magneticum pathfinder & magneticum. Web portal for the Magneticum Pathfinder Simulation developed by Klaus Dolag, last accessed: 06.03.2022. URL http://www.magneticum.org/simulations.html

Dolag, K., Borgani, S., Murante, G., & Springel, V. (2009). Substructures in hydrodynamical cluster simulations. *MNRAS*, *399*(2), 497–514.

Dolag, K., Mevius, E., & Remus, R.-S. (2017). Distribution and Evolution of Metals in the Magneticum Simulations. *Galaxies*, *5*(3), 35.

Dolag, K., Murante, G., & Borgani, S. (2010). Dynamical difference between the cD galaxy and the diffuse, stellar component in simulated galaxy clusters. *MNRAS*, *405*(3), 1544–1559.

Doroshkevich, A. G. (1970). Spatial structure of perturbations and origin of galactic rotation in fluctuation theory. *Astrophysics*, *6*(4), 320–330.

Drake, F. D. (1958). *Neutral Hydrogen in Galactic Clusters.*. Ph.D. thesis, HARVARD UNIVERSITY.

Dressler, A. (1980). Galaxy morphology in rich clusters: implications for the formation and evolution of galaxies. *ApJ*, *236*, 351–365.

Dressler, A., Lynden-Bell, D., Burstein, D., Davies, R. L., Faber, S. M., Terlevich, R., & Wegner, G. (1987). Spectroscopy and Photometry of Elliptical Galaxies. I. New Distance Estimator. *ApJ*, *313*, 42.

Dubois, Y., Devriendt, J., Slyz, A., & Teyssier, R. (2010). Jet-regulated cooling catastrophe. *MNRAS*, *409*(3), 985–1001.

Dubois, Y., Pichon, C., Welker, C., Le Borgne, D., Devriendt, J., Laigle, C., Codis, S., Pogosyan, D., Arnouts, S., Benabed, K., Bertin, E., Blaizot, J., Bouchet, F., Cardoso, J. F., Colombi, S., de Lapparent, V., Desjacques, V., Gavazzi, R., Kassin, S., Kimm, T., McCracken, H., Milliard, B., Peirani, S., Prunet, S., Rouberol, S., Silk, J., Slyz, A., Sousbie,

T., Teyssier, R., Tresse, L., Treyer, M., Vibert, D., & Volonteri, M. (2014). Dancing in the dark: galactic properties trace spin swings along the cosmic web. *MNRAS*, *444*(2), 1453–1468.

Eckert, D., Jauzac, M., Shan, H., Kneib, J.-P., Erben, T., Israel, H., Jullo, E., Klein, M., Massey, R., Richard, J., & Tchernin, C. (2015). Warm-hot baryons comprise 5-10 per cent of filaments in the cosmic web. *Nature*, *528*(7580), 105–107.

Einasto, J. (1965). On the Construction of a Composite Model for the Galaxy and on the Determination of the System of Galactic Parameters. *Trudy Astrofizicheskogo Instituta Alma-Ata*, *5*, 87–100.

Einasto, J., Kaasik, A., & Saar, E. (1974). Dynamic evidence on massive coronas of galaxies. *Nature*, *250*(5464), 309–310.

Elíasdóttir, Á., Limousin, M., Richard, J., Hjorth, J., Kneib, J.-P., Natarajan, P., Pedersen, K., Jullo, E., & Paraficz, D. (2007). Where is the matter in the Merging Cluster Abell 2218? *arXiv e-prints*, (p. arXiv:0710.5636).

Ellis, G. F. R., Maartens, R., & MacCallum, M. A. H. (2012). *Relativistic Cosmology*.

Elvis, M. (1976). Ariel V Sky Survey: long-term monitoring of the X-ray emission from the Coma Cluster and NGC 4151. *MNRAS*, *177*, 7P–12.

Faber, S. M., & Jackson, R. E. (1976). Velocity dispersions and mass-to-light ratios for elliptical galaxies. *ApJ*, *204*, 668–683.

Fakhouri, O., & Ma, C.-P. (2008). The nearly universal merger rate of dark matter haloes in ΛCDM cosmology. *MNRAS*, *386*(2), 577–592.

Fakhouri, O., & Ma, C.-P. (2009). Environmental dependence of dark matter halo growth - I. Halo merger rates. *MNRAS*, *394*(4), 1825–1840.

Fakhouri, O., & Ma, C.-P. (2010). Dark matter halo growth - II. Diffuse accretion and its environmental dependence. *MNRAS*, *401*(4), 2245–2256.

Fakhouri, O., Ma, C.-P., & Boylan-Kolchin, M. (2010). The merger rates and mass assembly histories of dark matter haloes in the two Millennium simulations. *MNRAS*, *406*(4), 2267–2278.

Ferraris, M., Francaviglia, M., & Spallicci, A. (1996). Associated radius, energy and pressure of McVittie's metric, in its astrophysical application. *Nuovo Cimento B Serie*, *111*, 1031.

Fort, B., & Mellier, Y. (1994). Arc(let)s in clusters of galaxies. *A&A Rev.*, *5*(4), 239–292.

Frenk, C. S., Evrard, A. E., White, S. D. M., & Summers, F. J. (1996). Galaxy Dynamics in Clusters. *ApJ*, *472*, 460.

Friedmann, A. (1922). Über die Krümmung des Raumes. *Zeitschrift fur Physik*, *10*, 377–386.

Gao, L., & White, S. D. M. (2007). Assembly bias in the clustering of dark matter haloes. *MNRAS*, *377*(1), L5–L9.

Gao, L., White, S. D. M., Jenkins, A., Stoehr, F., & Springel, V. (2004). The subhalo populations of ΛCDM dark haloes. *MNRAS*, *355*(3), 819–834.

Gingold, R. A., & Monaghan, J. J. (1977). Smoothed particle hydrodynamics: theory and application to non-spherical stars. *MNRAS*, *181*, 375–389.

Giocoli, C., Tormen, G., & van den Bosch, F. C. (2008). The population of dark matter subhaloes: mass functions and average mass-loss rates. *MNRAS*, *386*(4), 2135–2144.

Giovannini, G., Tordi, M., & Feretti, L. (1999). Radio halo and relic candidates from the NRAO VLA Sky Survey. *New A*, *4*(2), 141–155.

Glazebrook, K., Nanayakkara, T., Esdaile, J., Espejo, J. M., Jacobs, C., Kacprzak, G. G., Labbe, I., Marchesini, D., Marsan, C., Oesch, P., Papovich, C., Remus, R.-S., Schreiber, C., Straatman, C., Tran, K.-V., & Urbina, C. L. (2021). How Many Quiescent Galaxies are There at 3. JWST Proposal. Cycle 1, ID. #2565.

Gómez, J. S., Padilla, N. D., Helly, J. C., Lacey, C. G., Baugh, C. M., & Lagos, C. D. P. (2022). Halo merger tree comparison: impact on galaxy formation models. *MNRAS*, *510*(4), 5500–5519.

Granata, G., Mercurio, A., Grillo, C., Tortorelli, L., Bergamini, P., Meneghetti, M., Rosati, P., Caminha, G. B., & Nonino, M. (2022). Improved strong lensing modelling of galaxy clusters using the Fundamental Plane: Detailed mapping of the baryonic and dark matter mass distribution of Abell S1063. *A&A*, *659*, A24.

Gunn, J. E., & Gott, I., J. Richard (1972). On the Infall of Matter Into Clusters of Galaxies and Some Effects on Their Evolution. *ApJ*, *176*, 1.

Hahn, O., Carollo, C. M., Porciani, C., & Dekel, A. (2007). The evolution of dark matter halo properties in clusters, filaments, sheets and voids. *MNRAS*, *381*(1), 41–51.

Hahn, O., Porciani, C., Dekel, A., & Carollo, C. M. (2009). Tidal effects and the environment dependence of halo assembly. *MNRAS*, *398*(4), 1742–1756.

Hamilton, A. (2020). ASTR 3740 Relativity and Cosmology - 10 Homogeneous, Isotropic Cosmology.
URL https://jila.colorado.edu/~ajsh/astr3740_14/flrw.pdf

Han, J., Cole, S., Frenk, C. S., Benitez-Llambay, A., & Helly, J. (2018a). HBT+: an improved code for finding subhaloes and building merger trees in cosmological simulations. *MNRAS*, *474*(1), 604–617.

Han, J., Cole, S., Frenk, C. S., & Jing, Y. (2016). A unified model for the spatial and mass distribution of subhaloes. *MNRAS*, *457*(2), 1208–1223.

Han, J., Li, Y., Jing, Y., Nishimichi, T., Wang, W., & Jiang, C. (2019). The multidimensional dependence of halo bias in the eye of a machine: a tale of halo structure, assembly, and environment. *MNRAS*, *482*(2), 1900–1919.

Han, S., Smith, R., Choi, H., Cortese, L., Catinella, B., Contini, E., & Yi, S. K. (2018b). YZiCS: Preprocessing of Dark Halos in the Hydrodynamic Zoom-in Simulation of Clusters. *ApJ*, *866*(2), 78.

Harrison, E. R. (1970). Fluctuations at the Threshold of Classical Cosmology. *Phys. Rev. D*, *1*(10), 2726–2730.

Hayashi, E., & Navarro, J. F. (2003). Structural Evolution of Substructure. In J. Makino, & P. Hut (Eds.) *Astrophysical Supercomputing using Particle Simulations*, vol. 208, (p. 403).

Heavens, A., Refregier, A., & Heymans, C. (2000). Intrinsic correlation of galaxy shapes: implications for weak lensing measurements. *MNRAS*, *319*(2), 649–656.

Hernquist, L. (1990). An Analytical Model for Spherical Galaxies and Bulges. *ApJ*, *356*, 359.

Herschel, W. (1785). On the construction of the heavens. by william herschel, esq. f. r. s. *Philosophical Transactions of the Royal Society of London*, *75*, 213–266. URL http://www.jstor.org/stable/106755

Hester, J. A. (2006). Ram Pressure Stripping in Clusters and Groups. *ApJ*, *647*(2), 910–921.

Hirschmann, M., Dolag, K., Saro, A., Bachmann, L., Borgani, S., & Burkert, A. (2014). Cosmological simulations of black hole growth: AGN luminosities and downsizing. *MNRAS*, *442*(3), 2304–2324.

Holmberg, E. (1941). On the Clustering Tendencies among the Nebulae. II. a Study of Encounters Between Laboratory Models of Stellar Systems by a New Integration Procedure. *ApJ*, *94*, 385.

Hoyle, F. (1949). *Problems of Cosmical Aerodynamics")*. Dayton, Ohio: Burgers J. M., van de Hulst H. C., eds.

Hubble, E. (1934). The Distribution of Extra-Galactic Nebulae. *ApJ*, *79*, 8.

Hudson, M. J., Gillis, B. R., Coupon, J., Hildebrandt, H., Erben, T., Heymans, C., Hoekstra, H., Kitching, T. D., Mellier, Y., Miller, L., Van Waerbeke, L., Bonnett, C., Fu, L., Kuijken, K., Rowe, B., Schrabback, T., Semboloni, E., van Uitert, E., & Velander, M. (2015). CFHTLenS: co-evolution of galaxies and their dark matter haloes. *MNRAS*, *447*(1), 298–314.

Hunter, J. D. (2007). Matplotlib: A 2d graphics environment. *Computing in Science & Engineering*, *9*(3), 90–95.

Jauzac, M., Eckert, D., Schwinn, J., Harvey, D., Baugh, C. M., Robertson, A., Bose, S., Massey, R., Owers, M., Ebeling, H., Shan, H. Y., Jullo, E., Kneib, J. P., Richard, J., Atek, H., Clément, B., Egami, E., Israel, H., Knowles, K., Limousin, M., Natarajan, P., Rexroth, M., Taylor, P., & Tchernin, C. (2016). The extraordinary amount of substructure in the Hubble Frontier Fields cluster Abell 2744. *MNRAS*, *463*(4), 3876–3893.

Jauzac, M., Richard, J., Jullo, E., Clément, B., Limousin, M., Kneib, J. P., Ebeling, H., Natarajan, P., Rodney, S., Atek, H., Massey, R., Eckert, D., Egami, E., & Rexroth, M. (2015). Hubble Frontier Fields: a high-precision strong-lensing analysis of the massive galaxy cluster Abell 2744 using ~180 multiple images. *MNRAS*, *452*(2), 1437–1446.

Jenkins, A., Frenk, C. S., White, S. D. M., Colberg, J. M., Cole, S., Evrard, A. E., Couchman, H. M. P., & Yoshida, N. (2001). The mass function of dark matter haloes. *MNRAS*, *321*(2), 372–384.

Jiang, F., & van den Bosch, F. C. (2016). Statistics of dark matter substructure - I. Model and universal fitting functions. *MNRAS*, *458*(3), 2848–2869.

Jiang, F., & van den Bosch, F. C. (2017). Statistics of dark matter substructure - III. Halo-to-halo variance. *MNRAS*, *472*(1), 657–674.

Jullo, E., Kneib, J. P., Limousin, M., Elíasdóttir, Á., Marshall, P. J., & Verdugo, T. (2007). A Bayesian approach to strong lensing modelling of galaxy clusters. *New Journal of Physics*, *9*(12), 447.

Jung, C. (1933). *Modern Man in Search of Soul*. London: Kegan Paul, Trench, Trubner and Co.

Kaiser, N., & Squires, G. (1993). Mapping the Dark Matter with Weak Gravitational Lensing. *ApJ*, *404*, 441.

Kamionkowski, M., & Kovetz, E. D. (2016). The quest for b modes from inflationary gravitational waves. *Annual Review of Astronomy and Astrophysics*, *54*(1), 227–269. URL https://doi.org/10.1146/annurev-astro-081915-023433

Kamionkowski, M., & Kovetz, E. D. (2016). The Quest for B Modes from Inflationary Gravitational Waves. *ARA&A*, *54*, 227–269.

Kassiola, A., & Kovner, I. (1993). Elliptic Mass Distributions versus Elliptic Potentials in Gravitational Lenses. *ApJ*, *417*, 450.

Kauffmann, G., Colberg, J. M., Diaferio, A., & White, S. D. M. (1999). Clustering of galaxies in a hierarchical universe - I. Methods and results at z=0. *MNRAS*, *303*(1), 188–206.

Khandai, N., Di Matteo, T., Croft, R., Wilkins, S., Feng, Y., Tucker, E., DeGraf, C., & Liu, M.-S. (2015). The MassiveBlack-II simulation: the evolution of haloes and galaxies to z ∼ 0. *MNRAS*, *450*(2), 1349–1374.

Kinney, W. H. (2003). Cosmology, inflation, and the physics of nothing. *arXiv e-prints*, (pp. astro–ph/0301448).

Klypin, A., Gottlöber, S., Kravtsov, A. V., & Khokhlov, A. M. (1999). Galaxies in N-Body Simulations: Overcoming the Overmerging Problem. *ApJ*, *516*(2), 530–551.

Klypin, A., Yepes, G., Gottlöber, S., Prada, F., & Heß, S. (2016). MultiDark simulations: the story of dark matter halo concentrations and density profiles. *MNRAS*, *457*(4), 4340–4359.

Klypin, A. A., Trujillo-Gomez, S., & Primack, J. (2011). Dark Matter Halos in the Standard Cosmological Model: Results from the Bolshoi Simulation. *ApJ*, *740*(2), 102.

Knebe, A., Knollmann, S. R., Muldrew, S. I., Pearce, F. R., Aragon-Calvo, M. A., Ascasibar, Y., Behroozi, P. S., Ceverino, D., Colombi, S., Diemand, J., Dolag, K., Falck, B. L., Fasel, P., Gardner, J., Gottlöber, S., Hsu, C.-H., Iannuzzi, F., Klypin, A., Lukić, Z., Maciejewski, M., McBride, C., Neyrinck, M. C., Planelles, S., Potter, D., Quilis, V., Rasera, Y., Read, J. I., Ricker, P. M., Roy, F., Springel, V., Stadel, J., Stinson, G., Sutter, P. M., Turchaninov, V., Tweed, D., Yepes, G., & Zemp, M. (2011). Haloes gone MAD: The Halo-Finder Comparison Project. *MNRAS*, *415*(3), 2293–2318.

Kneib, J. P., Ellis, R. S., Smail, I., Couch, W. J., & Sharples, R. M. (1996). Hubble Space Telescope Observations of the Lensing Cluster Abell 2218. *ApJ*, *471*, 643.

Kochanek, C. S. (2004). The saas fee lectures on strong gravitational lensing.
URL https://arxiv.org/abs/astro-ph/0407232

Komatsu, E., Smith, K. M., Dunkley, J., Bennett, C. L., Gold, B., Hinshaw, G., Jarosik, N., Larson, D., Nolta, M. R., Page, L., Spergel, D. N., Halpern, M., Hill, R. S., Kogut, A., Limon, M., Meyer, S. S., Odegard, N., Tucker, G. S., Weiland, J. L., Wollack, E., & Wright, E. L. (2011). Seven-year Wilkinson Microwave Anisotropy Probe (WMAP) Observations: Cosmological Interpretation. *ApJS*, *192*(2), 18.

Koopmans, L. V. E., Treu, T., Bolton, A. S., Burles, S., & Moustakas, L. A. (2006). The Sloan Lens ACS Survey. III. The Structure and Formation of Early-Type Galaxies and Their Evolution since z ~1. *ApJ*, *649*(2), 599–615.

Kravtsov, A. V., & Borgani, S. (2012). Formation of galaxy clusters. *Annual Review of Astronomy and Astrophysics*, *50*(1), 353–409.
URL https://doi.org/10.1146/annurev-astro-081811-125502

Kutner, M. L. (2003). *Astronomy: A Physical Perspective*.

Lacey, C., & Cole, S. (1993). Merger rates in hierarchical models of galaxy formation. *MNRAS*, *262*(3), 627–649.

Lacey, C., & Cole, S. (1994). Merger Rates in Hierarchical Models of Galaxy Formation - Part Two - Comparison with N-Body Simulations. *MNRAS*, *271*, 676.

Landau, L. D., & Lifshitz, E. M. (1975). *The classical theory of fields*.

Laporte, C. F. P., White, S. D. M., Naab, T., & Gao, L. (2013). The growth in size and mass of cluster galaxies since z = 2. *MNRAS*, *435*(2), 901–909.

Larson, R. B., Tinsley, B. M., & Caldwell, C. N. (1980). The evolution of disk galaxies and the origin of S0 galaxies. *ApJ*, *237*, 692–707.

Lemaître, G. (1927). Un Univers homogène de masse constante et de rayon croissant rendant compte de la vitesse radiale des nébuleuses extra-galactiques. *Annales de la Société Scientifique de Bruxelles*, *47*, 49–59.

Li, Y., Mo, H. J., & Gao, L. (2008). On halo formation times and assembly bias. *MNRAS*, *389*(3), 1419–1426.

Liddle, A. R. (1999). An Introduction to Cosmological Inflation. In A. Masiero, G. Senjanovic, & A. Smirnov (Eds.) *High Energy Physics and Cosmology, 1998 Summer School*, (p. 260).

Lima, M., Jain, B., & Devlin, M. (2010). Lensing magnification: implications for counts of submillimetre galaxies and SZ clusters. *MNRAS*, *406*(4), 2352–2372.

Limber, D. N. (1959). Effects of Intracluster Gas and Duct upon the Virial Theorem. *ApJ*, *130*, 414.

Limber, D. N. (1962). Kinematics and Dynamics of Clusters of Galaxies. In G. C. McVittie (Ed.) *Problems of Extra-Galactic Research*, vol. 15, (p. 239).

Limber, D. N., & Mathews, W. G. (1960). The Dynamical Stability of Stephan's Quintet. *ApJ*, *132*, 286.

Limousin, M., Richard, J., Jullo, E., Kneib, J.-P., Fort, B., Soucail, G., Elíasdóttir, Á., Natarajan, P., Ellis, R. S., Smail, I., Czoske, O., Smith, G. P., Hudelot, P., Bardeau, S., Ebeling, H., Egami, E., & Knudsen, K. K. (2007). Combining Strong and Weak Gravitational Lensing in Abell 1689. *ApJ*, *668*(2), 643–666.

Lotz, J. M., Koekemoer, A., Coe, D., Grogin, N., Capak, P., Mack, J., Anderson, J., Avila, R., Barker, E. A., Borncamp, D., Brammer, G., Durbin, M., Gunning, H., Hilbert, B., Jenkner, H., Khandrika, H., Levay, Z., Lucas, R. A., MacKenty, J., Ogaz, S., Porterfield, B., Reid, N., Robberto, M., Royle, P., Smith, L. J., Storrie-Lombardi, L. J., Sunnquist, B., Surace, J., Taylor, D. C., Williams, R., Bullock, J., Dickinson, M., Finkelstein, S., Natarajan, P.,

Richard, J., Robertson, B., Tumlinson, J., Zitrin, A., Flanagan, K., Sembach, K., Soifer, B. T., & Mountain, M. (2017). The Frontier Fields: Survey Design and Initial Results. *ApJ*, *837*(1), 97.

Lotz, M., Dolag, K., Remus, R.-S., & Burkert, A. (2021). Rise and fall of post-starburst galaxies in Magneticum Pathfinder. *MNRAS*, *506*(3), 4516–4542.

Lotz, M., Remus, R.-S., Dolag, K., Biviano, A., & Burkert, A. (2019). Gone after one orbit: How cluster environments quench galaxies. *MNRAS*, *488*(4), 5370–5389.

Lovisari, L., Reiprich, T. H., & Schellenberger, G. (2015). Scaling properties of a complete X-ray selected galaxy group sample. *A&A*, *573*, A118.

Lucy, L. B. (1977). A numerical approach to the testing of the fission hypothesis. *AJ*, *82*, 1013–1024.

Ludlow, A. D., Navarro, J. F., Boylan-Kolchin, M., Bett, P. E., Angulo, R. E., Li, M., White, S. D. M., Frenk, C., & Springel, V. (2013). The mass profile and accretion history of cold dark matter haloes. *MNRAS*, *432*(2), 1103–1113.

Lynds, R., & Petrosian, V. (1986). Giant Luminous Arcs in Galaxy Clusters. In *Bulletin of the American Astronomical Society*, vol. 18, (p. 1014).

Marini, I., Borgani, S., Saro, A., Granato, G. L., Ragone-Figueroa, C., Sartoris, B., Dolag, K., Murante, G., Ragagnin, A., & Wang, Y. (2021). Velocity dispersion of brightest cluster galaxies in cosmological simulations. *MNRAS*, *507*(4), 5780–5795.

Martin, G., Bazkiaei, A. E., Iodice, M. S. E., Mihos, J. C., Montes, M., Benavides, J. A., Brough, S., Carlin, J. L., Collins, C. A., Duc, P. A., Gómez, F. A., Galaz, G., Hernández-Toledo, H. M., Jackson, R. A., Kaviraj, S., Knapen, J. H., Martínez-Lombilla, C., McGee, S., O'Ryan, D., Prole, D. J., Rich, R. M., Román, J., Shah, E. A., Starkenburg, T. K., Watkins, A. E., Zaritsky, D., Pichon, C., Armus, L., Bianconi, M., Buitrago, F., Busá, I., Davis, F., Demarco, R., Desmons, A., García, P., Graham, A. W., Holwerda, B., Hon, D. S. H., Khalid, A., Klehammer, J., Klutse, D. Y., Lazar, I., Nair, P., Noakes-Kettel, E. A., Rutkowski, M., Saha, K., Sahu, N., Sola, E., Vázquez-Mata, J. A., Vera-Casanova, A., & Yoon, I. (2022). Preparing for low surface brightness science with the Vera C. Rubin Observatory: characterisation of tidal features from mock images. *MNRAS*.

Mather, J. C., Cheng, E. S., Eplee, J., R. E., Isaacman, R. B., Meyer, S. S., Shafer, R. A., Weiss, R., Wright, E. L., Bennett, C. L., Boggess, N. W., Dwek, E., Gulkis, S., Hauser, M. G., Janssen, M., Kelsall, T., Lubin, P. M., Moseley, J., S. H., Murdock, T. L., Silverberg, R. F., Smoot, G. F., & Wilkinson, D. T. (1990). A Preliminary Measurement of the Cosmic Microwave Background Spectrum by the Cosmic Background Explorer (COBE) Satellite. *ApJ*, *354*, L37.

Maulbetsch, C., Avila-Reese, V., Colín, P., Gottlöber, S., Khalatyan, A., & Steinmetz, M. (2007). The Dependence of the Mass Assembly History of Cold Dark Matter Halos on Environment. *ApJ*, *654*(1), 53–65.

McBride, J., Fakhouri, O., & Ma, C.-P. (2009). Mass accretion rates and histories of dark matter haloes. *MNRAS*, *398*(4), 1858–1868.

McVittie, G. C. (1933). The Mass-Particle in an Expanding Universe. *Monthly Notices of the Royal Astronomical Society*, *93*(5), 325–339.
URL https://doi.org/10.1093/mnras/93.5.325

Melia, F. (2012). The cosmic spacetime.

Meneghetti, M., Davoli, G., Bergamini, P., Rosati, P., Natarajan, P., Giocoli, C., Caminha, G. B., Metcalf, R. B., Rasia, E., Borgani, S., Calura, F., Grillo, C., Mercurio, A., & Vanzella, E. (2020). An excess of small-scale gravitational lenses observed in galaxy clusters. *Science*, *369*(6509), 1347–1351.

Merten, J., Coe, D., Dupke, R., Massey, R., Zitrin, A., Cypriano, E. S., Okabe, N., Frye, B., Braglia, F. G., Jiménez-Teja, Y., Benítez, N., Broadhurst, T., Rhodes, J., Meneghetti, M., Moustakas, L. A., Sodré, J., L., Krick, J., & Bregman, J. N. (2011). Creation of cosmic structure in the complex galaxy cluster merger Abell 2744. *MNRAS*, *417*(1), 333–347.

Meszaros, P. (1974). The behaviour of point masses in an expanding cosmological substratum. *A&A*, *37*(2), 225–228.

Mitra, A. (2012). Deriving friedmann robertson walker metric and hubble's law from gravitational collapse formalism. *Results in Physics*, *2*, 45–49.
URL https://www.sciencedirect.com/science/article/pii/S2211379712000095

Mo, H., van den Bosch, F. C., & White, S. (2010). *Galaxy Formation and Evolution*.

Moliné, Á., Sánchez-Conde, M. A., Aguirre-Santaella, A., Ishiyama, T., Prada, F., Cora, S. A., Croton, D., Jullo, E., Metcalf, R. B., Oogi, T., & Ruedas, J. (2021). LCDM halo substructure properties revealed with high resolution and large volume cosmological simulations. *arXiv e-prints*, (p. arXiv:2110.02097).

Moliné, Á., Sánchez-Conde, M. A., Palomares-Ruiz, S., & Prada, F. (2017). Characterization of subhalo structural properties and implications for dark matter annihilation signals. *MNRAS*, *466*(4), 4974–4990.

Moore, B., Katz, N., Lake, G., Dressler, A., & Oemler, A. (1996). Galaxy harassment and the evolution of clusters of galaxies. *Nature*, *379*(6566), 613–616.

Mukhanov, V. (2005). *Physical Foundations of Cosmology*.

Muldrew, S. I., Pearce, F. R., & Power, C. (2011). The accuracy of subhalo detection. *MNRAS*, *410*(4), 2617–2624.

Myers, S. T., Baker, J. E., Readhead, A. C. S., Leitch, E. M., & Herbig, T. (1997). Measurements of the Sunyaev-Zeldovich Effect in the Nearby Clusters A478, A2142, and A2256. *ApJ*, *485*(1), 1–21.

Nandra, R., Lasenby, A. N., & Hobson, M. P. (2012). The effect of a massive object on an expanding universe. *Monthly Notices of the Royal Astronomical Society*, *422*(4), 2931–2944.
URL http://dx.doi.org/10.1111/j.1365-2966.2012.20618.x

Narayan, R., & Bartelmann, M. (1996). Lectures on Gravitational Lensing. *arXiv e-prints*, (pp. astro–ph/9606001).

Navarro, J. F., Frenk, C. S., & White, S. D. M. (1996). The Structure of Cold Dark Matter Halos. *ApJ*, *462*, 563.

Nelson, D., Pillepich, A., Springel, V., Weinberger, R., Hernquist, L., Pakmor, R., Genel, S., Torrey, P., Vogelsberger, M., Kauffmann, G., Marinacci, F., & Naiman, J. (2018). First results from the IllustrisTNG simulations: the galaxy colour bimodality. *MNRAS*, *475*(1), 624–647.

Nesseris, S., & Perivolaropoulos, L. (2004). Fate of bound systems in phantom and quintessence cosmologies. *Phys. Rev. D*, *70*(12), 123529.

Neto, A. F., Gao, L., Bett, P., Cole, S., Navarro, J. F., Frenk, C. S., White, S. D. M., Springel, V., & Jenkins, A. (2007). The statistics of Λ CDM halo concentrations. *MNRAS*, *381*(4), 1450–1462.

Newton, I. (1687). *Philosophiae Naturalis Principia Mathematica ("Mathematical Principles of Natural Philosophy")*. London.

Niemiec, A., Jullo, E., Limousin, M., Giocoli, C., Erben, T., Hildebrant, H., Kneib, J.-P., Leauthaud, A., Makler, M., Moraes, B., Pereira, M. E. S., Shan, H., Rozo, E., Rykoff, E., & Van Waerbeke, L. (2017). Stellar-to-halo mass relation of cluster galaxies. *MNRAS*, *471*(1), 1153–1166.

Noether, E. (1918). Invariante variationsprobleme. *Nachrichten von der Gesellschaft der Wissenschaften zu Göttingen, Mathematisch-Physikalische Klasse*, *1918*, 235–257.
URL http://eudml.org/doc/59024

Okabe, N., Futamase, T., Kajisawa, M., & Kuroshima, R. (2014). Subaru Weak-lensing Survey of Dark Matter Subhalos in the Coma Cluster: Subhalo Mass Function and Statistical Properties. *ApJ*, *784*(2), 90.

Olive, K. A., Schramm, D. N., Steigman, G., Turner, M. S., & Yang, J. (1981). Big-bang nucleosynthesis as a probe of cosmology and particle physics. *ApJ*, *246*, 557–568.

Oser, L., Ostriker, J. P., Naab, T., Johansson, P. H., & Burkert, A. (2010). The Two Phases of Galaxy Formation. *ApJ*, *725*(2), 2312–2323.

Ostriker, J. P., Peebles, P. J. E., & Yahil, A. (1974). The Size and Mass of Galaxies, and the Mass of the Universe. *ApJ*, *193*, L1.

Owers, M. S., Hudson, M. J., Oman, K. A., Bland-Hawthorn, J., Brough, S., Bryant, J. J., Cortese, L., Couch, W. J., Croom, S. M., van de Sande, J., Federrath, C., Groves, B., Hopkins, A. M., Lawrence, J. S., Lorente, N. P. F., McDermid, R. M., Medling, A. M., Richards, S. N., Scott, N., Taranu, D. S., Welker, C., & Yi, S. K. (2019). The SAMI Galaxy Survey: Quenching of Star Formation in Clusters I. Transition Galaxies. *ApJ*, *873*(1), 52.

Owers, M. S., Randall, S. W., Nulsen, P. E. J., Couch, W. J., David, L. P., & Kempner, J. C. (2011). The Dissection of Abell 2744: A Rich Cluster Growing Through Major and Minor Mergers. *ApJ*, *728*(1), 27.

Paczynski, B. (1987). Giant luminous arcs discovered in two clusters of galaxies. *Nature*, *325*(6105), 572–573.

Page, T. (1952). Radial Velocities and Masses of Double Galaxies. *ApJ*, *116*, 63.

Peñarrubia, J., Benson, A. J., Walker, M. G., Gilmore, G., McConnachie, A. W., & Mayer, L. (2010). The impact of dark matter cusps and cores on the satellite galaxy population around spiral galaxies. *MNRAS*, *406*(2), 1290–1305.

Peñarrubia, J., Navarro, J. F., & McConnachie, A. W. (2008). The Tidal Evolution of Local Group Dwarf Spheroidals. *ApJ*, *673*(1), 226–240.

Peebles, P. J. E. (1993). *Principles of Physical Cosmology*.

Peebles, P. J. E., & Yu, J. T. (1970). Primeval Adiabatic Perturbation in an Expanding Universe. *ApJ*, *162*, 815.

Peirani, S., Sonnenfeld, A., Gavazzi, R., Oguri, M., Dubois, Y., Silk, J., Pichon, C., Devriendt, J., & Kaviraj, S. (2019). Total density profile of massive early-type galaxies in HORIZON-AGN simulation: impact of AGN feedback and comparison with observations. *MNRAS*, *483*(4), 4615–4627.

Pellegrini, S., & Ciotti, L. (2006). Reconciling optical and X-ray mass estimates: the case of the elliptical galaxy NGC3379. *MNRAS*, *370*(4), 1797–1803.

Pen, U.-L., Lee, J., & Seljak, U. (2000). Tentative Detection of Galaxy Spin Correlations in the Tully Catalog. *ApJ*, *543*(2), L107–L110.

Penzias, A. A., & Wilson, R. W. (1965). A Measurement of Excess Antenna Temperature at 4080 Mc/s. *ApJ*, *142*, 419–421.

Planck Collaboration (2020). Planck 2018 results. VI. Cosmological parameters. *A&A*, *641*, A6.

Planelles, S., Borgani, S., Fabjan, D., Killedar, M., Murante, G., Granato, G. L., Ragone-Figueroa, C., & Dolag, K. (2014). On the role of AGN feedback on the thermal and chemodynamical properties of the hot intracluster medium. *MNRAS*, *438*(1), 195–216.

Plummer, H. C. (1911). On the problem of distribution in globular star clusters. *MNRAS*, *71*, 460–470.

Porciani, C., Dekel, A., & Hoffman, Y. (2002). Testing tidal-torque theory - I. Spin amplitude and direction. *MNRAS*, *332*(2), 325–338.

Postman, M., Coe, D., Benítez, N., Bradley, L., Broadhurst, T., Donahue, M., Ford, H., Graur, O., Graves, G., Jouvel, S., Koekemoer, A., Lemze, D., Medezinski, E., Molino, A., Moustakas, L., Ogaz, S., Riess, A., Rodney, S., Rosati, P., Umetsu, K., Zheng, W., Zitrin, A., Bartelmann, M., Bouwens, R., Czakon, N., Golwala, S., Host, O., Infante, L., Jha, S., Jimenez-Teja, Y., Kelson, D., Lahav, O., Lazkoz, R., Maoz, D., McCully, C., Melchior, P., Meneghetti, M., Merten, J., Moustakas, J., Nonino, M., Patel, B., Regös, E., Sayers, J., Seitz, S., & Van der Wel, A. (2012). The Cluster Lensing and Supernova Survey with Hubble: An Overview. *ApJS*, *199*(2), 25.

Power, C., Navarro, J. F., Jenkins, A., Frenk, C. S., White, S. D. M., Springel, V., Stadel, J., & Quinn, T. (2003). The inner structure of ΛCDM haloes - I. A numerical convergence study. *MNRAS*, *338*(1), 14–34.

Prada, F., Klypin, A. A., Cuesta, A. J., Betancort-Rijo, J. E., & Primack, J. (2012). Halo concentrations in the standard Λ cold dark matter cosmology. *MNRAS*, *423*(4), 3018–3030.

Press, W. H., & Schechter, P. (1974). Formation of Galaxies and Clusters of Galaxies by Self-Similar Gravitational Condensation. *ApJ*, *187*, 425–438.

Ragagnin, A., Dolag, K., Moscardini, L., Biviano, A., & D'Onofrio, M. (2019). Dependency of halo concentration on mass, redshift and fossilness in Magneticum hydrodynamic simulations. *MNRAS*, *486*(3), 4001–4012.

Ragagnin, A., Meneghetti, M., Bassini, L., Ragone-Figueroa, C., Granato, G. L., Despali, G., Giocoli, C., Granata, G., Moscardini, L., Bergamini, P., Rasia, E., Valentini, M., Borgani, S., Calura, F., Dolag, K., Grillo, C., Mercurio, A., Murante, G., Natarajan, P., Rosati, P., Taffoni, G., Tornatore, L., & Tortorelli, L. (2022). Galaxies in the central regions of simulated galaxy clusters. *arXiv e-prints*, (p. arXiv:2204.09067).

Ragone-Figueroa, C., Granato, G. L., Ferraro, M. E., Murante, G., Biffi, V., Borgani, S., Planelles, S., & Rasia, E. (2018). BCG mass evolution in cosmological hydro-simulations. *MNRAS*, *479*(1), 1125–1136.

Ramakrishnan, S., Paranjape, A., Hahn, O., & Sheth, R. K. (2019). Cosmic web anisotropy is the primary indicator of halo assembly bias. *MNRAS*, *489*(3), 2977–2996.

Reed, D., Gardner, J., Quinn, T., Stadel, J., Fardal, M., Lake, G., & Governato, F. (2003). Evolution of the mass function of dark matter haloes. *MNRAS*, *346*(2), 565–572.

Rees, M. J., & Sciama, D. W. (1968). Large-scale Density Inhomogeneities in the Universe. *Nature*, *217*(5128), 511–516.

Remus, R.-S., Burkert, A., Dolag, K., Johansson, P. H., Naab, T., Oser, L., & Thomas, J. (2013). The Dark Halo—Spheroid Conspiracy and the Origin of Elliptical Galaxies. *ApJ*, *766*(2), 71.

Remus, R.-S., Dolag, K., & Hoffmann, T. (2017a). The Outer Halos of Very Massive Galaxies: BCGs and their DSC in the Magneticum Simulations. *Galaxies*, *5*(3), 49.

Remus, R.-S., Dolag, K., Naab, T., Burkert, A., Hirschmann, M., Hoffmann, T. L., & Johansson, P. H. (2017b). The co-evolution of total density profiles and central dark matter fractions in simulated early-type galaxies. *MNRAS*, *464*(3), 3742–3756.

Remus, R.-S., & Forbes, D. A. (2021). Accreted or Not Accreted? The Fraction of Accreted Mass in Galaxies from Simulations and Observations. *arXiv e-prints*, (p. arXiv:2101.12216).

Rennehan, D., Babul, A., Hayward, C. C., Bottrell, C., Hani, M. H., & Chapman, S. C. (2020). Rapid early coeval star formation and assembly of the most-massive galaxies in the Universe. *MNRAS*, *493*(4), 4607–4621.

Retana-Montenegro, E., van Hese, E., Gentile, G., Baes, M., & Frutos-Alfaro, F. (2012). Analytical properties of Einasto dark matter haloes. *A&A*, *540*, A70.

Richstone, D. O. (1976). Collisions of galaxies in dense clusters. II. Dynamical evolution of cluster galaxies. *ApJ*, *204*, 642–648.

Roberts, I. D., van Weeren, R. J., McGee, S. L., Botteon, A., Ignesti, A., & Rottgering, H. J. A. (2021). LoTSS jellyfish galaxies. II. Ram pressure stripping in groups versus clusters. *A&A*, *652*, A153.

Robertson, H. P. (1935). Kinematics and World-Structure. *ApJ*, *82*, 284.

Rosati, P., Balestra, I., Grillo, C., Mercurio, A., Nonino, M., Biviano, A., Girardi, M., Vanzella, E., & Clash-VLT Team (2014). CLASH-VLT: A VIMOS Large Programme to Map the Dark Matter Mass Distribution in Galaxy Clusters and Probe Distant Lensed Galaxies. *The Messenger*, *158*, 48–53.

Rosati, P., Borgani, S., & Norman, C. (2002). The Evolution of X-ray Clusters of Galaxies. *ARA&A*, *40*, 539–577.

Rugh, S. E., & Zinkernagel, H. (2010). Weyl's principle, cosmic time and quantum fundamentalism.

Sachs, R. K., & Wolfe, A. M. (1967). Perturbations of a Cosmological Model and Angular Variations of the Microwave Background. *ApJ*, *147*, 73.

Sandvik, H. B., Möller, O., Lee, J., & White, S. D. M. (2007). Why does the clustering of haloes depend on their formation history? *MNRAS*, *377*(1), 234–244.

Sanford, P. W., & Ives, J. C. (1976). Ariel results on extragalactic X-ray sources. *Philosophical Transactions of the Royal Society of London Series A*, *350*(1663), 491–503.

Sarazin, C. L. (1988). *X-Ray Emission from Clusters of Galaxies*. Cambridge University Press.

Saro, A., Borgani, S., Tornatore, L., Dolag, K., Murante, G., Biviano, A., Calura, F., & Charlot, S. (2006). Properties of the galaxy population in hydrodynamical simulations of clusters. *MNRAS*, *373*(1), 397–410.

Saunders, W., Bridges, T., Gillingham, P., Haynes, R., Smith, G. A., Whittard, J. D., Churilov, V., Lankshear, A., Croom, S., Jones, D., & Boshuizen, C. (2004). AAOmega: a scientific and optical overview. In A. F. M. Moorwood, & M. Iye (Eds.) *Ground-based Instrumentation for Astronomy*, vol. 5492 of *Society of Photo-Optical Instrumentation Engineers (SPIE) Conference Series*, (pp. 389–400).

Schaye, J., Crain, R. A., Bower, R. G., Furlong, M., Schaller, M., Theuns, T., Dalla Vecchia, C., Frenk, C. S., McCarthy, I. G., Helly, J. C., Jenkins, A., Rosas-Guevara, Y. M., White, S. D. M., Baes, M., Booth, C. M., Camps, P., Navarro, J. F., Qu, Y., Rahmati, A., Sawala, T., Thomas, P. A., & Trayford, J. (2015). The EAGLE project: simulating the evolution and assembly of galaxies and their environments. *MNRAS*, *446*(1), 521–554.

Schmidt, W., Schmidt, J. P., & Grete, P. (2021). Turbulence in the intragroup and circumgalactic medium. *A&A*, *654*, A115.

Schulze, F., Remus, R.-S., Dolag, K., Burkert, A., Emsellem, E., & van de Ven, G. (2018). Kinematics of simulated galaxies - I. Connecting dynamical and morphological properties of early-type galaxies at different redshifts. *MNRAS*, *480*(4), 4636–4658.

Schwinn, J., Baugh, C. M., Jauzac, M., Bartelmann, M., & Eckert, D. (2018). Uncovering substructure with wavelets: proof of concept using Abell 2744. *MNRAS*, *481*(4), 4300–4310.

Schwinn, J., Jauzac, M., Baugh, C. M., Bartelmann, M., Eckert, D., Harvey, D., Natarajan, P., & Massey, R. (2017). Abell 2744: too much substructure for ΛCDM? *MNRAS*, *467*(3), 2913–2923.

Seitz, S., Thomas, J., & Halder, A. (2022). Strong gravitational lensing. Last accessed: 17.04.2022.
URL http://www.usm.lmu.de/Lehre/Lehrveranstaltungen/Praktikum/materials/gravlens/Strong_lensing_manual.pdf

Shaw, L. D., Weller, J., Ostriker, J. P., & Bode, P. (2006). Statistics of Physical Properties of Dark Matter Clusters. *ApJ*, *646*(2), 815–833.

Sheth, R. K., Mo, H. J., & Tormen, G. (2001). Ellipsoidal collapse and an improved model for the number and spatial distribution of dark matter haloes. *MNRAS*, *323*(1), 1–12.

Sheth, R. K., & Tormen, G. (1999). Large-scale bias and the peak background split. *MNRAS*, *308*(1), 119–126.

Shi, X. (2016). Locations of accretion shocks around galaxy clusters and the ICM properties: insights from self-similar spherical collapse with arbitrary mass accretion rates. *MNRAS*, *461*(2), 1804–1815.

Shi, X., Komatsu, E., Nagai, D., & Lau, E. T. (2016). Analytical model for non-thermal pressure in galaxy clusters - III. Removing the hydrostatic mass bias. *MNRAS*, *455*(3), 2936–2944.

Silk, J. (1968). Cosmic Black-Body Radiation and Galaxy Formation. *ApJ*, *151*, 459.

Smargon, A., Mandelbaum, R., Bahcall, N., & Niederste-Ostholt, M. (2012). Detection of intrinsic cluster alignments to 100 h^{-1} Mpc in the Sloan Digital Sky Survey. *MNRAS*, *423*(1), 856–861.

Smith, S. (1936). The Mass of the Virgo Cluster. *ApJ*, *83*, 23.

Smoot, G. F., Bennett, C. L., Kogut, A., Wright, E. L., Aymon, J., Boggess, N. W., Cheng, E. S., de Amici, G., Gulkis, S., Hauser, M. G., Hinshaw, G., Jackson, P. D., Janssen, M., Kaita, E., Kelsall, T., Keegstra, P., Lineweaver, C., Loewenstein, K., Lubin, P., Mather, J., Meyer, S. S., Moseley, S. H., Murdock, T., Rokke, L., Silverberg, R. F., Tenorio, L., Weiss, R., & Wilkinson, D. T. (1992). Structure in the COBE Differential Microwave Radiometer First-Year Maps. *ApJ*, *396*, L1.

Soucail, G., Fort, B., Mellier, Y., & Picat, J. P. (1987). A blue ring-like structure in the center of the A 370 cluster of galaxies. *A&A*, *172*, L14–L16.

Soucail, G., Mellier, Y., Fort, B., Mathez, G., & Cailloux, M. (1988). The giant arc in A 370 : spectroscopic evidence for gravitational lensing from a source at Z=0.724. *A&A*, *191*, L19–L21.

Spitzer, J., Lyman, & Baade, W. (1951). Stellar Populations and Collisions of Galaxies. *ApJ*, *113*, 413.

Springel, V. (2004). The largest N-body simulation of the universe. MPA research highlight of August 2004. Last accessed: 17.04.2022.
URL https://wwwmpa.mpa-garching.mpg.de/mpa/research/current_research/hl2004-8/hl2004-8-en.html

Springel, V. (2005). The cosmological simulation code gadget-2. *Monthly Notices of the Royal Astronomical Society*, *364*(4), 1105–1134.
URL http://dx.doi.org/10.1111/j.1365-2966.2005.09655.x

Springel, V. (2010). E pur si muove: Galilean-invariant cosmological hydrodynamical simulations on a moving mesh. *MNRAS*, *401*(2), 791–851.

Springel, V. (2010). E pur si muove:galilean-invariant cosmological hydrodynamical simulations on a moving mesh. *Monthly Notices of the Royal Astronomical Society*, *401*(2), 791–851.
URL http://dx.doi.org/10.1111/j.1365-2966.2009.15715.x

Springel, V., Wang, J., Vogelsberger, M., Ludlow, A., Jenkins, A., Helmi, A., Navarro, J. F., Frenk, C. S., & White, S. D. M. (2008). The Aquarius Project: the subhaloes of galactic haloes. *MNRAS*, *391*(4), 1685–1711.

Springel, V., White, S. D. M., Jenkins, A., Frenk, C. S., Yoshida, N., Gao, L., Navarro, J., Thacker, R., Croton, D., Helly, J., Peacock, J. A., Cole, S., Thomas, P., Couchman, H., Evrard, A., Colberg, J., & Pearce, F. (2005). Simulations of the formation, evolution and clustering of galaxies and quasars. *Nature*, *435*(7042), 629–636.

Springel, V., White, S. D. M., Tormen, G., & Kauffmann, G. (2001). Populating a cluster of galaxies - I. Results at [formmu2]z=0. *MNRAS*, *328*(3), 726–750.

Springel, V., Yoshida, N., & White, S. D. (2001). Gadget: a code for collisionless and gasdynamical cosmological simulations. *New Astronomy*, *6*(2), 79–117.
URL http://dx.doi.org/10.1016/S1384-1076(01)00042-2

Sunyaev, R. A., & Zeldovich, Y. B. (1972). The Observations of Relic Radiation as a Test of the Nature of X-Ray Radiation from the Clusters of Galaxies. *Comments on Astrophysics and Space Physics*, *4*, 173.

Takada, M., & Jain, B. (2003). The three-point correlation function in cosmology. *MNRAS*, *340*(2), 580–608.

Teklu, A. F., Remus, R.-S., Dolag, K., Arth, A., Burkert, A., Obreja, A., & Schulze, F. (2018). Declining Rotation Curves at z = 2 in ΛCDM Galaxy Formation Simulations. *ApJ*, *854*(2), L28.

Teklu, A. F., Remus, R.-S., Dolag, K., Beck, A. M., Burkert, A., Schmidt, A. S., Schulze, F., & Steinborn, L. K. (2015). Connecting Angular Momentum and Galactic Dynamics: The Complex Interplay between Spin, Mass, and Morphology. *ApJ*, *812*(1), 29.

Teyssier, R., Moore, B., Martizzi, D., Dubois, Y., & Mayer, L. (2011). Mass distribution in galaxy clusters: the role of Active Galactic Nuclei feedback. *MNRAS*, *414*(1), 195–208.

Thomson, J. J. (1906). *Conduction of electricity through gases*. Cambridge University Press.

Tignol, J.-P. (2001). *Galois' Theory of Algebraic Equations*. WORLD SCIENTIFIC.
URL https://www.worldscientific.com/doi/abs/10.1142/4628

Trayford, J. W., Theuns, T., Bower, R. G., Crain, R. A., Lagos, C. d. P., Schaller, M., & Schaye, J. (2016). It is not easy being green: the evolution of galaxy colour in the EAGLE simulation. *MNRAS*, *460*(4), 3925–3939.

Tremaine, S. D., & Richstone, D. O. (1977). A test of a statistical model for the luminosities of bright cluster galaxies. *ApJ*, *212*, 311–316.

Vajgel, B., Lopes, P. A. A., Jones, C., Forman, W. R., & Murray, S. S. (2014). Properties of Galaxy Groups Selected from Chandra X-ray Observations of the Boötes Field. In *Revista Mexicana de Astronomia y Astrofisica Conference Series*, vol. 44 of *Revista Mexicana de Astronomia y Astrofisica Conference Series*, (pp. 199–199).

van den Bosch, F. (2022). Theory of galaxy formation. Lecture notes, last accessed: 06.03.2022.
URL https://campuspress.yale.edu/astro610/

van den Bosch, F. C., Tormen, G., & Giocoli, C. (2005). The mass function and average mass-loss rate of dark matter subhaloes. *MNRAS*, *359*(3), 1029–1040.

van Kampen, E., Jimenez, R., & Peacock, J. A. (1999). Overmerging and mass-to-light ratios in phenomenological galaxy formation models. *MNRAS*, *310*(1), 43–56.

van Leeuwen, D. (2022). A julia package for gaussian mixture models (gmms). Last accessed: 02.04.2022.
URL https://github.com/davidavdav/GaussianMixtures.jl

Vijayaraghavan, R., & Ricker, P. M. (2013). Pre-processing and post-processing in group-cluster mergers. *MNRAS*, *435*(3), 2713–2735.

Vogelsberger, M., Genel, S., Springel, V., Torrey, P., Sijacki, D., Xu, D., Snyder, G., Nelson, D., & Hernquist, L. (2014). Introducing the illustris project: simulating the coevolution of dark and visible matter in the universe. *Monthly Notices of the Royal Astronomical Society*, *444*(2), 1518–1547.
URL http://dx.doi.org/10.1093/mnras/stu1536

Voit, G. M. (2005). Tracing cosmic evolution with clusters of galaxies. *Reviews of Modern Physics*, *77*(1), 207–258.

Voit, G. M., Kay, S. T., & Bryan, G. L. (2005). The baseline intracluster entropy profile from gravitational structure formation. *MNRAS*, *364*(3), 909–916.

Vulcani, B., Fritz, J., Poggianti, B. M., Bettoni, D., Franchetto, A., Moretti, A., Gullieuszik, M., Jaffé, Y., Biviano, A., Radovich, M., & Mingozzi, M. (2020). GASP XXIV. The History of Abruptly Quenched Galaxies in Clusters. *ApJ*, *892*(2), 146.

Wagoner, R. V., Fowler, W. A., & Hoyle, F. (1967). On the Synthesis of Elements at Very High Temperatures. *ApJ*, *148*, 3.

Walker, A. G. (1937). On Milne's Theory of World-Structure. *Proceedings of the London Mathematical Society*, *42*, 90–127.

Walker, S., Simionescu, A., Nagai, D., Okabe, N., Eckert, D., Mroczkowski, T., Akamatsu, H., Ettori, S., & Ghirardini, V. (2019). The Physics of Galaxy Cluster Outskirts. *Space Sci. Rev.*, *215*(1), 7.

Wang, H. Y., Mo, H. J., & Jing, Y. P. (2007). Environmental dependence of cold dark matter halo formation. *MNRAS*, *375*(2), 633–639.

Weisstein, E. W. (2022a). Circle-circle intersection. From MathWorld–A Wolfram Web Resource, last accessed: 06.03.2022.
URL https://mathworld.wolfram.com/Circle-CircleIntersection.html

Weisstein, E. W. (2022b). Quartic equation. From MathWorld–A Wolfram Web Resource, last accessed: 06.03.2022.
URL https://mathworld.wolfram.com/QuarticEquation.html

Weisstein, E. W. (2022c). Sphere point picking. From MathWorld–A Wolfram Web Resource, last accessed: 06.03.2022.
URL https://mathworld.wolfram.com/SpherePointPicking.html

Wetzel, A. R., Cohn, J. D., White, M., Holz, D. E., & Warren, M. S. (2007). The Clustering of Massive Halos. *ApJ*, *656*(1), 139–147.

Wetzel, A. R., & White, M. (2010). What determines satellite galaxy disruption? *MNRAS*, *403*(2), 1072–1088.

White, M., Cohn, J. D., & Smit, R. (2010). Cluster galaxy dynamics and the effects of large-scale environment. *MNRAS*, *408*(3), 1818–1834.

White, S. D. M. (1984). Angular momentum growth in protogalaxies. *ApJ*, *286*, 38–41.

Wilkinson, A., Almaini, O., Chen, C.-C., Smail, I., Arumugam, V., Blain, A., Chapin, E. L., Chapman, S. C., Conselice, C. J., Cowley, W. I., Dunlop, J. S., Farrah, D., Geach, J., Hartley, W. G., Ivison, R. J., Maltby, D. T., Michałowski, M. J., Mortlock, A., Scott, D., Simpson, C., Simpson, J. M., van der Werf, P., & Wild, V. (2017). The SCUBA-2 Cosmology Legacy Survey: the clustering of submillimetre galaxies in the UKIDSS UDS field. *MNRAS*, *464*(2), 1380–1392.

Wilkinson, A., Almaini, O., Wild, V., Maltby, D., Hartley, W. G., Simpson, C., & Rowlands, K. (2021). From starburst to quiescence: post-starburst galaxies and their large-scale clustering over cosmic time. *MNRAS*, *504*(3), 4533–4550.

Wolf, M. (1901). Ein merkwürdiger Haufen von Nebelflecken. *Astronomische Nachrichten*, *155*, 127.

Wolf, M. (1906). Über einen Nebelfleck-Haufen im Perseus. *Astronomische Nachrichten*, *170*, 211.

Xu, G. (1995). A New Parallel N-Body Gravity Solver: TPM. *ApJS*, *98*, 355.

Yahagi, H., Nagashima, M., & Yoshii, Y. (2004). Mass Function of Low-Mass Dark Halos. *ApJ*, *605*(2), 709–713.

Zeldovich, Y. B. (1972). A hypothesis, unifying the structure and the entropy of the Universe. *MNRAS*, *160*, 1P.

Zwicky, F. (1933). Die Rotverschiebung von extragalaktischen Nebeln. *Helvetica Physica Acta*, *6*, 110–127.

Zwicky, F. (1937). Nebulae as Gravitational Lenses. *Physical Review*, *51*(4), 290–290.

Acknowledgments

What an interesting and exciting year this has been. This work represents the culmination of countless discussions at all hours of the day (and night), of much encouragement and creative input. It would not have been possible without all of the wonderful people around me, for which I thank you all. However, I would like to extend my gratitude to a few people in particular.

First and foremost I would like to thank Klaus Dolag, for the opportunity to work on this fascinating topic as well as the unending support throughout this year. Your accommodations with digital meetings and around-the-hour feedback have been invaluable to me, for which I thank you. Much to learn I still have, but deliver my best I will. Then, I would like to thank Andreas Burkert, for your interest and helpful suggestions during this year, as well as the space for exciting scientific discussions which you have provided. I would also like to thank Veronica Biffi for the insightful explanations and for the time which you took week after week.

I would like to thank Rhea-Silvia Remus for the countless moments of inspiration which you provided whenever I hit a brick wall, and for the countless hours of theory debating. Thank you for being you. I am also thankful to Lucas Valenzuela, for the numerous helpful programming tips and tricks as well as the poignant comments without which I would never have gotten this far.

I would then like to thank my family, for far too many things to list here. The support which you provide me is unparalleled, and I am grateful for all the conversations and the good food whenever I've forgotten to cook again. I would also like to thank my friends, who have weathered once more my desire to enrich all of those around me with physics fun facts. I hold all of you very dearly.

Selbstständigkeitserklärung

Hiermit erkläre ich, die vorliegende Arbeit selbstständig verfasst zu haben und keine anderen als die in der Arbeit angegebenen Quellen und Hilfsmittel benutzt zu haben.

München, [22.04.2022]

_____

Lucas C. Kimmig